ANALYSIS OF TUMOUR ANGIO-ARCHITECTURE AND BLOOD FLOW USING MICROCOMPUTED TOMOGRAPHY AND LATTICE BOLTZMANN SIMULATIONS

BY

AMOS AKINOLA FOLARIN

Bioinformatics Group, Academic Department of Oncology, Royal Free and University College Medical School, Royal Free Campus, University College London, NW3 2PF.

Submitted in fulfilment of the degree of Doctor of Philosophy at the University of London

Principal supervisor: Dr Sylvia Nagl

30 September 2007

ProQuest LLC
789 East Eisenhower Parkway
P.O. Box 1346
Ann Arbor, MI 48106-1346

Abstract

The precise architecture of the vascular system is critical to its many specialised functions. In sharp contrast tumour vascular architecture is highly disorganised and dysfunctional. The reason for this is the grossly abnormal angiogenic signalling prevalent in the tumour microenvironment. Aberrant tumour vasculature is a key determinant of spatial and temporal heterogeneities of blood flows. Additionally, irregularities in the tumour vascular wall, a lack of functional lymphatics and a severely retarded trans-mural hydrostatic pressure gradient also diminish convective transport out of the vessels. Diffusion therefore remains the dominant transport mode in tumours and presents a considerable barrier to macromolecular therapy (e.g. Antibody-directed enzyme prodrug therapy (ADEPT)).

A number of recent studies of vascular morphology in both clinical and xenograft tumours have demonstrated the existence of type-specific architectures. Precisely how these type-specific architectures translate to blood flow through the vascular system had not been determined. To address this we have developed a method for studying the 3D architecture of the tumour and simulating flows through it. This technique uses corrosion casts to capture the 3D tumour vascular system. 3D morphometry was determined by stereoimaging and X-ray micro-computed tomography. A computational fluid dynamics model was then used to study the hydrodynamics of the vascular networks.

My results show that vessel structure and architecture varies in clinical colon cancers, but these differences were substantially smaller than those of two human colorectal xenografts (LS147T and SW1222) commonly used in pre-clinical studies. The results also provide evidence that LS147T is, in general, a closer model to most clinical colorectal tumours than SW1222.

To our knowledge this is the first attempt to utilise X-ray micro-computed tomography to study vascular corrosion casts of tumours, and using this data, produce 3D flow profiles.

Contents

CHAPTER 4: Comparative study of colonic tumour vascular architecture

CHAPTER 5: Blood flow simulation in tumour vasculature

Chapter 6: Further work and development

Figures

Tables

Acknowledgements

This thesis details the work carried out between 2003-2007 in England (University College London, UCL), Germany (University of Mainz) and Finland (University of Jyvaskyla).

I firstly extend thanks to my supervisors on this project Dr Sylvia Nagl, Dr Barbara Pedley and the staff at UCL's Academic Department of Oncology. I would also like to thank my collaborators, Professor Moritz Konerding (University of Mainz), Professor Babatunde Ogunnaike (University of Delaware), Professor Jussi Timonen, Keijo Mattila, Dr Marko Myllys and Dr Jari Hyväluoma (University of Jyvaskyla) for their continued assistance and advice on the production of vascular corrosion casts, X-ray micro-computed tomography and Lattice Boltzmann Simulations used throughout this project. The financial support of the Medical Research Council (MRC) and University of Jyvaskyla is also gratefully acknowledged.

Finally, I should like to thank Laura Seabright and my family for their constant support and encouragement during this work.

Declaration

I, Amos Akinola Folarin, confirm that the work presented in this thesis is my own. Where information has been derived from other sources, I confirm that this has been indicated in the thesis.

.....

Amos Akinola Folarin
Date:

Amos Folarin, September 2007

CHAPTER 1: Introduction

1.1 Introduction, problem definition and objectives

Animal model systems of tumours have been used extensively in the study of tumour biology [Kubota, 1994] and drug development research [Pedley et al., 2001;Sharma et al., 2005]. However there are significant limitations to the experimental studies which can be carried out on human tumours *in-situ,* so animal model systems are been used to bridge this gap. These animal models broadly fall into two categories: xenografts and induced tumours. There are however shortcomings with both systems. In xenografts, human tissue is being grown in animal tissue (either orthotopically or ectopically) whereas with induced tumours an animal tumour resides within animal tissue. Neither system adequately replicates the behaviour of clinical tumours and so it is often the case that therapies will display entirely different responses in the model system [Rofstad, 1994;Goldbrunner et al., 2004;Retsky et al., 1994;Tan et al., 2005].

Modern computing advances have now raised the possibility of modelling many aspects the human-tumour *in-silico* [Alarcon et al., 2004]. The concept proposed here is similar in kind to projects such as the Cardiome heart model [Bassingthwaighte et al., 1998;Smith et al., 2000], BEACON liver projects [UCL BEACON project, 2007] and Microcirculation Physiome [Popel et al., 1999;Popel et al., 1998].

A tumour is a vastly complicated biological system. Time and length scale ranges involved in biological systems have until recently been inhibitive to integrative *in-silico* biology. It is however possible to approach this by considering important constituents of the system, as small collectives, which satisfy the objectives of the model. With this in mind, the project focus was centred on modelling the tumour vascular architecture and blood flow through this structure. The vascular system plays a crucial part in the delivery of intravenous therapy, nutrients and tissue oxygen. In a tumour, tissue oxygenation affects metabolic rates, cell division and radiotherapy (including some chemotherapy) efficacy [Vaupel et al., 1989]. The central role played by the vascular system in tumour physiology makes it a high priority for any tumour model. Consequently a morphologically accurate model of the tumour vascular system would provide an excellent framework to incorporate other components such as cells, extracellular matrix and therapeutic agents at a later date with the possibility for its use in simulations of the tumour: growth, microenvironment and therapeutic delivery.

The principal objectives of this thesis are:

I. To provide a characterisation of the vasculature in human colorectal cancer (adenoma/carcinoma) and experimental colorectal tumours grown as xenografts in nude mice.
II. Provide a novel system for defining three-dimensional geometries for use in blood flow models.
III. To provide new paradigms and methodologies to tackle microvascular blood flow models.
IV. Provide a characterisation of blood flow in the different vascular systems of the model tumours.
V. Demonstrate possibility for modelling flow in whole tumour vascular systems represented by a whole xenograft tumour.

[Chapters 1&2] provide a review of the biological background of cancer, tumour angiogenesis (vessel formation) and the biological models currently in use. A review of computational models of (i) vascular network formation and (ii) blood flow was carried out in [Chapter 3]. Aims 1& 2 are addressed in [Chapter 4]. Aims 3, 4 & 5 are addressed in [Chapter 5]. Considerations of future work and extensions to the project are discussed in [Chapter 6].

1.2.1 Cancer

In the industrialised world cancer is currently only surpassed by cardiovascular disease as the leading cause of disease related fatalities. It is estimated by the World Health Organisation (WHO) that approximately six million people die each year from various forms of cancer. Further to this, as cancer is predominantly an age linked disease, this figure is expected to increase as the average population life expectancy rises.

The process of oncogenic transformation can broadly be depicted as the loss of control over cell division in conjunction with cellular immortalisation. Although these processes are highly regulated with many layers of control, these are often breached

sequentially over the transformation process in some cases taking several years from the first transformation event. Generally cells are most vulnerable to mutation during the process of division where changes are readily incorporated into the newly synthesised DNA. For this reason, tissues which continuously undergo cell division are more commonly associated with cancer than others (immune cells, gut lining, skin cells). These Mutations are generally the result of oncogenic agents which can be classed into physical, chemical and biological groups, each with their own particular mode of producing changes at the DNA level. Physical agents (e.g. X-rays or UV-light) and chemical agents (e.g Ethyl-nitroso-urea) produce chemical changes to DNA bases. Whereas biological agents such as viruses (e.g. Human Papillomaviruses) and bacterial (e.g. Agrobacterium Tumefaciens) act by inserting genes into the cell/genome, these insertions may directly disrupt endogenous genes or induce new oncogenic behaviour through newly introduced genes. Mutations can arise spontaneously at the level of individual nucleotides or during the normal 'cross-over' mechanism through which chromosomes exchange genetic material. The resulting effects of oncogenic transformations are modifications of oncogene and/or tumour suppressor gene expression through which the tumour phenotype is realised.

While the causes of cancer originate at the microscopic (intracellular) scale, the mesoscopic (cellular) and macroscopic (tissue) scales are also vitally important in the development of the tumour. The cellular scale orchestrates processes such as migration of metastatic cells, angiogenesis and hypoxia. Tissue level events include blood flow and the tumour invasion front.

Angiogenesis is requirement for a tumour to develop beyond the 1-2 mm diameter [Folkman et al., 1989]. Through this process the tumour actually sequesters the body's own blood supply to nourish its demand for metabolites. The endogenous system for stimulating angiogenesis is hijacked by the tumour to its own ends. This process is not properly regulated when induced by cancer, resulting in highly aberrant vascular architecture.

Due to the pleiotropic nature of cancer, treatments for it are considerably wide ranging. Traditional chemotherapeutics have tended to favour small molecular weight agents, but in the post-genomic era this is now changing. The majority of new therapeutics in

development are principally macromolecular i.e. protein, nano-particle (liposomes and viruses) and cellular. One of the common obstacles to the efficacy of these macromolecular therapies is their poor delivery profiles. These delivery profiles are characterised by heterogeneous distribution and reduced transvascular and interstitial transport within the tumour.

1.2.2 Colo-rectal cancers

Colorectal cancers are the second and third most common cause of cancer related death in the United States and UK respectively. As can be seen in [Figure 1.1] an encouraging reduction in mortality rates of 26% in men and 42% in women has been achieved over the last 35 years [Office For National Statistics, 2006]. As with many cancers, colorectal cancer is primarily age linked, with presentation most frequent in patients older than 50 years, incidence peaking within the range of 60-70 years of age.

Figure 1.1. Colorectal cancer mortality rates

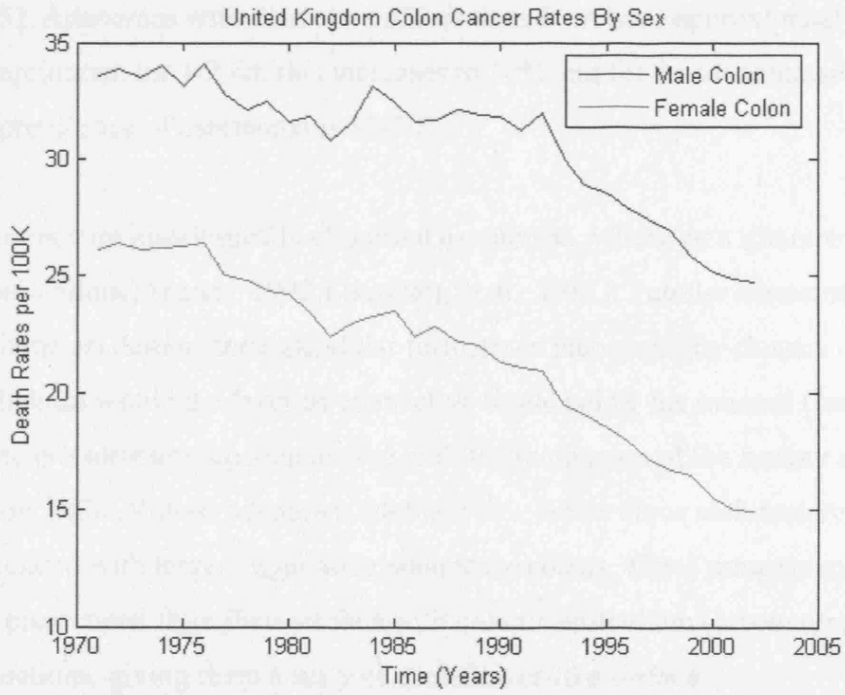

Figure 1.1. Rates of colon cancer mortality over the last 30years, by sex. Data have been age standardised using the European standard population [Office For National Statistics, 2006].

Adenomas are found in 5-10% of asymptomatic patients older than 40 years old. The presence of adenoma polyp(s) within the bowl indicates the transformation of the colonic mucosa into a premalignant state.

The progression of adenoma to carcinoma has been well substantiated [Muto et al., 1975]. Evidence to support this includes: 1) a similar mapping of adenomas and carcinomas in the colon, 2) comparative prevalence of adenomas and carcinomas in the populations having varied colonic cancer risk levels, 3) increased risk of carcinoma in patients with adenomas and the subsequent decrease of carcinoma risk in patients where adenomas have been removed and 4) the similarity of DNA constitution of adenomas and carcinomas. Although approximately 5% of adenomas will progress to form a carcinoma, the presence of adenomatous growths is not a prerequisite for carcinoma formation. On occasion a carcinoma may arise from premalignant areas of dysplasia within the flat mucosa.

The propensity of the adenoma to progress into adenocarcinoma has been noted to depend primarily on size and histological classification [Buetow et al., 1995;Muto et al., 1975]. Adenomas with diameters of less than 1 cm have approximately a 1% prevalence of carcinoma, for 1-2 cm this increases to 10% and for an adenoma greater than 2 cm the prevalence of carcinoma is 30-50%.

Adenoma are histologically classified as: tubular, villous or a mixture of both (tubulovillous) [Potter, 1992;Eisenberg et al., 1982]. Tubular adenomas (typically 1 cm in diameter) demonstrate glandular formations incorporating clusters of colonic epithelium within the layer of connective tissue below the mucosa (*lamina propria).* These are sometimes pedunculated with the main mass of the tumour extended on a narrow stalk. Villous adenomas (defined by >80% villous architecture) are often associated with larger, aggressive adenocarcinomas. These tumours exhibit thin branch-like projections from their surface with colonic epithelium surrounding these projections, giving them a furry or cauliflower-like surface.

Characteristics of the adenocarcinoma often depend on location within the colon. Adenocarcionmas on the right side (ascending colon) are usually polypoid tumours, and may be associated with chronic bleading and intussusception. On the left side

(descending colon), annular constricting lesion are more commonly observed; these tumours spread through the circumferential lymphatics of the muscularis propria (a concentric layers of muscle below the mucosa) resulting in reduction of the bowel lumen.

A number of genetic anomalies are known to be associated with around 6% of colorectal carcinoma. These include familial adenomatous polyposis coli syndrome, hereditary nonpolyposis colon cancer syndrome and certain hamartomatous polyposis syndromes. Patients with familial polyposis of the colon (FPC), traced to an abnormality in chromosome 5q, develop numerous adenoma polyps at a mean age of 40 years (20 years before presentation of non-FPC related colorectal cancers in the general population). Due to increased time available for progression and the large number of polyps, patients with FPC have a greatly increased risk of developing adenocarcinoma[Nishisho et al., 1991;Buetow et al., 1995].

The colon carcinomas are staged according to their growth characteristics. Older staging schemes such as the original Dukes and Astler-Coller classification methods have to some extent been replaced by the Tumour-Node-Metastasis (TNM) classification [Sobin and Wittekind, 2002]. The TNM scheme provides classification based on the extent of tumour invasion, lymph node invasion and metastasis. From the gut lumen-wall going outward, the layers of the bowel are mucosa (comprised of epithelium, basement membrane, lamina propria, muscularis mucosae), submucosa, muscularis propria, subserosa [Figure 1.2].

In contrast to other gastrointestinal cancers there is no significant difference between colon carcinoma *in-situ* (confined to the epithelium) and intramucosal colon carcinoma (inclusive of tumours extending into the lamina propria) due to the colonic lamina propria's lack of lymphatics. Adenocarcinomas are consequently only considered invasive once they have entered the submucosa, where they have access to the local lymphatic system. At this point the risk of metastasis rises with increasing penetration of the disease. Metastases from colon carcinoma are most regularly seen in the liver with 75% of cases localised to this organ. The high incidence of liver metastatic disease from colon carcinoma is primarily due to drainage of the portal vein from the colon. Rectal carcinoma may additionally drain into the systemic venous system and therefore

may manifest disease in other areas of the body bypassing the liver; it is otherwise uncommon to observe more distant metastasis without associated disease in the liver.

Figure 1.2 A cross-section of the colon

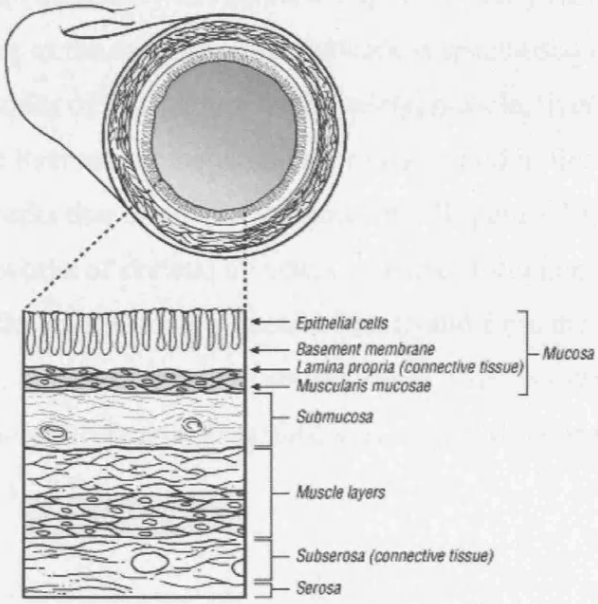

Figure 1.2. A cross-section of the colon showing the different layers of tissue [Patientcenters, 2007].

In addition to the metastatic importance of the vascular system in colorectal cancers, there is evidence of distinctive vascular structure in adenomas and adenocarcionmas of the colon [Konerding et al., 2001]. Pavalopolos *et al.* studied several parameters in relation to the vascular morphology, this study highlights an inverse correlation between microvascular density and Dukes stage classification of the colorectal tumours studied. Vessel shape parameters, and branching frequencies in this study were also found to be significantly different in both adenomas and carcinomas [Pavlopoulos et al., 1998].

1.3 The micro-vascular system

The properties of blood flow through the vascular system are highly dependent on the geometry of the network [Popel and Johnson, 2005]. A microvascular network consists of a number of vessels supplied by one or more feeding arterioles and drained by one or more collecting venules. These networks are usually three dimensional in structure (exceptions such as the mesentery and retina are approximately two-dimensional). The characteristic structure of the microvascular network is specialised to the function of the tissue of origin; examples of vasculature from skeletal muscle, liver and gut are shown in [Figure 1.3]. In the liver where the vasculature is involved in filtration, sinusoids form hexagonal networks that drain into a central vein [Figure 1.3 (A)]. In the microvasculature networks of skeletal muscle, capillaries form numerous parallel channels enabling efficient transport of metabolites to and from the fibrils of muscle cells [Figure 1.3 (B)]. In the colon where absorption of water is carried out, the sub-mucosa capillary network form a large surface area with a hexagonal/rhomboidal geometry [Figure 1.3 (C&D)].

Figure 1.3. Vascular architecture in different organs

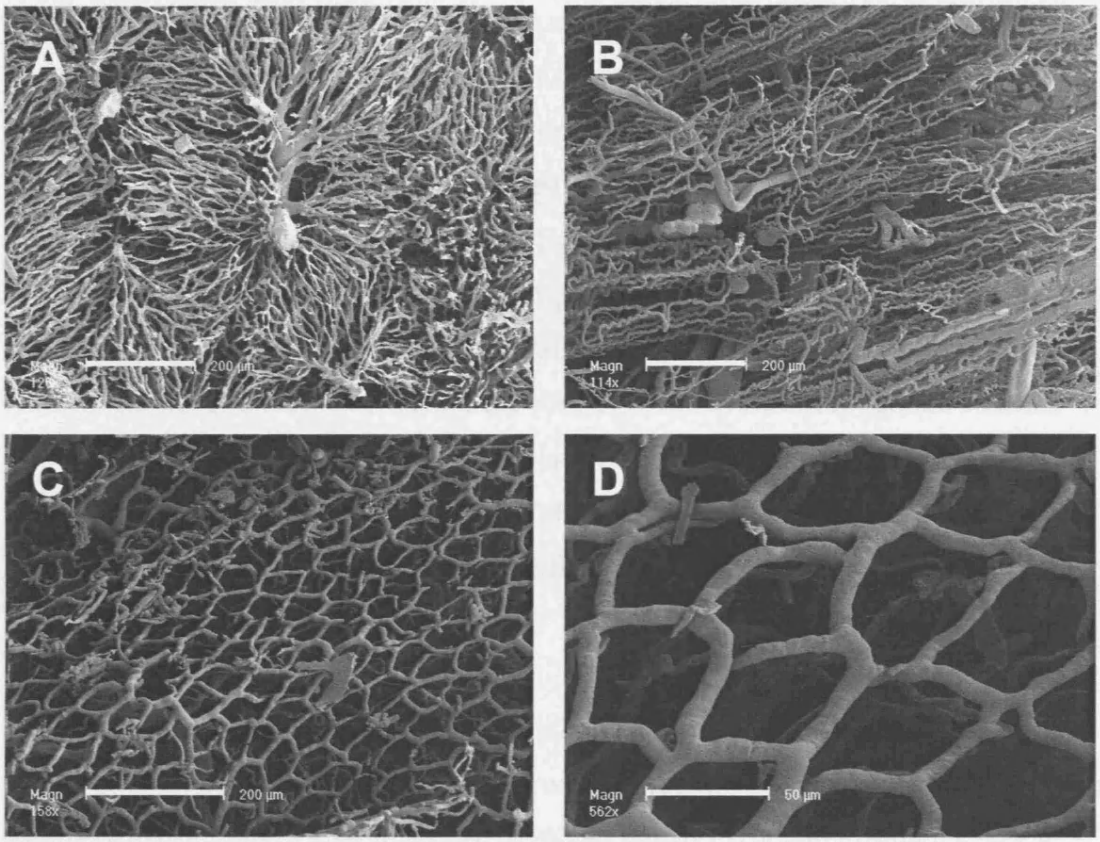

Figure 1.3. Examples of different vascular morphology as demonstrated by corrosion casting in (A) Liver islet vessels, (B) Skeletal Muscle, (C) Low resolution Colon and (D) high resolution colon. (A-C) bar = 200µm and (D) bar = 50µm. Images were donated by Professor Moritz Konerding.

Blood pumped from the heart extends through the aorta down a series of roughly cylindrical vessel elements. The portion of vasculature proximal to the capillary bed is termed the arterial side (decreasing vessel diameter, and length) and the vasculature distal to the capillary bed is termed the venular side (increasing vessel diameter and length). The thickness of vessel wall throughout the vascular system varies with vessel calibre. This vessel wall from the inside-out consists of a hydrated glycoprotein layer, endothelial cells, basement membrane, smooth muscle and concentric layers of connective tissue. The function of the wall in the arterial side is to store hydrostatic pressure and regulate blood flow; here it is thick and elastic. By comparison in the capillary system, the wall is thin and fenestrated to facilitate bi-directional transport.

The arteriolar vessels are characterised by elongated endothelial cells (which are aligned axially with the shear forces in the vessels). In many organs the arterioles are structured with an arcade arrangement in vessels ≥25μm diameter and a sequential, tree-like branching morphology in smaller arterioles. Flow in the arterioles is dependent on the status of the cardiac cycle. In the larger arterial vessels, flow is markedly pulsatile. This oscillating velocity is increasingly stabilised as blood extends distally through the arterial system. The decreasing diameter of vessels through the arterial side of the network results in increasing intra-vascular pressure. This is highest in the arterioles where the ratio of the vessel diameter to wall thickness is largest (arteriolar walls are both elastic and contractile). Much of the control of blood flow through the vascular system is performed by altering the arteriolar vessel diameter (through smooth muscle layer contraction/relaxation). The effect of this can be quite dramatic, according to Poiseuille's law [Section 3.3.2] a 2 fold uniform drop in the vessel radius leads to a 16 times drop in net flow.

The capillary vessels are composed of endothelial cells which are in turn covered by a patchwork of pericyte cells and finally the whole structure is embedded within the basal lamina (a dense form of specialised extracellular matrix). Though capillaries lack a smooth muscle layer, they may retain some contractile function through the pericyte cells [Yamagishi and Imaizumi, 2005]. The capillary network constitutes to the bulk of the vascular system. These vessels are all fairly narrow with a diameter generally less than 10μm [Bloor, 1968]. In the peripheral circulation the capillary surface area constitutes around $70m^2$ in an average human. This large surface area is integral to effective transmural transport (both convective & diffusive). Interstitial fluid transfer occurs through specialised channels such as aquaporins and inter-endothelial clefts (fenestrations) or pores. Pore size may be affected by angiogenic factors such as Vascular Endothelial Growth Factor which induces motility in endothelial cells [McDonald and Baluk, 2002].

On the luminal side of the capillary is a 1μm glycocalyx consisting of glycoproteins, glycosaminoglycans and proteo-glycans [Pries et al., 2000] [Desjardins and Duling, 1990]. This hydrated polysaccharide layer performs an important role in lubrication of red blood cell passage and modulating the hydrodynamic resistance. A six fold flow

resistance is attributed to the presence of the glycocalyx in the capillaries, due to the effective reduction in vessel calibre [Secomb et al., 2002].

The post-capillary venules, around 6-8μm in diameter, collect blood directly from the capillaries and transport it to the veins. These vessels, like capillaries, also lack a smooth muscle layer where diameter is <50μm. The venous and arteriolar networks are similar in branching architecture except the venous vessels are more numerous, with individual vessel elements shorter and wider. The endothelial cells lining the venules like the arterioles have a characteristic shape and can be identified by their rounder form.

CHAPTER 2: Studying the tumour vascular system

2.1 Tumour angiogenesis

Unlike normal vasculature, tumour vessels are both structurally and functionally abnormal, resulting in spatial and temporal heterogeneity of blood flow through the tumour vascular network. The resulting microenvironment is characterised by interstitial hypertension, hypoxia and acidosis[Jain, 1999;Munn, 2003]. While adaptations in cancer cell metabolic behaviour (e.g. Warburg Effect) enables their survival in this environment, the delivery and efficacy of nutrient and therapeutic delivery are greatly reduced and greatly heterogeneous in distribution.

In order for an *in-vivo* tumour to grow beyond 1mm in diameter, the so-called avascular stage, it must recruit the host vascular system to supply nutriment and oxygen to its cells by stimulating angiogenesis. Angiogenesis is a complex, multi-step process involving endothelial cell activation, proliferation, migration, degradation of the extracellular matrix, and normally only occurs during wound healing, embryogenesis, and regeneration of the uterus lining. While the molecular components of angiogenesis are mostly known, the precise manner with which they orchestrate the growth and development of angiogenesis is still poorly understood.

There are a great number of angiogenesis mediators [Table 2.1] which arise from a range of sources: cancer cells, extracellular matrix, stromal cells, blood, and endothelial cells. The most studied of these factors is the Vascular Endothelial Growth Factor (VEGF) family [Cheung et al., 1998;Grunstein et al., 1999;Holash et al., 1999]. This group of chemokines is mainly under the regulation of the Hypoxia Response Element (HRE) and its transcription factor Hypoxia Inducible Factor-1 (HIF) [Bando et al., 2003]. Hypoxia or low pO_2 is not the only trigger of angiogenic factors; others include low pH, and hypoglycaemia.

Table 2.1 Angiogenesis factors	
Activators	***Function***
VEGF family members	Stimulate angiogenesis, vessel permeability
VEGFR1, NRP-1	Integrate angiogenic and survival signals
Ang1 and Tie2	Stabilize vessels, Reduce permeability
PDGF-BB and receptors	Recruit smooth muscle cells
TGF-β, endoglin, TGF-β receptors	Stimulate extracellular matrix production
FGF, HGF, MCP-1	Stimulate angiogenesis and arteriogenesis
Integrins	Receptors for macromolecules
VE cadherin; PECAM (CD31)	Endothelial junction molecules
Ephrins	Regulate arterial/venous specification
Plasminogen activators, MMPs	Remodel matrix, release and activate growth factors
PAI-1	Stabilise nascent vessels
NOS;COX-2	Stimulate angiogenesis and vasodilation
AC133	Regulate angioblast differentiation
Chemokines	Pleiotropic role in angiogenesis
Id1/Id3	Determine endothelial plasticity
Table 2.1. Adapted from [Carmeliet and Jain, 2000]	

In the current schematic VEGF from hypoxic tumour cells diffuses into the surrounding tissue and initiates growth of vascular sprouts from existing vessels. These sprouts migrate towards and penetrate the tumour forming its vascular system. This new vascular system does not develop in the same manner as in the surrounding tissue, [Konerding et al., 1999;Konerding et al., 1995]. Grunstein *et al.* demonstrate a schematic for the action of the VEGF isoforms in recruitment and expansion of tumour vasculature [Figure 2.1]. It is likely that the isoforms function in concert to initially recruit peripheral vessels then expand tumour vascularisation. The ability to induce vascular expansion appears related to the heparin binding capacity of the VEGF isoform which determines how strongly it is associated with the extracellular matrix (ECM). Recruitment of host vessels requires diffusible isoform with fewer heparin binding domains; the converse is true for the vascularisation process. Yu *et al.* demonstrate this behaviour in a study on the ability of VEGF isoforms to recover angiogenic potential of a VEGF-negative melanoma cell line. $VEGF_{121}$, $VEGF_{165}$ and $VEGF_{189}$ have none, one,

or two, heparin binding domains respectively, due to their differential splicing. The number of heparin binding domains strongly affects diffusibility of the cytokine within the interstitium. $VEGF_{189}$ has such a high affinity for the ECM that it remains bound to the periphery of its producing cell. The resulting vascular phenotypes of the rescued melanomas exhibit dramatically different vascular architectures [Yu et al., 2002].

Other factors also appear to affect the structure of the vascular system. Konerding *et al.* studied the effects of a different angiogenesis factor, FGF-2 on the vascular architecture of HEC-1-B cells. FGF-2 expressing cells were found to produced more tortuous vasculature with wider vessel diameters compared to controls [Konerding et al., 1998]. Giavazzi *et al.* also investigated the effects of FGF-2 and found a synergistic effect between VEGF and FGF-2 on tumour vascularisation [Giavazzi et al., 2003]. In another study, deficiency in matrix metalloprotease (MMP-9) was shown by Chantrain *et al.* to result in a dramatic reduction of microvascular density and size in neuroblastoma tumours [Chantrain et al., 2004].

The angiogenic sprouts tip cells are currently a highly active research area. These filopodia in turn guide the motion of the whole sprout and hence structure of the nascent vessel. Factors which affect the guiding of these sprouts tip cells may shed some light on where the deregulation is occurring in tumour angiogenesis and how these processes result in tumour specific vascular architectures. Recently, the filopodia of sprout tip cells have been shown to be affected by factors such as neutropillin-1 and VEGF [Gerhardt et al., 2004]. Disruption or removal of VEGF gradients are also shown to prevent the correct navigation of the filopodia [Gerhardt et al., 2003].

Figure 2.1. Action of VEGF isoforms in tumour angiogenesis

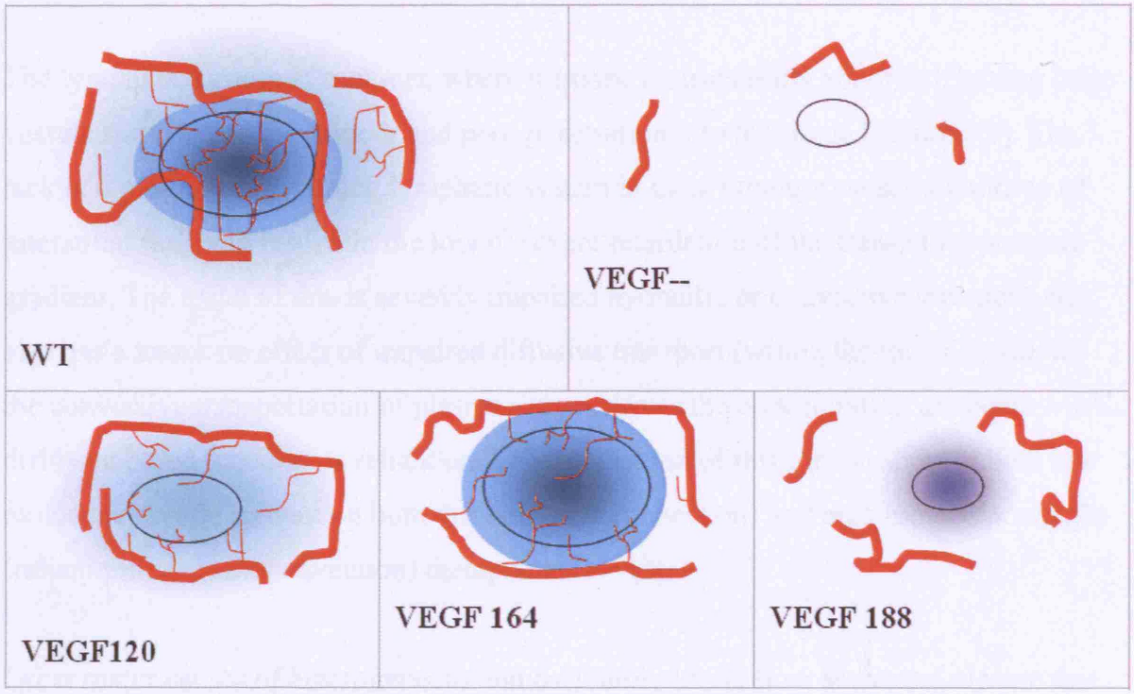

Figure 2.1. A proposed model of tumour VEGF signalling gradient. WT is the normal tumour type expressing all VEGF isoforms, VEGF-- is a VEGF knockout tumour line expressing no VEGF and hence is largely avascular. VEGF120 produces a diffuse signal (light blue) which recruits peripheral vessels but does little to vascularise the tumor itself. VEGF164 can both recruit vessels with a partially diffusible signal and vascularise the tumor with a partially cell-associated signal. VEGF188 fails to adequately recruit the host vasculature, but vascular endothelium which is captured forms a hypervascular capillary network due to the high local concentration of VEGF. Adapted from [Grunstein et al., 2000]

Tumour vasculature is characterised as being 'chaotic', this description more specifically arises from the vessels tortuous paths, loss of hierarchy, blind-endings and heterogeneous vessel calibres and densities. Additionally most tumours are characterised by leaky vasculature, with enlarged pores, reduced basement membrane, smooth muscle and pericyte coverage [Munn, 2003]. In a number of recent studies that differentially mark tumour cells and vascular endothelium, the vascular architecture is often observed to be composed of a mosaic of both cell types. These studies suggest incorporation of tumour cells into the endothelium is a likely precursor step to metastases [Ruoslahti, 2002;Carmeliet and Jain, 2000]. In some cases there is also evidence for vascular mimicry [Figure 2.2] [McDonald et al., 2000;Maniotis et al.,

1999], a phenomenon where tumour cells form vessel-like channels, lined with extracellular matrix rather than endothelial cells.

The lymphatic system in tumours, where it exists, is structurally abnormal, having large vessels surrounding the tumour and poor penetration into the tissue [Figure 2.2]. The lack of a properly functioning lymphatic system in most tumours causes a build-up of interstitial fluid and results in the loss or severe retardation of the transmural pressure gradient. The result of this is severely impaired hydraulic or convective transport, and also has a knock on effect of impaired diffusive transport (within the intersititum), as the convective transportation of plasma solutes drives the concentration gradients which diffusion based transport is reliant on. The implication of this for transport of both low molecular weight (reliant on both diffusion and convection) and high molecular weight (reliant primarily on convection) therapeutics is vast.

Other major causes of heterogeneous and oscillatory blood flow are vessel closure due to oncotic pressure on the vascular wall, caused by lack of contact inhibition, high interstitial fluid pressure (IFP) [Mollica et al., 2003], and microthrombi [Munn, 2003]. It is the abnormal structural architecture of the tumour vasculature that is primarily responsible for reduced delivery of metabolites in the tumour; coupled with the increased burden of highly metabolically active cells, these factors result in a spatial patterning of normoxia, hypoxia and necrosis in the tumour mass [Figure 4.3].

The prominent role of abnormal vasculature as a general component of solid tumours has established it as a prime target for therapy [Longo et al., 2002], with anti-vascular agents (e.g. Combretastatin-A4-P) and anti-angiogenic agents (e.g. Bevacizumab (Avastin®)) recently receiving licenses for treatment of colon cancers.

Figure 2.2. Vascular anomalies in tumours

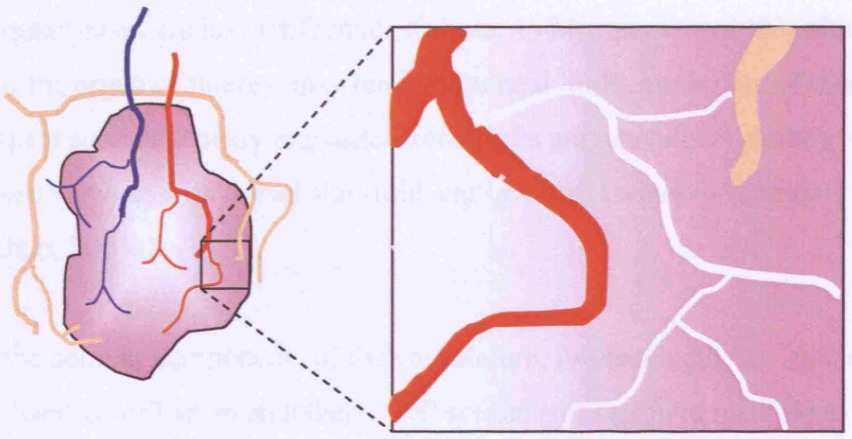

Figure 2.2. Typical vascular organisation in a tumour (pink): blood vessels arteries (red), veins (blue) and lymphatic vessels (yellow). Where lymphatic vessels exist they are largely restricted to the periphery of the tumour. The inset shows how 'vascular mimicry' occurs, here channels (white) lined with tumour cells may act as pseudo-vascular pathways for the blood. Adapted from [Ruoslahti, 2002].

2.2.1 Techniques for studying tumour vascular architecture

The biology of tumour vascular architecture has principally elicited studies *in-vivo*, *ex-vivo* and *in-vitro*. It is difficult to study primary (clinical) micro-vascular architecture within human samples which represent the gold standard. Consequently studies on primary tumour vascular architecture still remain the exception and are largely limited to the *ex-vivo* case [Konerding et al., 2001]. To address problems associated with studying primary tumours, alternative models include: induced tumours and subcutaneous/orthotopic xenografts which provide a more readily available system for biological studies.

Animal models have for a long time provided a system with which to investigate tumour biology *in-vivo*, however, there are some inherent problems pertaining to the controllability of these models. With induced tumours (e.g. dimethylhydrazine dihydrochloride induced rat colon carcinoma)[Skinner et al., 1990] the tumour tissue is syngeneic to the animal host and may not necessarily correspond to the *in-situ* case in humans. In the case of xenografts [Steinberg et al., 1989] the problem lies with the

incompatibility of human tumours growing in animal tissue. In spite of their drawbacks xenograft models remain the most convenient system for studying approximate tumour behaviour. Further improvements are achieved by using orthotopic xenograft models, which in many cases are less artifactual [Kubota, 1994;Yao et al., 2003] although location of the organ of interest may render practical limits on the use of these models. In this respect subcutaneously implanted xenografts are convenient as they can be immobilised viewing with dorsal skin-fold, ear or cranial window chambers [Leunig et al., 1992;Jain, 2001a].

To study the cellular components of the vasculature, *in-vitro* methods, such as the Boyden Chamber, utilise an endothelial cell source and a growth medium to construct rudimentary vascular networks [Woo et al., 2007]. Similarly *Ex-vivo* methods such as the Aortic/Vena cava Ring Assay use whole vascular tissue explants [Ruggeri et al., 2002;Nicosia et al., 2005;Ruggeri et al., 2002]. The advantage of these systems is their relative simplicity, enabling the constituents of the system to be controllable adjusted (e.g. assessment of drugs). Although the vasculature produced in *in-vitro/ex-vivo* systems is morphologically incomplete, simple principles of angiogenesis have been demonstrated by Serini et al. [Serini et al., 2003] where a mono-layer of endothelial cells in matrigel is shown to assemble into vessel-like tubes (the mathematical modelling of angiogenesis patterns formed here are discussed in [Chapter 3]).

2.2.2 Delimiting the vascular system and corrosion casting

Some structural aspects of the vascular system such as vessel diameter can be estimated from two dimensional sections stained with a vascular marker such as Factor VIII (Von Willebrand factor) [Pavlopoulos et al., 1998]. However, the full structural and topological aspects of the vascular network can only be appreciated in three dimensions [Malkusch et al., 1995].

Early angiographic techniques utilised opaque filling substances such as india-ink or wax to delimit the vascular network. Once filled the intervening tissue is either corroded away or cleared with a clearing agent such as methylsalicylate prior to microscopic imaging. More recently acrylic based filling agents such as MERCOX[Fait et al.,

1998;Malkusch et al., 1995] and silicone rubber based agents such as Microfill [Bentley et al., 2002] have been used to define the vascular system in a range of different tissues. The microvascular structure is especially well preserved with MERCOX casts due to the low viscosity of this casting medium's unpolymerised state, which allows recovery of excellent detail of the microvascular structure such as endothelial nuclei protrusion into the vessel lumen.

2.2.3 Morphometry of corrosion casts

The main advantage of corrosion casts is that the whole terminal vascular system can be replicated, capturing structural, topological and topographical details of the endothelial luminal surface. The method fully preserves the vascular space in three-dimensions so once the tissue is chemically removed, the vascular architecture can be studied.

As the vascular architecture is a geometrically complex structure, it is therefore not straightforward to define numerically. An attempt to capture the topological character of tumour vascular casts through fractal geometry was made by Baish *et al.* using skeletonised images of two-dimensional projections of the cast structure. *Fractal dimension* (a measure of the tortousity) and *Shortest path* (a measure of the shortest connected path across the image) were then calculated from these skeletonised images [Baish and Jain, 2000]. Both these measures reveal that tumours varied substantially from the more regular normal vasculature. A criticism of this system is it failed to take advantage of the three-dimensional qualities of the vascular cast, instead relying on a projection of the cast into two-dimensions, and it could be argued that this not only results in a loss of information but could introduce substantial error as the topology of the structure is not preserved [Figure 3.5].

Scanning electron micrographs (SEM) provide a very high resolution image of tumour corrosion casts [Figure 2.3 (A)]. Using a parallax pair of SEM images [Figure 2.3 (B)] with a know tilt angle, three-dimensional measures of linear distances and angles can be made [Fait et al., 1998;Konerding et al., 2001;Malkusch et al., 1995;Steinberg et al., 1989;Skinner et al., 1990]. Measurements are calculated as a function of equivalent pairs of x-y coordinates on each image. Linear distances were measured using two pairs

of points and angles with 3 pairs of points. Using this method Konerding *et al.* measured *Inter-vessel distance, Inter-branch distance, Mean vessel diameter, Percental variation from mean vessel diameter, Branching angle* of tumour corrosion casts [Konerding et al., 2001;Konerding et al., 1995;Konerding et al., 1999]. The distributions of the measured parameters highlight the statistical differences between vasculature of the tumours in these studies.

The importance of using three-dimensional measurements is highlighted in a study by Minnich *et al.* which compared two-dimensional and three-dimensional measurements of the microvasculature in Xenopus laevis tadpole gill filters. An error in vessel lengths of up to 58.84% was found depending on the orientation of measured vessels [Minnich and Lametschwandtner, 2000]. Malkush *et al.* in another study claim errors of around 2.5% should be expected in the two-dimensional measures [Malkusch et al., 1995]. This is clearly an important issue as most reports (and some clinical assays) rely on two-dimensional tissue sections. Additionally two-dimensional morphometry studies of vessel density, length, diameter and cross-section, may also vary with orientation, staining and counting techniques.

Though stereo-imaging methods preserve the three-dimension quality, they are unable to define the topology of the vascular network. The shortfall of these systems is that they attempt to yield some information about the vascular architecture from what are essentially two-dimensional images of the cast, for more sophisticated analysis to be carried out, the analysis must be conducted on a volumetric structure.

Figure 2.3. Scanning electron micrographs of tumour corrosion casts

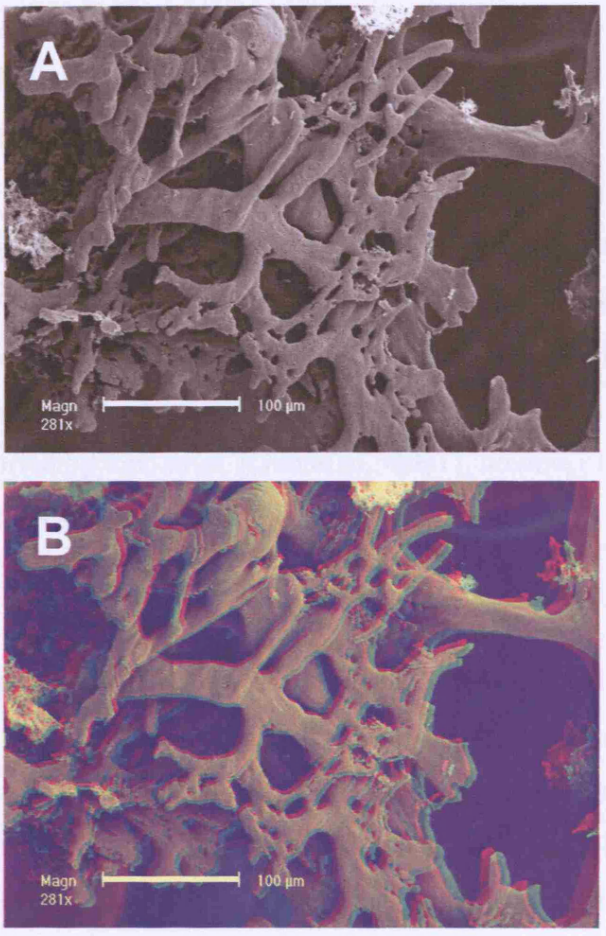

Figure 2.3. Electron micrographs of tumour vessels from a LS147T xenograft from work carried out in Chapter 4. (A) A mono-image and (B) a composite stereo-image with a parallax of 6°.

2.2.4 Tomographic methods

All methods of visualising the three-dimensional volume involve some form of tomography, that is to say the structure is split into successive images along one axis, commonly referred to as a 'z-stack'. The most basic method of generating a z-stack involves physically sectioning the tissue by serial microtomy [Brey et al., 2002]. This method is not generally practical as in many cases, aside from the considerable effort involved, there are technical problems with image registration of the smallest vessels and loss or distortion of individual sections.

Collection of the serial sections may be automated to some extent by the use of laser confocal [Zipfel et al., 2003;Soltanian-Zadeh et al., 2001;Maddah et al., 2005] or multi-photon [Barber et al., 2003b] microscopy. With both these systems the image is derived from a thin plane of focus with a minimal amount of blurring from contiguous sections just outside the plane of focus. In this way serial "optical sections" may be acquired by adjusting the depth of the focal plane without physically sectioning the sample. Data acquisition with these systems are highly dependent on optical transmission of the tissue in question, and z-stacks of greater than ~50μm (con-focal) and ~200μm (multi-photon) represent the current limits of these technology. Some success using laser-confocal microscopy to quantifying microvascular density (compared with a light microscopy technique) was reported by Guo *et al.* [Guo et al., 2001], however for parameters other than micro-vascular density this technique would appear limited to small volumes of tissue.

For visualising high resolution biological tissue both laser confocal and two/multi-photon microscopy are effective in conjunction with appropriate fluorescent markers [Alexandrakis et al., 2004;Barber et al., 2003a]. Aside from penetration of light in to the sample, these techniques often suffer from image convolution problems where fluorescence intensity is affected by contributions from the area surrounding the region of interest. Image convolution can however be ameliorated to some extent by using anti-bleaching agents, and deconvolution algorithms which adjust the intensity spread based on a model point spread function [Fink et al., 1998].

To visualise whole tumours greater than a few millimetres in diameter, newer methods which do not rely on the visual spectrum of light can be used. These methods exploit radio waves or X-rays which probe deeper into the tissue than ordinary visible laser light, and include: Micro-computed Tomography (micro-CT or μCT), Volume Computed Tomography (VCT) and Magnetic Resonance Microscopy (MRM or μMRI).

Micro-computed tomography provides a means to study three dimensional structures non-destructively at sub-micron resolution. Micro-CT cone-beam reconstruction algorithm developed by Feldkamp *et al.* and was initially used to investigate the microstructure of bone[Feldkamp et al., 1984]. Micro-CT scanners consist of an X-ray source (usually a polychromatic cone beam although synchrotron beam may also be

used), a rotating specimen stage, an X-ray-to-visible light scintillator and a charge-coupled device (CCD) based digital video camera. The sample is scanned by rotating it at a small angular increment in the X-ray beam, at each rotation step a transmission image (or shadowgram) is captured by the CCD device and repeated through a period of either 180° or 360°. X-ray attenuation is dependent on the X-ray energy spectrum. Prefiltration of the X-ray beam to yield a more monochromatic beam reduces problems related to beam hardening. For very high resolution images, more uniform synchrotron X-rays may be used. Once a series of transmission images are acquired they are reconstructed to a three-dimensional image using a modified Feldkamp filtered back-projection algorithm. The resulting image stack can then be rendered for volume or surface using a 3D ray tracing algorithm, an example of an angiograph we produced with this method is shown in [Figure 2.4 (A)]. The magnification factor is dependent on the desired volume and resolution of the scan, for example a cube of $1cm^3$ scanned at $2\mu m^3$ yield approximately 30GB of image data.

The quality of the micro-CT image is strongly influenced by the relative X-ray attenuation of the volume of interest and the surrounding media; to this end microangiographical studies using this technique generally require an intravascular contrast agent to delimit vessel boundaries [Bentley et al., 2002;Maehara, 2003]. The volumetric 'images' obtained using micro-computed tomography represent three-dimensional arrays of voxels, each with greyscale values indicating local X-ray opacity.

Magnetic Resonance Microscopy (MRM) is a high resolution adaptation [Maxwell et al., 2002] of Magnetic Resonance Imaging (MRI) [Gillies et al., 2002;Leach, 2001] a system commonly used to study clinical tumours *in-vivo*. The resolution of magnetic resonance microscopy depends directly on the magnetic field strength and improvement in super-conducting technology has lead to greatly increased resolving power with resolution of up to 1μm reported by Glover *et al.*[Glover P and Mansfield P, 2002]. Radio waves used in MRM readily penetrate and are non-destructive to biological tissue, a considerable advantage where living tissue is being studied. MRM can also be tuned to the signature of specific molecular species, enabling various metabolic processes to be assayed in real-time. Three dimensional angiographs can be generated with MRM using contrast agents such as BSA-diethylenetriaminepentaacetic anhydride-

gadolinium (GdAlbumin) [Erickson et al., 2003] an example of which is show in [Figure 2.4 (B)].

Volume Computed Tomography (VCT) is a new technology which utilises X-rays in a similar manner to micro-CT. A prototype VCT machine was used by Kiessling *et al.* to study the whole vascular system of mice bearing a subcutaneous xenografts [Kiessling et al., 2004] [Figure 2.4 (C&D)]. By using two flat-panel detectors with pixel sizes of $<40\mu m^2$, reconstruction voxel resolution of $0.4\mu m^3$ are reported with a scan acquisition time of only 16 seconds. VCT thus combines many of the advantages of micro-CT and clinical Computed Tomography (CT) scanners.

Figure 2.4. Methods for acquiring three-dimensional tumour microangiographies

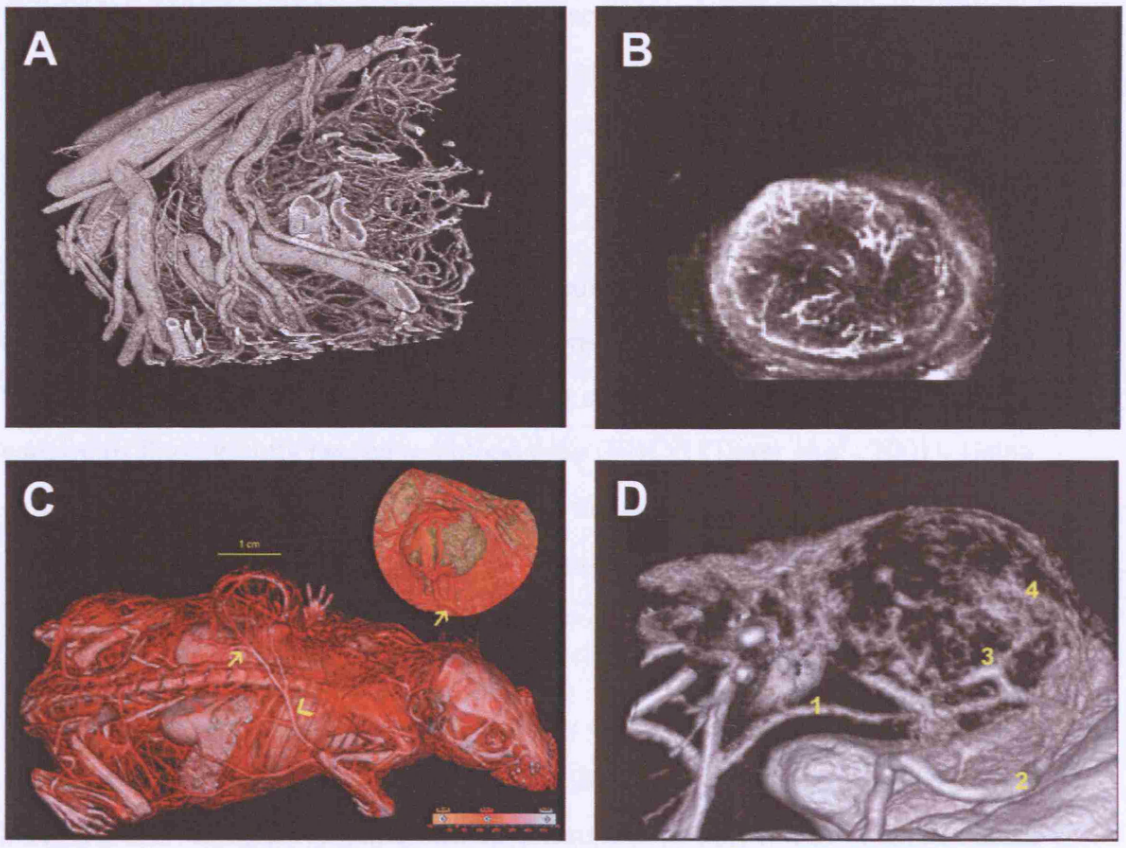

Figure 2.4. Examples of microangiography using different tomographic methods (A) X-ray microcomputed tomography of human colon carcinoma corrosion cast from [Chapter 4], (B) enhanced contrast magnetic resonance microscopy of R3230Ac mammary carcinoma xenograft [Erickson et al., 2003], (C) volume computed tomography of a whole mouse bearing human skin carcinoma xenograft (inset), yellow arrows indicate equivalent vessels on whole scan and inset, and (D) a high resolution rendering of the perfused vessels in (C), numbering indicated major feeding vessels (images from C & D were adapted from [Kiessling et al., 2004]).

2.2.5 Measuring aspects of blood flow and transport

In addition to the architecture of the microvasculature, other factors are also important in determining blood flow and transport in tumours. Parameters such as blood velocity/flow rates, blood viscosity, and interstitial fluid pressure all effect the perfusion of nutrients and therapeutic agents.

Blood flow is a dynamic property of the vascular system and requires measurements to be made directly from live or anaesthetised animals within short timescales. Acquiring blood flow velocities can be performed using an intravital microscope and video-capture of fluorescently tagged red blood cells (RBCs) [Tozer et al., 2001]. Using similar techniques to determine local blood velocity, different flow properties in normal and tumour vessels was demonstrated by a number of authors [Leunig et al., 1992] [Yuan et al., 1994;Pries et al., 1995b] [Figure 2.5 (A&B)].

Viscosity is an important component of many of the theoretical models, affecting turbulence in larger vessels and vascular rheology in smaller vessels. Though blood viscosity is a very difficult parameter to measure *in-vivo*, it can be estimated using a rheometer or a capillary viscometer [Marinakis et al., 1999].

Once within the tumour vascular system, aspects such as trans-vascular pressure gradients now determine how efficiently components being carried in the blood are delivered. A key factor affecting the trans-vascular pressure gradient and hence transport in tumours is the Interstitial Fluid Pressure (IFP) which is normally high [Jain, 1994]. IFP can be measured using the wick in needle method [Boucher et al., 1990] or micropipette and a servo-null system [Boucher et al., 1996;Pries et al., 1997].

The deficiencies in transport of oxygen result in zones of hypoxia and normoxia forming throughout solid tumours. These zones in the tumour can readily be studied using fluorescently labelled markers such as pimonidazole (hypoxia marker), and carbocyanin and Hochest 33341 (perfusion markers), and a standard epifluorescence microscope. Quantification of the fluorescently labelled zones of tissue can be determined as a function of their distance from the vessel wall using an *ImageJ* macro [Tong et al., 2004]. Local permeability of the tumour vessels to various macromolecules

can also be measured using the intravital microscope [Leunig et al., 1992;Yuan et al., 1995].

Figure 2.5. Correlation between vessel diameter and blood velocity in normal and tumour vessels

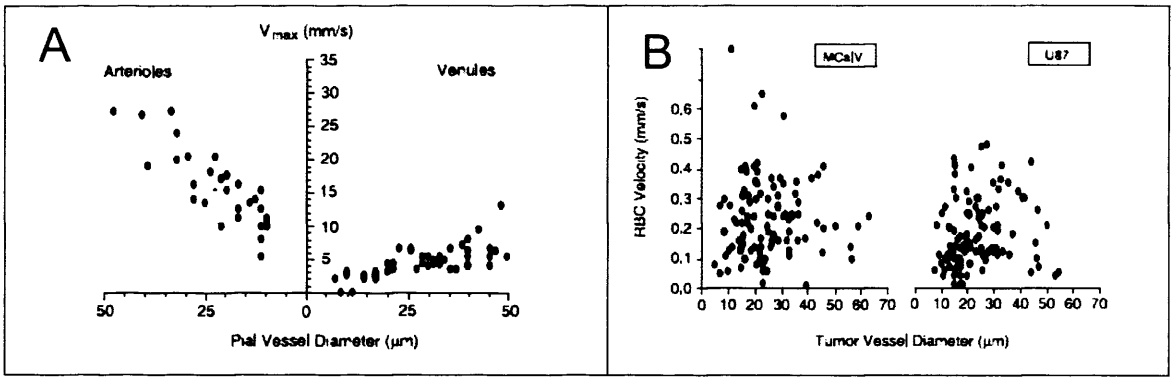

Figure 2.5. (A) Correlation between vessel diameter and flow rates in normal phial vessels (Arterioles and Venules). (B) Loss of correlation between the diameter and flow rates is a hallmark of disorganised vessels in (MCaIV murine mammary carcinoma and human glioma U87 xenograft) [Yuan et al., 1994].

CHAPTER 3: In-silico models of the vascular system

3.1 Introduction

The relationship between structure and function in the vascular system has been the source of much study in the last century, with many complex phenomena being observed. Some of the computational approaches to modelling tumour vascular networks [Section 3.2.1-2] and blood flow [Section 3.3.1-4] are reviewed in this chapter.

3.2.1 Models of vascular architecture

These models aim to either describe the structure of a vascular system phenomenologically or empirically. Although continuum models are discussed here they are not generally used to describe network formation but are included in this discussion as they form the basis of some discrete models of the vessel networks.

3.2.2 Continuum models

These 'high-level' models of angiogenesis represent components of the system, such as endothelial cell density as continuous variables rather than discrete quantities. Although this approach is perhaps course grained it can be effective where there are a large number of entities whose collective behaviour can be abstracted.

Blood vessels are built primarily from endothelial cells which under complex angiogenic stimulus can organise into vascular systems *in-vivo*. It was observed during *in-vitro* experiments on matrigel plates that these motile cells retain the ability to 'self-organise' into 'vessel-like' patterns. The self organising behaviour of endothelial cells in a simplified biological system was studied by Serini *et al.* using an adhesion-type model [Serini et al., 2003]. The adhesion-type model (commonly used in pattern formation) was constructed with the assumptions that: i) cell population can be described by a continuous distribution of density n and velocity $\vec{v}$ depending of the point $\vec{x}$ and the presence of a concentration gradient c of the chemoattractant, ii) cell population in the early stages of its development can be described as a fluid of non-

directly interacting particles, iii) cells are accelerated by chemoattractant, and iv) chemoattractants are released by cells, diffuse and degrade in finite time. With these assumptions the following equations are obtained:

$$\frac{\partial n}{\partial t} + \nabla.(n\vec{v}) = 0 \qquad [3.1]$$

$$\frac{\partial \vec{v}}{\partial t} + \vec{v}.\nabla\vec{v} = \beta\nabla c \qquad [3.2]$$

$$\frac{\partial c}{\partial t} = D\Delta c + \alpha n - \tau^{-1}c \quad [3.3]$$

where in relation to the chemoattractant, D is the diffusion coefficient, α rate of release, τ rate of degradation and β the strength of cellular response.

Equation [3.1] describes mass balance, [3.2] is a momentum balance with a chemo-tactic force term, and [3.3] is a diffusion equation for the chemoattractant produced by endothelial cells and degrading in time. The correlation between the biological and computational models produces remarkably similar patterns, replicating behaviour such as the loss of network formation below a critical cell density [Figure 3.1 (A&E)] and formation of a 'swiss-cheese' structure at high cell densities [Figure 3.1 (D&H)]. The importance of the chemoattractant gradient on the network formation is demonstrated by saturating the matrigel with exogenous VEGF-A [Figure 3.1 (I-J)] this is replicated in the simulation by removing the chemoattractant term from the equation [3.3] [Figure 3.1 (K&L)]. Similar behaviour has been noted by Gerhart et al. in studies on endothelial sprout tip guidance [Gerhardt et al., 2004;Gerhardt et al., 2003]. Although this study did not explicitly consider tumour angiogenesis, the development response by the endothelial cells to the VEGF saturated gradient has many interesting parallels with the hypothesis surrounding abnormal tumour vascular development [Section 2.1].

Figure 3.1. *In-vitro* and *in-silico* models of endothelial cell aggregation

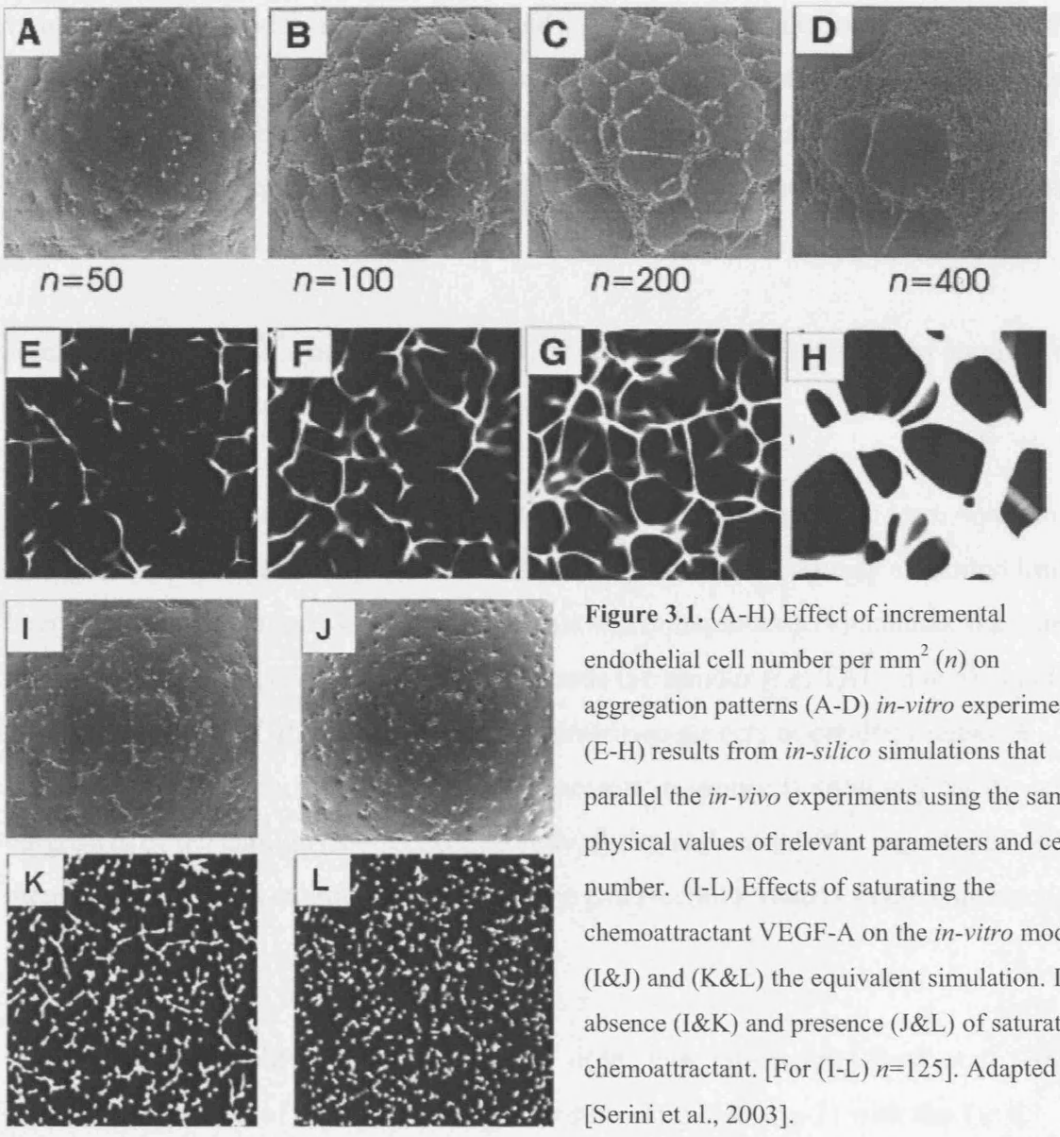

Figure 3.1. (A-H) Effect of incremental endothelial cell number per mm^2 (n) on aggregation patterns (A-D) *in-vitro* experiment, (E-H) results from *in-silico* simulations that parallel the *in-vivo* experiments using the same physical values of relevant parameters and cell number. (I-L) Effects of saturating the chemoattractant VEGF-A on the *in-vitro* model (I&J) and (K&L) the equivalent simulation. In the absence (I&K) and presence (J&L) of saturated chemoattractant. [For (I-L) n=125]. Adapted from [Serini et al., 2003].

Endothelial cells in preformed vessels also sprout and form new structures. These processes are known to depend on more static extracellular matrix factors such as fibronectin and more mobile diffusive chemoattractants generically termed tumour angiogenesis factors (TAFs). Most models focus primarily on the impact of a single tumour angiogenesis factor, in reality there are many other factors which influence sprout formation and guidance in different ways, some of which are summarised on [Table 2.1].

Sprout formation is considered by Orme *et al* [Orme and Chaplain, 1996], using a reaction-diffusion model on a one-dimensional domain representative of the parent vessel wall. This model is further expanded by Levine *et al.* [Levine et al., 2001] where the budding site is determined by the interaction of endothelial cells, TAFs, fibronectin, and proteases. Two-dimensional continuum models of this process were developed further by Orme *et al.* [Orme and Chaplain, 1997] and Anderson *et al.* [Anderson and Chaplain, 1998].

Anderson *et al.* use this model of endothelial cell density, chemotaxis and haptotaxis [Figure 3.2 (A)], to investigate the effects on cell migration.

Simulations over three dimensionless time points with the haptotactic term equal to zero, showed that spatiotemporal evolution of endothelial cell density exhibited limited lateral movement [Figure 3.2 (B)]. In contrast where haptotaxis is included, the 'sprout tips' are seen to fuse and cell migration towards the tumour (i.e. TAF source) is much slower [Figure 3.2 (C)]. The results demonstrate two aspects of capillary network formation. Firstly, a sufficiently strong chemotactic response is necessary for the initial outgrowth of the capillary network. Secondly, the model reveals the importance of interactions between endothelial cells and the extra-cellular matrix in the haptotactic response.

A further study considers vessel maturation of the nascent sprouts [Plank et al., 2004]. Here the interaction of antagonistic angiopoietins (ang-1 & ang-2) with the Tie-2 receptor on initiation and maturation of the growing stalk are of great importance. Ang-2 leads to the destabilisation of the ECs from the matrix and is important to the initiation of stalk formation, which will only occur in the presence of VEGF. Ang-1 has the opposite effect, stabilising the EC interactions. The balance of these factors is important not only in the formation but the also the remodelling of the vascular network.

Figure 3.2. Endothelial cell migration

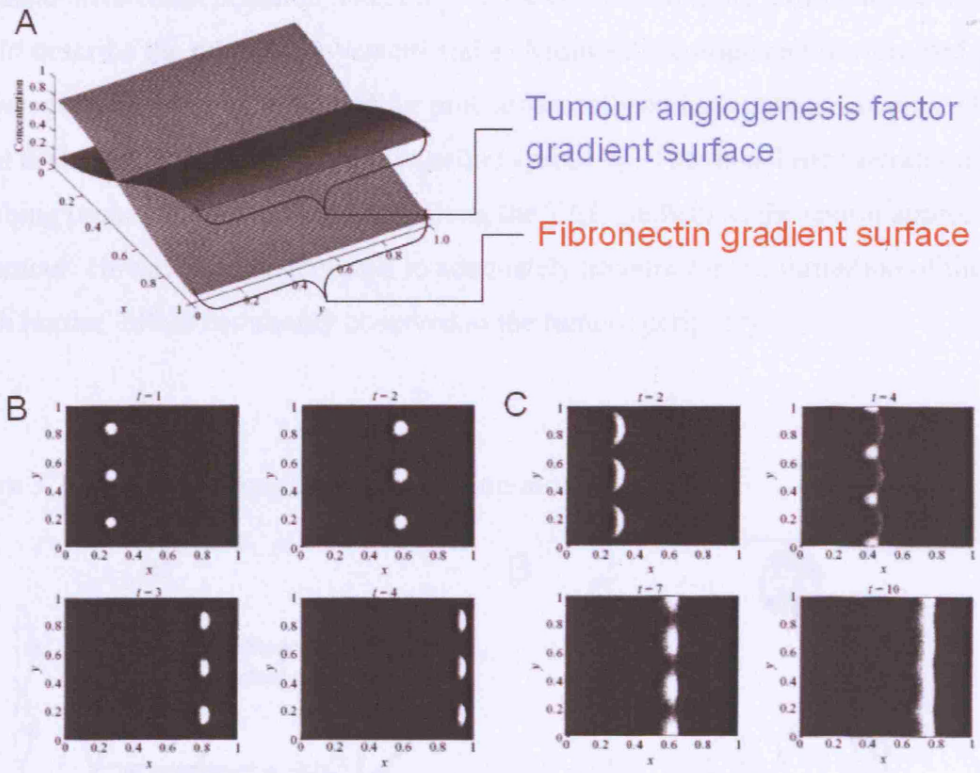

Figure 3.2. (A) Haptotaxis fibronectin concentration gradient (red) and chemotaxis TAF gradient (blue) [TAF gradient slopes away from the tumour source, while fibronectin increases], (B) two dimensional endothelial cell density evolution without haptotaxis over an initial plus 3 further time points and (C) two dimensional endothelial cell density evolution with haptotaxis over an initial plus 3 further time points. In both (B) & (C) the primary vessel is on the left and the tumour on the right. Adapted from [Anderson and Chaplain, 1998]

3.2.3.1 Discrete models of vascular architecture

Discrete models are required in order to gain a finer resolution of aspects such as sprout branching and anastomosis, and are also required to describe the angioarchitecture from the stand point of modelling flow.

Biologically the sprout tip cell with its filopodia [Figure 3.3 (A)] governs the motion of the sprout in response to signals in the surrounding media; this forms the basic unit for many discrete models. A model of the sprout tip was considered by Stokes *et al.*, where

each sprout tip is characterised by a position and velocity at a given time [Stokes and Lauffenburger, 1991] [Figure 3.3(B)]. The evolution of the tip is governed by a stochastic differential equation that comprises a viscous damping term, a white noise term to describe the random movement and a chemotactic component for directed movement. Branching is accounted for probabilistically and anastomosis occurs when a sprout tip is within one cells width of another sprout tip. The model incorporates a branching probability which increases along the TAF gradient as the sprout approaches the tumour. However the model fails to adequately account for the formation of the 'brush border' effect commonly observed in the tumour periphery.

Figure 3.3. Sprout tip structure and migration model

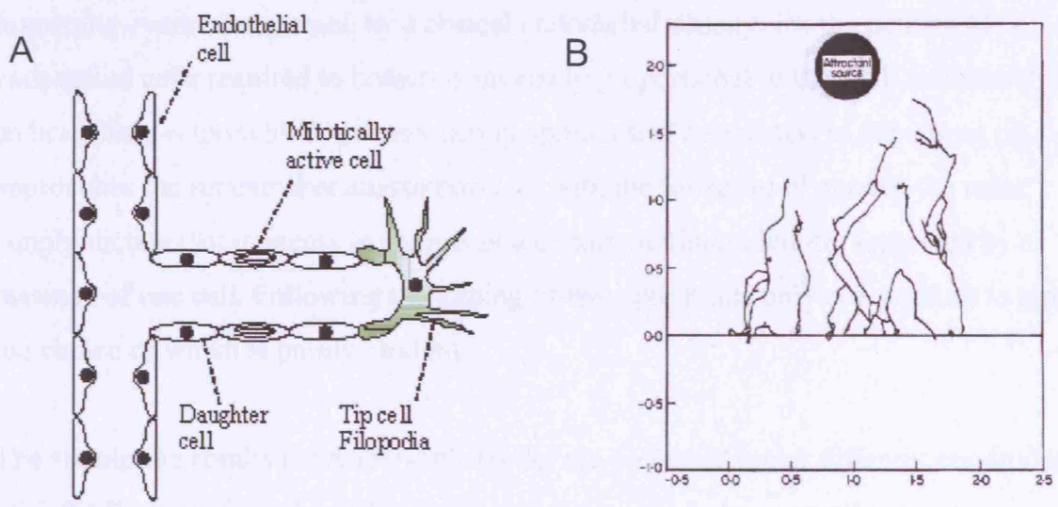

Figure 3.3. (A) Schematic of an angiogenic sprout. This idealised abstraction is used as the basis of most discrete models, adapted from [Anderson and Chaplain, 1998]. (B) Stokes and Lauffenburger's discrete model (1991) the primary vessel is represented by the horizontal line (units in mm) [Stokes and Lauffenburger, 1991].

The discrete sprout tip model is developed further by Anderson *et al.* [Anderson and Chaplain, 1998]. This model defines its nearest neighbour interactions from a discretisation of the continuum model used to generate the endothelial cell densities in [Section 3.2.2]. Discretisation was carried out using Euler finite difference approximation (discretisation of the endothelial equation is available in the appendix of Anderson *et al.* [Anderson and Chaplain, 1998]). This equation is used to determine the

EC density in discrete time and space, achieved by averaging the density of four surrounding neighbors at the previous time step. Five coefficients $P_0 - P_4$ from the discrete equation are used to simulate the motion of an individual endothelial-cell under the influence of chemotactic, haptotactic and random movement (equation [3.4]). These coefficients can be considered as being proportional to the probabilities of the sprout tip cell remaining stationary (P_0), moving left (P_1), right (P_2), up (P_3) or down (P_4). Each of the coefficients P_1–P_4 consists of three components given by:

$$P_n = random\ movement + biased{:}chemotactic + biased{:}haptotactic \qquad [3.4]$$

The phenomenological rules governing branching and anastomosis are defined as follows: i) Branching only occurs at sprout tips, ii) there is a time delay between branching events determined by a critical endothelial density, iii) the density of endothelial cells required to branch is inversely proportional to the TAF concentration so branching is more likely (consequently sprouts will be shorter) as the sprout tip approaches the tumour. For anastomosis, as with the Stokes *et al.* model, the rules simply dictate that it occurs in sprouts of a certain minimum length, separated by a distance of one cell. Following the joining of two sprout tips only one goes on to grow, the choice of which is purely random.

The simulation results for Anderson's model are presented under different conditions of: i) TAF source (circular or linear representative of a large or small tumour respectively), ii) the presence or absence of haptotaxis and iii) presence or absence of endothelial cell proliferation [not shown here]. The spatiotemporal evolutions of 5 sprout tips are considered over 4 time steps [Figure 3.4 (A-F)]. The first two simulation runs are without haptotaxis. In both these runs, the sprouts rapidly proceed towards the TAF source. The first case [Figure 3.4 (A)] matches areas of high endothelial cell density described by the continuum model in [Figure 3.2 (B)]. The second case [Figure 3.4 (B)] shows a TAF profile with a different radial geometry, here sprouts converge rapidly TAF source again showing little branching. The next two simulations include haptotaxis in the model [Figure 3.4 (C)] linear and [Figure 3.4 (D)] radial TAF sources. Anastomosis can bee see to occur in both cases at relatively early time points and the degree of branching is dramatically increased, further to this the time taken to migrate is significantly increased $t = 20$ in comparison to the chemotaxis-only case where

vascularisation has occurred by $t = 10$. In both these models the formation of the brush-border occurs, again there is agreement with the cell densities of continuum model [Figure 3.2 (C)] and the branching in [Figure 3.4 (C)].

The results from the discrete model simulations confirm the predictions of the continuum model that both chemotaxis and haptotaxis are required for the formation of a capillary network at a large scale. These simulation results show the important large-scale features of angiogenesis can be described qualitatively using a continuum model. Although the vascular networks generated here are "firmly based on underpinning biological processes such as chemokinesis, chemotaxis and haptotaxis" they are by no means an accurate description of the tumour vascular system.

Figure 3.4. A discrete model of tumour angiogenesis

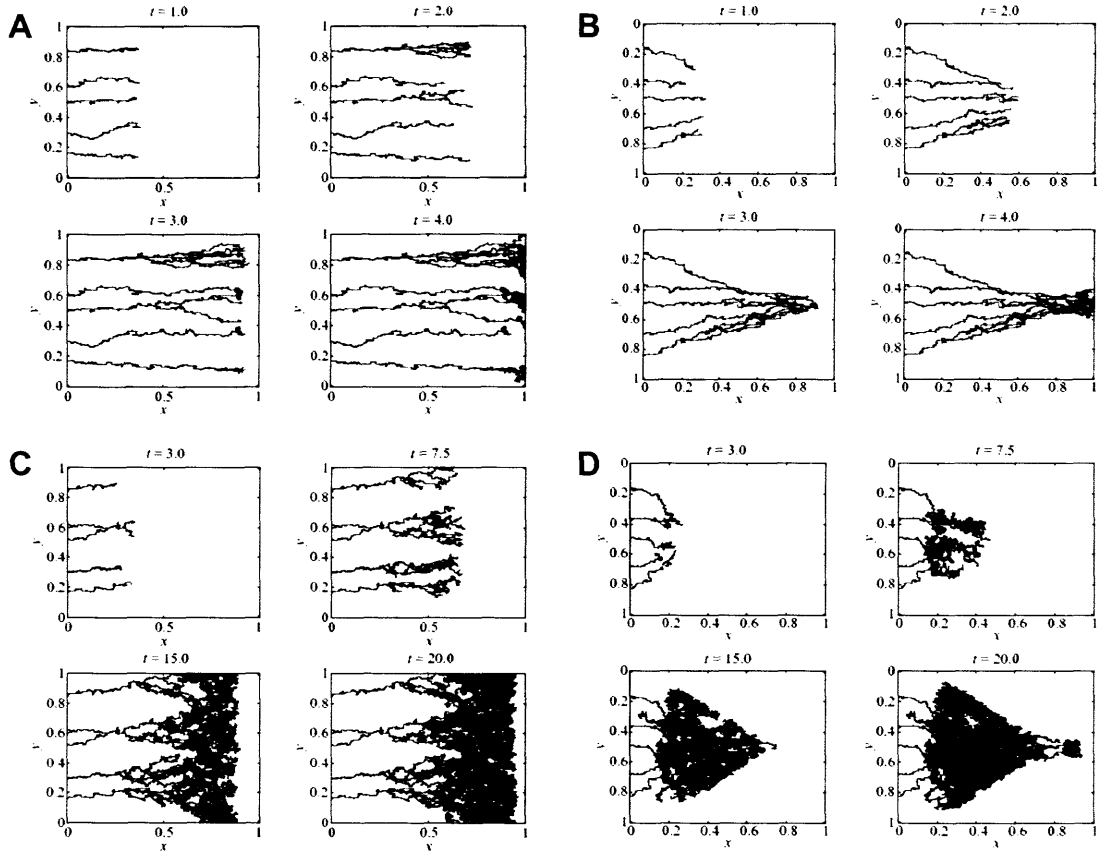

Figure 3.4. Numerical simulation results from Anderson et al. 1998, parent vessels at x=0, and tumour TAF source at x=1 (linear) or at x=0.5 (radial). Each simulation is presented over 4 time points.
(A) Migration of sprout tips towards a linear TAF source without haptotaxis, shows similar results to the analagous continuum model simulation which show little lateral movement. Additionally the discrete model shows no branching and consequently little anastomosis. Sprouts connect with the tumour by the forth time point.
(B) Used the same parameter values as simulation (A), with a circular TAF source in place of a linear one. The convergence of sprouts in the middle of the y-axis is due to the radial geometry of the TAF. Note very little anastomosis occurs here too.
(C) Migration of the sprout tips towards a linear TAF source in the presence of both haptotaxis and chemotaxis. Both extensive sprouting and anastomosis are observed resulting in the formation of the 'brush border' effect.
(D) This includes the same parameters as in (B) with the exception that haptotaxis is included in this model. Again early anastomosis is observed and some sprouts are even seen to migrate away from the TAF source. From [Anderson and Chaplain, 1998].

3.2.3.2 An empirical approach to modelling vascular architecture

In contrast to the more phenomenological models above, a different approach to modelling vascular architecture was proposed by Baish *et al.* This model used the fractal dimension of vascular networks to select percolation networks statistically representative of tumour and normal tissues [Baish et al., 1996;Baish and Jain, 2000] [Figure 3.5 (A)]. The chaotic nature of tumour vasculature makes a unified numerical quantification of the shape of these structures very difficult in ordinary Euclidian space (although as seen in [Chapter 4] distribution of a range of parameters can be used to quantify certain aspects of the tumour vasculature). In contrast, fractal geometry can be used to reveal how the irregularities of vasculature may be described by the number of similarly shaped vessels at other scales. An estimate of vessel tortuosity, taken as a minimum path dimension, is also measured from the skeletonised images.

Following a study by Gazit *et al.* on scale-invariant behaviour in vascular network formation [Gazit et al., 1995], Baish *et al.* devised a model representation of tumour vascular networks for use in mathematical modelling of flow and oxygen distributions. The fractal dimension was derived from skeletonised two-dimensional images vessels from both tumours and normal tissues [Figure 3.5 (B)] and estimated using the box counting method [Bunde and Havlin, 2004]. A caveat of this approach is fractal scaling only applies over a narrow range of length scales in the vascular system and it is unknown if the scaling extends to larger vessels. For a truly fractal system scaling applies over an infinite series, which is certainly not the case in this instance.

In order to model the complex tumour vascular structure, a particular flavour of percolation theory called 'invasion percolation' [Wilkinson and Willemsen, 1983] has been found to be particularly useful. The model of the vascular network starts with a square lattice initialised with uniformly distributed random values. Invasion percolation is realized by first selecting a start point at the bottom-left corner and invading the weakest point on the grid at adjacent to the current position; this growth is iterated until the required occupancy is reached. The network is then pruned by removing regions with zero flow (dead ends) to provide the 'backbone', blood vessels are then assumed to connect all adjacent lattice sites on this backbone. Selecting the occupancy enables the level of geometrical heterogeneity to be controlled by the fractal dimension.

Figure 3.5. Flow in two dimensional percolation networks

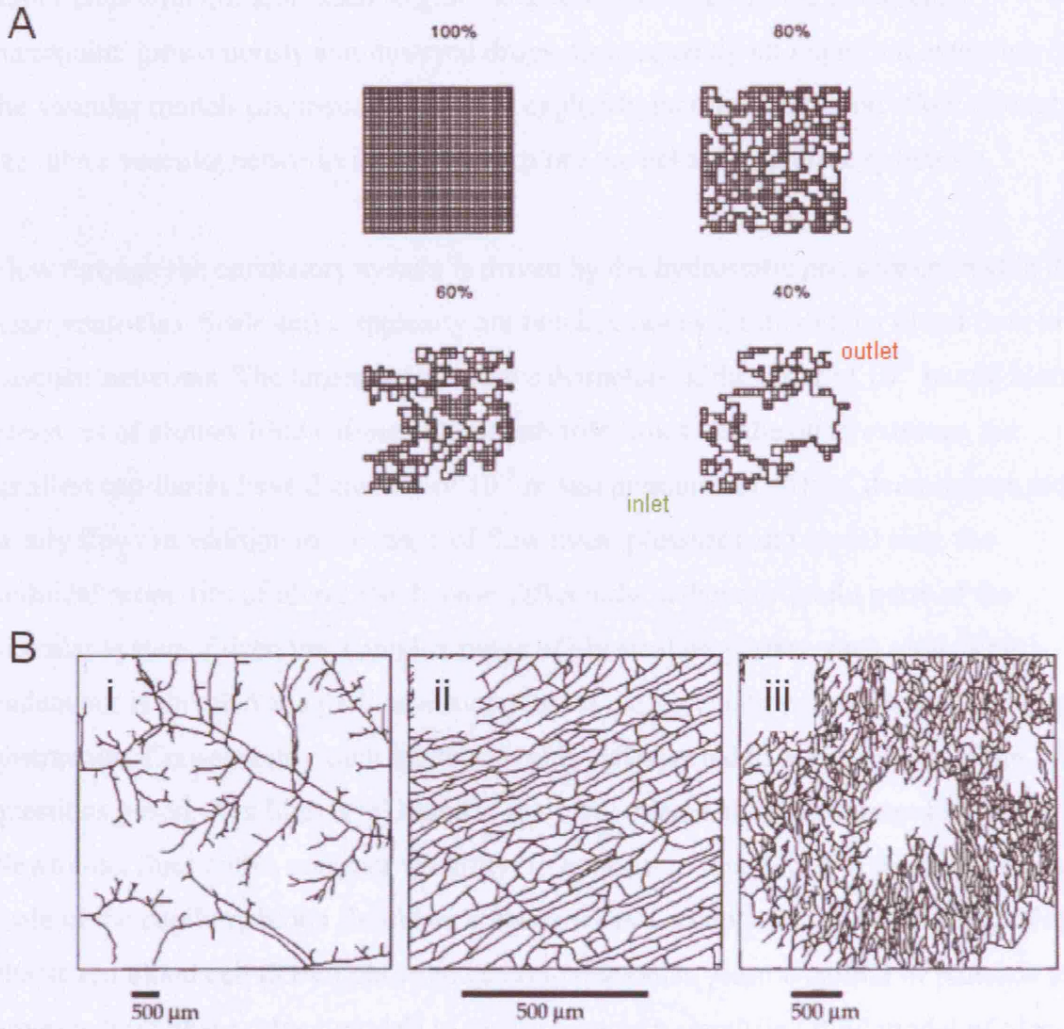

Figure 3.5. (A) Invasion percolation networks at various levels of % occupancy. Growth begins in the bottom left. The flow in each network is shown with the inlet at the bottom-left (green) and outlet at the top-right (red). The fractal dimensions of the 100, 80, 60, and 40% occupancy networks are approximately 2.0, 1.9, 1.8, and 1.6 respectively. (B) Skeletonized vascular patterns for (i) normal subcutaneous arteries and veins, (ii) normal subcutaneous capillaries, and (iii) an adenocarcinoma (LS174T xenograft tumour) [Baish et al., 1996].

3.3.1 Blood flow modelling

The newly developed vascular network functions to supply the expanding mass of tumor cells with nutrients such as glucose and oxygen and, from a therapeutic standpoint, intravenously administered drugs. Consequently an important extension of the vascular models discussed earlier is to explicitly incorporate 'blood' flow through the tumor vascular networks in order to explore the behavior in these systems.

Flow through the circulatory system is driven by the hydrostatic pressure created in the heart ventricles. Scale and complexity are two key issues for modelling blood flow in vascular networks. The largest arteries have diameters of the order of 10^{-2} m and blood pressures of around 10kPa, these exhibit pulsatile flows. At the other extreme, the smallest capillaries have diameters of 10^{-5} m and pressures of ~1kPa, demonstrate more steady flow. In addition to the range of flow rates, pressures and vessel size, the colloidal properties of blood also behave differently in these different parts of the vascular system. Given this complex range of physical properties, each modelling endeavour is directed at a particular hierarchy of the vasculature through some level of abstraction. Consequently each model can only be expected to answer some of the questions posed. At a high level blood is typically treated as an incompressible Newtonian fluid with a constant viscosity. In contrast to this, blood at the microscopic scale of the capillary blood should be considered as a compound fluid consisting of an elastic red blood cell (RBC) phase and a non-Newtonian plasma colloid of platelets and proteins fluid phase. Many models in reality assume a simplified fluid model of blood in some respects.

3.3.2 Concepts used in blood flow models

The following section contains a brief discussion of some important components in vascular flow modelling.

Reynolds number

Proposed by Osborne Reynolds [Reynolds, 1883], this dimensionless number is the ratio of inertial forces to viscous forces and is used to determine if a flow will be

laminar or turbulent. Laminar flow occurs at low Reynolds numbers, here viscous forces are dominant and flow is characterized by smooth, constant fluid motion. At high Reynolds numbers, flow is turbulent, and is dominated by inertial forces, resulting in random eddies, vortices and other flow fluctations. Flow in the microvascular vessels occurs at low Reynolds numbers and so the assumption of laminar flow is made for the purposes of most models.

$$\mathrm{Re} = \frac{\rho VL}{\mu} = \frac{VL}{\nu} \qquad [3.5]$$

where, ρ is the fluid density, V mean fluid velocity, L characteristic length, μ absolute dynamic fluid viscosity, and ν kinematic fluid viscosity (where $\nu = \mu / \rho$).

Hagen-Poiseuille Flow

Laminar flows through channels or tubes are observed to produce a parabolic velocity profile as frictional forces are transmitted from the wall regions of the fluid to the central axis (equation [3.9]) [Saltzman, 2001]. In the instance of a vessel modelled as a cylinder [Figure 3.6 (A)] using the equations for conservation of momentum, the following expression (the Navier-Stokes equation for viscous flow) is acquired.

$$\rho \frac{\partial \bar{v}}{\partial t} = -\nabla p + \mu \nabla^2 \bar{v} + \rho g \qquad [3.6]$$

where $\bar{v}$ is the fluid velocity, ρ is the fluid density, μ is the fluid viscosity, p is the hydrostatic pressure and g is the gravitational force. Flow in a cylinder under normal circumstances occurs only in the axial direction: $\bar{v} = v_z(r)\hat{k}$, where v_z is a function only of the radial distance r from the axis and $\hat{k}$ is the unit vector in the z direction. The z-component of the equation expressed in cylindrical coordinates is as follows:

$$\rho\left(\frac{\partial v_z}{\partial t} + v_r \frac{\partial v_z}{\partial r} + \frac{v_\theta}{r}\frac{\partial v_z}{\partial \theta} + v_z \frac{\partial v_z}{\partial z}\right) = -\frac{\partial p}{\partial z} + \mu\left[\frac{1}{r}\frac{\partial}{\partial r}\left(r\frac{\partial v_z}{\partial r}\right) + \frac{1}{r^2}\frac{\partial^2 v_z}{\partial \theta^2} + \frac{\partial^2 v_z}{\partial z^2}\right] + \rho g_z$$

[3.7]

This equation can be simplified by making the following key assumptions a) flow is at a steady state where $\frac{\partial v_z}{\partial t} = 0$, b) there is no radial flow i.e. flow is only in the axial direction v_z ,with $v_r=v_\theta=0$ and c) gravitational forces are insignificant ($g_z \sim 0$). With these assumptions equation [3.7] can be simplified to:

$$\frac{\partial p}{\partial z} = \mu \frac{1}{r} \frac{\partial}{\partial r}\left(r \frac{\partial v_z}{\partial r} \right) \qquad [3.8]$$

Equation [3.8] can be solved with the following conditions: $p=p_0$ at $z= z_0$; $p=p_L$ at $z = L$; $v_z = 0$ at $r=R$; and $\partial v_z/\partial r = 0$ at r = 0, to give:

$$v_z = \frac{p_0 - p_L}{4\mu L}\left(R^2 - r^2\right) \qquad [3.9]$$

giving a parabolic dependence of velocity on the radial position [Figure 3.6 (B)] characteristic of Hagen-Poiseuille flow. This equation can be integrated over the vessel cross-section to obtain the overall rate of blood flow Q:

$$Q = \int_0^{2\pi} \int_0^R v_z(r) r dr d\theta = \frac{(p_0 - p_L)\pi R^4}{8\mu L} \qquad [3.10]$$

Resistance to flow is a strong function of radius (R to the minus forth). This effect is responsible for the 80% blood pressure drop observed over the arterioles (diameter < 40 μm) and capillaries.

Figure 3.6. Poiseuille flow in a cylindrical channel

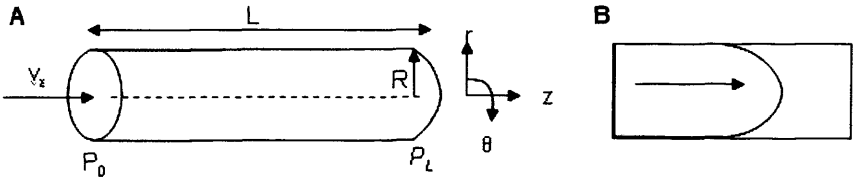

Figure 3.6. (A) Tube dimensions, P_0 and P_L are respectively the pressures at the inlet and outlet, with the inlet velocity V_z, L is the length of the element, R is the radius and θ is the angle between r and the positive z-axis. (B) A cross-section of the parabolic velocity profile characteristic of Poiseuille flow.

Darcy's Law

Henry Darcy description of flow through and isotropic porous medium is typically used to model flow out of the vessels and in the interstitium. This law is a simple proportional relationship between the discharge per unit area q, fluid viscosity μ, permeability of the porous media k and pressure gradient ∇P [Saltzman, 2001].

$$q = -\frac{k}{\mu}\nabla P \quad [3.11]$$

3.3.3 Single vessel blood flow models

Flow models at the microscopic scale tend to focus on a single capillary or a very simple network and are oriented around the haemodynamics of the RBCs, plasma, endothelial glycocalyx, and extravascular transport.

At the unit level of the individual capillary element, blood flow exhibits some unexpected properties described by the Fahraeus and Fahraeus-Lindqvist effects.

The flow of a colloidal suspension such as blood in a tube/channel results in the suspended elements aggregating along the longitudinal axis of flow [Figure 3.7 (A)]. This clustering behaviour of red blood cells in small vessels results in a cell free layer forming adjacent to the glycocalyx (cell wall) [Pries et al., 2000;Pries et al., 1997]. The clustering of RBCs is linked to the shear forces, which are parabolic across the vessel, and lower in the central axis of the channel than at the edges.

In a similar manner to the shear force, velocity profile is parabolic (though higher axially and lower peripherally), this phenomenon has been used to explain the lower haematocrit transit time by comparison to the plasma in a vessel segment. This lower transit time results in a lower haematocrit in the tube relative to the discharge haematocrit and has been termed the 'Fahraeus effect' [Goldsmith et al., 1989]. Dynamic model of RBC clustering have recently been presented by a number of authors using a range of different mathematical approaches: discrete particle method [Boryczko et al., 2003], immersed boundary method [Bagchi, 2007] and multi-component lattice-Boltzmann method [Sun and Munn, 2005;Ding and Aidun, 2006;Dupin et al., 2006;Dupin et al., 2007]. Blood cells in the finest capillaries occupy the whole vessel calibre and orient perpendicular to the plane of flow as shown in [Figure 3.7 (B)]. This stacking behaviour is termed the 'rouleaux' due to the similarities to a stack of coins and the velocity profile is blunted, not parabolic. At a simplistic level these rouleaux can be treated as a plug-flow, however, the stacking behaviour of RBCs has also been modelled by Boryczko *et al.* using their discrete particle method [Boryczko et al., 2003].

Figure 3.7. Behaviour of RBCs in vessels

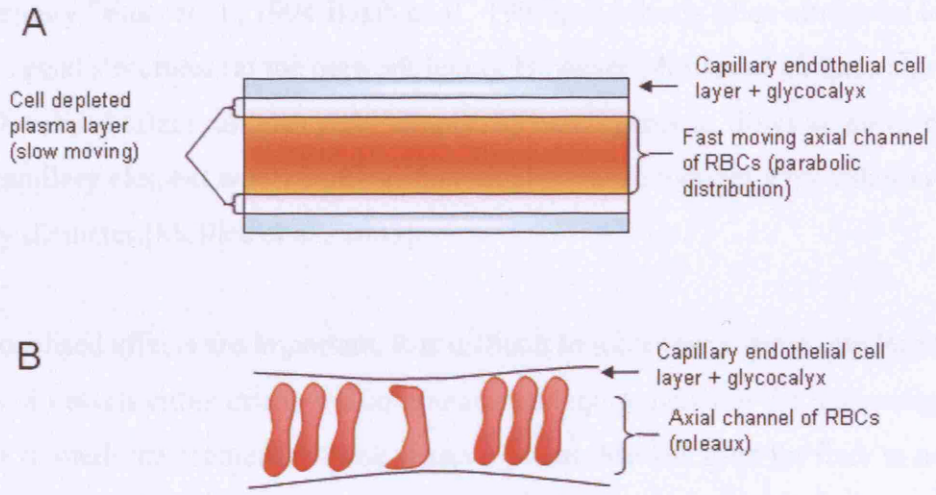

Figure 3.7. (A) Axial clustering of RBCs in the microvasculature. Here RBC distribution correlates with the velocity (or shear rate) in the vessel [Pries et al., 1996a] and (B) in the smallest capillaries (6-10 μm) of the microvasculature where vessel diameter is equivalent that of a RBC, the cells stack perpendicular to the direction of flow described as an axial-train or rouleaux, note deformation of the cells at the central constriction [Boryczko et al., 2003].

The Fahraeus-Lindqvist effect on the other hand, relates to the uncoupling of 'relative apparent viscosity' and haematocrit, as vessel diameter decreases [Figure 3.8 (A&B)]. Both Fahraeus and Fahraeus-Lindqvist effects may be reduced in tumours resulting in increased resistance to flow [Sevick and Jain, 1989].

The endothelial surface layer (ESL) or glycocalyx[1] is implicated in hydrodynamic resistance [Pries et al., 1997] and transport [Vink and Duling, 2000]. The influence of the ESL layer is estimated to increase the flow resistance by some 14-21%, equivalent to a uniform increase of 0.5-1 μm in diameter of the blood vessel. This effect can be seen in [Figure 3.8 (A&B)] where the diameter of vessel required for the equivalent drop in relative apparent viscosity is larger in *in-vivo* by comparison to *in-vitro* measures in equivalent calibre glass tubes where no ESL is present.

[1] A layer composed of proteoglycans and other constituents absorbed from the plasma.

Flow heterogeneity may be affected at the level of the individual vessel element. It is well documented that tumour blood flow is characterised by both spatial and temporal heterogeneity [Yuan et al., 1994;Baish et al., 1997], and this is often attributed to the chaotic vessel structures (at the network level). However Mollica *et al.* have shown that a more localised effect can also yield temporally heterogeneous flows at the level of a single capillary element where tumour interstitial pressure induces a modulation of the capillary diameter [Mollica et al., 2003].

While localised effects are important, it is difficult to incorporate them into larger systems of vessels either due to the computational requirements or the increasingly complex domain represented by these vessel systems. Models used for flow in networks of blood vessels are discussed in the next section.

Figure 3.8. Vessel diameter and viscosity

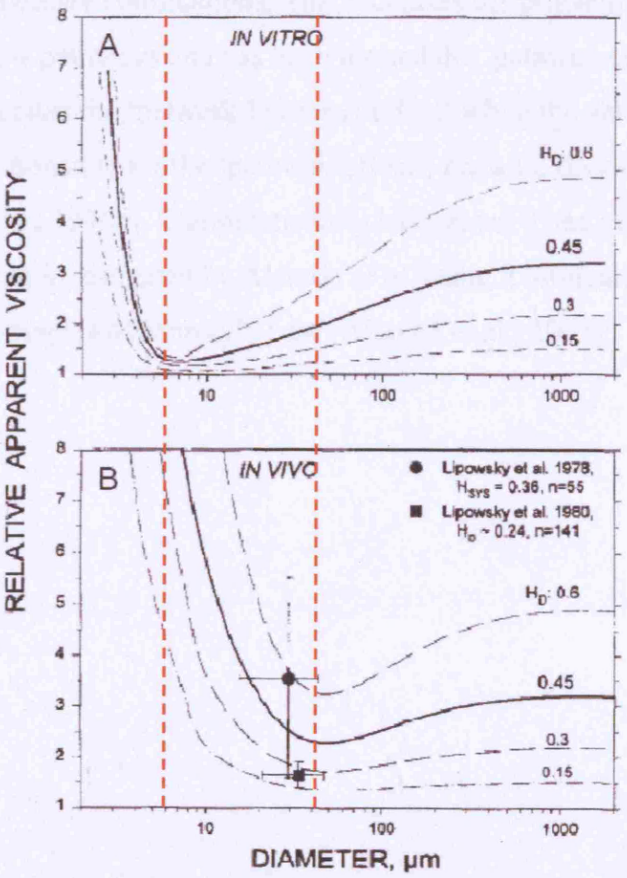

Figure 3.8. The Fahraeus-Lindqvist effect. Dependence of relative apparent viscosity on vessel diameter for different haematocrit (H_D) in (A) *in-vitro (glass capillary tubes)* and (B) *in-vivo (rat mesentery vessels)*. Notice the different positions of the minima (red dashed lines). Adapted from [Pries et al., 1996a].

3.3.4 Vessel network blood flow models

Blood flow in vessel geometries more complex than single vessel elements display phenomena that are determined from the properties of the network. These phenomena impact on the pressure, velocity and haematocrit distribution throughout the network.

Similar to the Fahraeus effect described in the previous section, the 'network Fahraeus effect' [Figure 3.9] concerns the uneven partitioning of the haematocrit at successive arteriolar bifurcations, leading to heterogeneous haematocrit and plasma ratios across the network. This, coupled with the tendency of RBCs to follow the higher flow rate pathways, leads to a positive correlation between haematocrit and flow velocity, and a ~20% reduction of discharge haematocrit in the capillaries relative to the feeding arterioles [Pries et al., 1995b]. In larger vessels the loss of relatively higher quantities of plasma to the daughter vessels causes a build up of haematocrit in larger vessels over successive bifurcations. This increases the probability of RBCs travelling through long flow pathways and has been termed the 'pathway effect'. Network geometry largely dictates the 'network Fahraeus effect' while the network topology is primarily responsible for the 'pathway effect', pressure distribution and resistance to flow [Pries et al., 1996b]. Computationally haematorcrit and vessel radius dependent viscosity have been investigated by Alarcon *et al.* using a bifurcating network model based on the principles of Murray's Law [Alarcon et al., 2005].

Figure 3.9. Plasma skimming

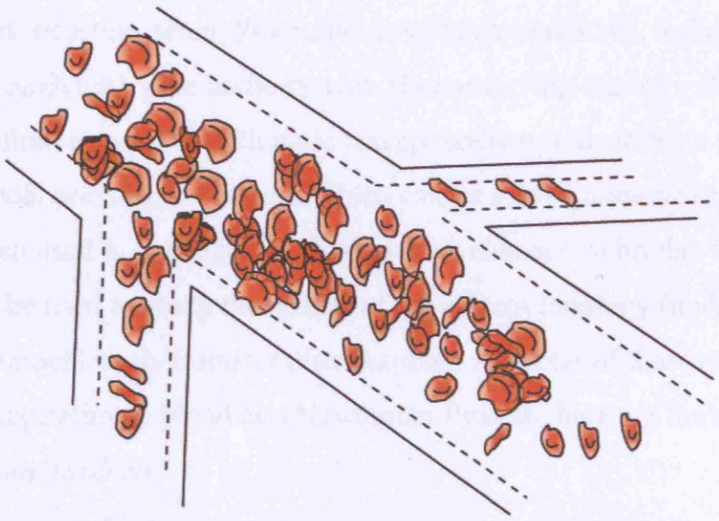

Figure 3.9. The network Fahraeus effect, 'plasma skimming' causes a haematocrit drop in progressively smaller vessels. The blood cell exclusion layer is shown by the dashed line.

Experimental studies of blood flow *in-vivo* at the network level of vessels present great technical challenges, as it is difficult to resolve the three-dimensional spatio-temporal behaviour of blood, and assay methods can easily affect such a sensitive dynamic system. Historically this has limited studies to certain tissues and methods (e.g. rat mesentery or window chamber models). To explore concepts where experimental studies may be impractical, numerical simulations of blood flow can provide a means investigate the behaviour of these systems.

A number of approaches taken to modelling blood flow in the models of tumour vasculature such as those in [Section 3.2.3.1 and 3.2.3.2] are discussed here.

A frequently approach to modelling flow in networks of vessels uses a network flow model represented by a system of connected cylindrical pipes of given length and radius [Figure 3.10 (A)]. Structure and topology of vessel networks are conserved by mapping them onto lattices for use in flow models [Figure 3.10 (B)]. A number of different lattice types, for example: two-dimensional square [Baish et al., 1996], two-dimensional hexagonal [Alarcon et al., 2004] and three-dimensional cubic [Stephanou et al., 2005]

lattices, have been used to model tumour vasculature, each differing in the nodal connectivity.

With the network structure setup, Poiseuille flow, equation [3.10], is then used to define the flow rate through each pipe in the system. By conserving mass (or flow if an incompressible fluid is used) at each node (except sources and sinks), a system of linear equations for nodal pressure is obtained which can be solved numerically. These nodal pressures are then used to calculate the flow in each element. With this type of model, simulations can be used to study the effects of the system topology (nodal connectivity) and geometry (vessel length/diameter distributions). A caveat of these network flow models is they approximate blood as a Newtonian fluid so there are limits to which interpretations can be taken.

These types of models may be useful for hypothesis formulation and simulation of clinically important parameters, such as the theoretical effect of drug action on the vascular network (e.g. vascular pruning in anti-angiogenesis/vascular therapies) and drug distributions through the network.

Figure 3.10. The network flow model

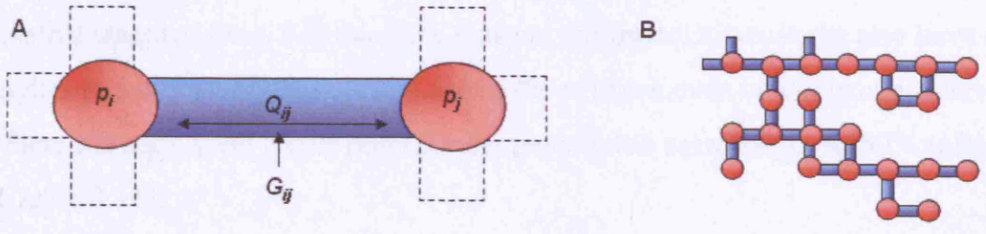

Figure 3.10. (A) The schematic for a single flow element in a network flow model, p_i and p_j are the pressure at node *i* and *j* respectively, the element *ij* has a flow rate of Q_{ij} and a conductance of G_{ij}; (B) a network of such elements representing a particular topology. Geometric features such as vessel diameter can also be specified for each element. Adapted from [McDougall et al., 2002].

A simplified network model consisting of a regular grid incorporating extravascular flow (Starling's law) and interstitial flow (Darcy's law), was used to explore the coupling of interstitial pressure to fluid flow directions with in tumours [Baish et al., 1997]. This model predicts that fluid flow may be altered in three ways, i) fluid may be forced in a more transverse direction, from the centre to the periphery, because of a loss of fluid at the tumour boundary, ii) improved vascular exchange may lead to fluid shortcuts in the interstitium and iii) the vascular flow could be reduced in areas with higher interstitial pressure. A key assumption of a constant haematocrit is made in this model, in the instances where fluid loss from the vessels exceeds 10% the haematocrit can be expected to increase enough to have an impact on effective blood viscosity.

The invasion percolation models of tumour vasculature [Figure 3.5 (A)] discussed in [Section 3.2.3.2] were also studied with a network flow model [Baish et al., 1996]. The influence of the more convoluted tumour network geometries are compared with those of more regular geometries of the same occupancy. This model demonstrates that regular, space-filling networks produce a fairly uniform distribution of flow rates in the vessels relative to their distance from the main diagonal of the network[2]. By comparison the percolation network simulations yield flow rates that are irregular across the network. As the flow divides in regular networks each pathway carries an equivalent burden, however, in the percolation networks the distribution of flow is highly asymmetric, and this non-uniformity results in areas in relative high flow and areas of relative stagnant flow. For the same reasons, symmetrical networks also have a far higher capacity, maintaining flow across the network even below occupancies of 10%, where the equivalent cutoff point for the percolation networks is 30-50% (after pruning) [Figure 3.11].

[2] In keeping with what might be expected in a healthy capillary bed. However incorporation of haematocrit terms can result in heterogeneous blood flow even in regular lattices [Alarcon et al., 2004].

Figure 3.11. Flow in regular and invasion percolation networks

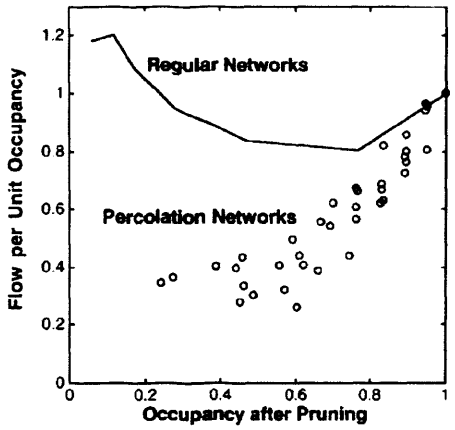

Figure 3.11. Flow efficiency through random and through space-filling, regular networks with the same arterio-venous pressure differential as measured by the flow per unit occupancy (regular networks - solid line and percolation networks - open circles). All flows are normalized to the flow through the fully occupied, regular network (32 x 32) [Baish et al., 1996].

The discrete model used to simulate vascular network growth by Anderson *et al.* was used by McDougall *et al* as the subject of flow studies of an injected tracer [McDougall et al., 2002;McDougall et al., 2006]. This model employs a two-dimensional network flow model similar to that used by Baish *et al.* The vascular geometries considered include networks generated from both linear and circular TAF sources [Figure 3.4 (C & D)]. The flow networks for these models were generated by mapping the vessel structures to a grid for simulation with each capillary element forming part of the microvasculature assigned a radius drawn from an input probability distribution function (type unspecified).

The algorithm used to track concentration profiles of an injected tracer (*drug*) is computed at each time step: i) the total amount of drug flowing into each node is calculated and ii) new drug concentrations were calculated for all outflow bonds based on the computed nodal values. Assumptions made by this model are listed here: i) perfect mixing at each node is assumed, ii) the blood is considered to be a Newtonian fluid, iii) the blood vessels are modeled as static impermeable cylinders, iv) no reaction

kinetics were assumed in the uptake of the drug (later simulations with a flow boundary condition, assume removal of any drug within 40 μm of the tumour).

Simulations with this model explore the implications of i) blood vessel radius, ii) fluid viscosity and iii) network structure, on fluid flow and drug distribution administered via bolus or continuous infusions regimes. The results from these simulations are substantial and the discussion of each is beyond the scope of this review, however the effect of the two different vessel structures, mean radius and viscosity are considered here.

The results of a tracer-drug constitutively infused into the parent vessel show how the two vessel geometries (Linear [Figure 3.12 (A)] and radial [Figure 3.12 (B)]) have substantially different flow profiles. Firstly branches 1 and 2 supply drug to the tumour, however branches 3-5 remove drug from the tumour. The effects of this tumour 'drug bypass' is particularly pronounced in the simulation with the circular tumour TAF source[3] [Figure 3.12 (B)] as the vessels connect up earlier than those in the linear-TAF-source model.

Changing the mean radius produced increases in the flow rate and therefore drug uptake, however this relationship is non-linear due to the relationship between element radius, volume, conductivity and the topology of the network.

In light of the well documented poor drug delivery in tumours [Jain, 1994], an interesting outcome of this modeling study is the predicted effect of viscosities on the drug distribution and uptake by the tumour [Figure 3.12 (C&D)]. Reducing blood viscosity in the simulation causes the drug to reach the tumour more rapidly as a consequence of the inverse relationship between viscosity and nodal flow rates. A similar effect to reducing the viscosity is observed by increasing the pressure gradient across the parent vessel (unpublished data). This is interesting as it suggests a possible therapeutic route which could be used as an adjuvant to conventional drugs. Ideas such as this have already been considered by Netti *et al.* who have used angiotensin-II to

[3] Symbolic of the vessel systems of a small tumour (radial TAF source) [Anderson and Chaplain, 1998].

enhance the trans-mural pressure gradient, in this case to improve convection of antibodies to a hypertensive tumour [Netti et al., 1999].

Figure 3.12. Dynamics of simulated drug distribution

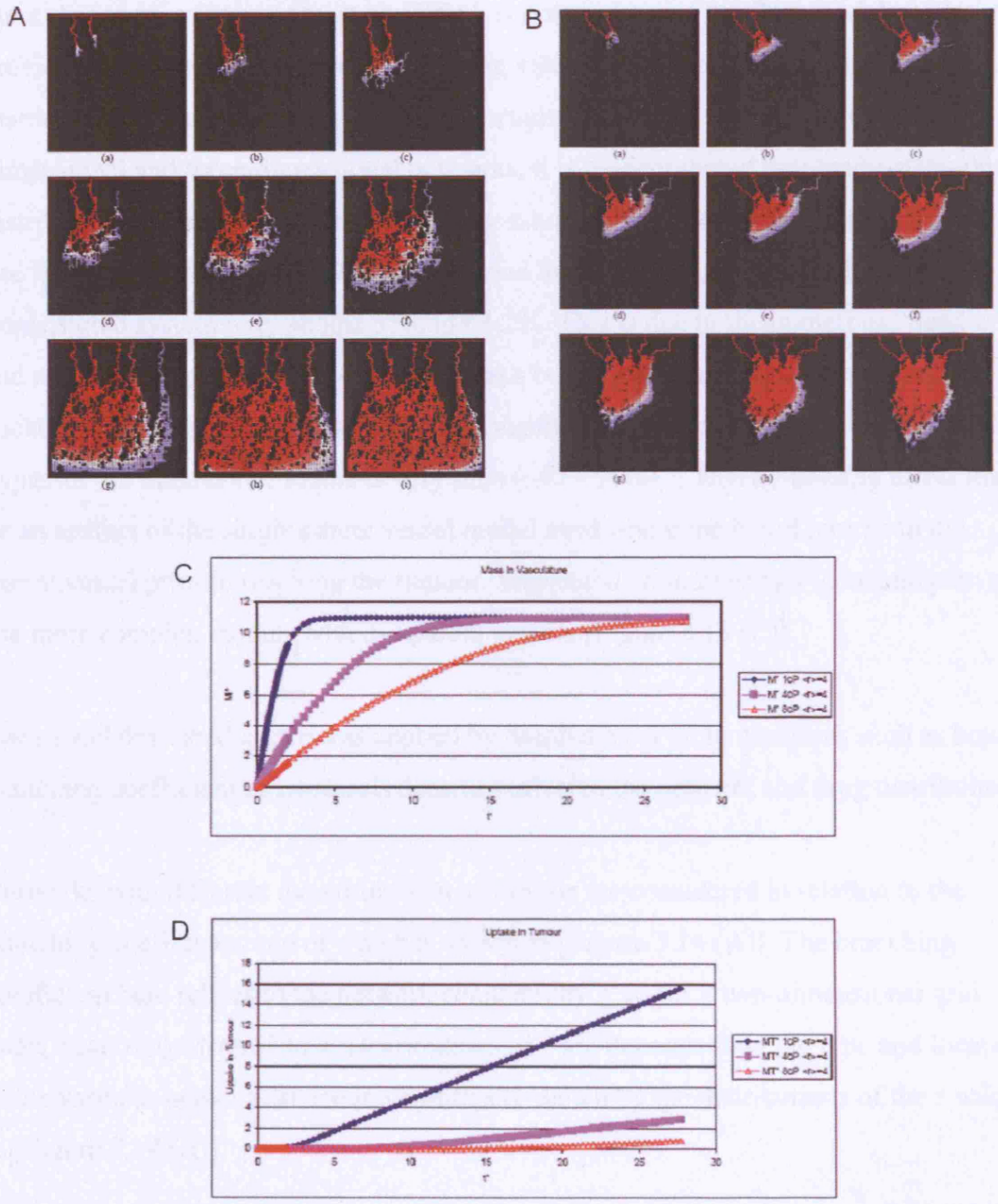

Figure 3.12. Blood flows in from the top left through the network along the various network bond elements and out at the top right. Snapshots of the tracer concentration as it flows from the parent vessel into the vascular network derived from (A) a linear TAF source and (B) a radial TAF source, under constitutive infusion of a tracer, coded (red = high), (white = intermediate) and (blue = low). Subscripts relate to the units of time: (a) t=240s, (b) t=720s, (c) t=1200s, (d) t=2400s, (e) t=3600s, (f) t=7200s, (g) t=16 800s, (h) t=36 000s, (i) t=62 400s. Plots of the total drug mass (y-axis) in the vasculature M^* (C), and the mass uptake by the tumour MT^* (D) for three different values of viscosity, under continuous infusion of drug into vasculature over time (x-axis). Viscosity (centipoises): 1 ('blue diamond' upper curve), 4 ('pink square' middle curve) and 6 ('orange triangle' lower curve) [McDougall et al., 2002].

Stéphanou *et al.* recently extended the network flow model used by McDougall *et al.* to three-dimensions [Stephanou et al., 2005]. A comparison of the flow models with the previous two-dimensional models exploring viscosity, network structure and vessel diameter show that dimensionality affects results [Figure 3.13 (A&B)]. In both two-dimensional and three-dimensional networks, it is evident that at the steady-state, drug distribution in the network is not uniformly saturated. In a two-dimensional capillary bed the drug only reaches between 65.4% and 80.9% saturation, whilst the three-dimensional system only attains 57% to 63.2%. This is due to the numerous "dead-end" and re-circulating capillaries within the brush border that contribute little to the flowing backbone of the vasculature, as with McDougall *et al.'s* model, the amount of drug that bypasses the tumour due to this is very high (~97 - 99%) [4]. This by-passing effect may be an artifact of the single parent vessel model used where the blood returns to the parent vessel prior to reaching the tumour. Stephanou *et al.* raise this issue and plan to use more complex models with 3-4 parent vessels [Figure 3.13 (C)].

The model described above was applied by Stephanou *et al.* to questions such as how branching coefficient anastomosis densities affected the network and drug distribution.

Networks with different quantities of anastomosis are considered in relation to the branching coefficient, one of which is shown in [Figure 3.14 (A)]. The branching coefficient here relates to the network connectivity z, so for a two-dimensional grid node, z can range from 1 to 4. Distributions of z are dependant on the type and location in the vascular network, an example of this is shown by the distributions of the z values in [Figure 3.14 (A)].

The effect of pruning, (i) random vessels (ii) low flow vessels, and (iii) high flow vessels, on drug uptake was also studied, an example is shown in [Figure 3.14 (B)]. Findings from this indicate that more efficient drug uptake (up to 130%) may be achieved by pruning the network. Up to the marked phase transition at 'fraction removed' of 0.06, drug delivery in the network is improved, thereafter it is strongly reduced. Targeting the low flow vessels shows remarkably little effect on the actual

[4] It should be noted that the value quoted here is derived from the model and does not represent an estimate of an *in-vivo* 'by-passing' effect, but rather demonstrate how this behaviour might manifest.

flow and delivery (analogous to targeting the newly formed vessels), in comparison the high flow rate vessels result in rapid shut-down of the flow to the tumour (analogous to targeting mature vessels). Interestingly some of these concepts are paralleled in a similar study made by Tong *et al.* where VEGF receptor-2 blockade with DC101 results in pruning and normalisation of the vascular network removing immature vessels and fortifying the remaining ones [Tong et al., 2004], the effect of this was deeper penetration of molecules into the tumors.

Figure 3.13. A three dimensional model of network flow

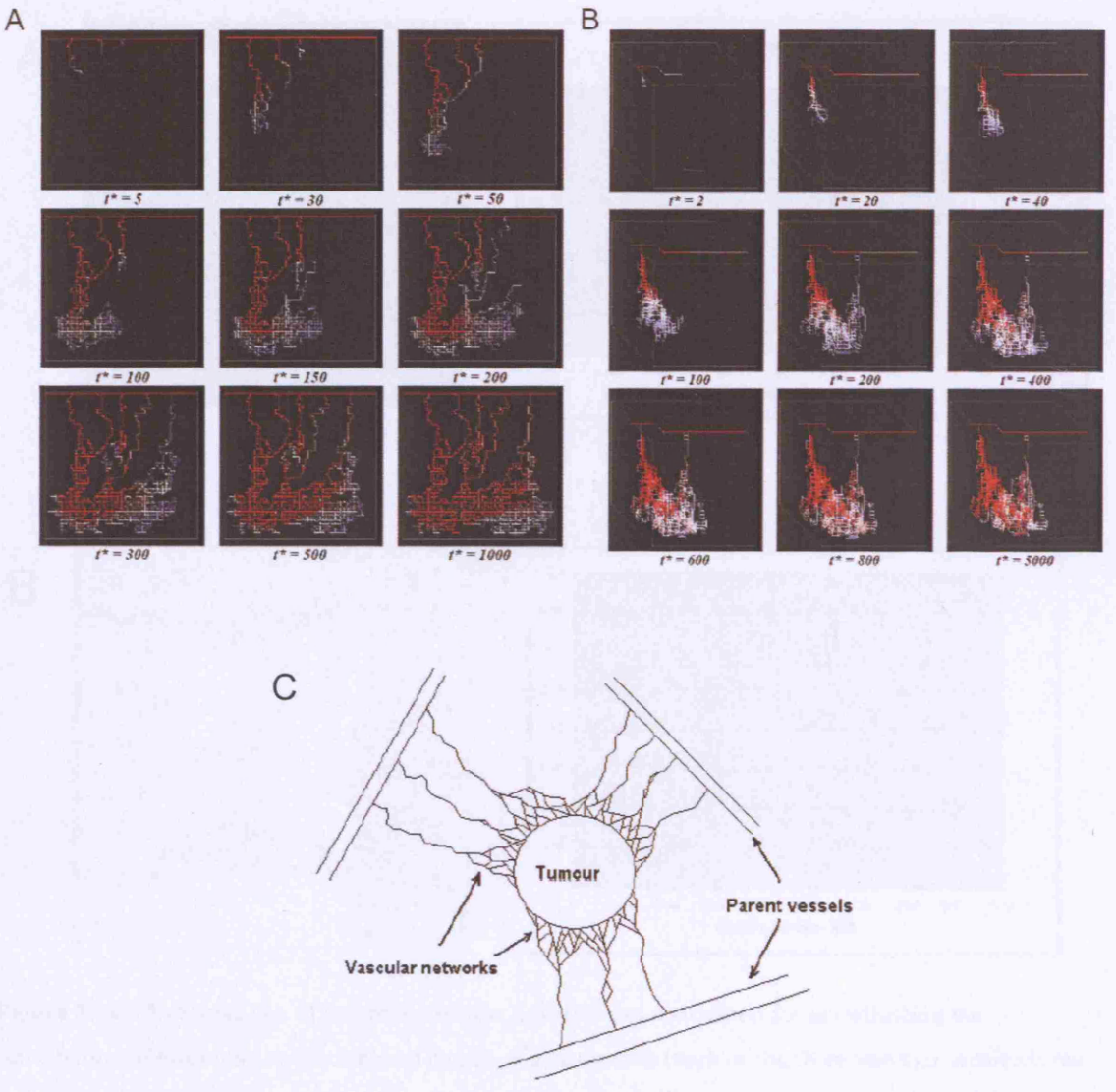

Figure 3.13. Drug distribution in (A) a two-dimensional vascular model, and (B) a three-dimensional vascular model, in either case a drug by-passing is observed (particularly emphasised in the three-dimensional model), drug distributions are colour-coded (red – high and blue – low) concentration. (C) A pending advancement on the current network flow modelling scheme where blood supply from multiple parent vessels will be considered [Stephanou et al., 2005].

Figure 3.14. Dynamics of blood flow with simulated vessel pruning

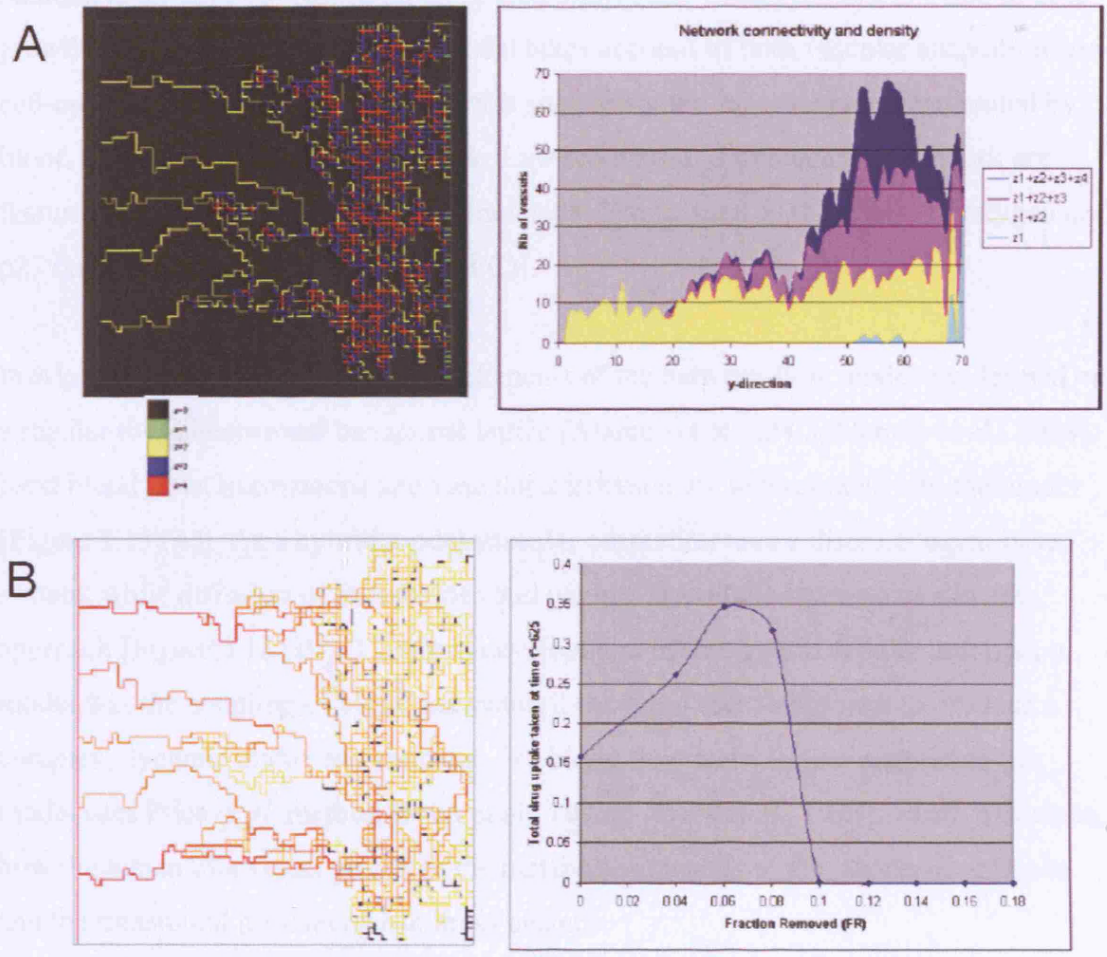

Figure 3.14. (A) Shows one of the three vascular architectures considered for investigating the contribution of branching coefficient and degree of anastomosis (each of the three vascular architectures had a different degree of anastomosis – not shown). The distribution on the right shows the different coefficients along the axis perpendicular to the parent vessel. (B) Shows the effects of random pruning vessels (black) from the vascular network until the fraction-removed is ~0.06 up to this point there is an increase in drug uptake received by the tumour. A sharp phase transition is observed passed this value and the drug uptake is markedly reduced [Stephanou et al., 2005].

The final network-oriented vascular model discussed here has attempted to combine several aspects of the tumour in a single model [Figure 3.15 (A-C)]. To this end, Alarcon *et al.* have developed an integrated multi-scale model for vascularised tumour growth [Alarcon et al., 2004]. The model takes account of both vascular adaptation and cell-cycle dynamics to investigate effects such as spatial inhomogeneity generated by blood flow through the vessel network. Layered on top of this vascular network are features occurring at the cellular and molecular levels, such as the effects of oxygen and p27 on the cell cycle [Figure 3.15 (B&C)].

In Alarcon *et al.'s* model, the vessel elements of the network flow model are defined on a regular two-dimensional hexagonal lattice [Alarcon et al., 2003;Alarcon et al., 2004]. Next blood flow, haematocrit and vascular adaptation are incorporated into the model [Figure 3.15 (A)]. As a hybrid model vascular adaptation uses a discrete 'agent based' system, while diffusion of chemokines and oxygen is modelled using a continuum approach [Figure 3.15 (B)]. The main development of this hybrid cellular automaton model was the coupling of blood haematocrit (oxygen) and cell growth to produce a complex, dynamic micro-environment. For blood flow and vascular adaptation the model uses Pries *et al.* method [Pries et al., 1995a] [Pries et al., 1998], which describes how the lumen of a vessel adapts to the metabolic demands of the surrounding tissue and the transmural pressure/shear stress balance.

All the computational models reviewed in this chapter, are highly idealised, relying for the most part on phenomenological rules to account for the biology. There is currently an initiative (Cancer Physiome project), where the goals are to develop very detailed models of a tumour which will take an integrative approach to modelling its various components. These models are intended to be more data driven and rigorously validated. One of the tumour types which may serve as focus for the Cancer Physiome is colon cancer, due to the large body of data available on this cancer [Alarcon et al., 2004]. To this end, the data produced in [Chapters 4 & 5] of this thesis are of real value to this venture.

Figure 3.15. An integrated model of tumour growth

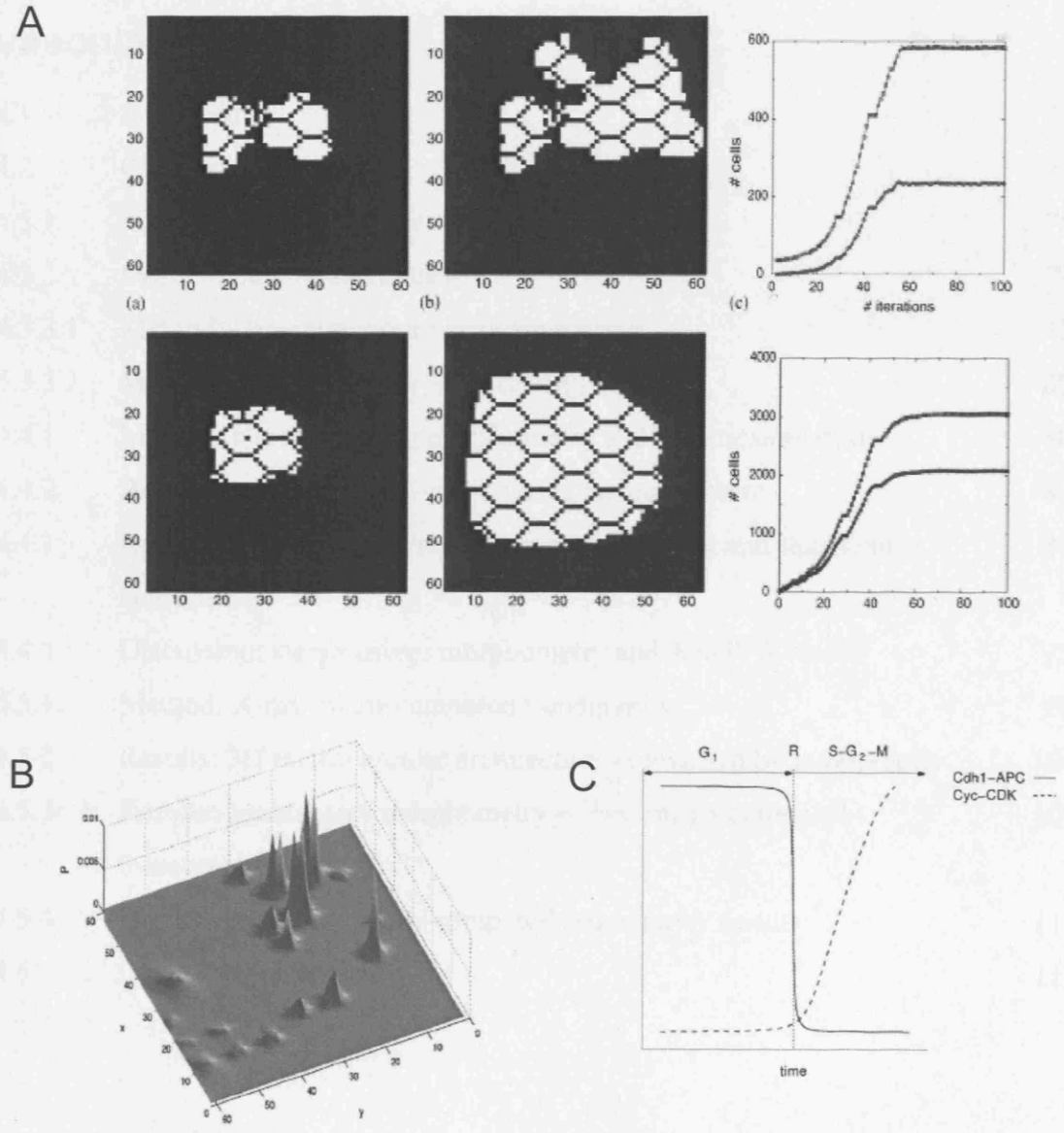

Figure 4.15. An Integrated: molecular, cellular and vascular model of tumour growth.
(A) Vascularised tumour model (white = tumour cells, vessels=hexagonal lattice), (B) the stationary distribution of oxygen, and (C) a growth model for cell division phases. Adapted from [Alarcon et al., 2004]

CHAPTER 4: Comparative study of colonic tumour vascular architecture

4.1 Introduction

In light of studies by Konerding *et al.* which demonstrated quantifiable differences in vessel architecture within regions of clinical tumours [Konerding et al., 2001] and type specificity in xenografts lines [Konerding et al., 1999]. It is clear the vascular architecture is strongly dependent on the local angiogenic environment. As xenografts are separated from their original tissues by a history of successive *passages*[5], this raises the question of how well, if at all, is the originating clinical vascular architecture conserved in a xenograft tumour of the same cancer type?

The focus of this chapter is a characterisation of tumour vascular systems in colonic cancers from both clinical and experimental tumours (xenografts). To achieve this, two quantitative studies of the corrosion cast morphology were carried out. The first method used a stereoimaging technique described by Konerding *et al.*; the second method utilises newly available X-ray micro-computed tomography (micro-CT). To our knowledge this is the first application of X-ray micro-computed tomography in the study of corrosion casts of tumour vasculature. Micro-CT proved to be an excellent method for generating microvascular angiographs, enabling new measures such as vessel surface area and tortuosity to be determined in three-dimensions.

Clinical colorectal tumours, derived from a number of locations in the lower bowel, have been used to create a numerous experimental xenograft tumours which are typically grown subcutaneously in nude mice. Some of these xenograft lines include: HT29(colon), SW1222(colon), LS147T(colon), SW480(colon), SW620(lymph node metastasis), SW48(colon), and SW837(rectum) [Richman and Bodmer, 1988].

For the comparative morphology work carried out in this chapter, two representative xenografts were selected for study: (1) LS147T [Figure 4.1 (A)] - a moderate-to-poorly differentiated tumour consisting of solid chords of cells with numerous *signet ring forms*, a few glandular acini and large necrotic regions [Figure 4.2 (A)] [Sharma et al., 2005] [Pedley et al., 2002], and (2) SW1222 [Figure 4.1(B)] - a well differentiated xenograft with noticeable structural organisation and morphology. Much of this tumour is organised into well defined glandular structures [Figure 4.2 (B)], lined with polarised

[5] The transplantations of tumour tissue in nude mice from one xenograft generation to another.

columnar-shaped cells and some mucus containing goblet cells. Focal clusters of signet ring cells are also observable in the more solid outer regions of SW1222 xenografts. The microvascular systems of these tumours result in a heterogeneous distribution of vessels and both xenografts display hypoxic regions which are particularly emphasized in LS147T, an example of which is shown in [Figure 4.3 (A&B)].

Figure 4.1. Xenograft tumours

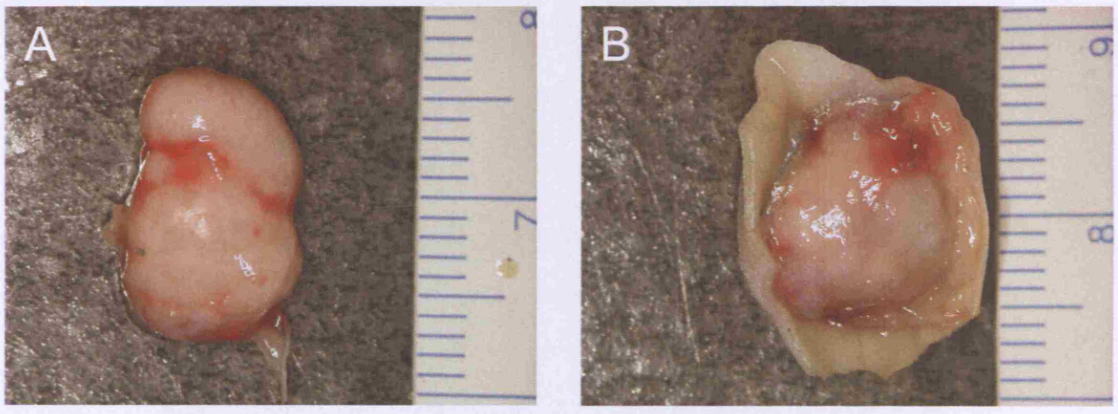

Figure 4.1. Subcutaneously grown colorectal xenograft tumours both tumours also show hemorrhagic regions: (A) LS147T and (B) SW1222 (mouse skin attached behind). Feeding vessels were kept attached to the structure.

Figure 4.2. Colon cancer xenograft histology

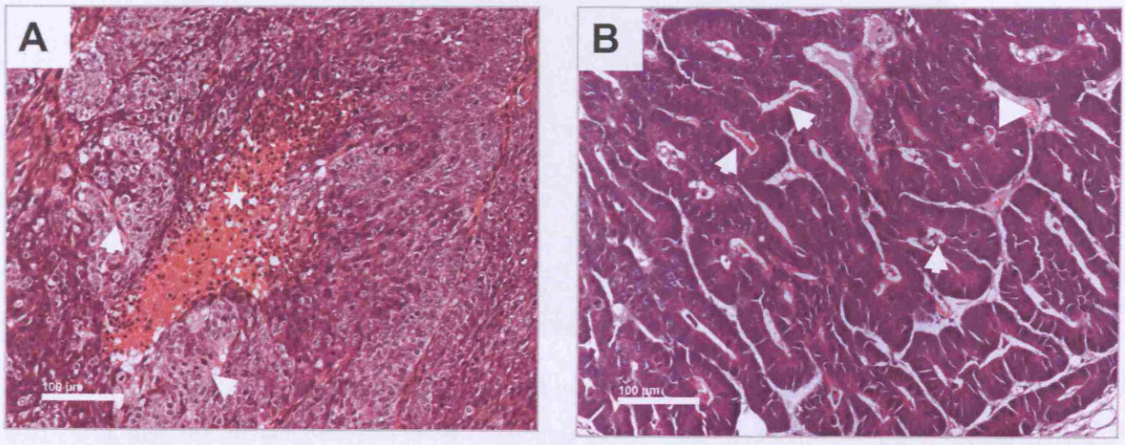

Figure 4.2. Histology sections of (A) LS147T and (B) SW1222 showing different glandular structures in each tissue, glandular acini (arrows), necrotic regions (asterisks) and vessel (triangle). The bar on each image represents 100 μm.

Figure 4.3. The distribution of vascular and perfused tissue in a xenograft

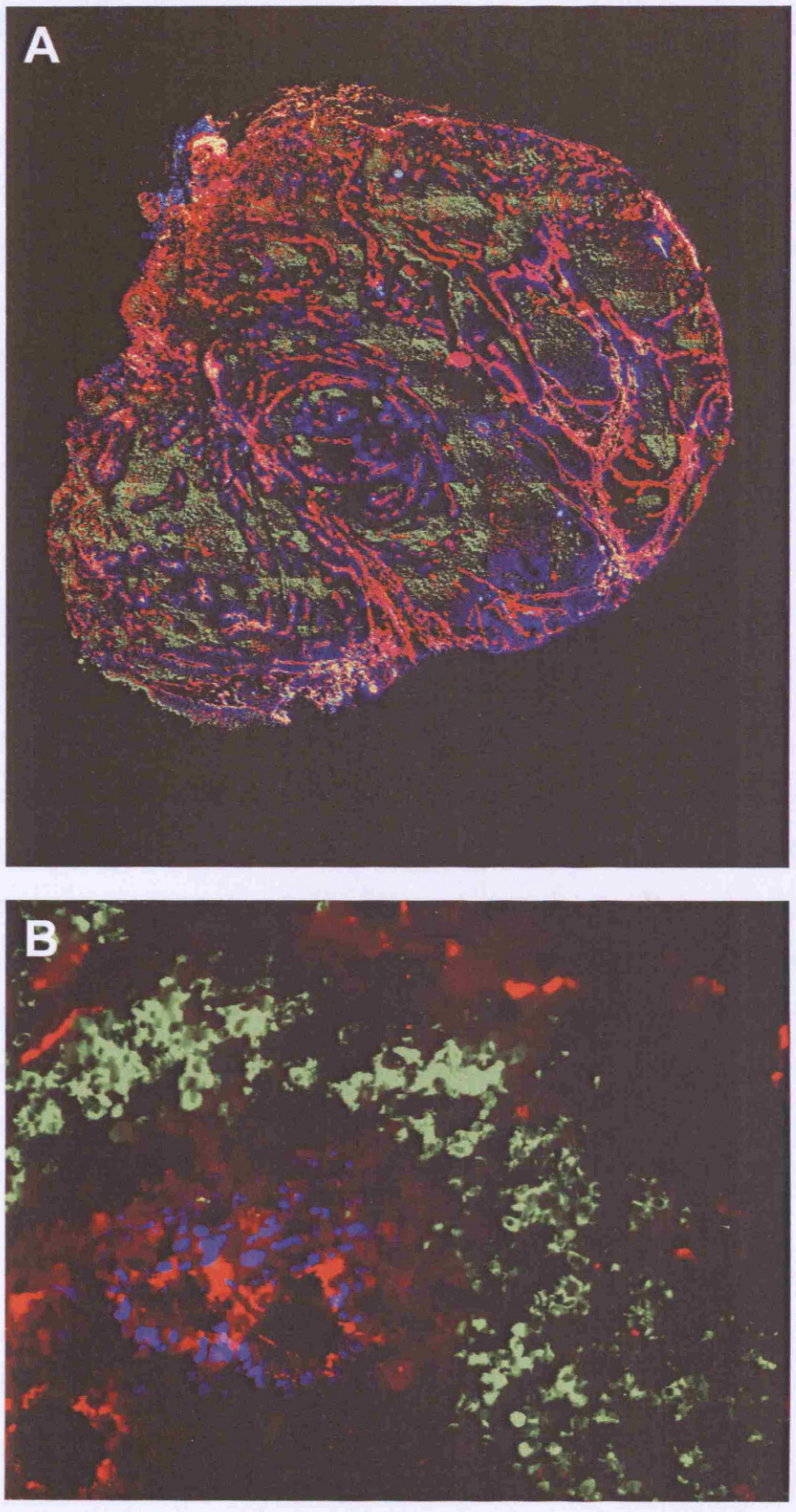

Figure 4.3. A composite image of three fluorescent markers for: vascular endothelial cells (anti-Factor-VIII - red), marking oxygen perfused tissue (Hoechest 33331- blue) and hypoxia marker (pimonidazole - green) in a LS147T tumour. (A) Low power magnification and (B) high power magnification. [Pedley et al., 2002]

Earlier in [Chapter 2] it was argued that the vascular system was best studied as a three dimensional structure. A number of different approaches such as 2-photon microscopy, physical sectioning and optical coherence tomography, were considered as possible methods to elucidate the three-dimensional vascular architecture. Initial studies determined that physical sectioning was impractical due to the technical difficulties associated with sectioning and image registration. In the case of two-photon microscopy, although a promising technique, this system is constrained to use with window chamber xenografts, and additionally was deemed to lack adequate penetration of the sample to make it viable for the intended purposes. No pilot studies were attempted with optical coherence tomography as the equipment was not readily available.

Of the available methods, corrosion casting best satisfied the goals of capturing three-dimensional vascular architecture of the tumour. Following initial work using stereoimaging, X-ray micro-computed tomography was employed for imaging and morphometry of cast architecture. This novel technique enables fully volumetric data to be generated, giving new insight into vascular structure, and represents the first use of this technique to study corrosion casts of tumour vasculature. From this volumetric data it is possible to accurately assess microvascular density, vessel cross-sectional area, specific vessel surface area and tortuosity of the microvasculature. It should be noted that the references to vessels in the context of corrosion casts relate to *a cast of the vessel lumen* and not the actual *vessel* (which includes layers of cells, and proteins discussed in [Section 1.3]).

4.2 Chapter aims

The goals of this chapter are to determine and quantify the three-dimensional structure of the tumour microvascular system in both clinical and experimental colonic tumours. A schematic of the workflow planned is shown in [Figure 4.4].

I. Corrosion cast architecture: This comprises the first phase of the project. Vascular corrosion casts will be produced for use in both stereo-imaging and microcomputed tomography morphology studies.

II. Stereo-imaging morphometry: The first morphometry study of cast architecture will be carried out to measure vessel branching angle, inter-branch distance, vessel diameter and inter-vessel distances by means of stereo-imaging.

III. X-ray micro computed tomography: X-ray micro computed tomography will be used to further explore the structure of the vascular cast. This will complement the stereo-imaging study by generating a volumetric representation of the vascular cast, and will enable previously undetermined parameters such as surface area and vessel cross-section area to be evaluated. This method will also be assessed as a possible alternative to stereo-image analysis.

Figure 4.4. Workflow schema

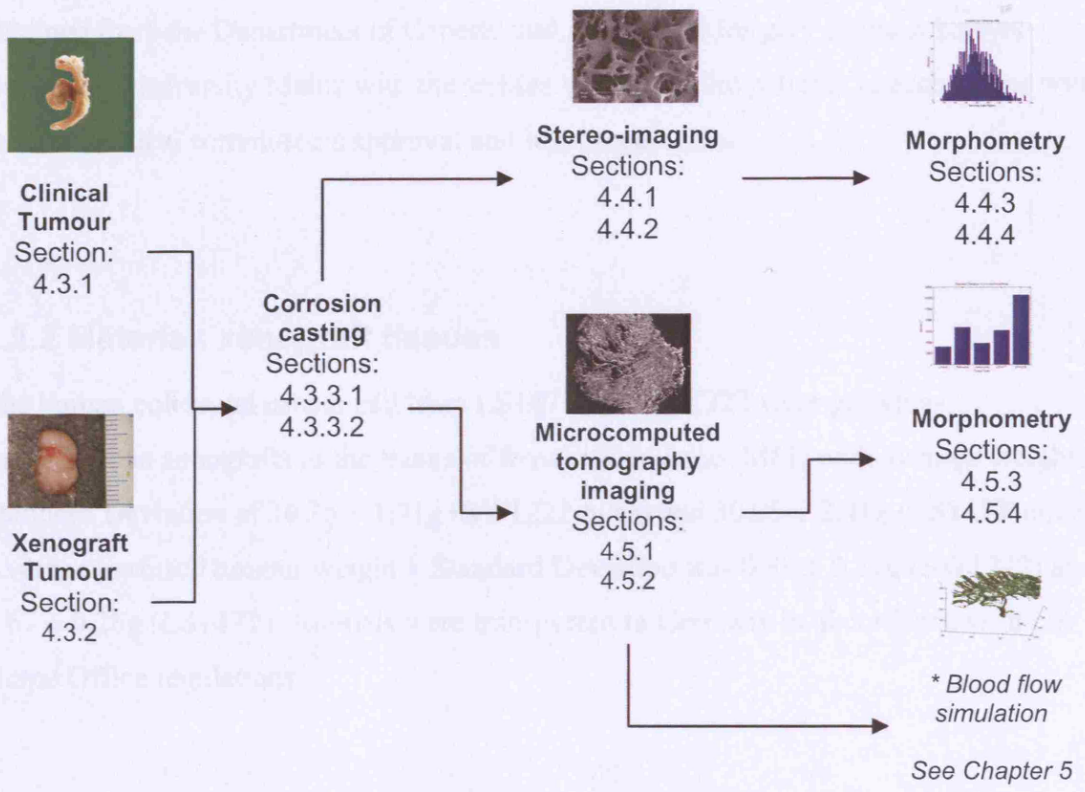

Figure 4.4. Shows the passage of work from a biological system through analysis and *in-silico* simulation. * Blood flow simulations carried out using the microcomputed tomography datasets of the tumour vascular systems are covered in chapter 5

4.3.1 Material: clinical tissues

The corrosion casting study included tumour specimens of clinical cancers excised from 20 patients (mean age 66 ± 3, 12 male, 8 female) undergoing surgery for primary adenocarcinoma, additional precancerous adenomas were found in 6 of these patients. For the adenoma samples: 1-6 samples of whole adenomas were taken from each of the 6 patients. For the adenocarcinoma samples: 3-5 blocks of adenocarcinomas tssue of 0.8-1cm in diameter were taken from the tumour center, periphery and luminal surface in each of the 20 patients. 2 Control tissue blocks representative of normal vascular architecture were taken from the normal gut mucosal at sites distal to the tumours in each of the 20 patients. The sub-division of adenocarcinoma tissue: tumour periphery,

luminal tumour surface and core are shown in [Figure 4.5 (A)]. The clinical samples and corrosion casting were obtained in collaboration with Professor Moritz Konerding [Konerding et al., 2001]. All of these surgical specimens and tissue samples were obtained from the Department of General and Abdominal Surgery of the Johannes Gutenberg-University Mainz with the written consent of the patients in accordance with the local ethical committee's approval and legal regulations.

4.3.2 Material: xenograft tissues

The human colorectal cancer cell lines LS147T and SW1222 were grown as subcutaneous xenografts in the flanks of female nude mice (MFI) with average weight ± Standard Deviation of 26.35 ± 1.71g (SW1222 mice) and 30.25 ± 2.41g (LS147T mice). Average perfused tumour weight ± Standard Deviation was 0.88 ± 0.27g (SW1222) and 0.67 ± 0.28g (LS147T). Animals were transported to Germany in accordance with UK Home Office regulations.

4.3.3.1 Method: clinical tumour corrosion casting

For the clinical tumours, fresh hemi-colonectomy specimens were excised from patients undergoing surgery for colorectal cancer. The main arteries of the excised tissue were cannulated and blood was flushed out with 37 °C heparinated buffered saline prior to injection with 80–120mls of the Mercox CL-2B epoxy polymer. 3–5 tissue samples with a diameter of 0.8–1.0cm were excised from the tumour centre, the periphery and the invasive edge and/or polyps. After an initial 24 hour in water at 80°C, tissue digestion was performed by soaking in NaOH (7%) for 1-2 weeks, changing the solution and washing frequently. Following successful removal of all tissue, final hardening of the cast was completed by freeze drying overnight. The sample was then mounted and prepared for scanning electron microscopy and microcomputed tomography.

4.3.3.2 Method: xenografts corrosion casting

For the colorectal xenografts, 6 tumours of each xenograft type (SW1222 and LS174T) were used for stereo-imaging. Under deep pentobarbital anaesthesia, forearms and hind legs of the mice were pinned to the dissection board and they were then thoracotomized. Forceps were pierced through the connective tissue behind the aorta and a suture was threaded through. The left ventricle was subsequently pierced with a broken pipette and drained of blood. Through the left ventricle incision the aorta was cannulated and secured with the pre-threaded suture. The right atrium was then opened and the vascular system flushed through with 15 millilitres of 37° C heparinated PBS solution (36-38°C, 0.9% NaCl, pH 7.4).

Prior to perfusion of the casting polymer, the right forearm was unpinned to relieve constriction and allow better perfusion. 7-10mls of Mercox CL-2B (Vilene Med. Co., Tokyo, Japan) diluted with 20% methylmethacrylate monomers (Merck, Darmstadt, Germany) was perfused through the mouse. The aorta was then clamped; the animal sacrificed and then soaked in water for 30 minutes to allow the polymer to set.

Post-curing, the tumour was excised for tissue digestion and histology staining, (half of one tumour from each of the two cell lines was formalin-fixed and processed to paraffin for haematoylin-eosin staining to show morphology. After an initial 24 hour in water at 80°C, tissue digestion was performed by soaking in NaOH (7%) for 1-2 weeks, changing the solution and washing frequently. Following successful removal of all tissue, final hardening of the cast was completed by freeze drying overnight. The sample was then mounted and prepared for scanning electron microscopy and microcomputed tomography.

4.4.1 Method: stereo-imaging morphometry and statistical analysis

Each cast was mounted onto a specimen stub (BAL-TEC AG, Walluf, Germany) with conductive silver paste (Plano, Marburg, Germany), stabilized with copper conductive bridges and coated with gold in an argon atmosphere to a thickness of 40-45 nm at an amperage of 30-35 nA (BAL-TEC AG, Walluf, Germany). 10-25 stereo-images of each cast were collected using a scanning electron microscope (Cambridge Stereoscan 180

SEM). Four parameters (inter-vessel distance, inter-branch angle, inter-branch distance and branching angle) [Figure 4.5 (B)] were calculated from stereo image pairs [Konerding et al., 2001;Konerding et al., 1999;Malkusch et al., 1995]. Image digitization, enhancement and 3D-morphometry (stereoptic) were carried out with the Kontron® KS 3000 (Kontron, Eching, Germany) image analysis application using additional macros developed by Malkusch *et al.* [Malkusch et al., 1995].

Measurements are calculated as a function of equivalent pairs of x-y coordinates on each image. The known parallax tilt of 6 degrees enables linear distances and angles to be calculated in three dimensions. Linear distances were measured using two pairs of points, equations [4.1-3], and branching angles with 3 pairs of points, equations [4.4-10]. Computation of the distances and angles are detailed in [Figure 4.6 (A&B)].

The depth is calculated using parallax angle:

$$z_{1r} = (x_{1r} - x_{1g})/(2*\sin(6/2)) \qquad [4.1]$$

$$z_{2g} = (x_{2r} - x_{2g})/(2*\sin(6/2)) \qquad [4.2]$$

The distance *c* is given by:

$$dx^2 = (x_{2r} - x_{1r})^2$$

$$dy^2 = (y_{2r} - y_{1r})^2$$

$$dz^2 = (z_{2r} - z_{1r})^2$$

$$c = \sqrt{dx^2 + dy^2 + dz^2} \qquad [4.3]$$

In a similar to manner to the calculation of linear distance depth, calculations the depth coordinates $Z_{1\text{-}3}$ is given by:

$$z_{1r} = (x_{1r} - x_{1g})/(2*\sin(6/2)) \qquad [4.4]$$

$$z_{2r} = (x_{2r} - x_{2g})/(2*\sin(6/2)) \qquad [4.5]$$

$$z_{3r} = (x_{3r} - x_{3g})/(2 * \sin(6/2)) \qquad [4.6]$$

The distances *a, b* and *c* is given by:

$$dx^2 = (x2r - x3r)^2 \qquad dx^2 = (x1r - x3r)^2 \qquad dx^2 = (x2r - x1r)^2$$

$$dy^2 = (y2r - y3r)^2 \qquad dy^2 = (y1r - y3r)^2 \qquad dy^2 = (y2r - y1r)^2$$

$$dz^2 = (z2r - z3r)^2 \qquad dz^2 = (z1r - z3r)^2 \qquad dz^2 = (z2r - z1r)^2$$

$$a = \sqrt{dx^2 + dy^2 + dz^2} \qquad b = \sqrt{dx^2 + dy^2 + dz^2} \qquad c = \sqrt{dx^2 + dy^2 + dz^2}$$

[4.7] [4.8] [4.9]

The angle θ between the branching vessel elements is then given by:

$$\theta = \arccos((b^2 + c - a^2)/(2bc))180/\pi \qquad [4.10]$$

Graphical display and statistical analysis were performed using MATLAB® (Mathworks, Natick, Massachusetts, USA). Means of each parameter class: branching angle, inter-branch distance, vessel diameter, and inter-vessel distance for each tissue were compared using a pairwise balanced one-way analysis of variance (ANOVA). This test requires an identical sample size across each tissue type, which was created by taking *N* data points (*N* being the number of samples in the smallest group), uniformly resampled (matlab *randsample*) without replacement, from the original data. Log_{10}-transformation was required to satisfy the normal distribution requirements of the ANOVA in the case of inter-branch distance, vessel diameter, and inter-vessel distance which were all skewed with a z-score >1.96 [Rorden, 2007]. In all tests the critical value was taken at 5%.

Figure 4.5. Carcinoma sub-regions and vascular architecture parameters

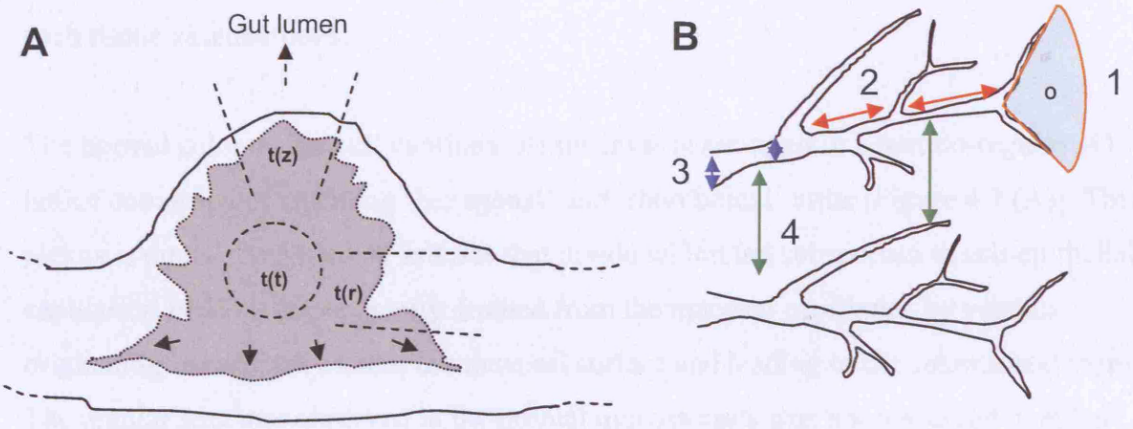

Figure 4.5. (A) Cross-section of a tumour/gut-wall neoplastic tissue (grey). Carcinoma sub regions selected for study: tumour periphery (tr), luminal tumour surface (tz), and tumour core (tt). (Gut lumen [dashed arrow], invasive front [solid arrows]). (B) Parameters measured by stereo-image morphometry: 1) branching angle (orange), 2) inter-branch distance (red), 3) vessel diameter (blue) and 4) inter-vessel distance (green).

Figure 4.6. Distance and angle calculations in stereoimaging

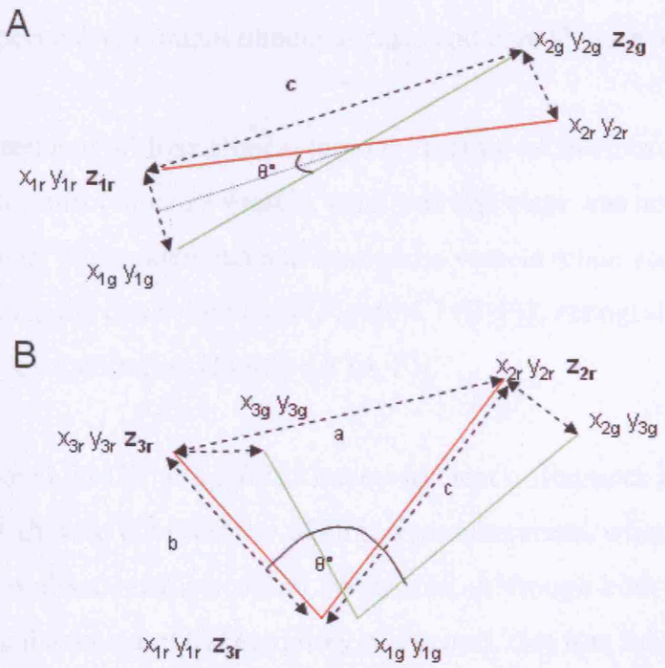

Figure 4.6. (A) For images *r (red)* and *g (green)* positions *x,y* refer to the coordinate positions on each image, *z* defines a calculated depth value. The value *c* is the calculated linear distance between the two three-dimensional coordinates $x_{1r}y_{1r}$, z_{1r} and $x_{2g}y_{2g}$, z_{2g}. (B) For images *r (red)* and *g (green)* positions *x,y* refer to the coordinate positions on each image, *z* defines a calculated depth value. The angle θ is the calculated angle between a three-dimensional bifurcation.

4.4.2 Results: qualitative observations of cast architecture

A number of distinct features are observable in the scanning electron micrographs of each tissue vascular casts.

The normal colonic mucosal capillary plexus layer is arranged in a pseudo-regular 3D lattice composed of repeating 'hexagonal' and 'rhomboidal' units [Figure 4.7 (A)]. This plexus is directly supplied by arteries that divide within the submucosa to sub-epithelial capillaries, blood is subsequently drained from the mucosal capillaries by venules originating immediately under the mucosal surface and leading to the submucosal veins. The regular structure observed in the normal mucosa casts was not preserved in either clinical samples (adenoma or carcinoma) or xenografts.

An extensively branched tree-like phenotype was observed in the adenoma vascular casts. Although branching hierarchy was best preserved in the adenoma [Figure 4.7 (B&C)], much of the architectural features commonly associated with tumour vasculature (heterogeneity, tortuosity, fenestrations and blind endings) were also present in the carcinoma periphery, luminal tumour surface and core [Figure 4.7 (D-F)].

It can clearly be seen that all four clinical tumour vascular architecture are abnormal when compared to control mucosa vessels, what was less clear was how they vary with respect to each other. While adenoma and carcinoma vessels retain some of the hierarchy observed in the control mucosa [Figure 4.7 (B-F)], xenograft vasculature was without comparable organisation [Figure 4.8 (A-F)].

Images of casts from LS147T and SW1222 showed clear differences in structure. In particular LS147T showed the presence of large avascular areas, which putatively were due to regions of localised necrosis within the tumour. Although both tumours showed an increase in vascularisation at the periphery of the cast, this was much more pronounced in SW1222 casts [Figure 4.8 (C)], in general this tumour was more vascularised. Smaller vessels in LS147T casts appeared narrow, poorly organised and frequently terminated in blind endings [Figure 4.8 (B)], in contrast to those of SW1222 [Figure 4.8 (C)], which were generally larger.

Some interesting, if less generalised, observations were made in a number of casts. In [Figure 4.8 (A)] abnormal growth surrounding a large feeding vessel entering a LS147T tumour is shown. Here the central vessel can just be made out underneath a dense mat of tortuous sprouts – this particular form of vessels was only seen in one cast. In a few LS147T and SW1222 casts, flattened nodules of the casting polymer formed into structures which did not resemble vessels [Figure 4.8 (D)]. Leaking polymer is indicative of the vascular tone and porosity as the casting polymer is normally too viscous to seep through the pores of normal vessels. The presence of abnormal vascular wall was a feature of a number of tumour casts where large pores and fenestrations are highlighted by stubs of extruded polymer. These extra-vascular extrusions of polymer were highly heterogeneous, ranging from small protrusions on the surface of the vessel to large globular domains (some of which may also possibly represent regions of blood lakes in the tumour [Konerding, 2005]). These extrusions of polymer were more common in the xenograft casts than the adenoma and carcinoma samples. A good example of aberrant vascular connectivity is shown in [Figure 4.8 (E&F)]. In this SW1222 xenograft there is a direct connection of an arteriole to a venule with no discernable intervening capillaries. Arterial-side vessels are identified by the shape of the oblong endothelial cell nuclei imprints (marked by the black arrow) in the cast polymer, whereas the venule endothelial nuclei indentations were more rounded (marked by the white arrow). Further anomalies in the local vessel morphology in [Figure 4.8 (E)] include the flattened vessels, which is consistent with compressive forces exerted by the tumour cells and elevated interstitial pressure.

To some extent a distinct core and periphery were observable in the xenografts, although these domains were sometimes not well defined. In some cases, densely vascularised regions were observed centrally in the xenograft and conversely avascular (and poorly vascularised) regions spread out to the peripheral regions of both xenograft types. This can also be seen in the staining of normoxic and hypoxic microenvironments in LS147T [Figure 4.3 (A)]. There is also some evidence to suggest that the core vessels are larger (and often flattened) in both xenografts [Figure 4.8 (E)] (though no time was available for quantitative study).

Figure 4.7. Examples of normal mucosa and clinical tumour vessels

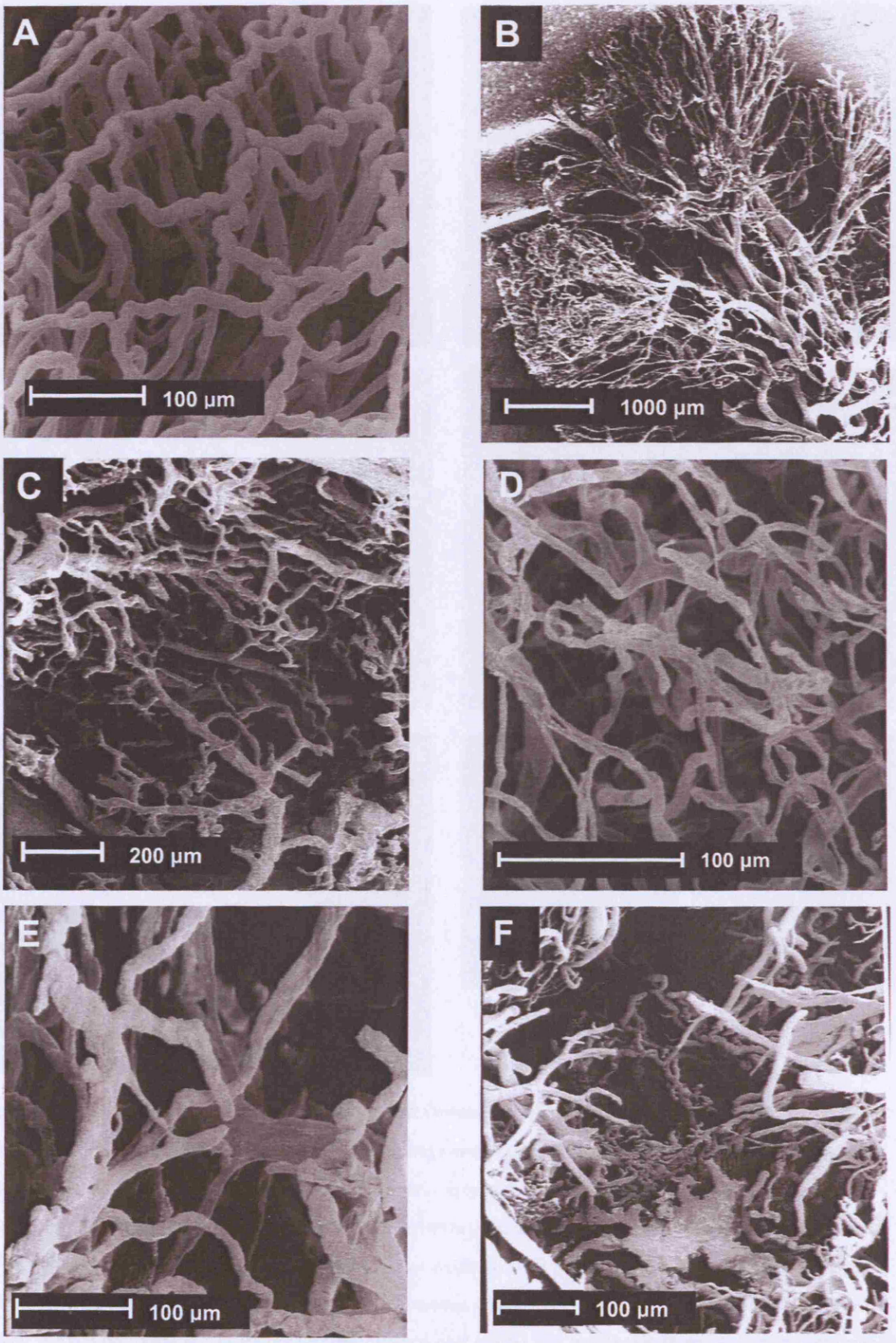

Figure 4.7. Scanning electron micrographs of the corrosion casts of the vessel lumens from (A) control mucosa, (B) adenoma low resolution, (C) adenoma high resolution, (D) carcinoma *periphery (tr)*, (E) carcinoma *luminal tumour surface (tz),* (F) carcinoma *core (tt)*. [from Konerding image Library]

Figure 4.8. Examples of LS147T and SW1222 vascular cast architecture

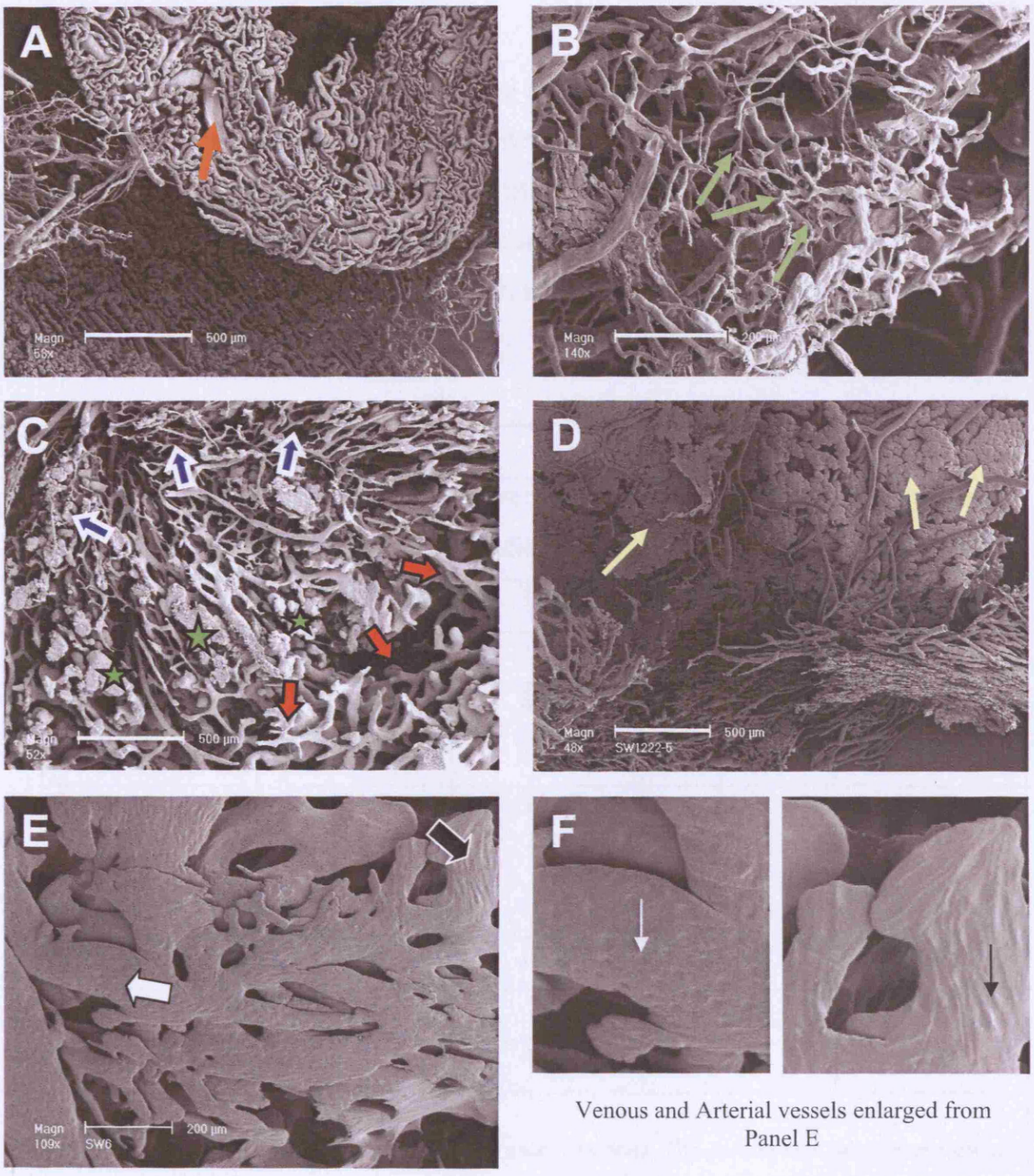

Figure 4.8. (A) LS147T abnormal vessel growth around a large supplying vessel (orange arrow), (B) LS147T poorly organised vessels with blind endings and shunts were commonly observed in the xenograft casts (green arrows), (C) SW1222 vessels appeared larger towards the core of the tumour, directions of the tumour core (red arrows) and periphery (blue arrows); exuding polymer (green stars), (D) SW1222 showing large globular extravascular extrusions of casting polymer (yellow arrows), (E) SW1222 demonstrates an example of an arterio-venous shunt; characteristic indentations of arteriole (black arrow) and venule (white arrow) endothelial cell nuclei can be clearly seen on two vessels which have no adjoining capillaries and (F) Enlarged sections from the previous panel showing characteristic endothelial cell indentations on the casting polymer. *Scale bars: 500µm (A,C,E) and 200µm(B,D).*

4.4.3 Results: quantitative stereo-image morphometry and statistical analysis

Stereo-imaging measurements, as described in [Section 4.4.1], were collected for each geometrical parameter (branching angle, inter-branch distance, vessel diameter and inter-vessel distance), and the resulting distributions of these parameters were analysed in order to demonstrate statistically significant differences between the cast architectures. The number of samples taken in each instance is listed in [Table 4.1].

Table 4.1. Stereoimaging measurements

	Branching angle	Inter-branch distance	Vessel diameter	Inter-vessel distance
Control	1806	3001	5000	1127
Adenoma	920	1104	3000	1142
Carcinoma*	6284	8889	15250	7200
Periphery – tr	2306	3517	5250	2627
Luminal Tumour Surface- tz	2236	3517	5250	2486
Core – tt	1742	1855	4750	2087
LS147T	860	793	1223	1107
SW1222	827	932	1243	979

Table 4.1. The number of sampled data points for each parameter. The *carcinoma** samples represent pooled data from *periphery (tr)*, *luminal tumour surface(tz)* and *core(tt)*. The *adenomas* are not separated into equivalent regions for analysis due to the relatively small size of the polyps.
The Control, Adenoma and Carcinoma data were kindly provided by Professor Moritz Konerding, University of Mainz, Germany. The Xenograft data (LS147T and SW1222) was collected by the Author at UCL's Clinical Oncology Dept. Royal Free Hospital, London.

The histograms of each of the geometrical parameters are shown in [Figures 4.9-12], ANOVA for each dataset are shown in [Figures 4.13-15].

Figure 4.9. Distribution of branching angles

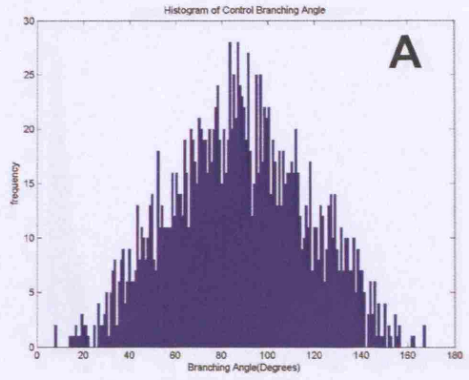

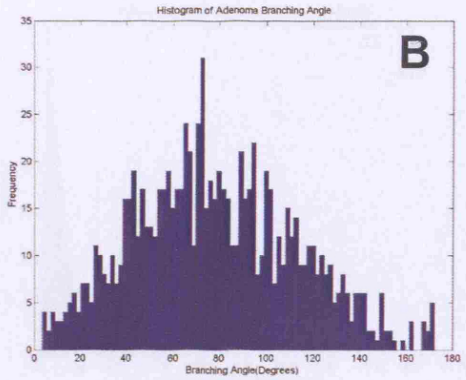

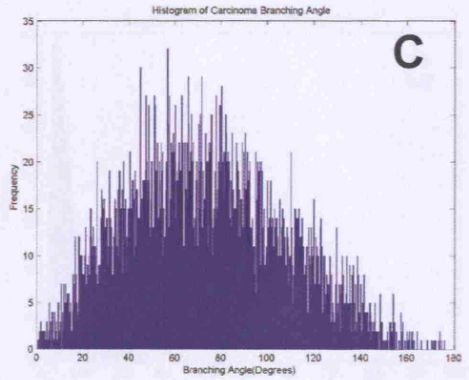

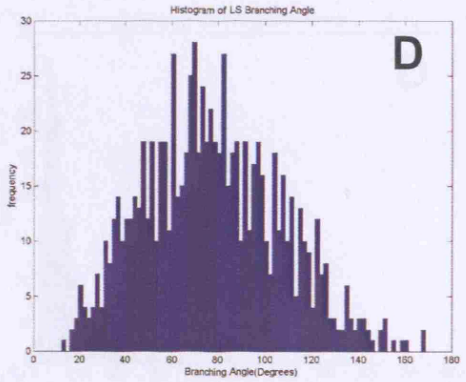

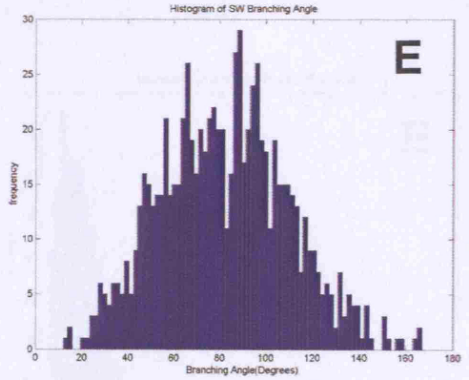

Tissue	Mean (degrees)	Standard Deviation	Skew
Control	87.14	29.10	0.01
Adenoma	77.74	34.81	0.26
Carcinoma	73.31	33.57	0.26
LS147T	77.16	29.30	0.286
SW1222	81.85	27.60	0.166

Figure 4.9. Histograms of branching angle distributions in: (A) normal mucosa, (B) adenoma, (C) adenocarcinoma, (D) LS147T and (E) SW1222.

Figure 4.10. Distribution of inter-branch distances

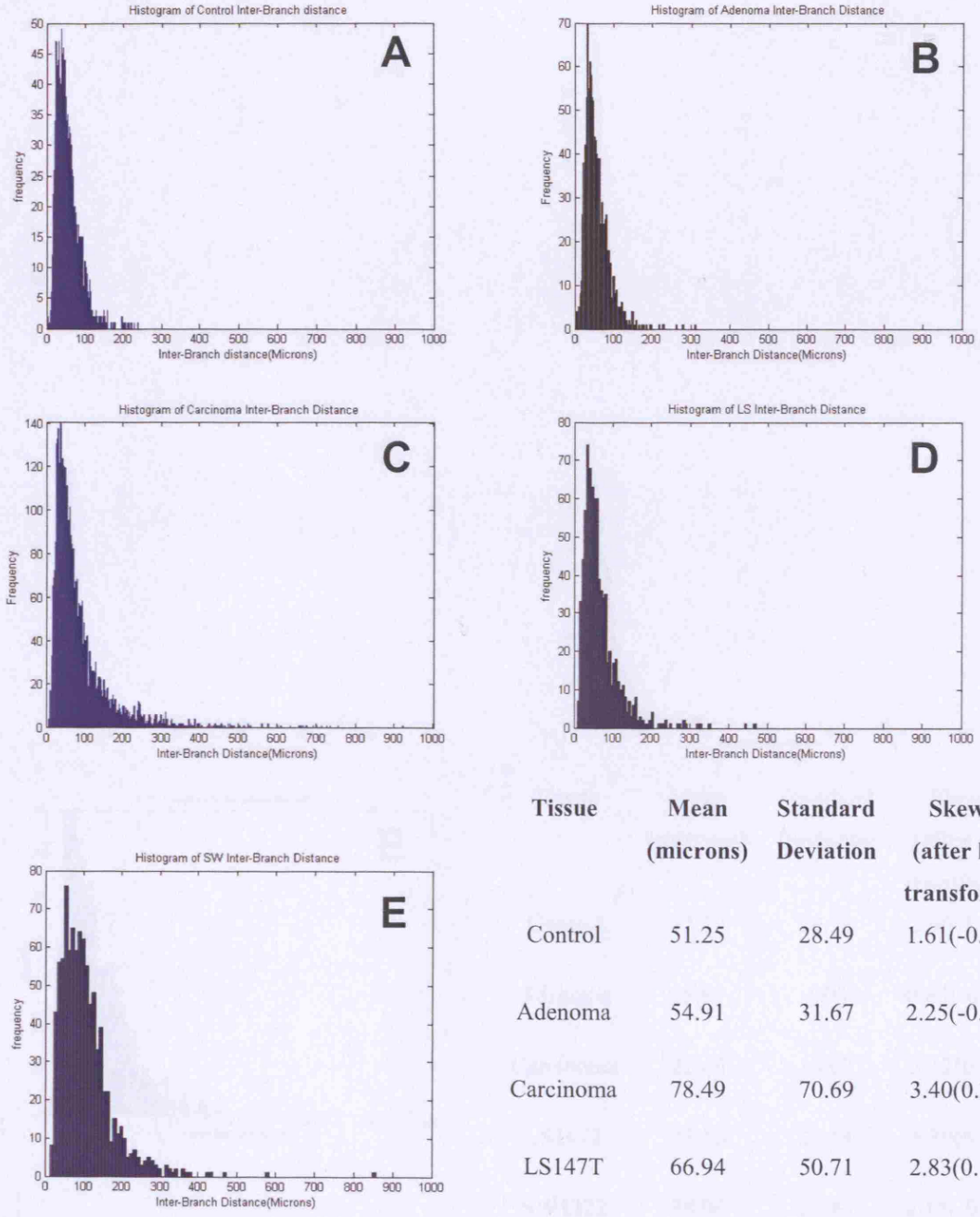

Tissue	Mean (microns)	Standard Deviation	Skew/ (after log transform)
Control	51.25	28.49	1.61(-0.23)
Adenoma	54.91	31.67	2.25(-0.25)
Carcinoma	78.49	70.69	3.40(0.30)
LS147T	66.94	50.71	2.83(0.18)
SW1222	104.75	70.89	2.81(-0.09)

Figure 4.10. Histograms of inter-branch distance distributions in: (A) normal mucosa, (B) adenoma, (C) adenocarcinoma, (D) LS147T and (E) SW1222.

Figure 4.11. Distribution of vessel diameters

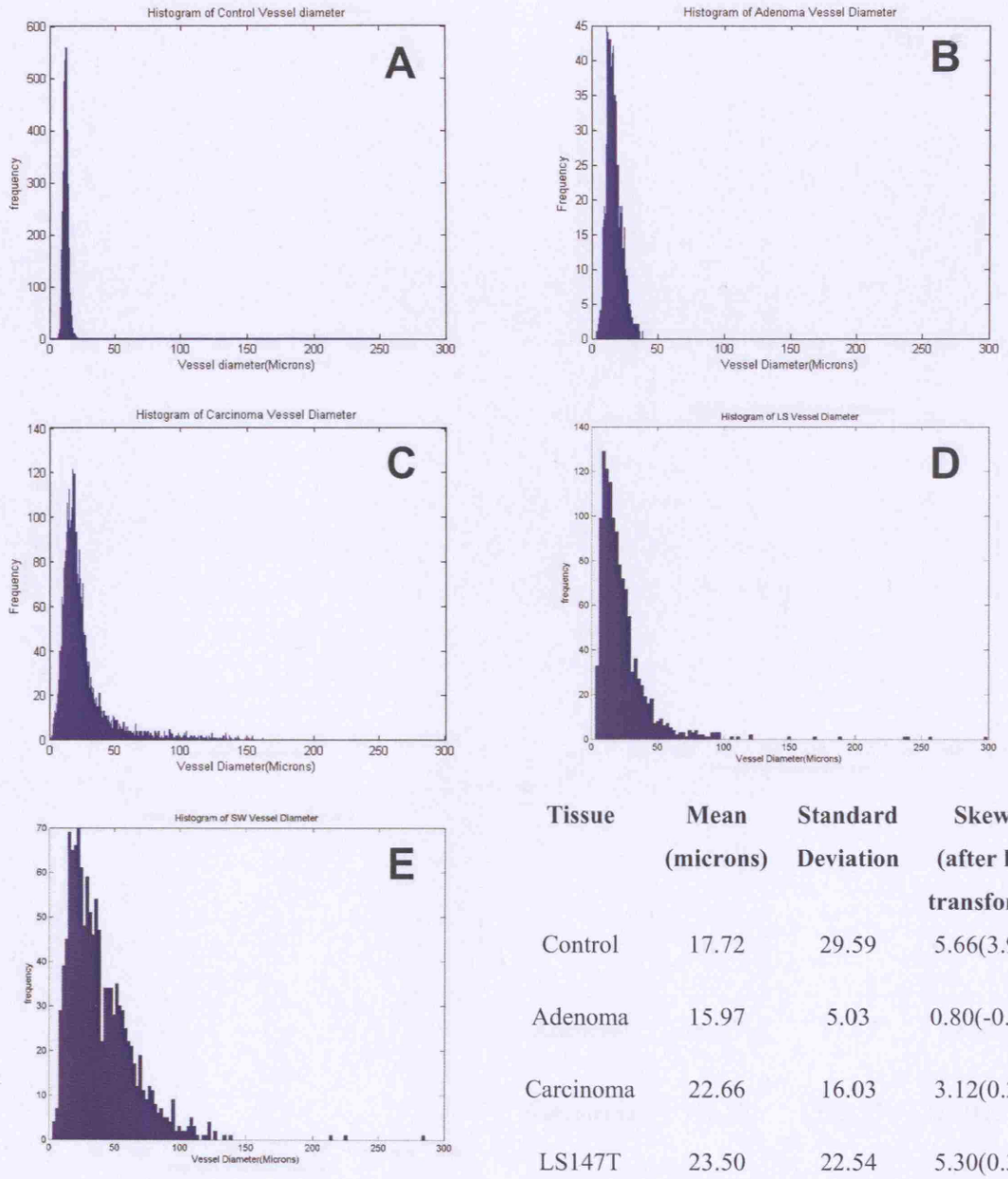

Tissue	Mean (microns)	Standard Deviation	Skew/ (after log transform)
Control	17.72	29.59	5.66(3.96)
Adenoma	15.97	5.03	0.80(-0.14)
Carcinoma	22.66	16.03	3.12(0.20)
LS147T	23.50	22.54	5.30(0.37)
SW1222	38.96	25.45	2.15(-0.18)

Figure 4.11. Histograms of vessel diameter distributions in: (A) normal mucosa, (B) adenoma, (C) adenocarcinoma, (D) LS147T and (E) SW1222.

Figure 4.12. Distribution of inter-vessel distances

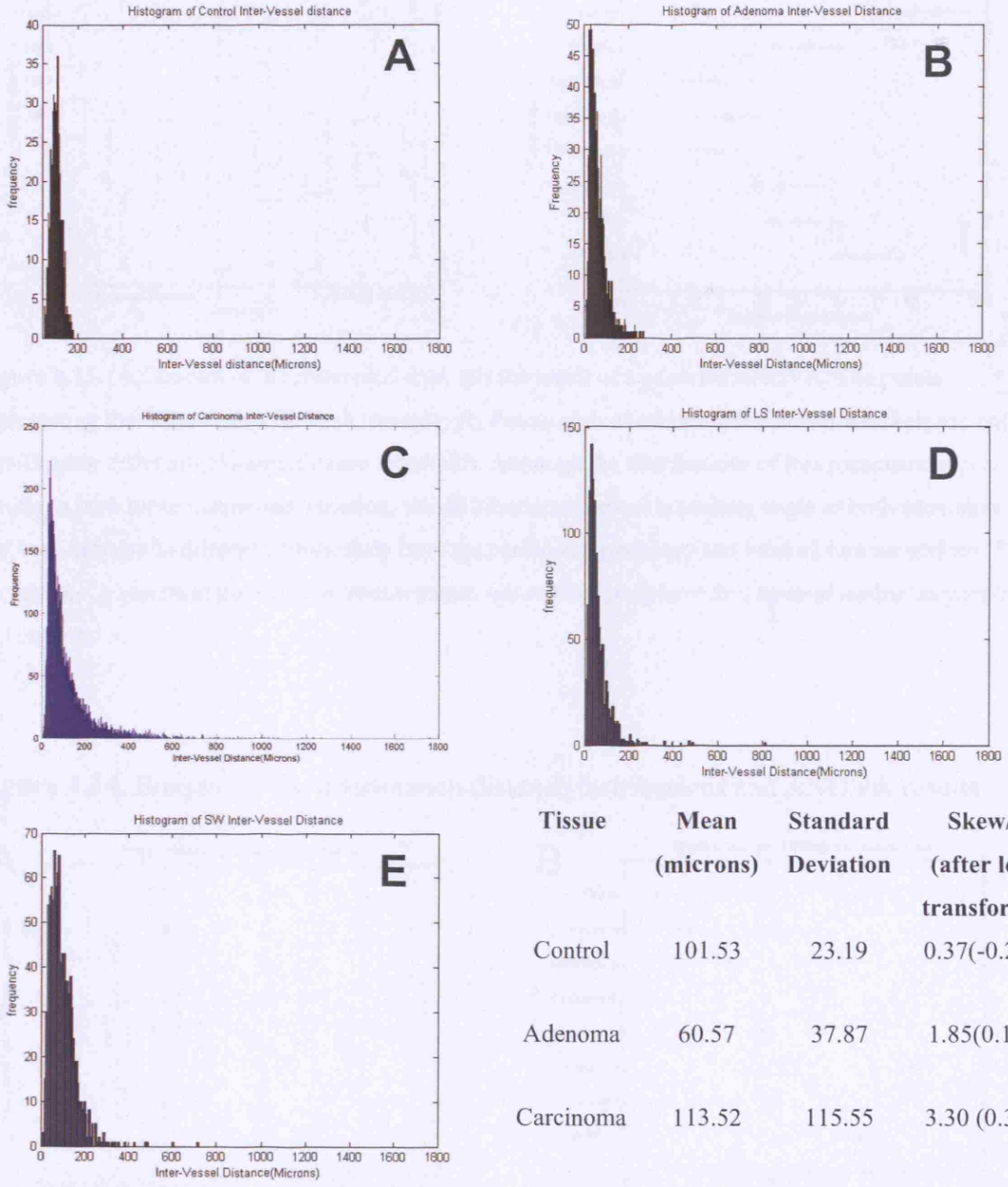

Tissue	Mean (microns)	Standard Deviation	Skew/ (after log transform)
Control	101.53	23.19	0.37(-0.24)
Adenoma	60.57	37.87	1.85(0.19)
Carcinoma	113.52	115.55	3.30 (0.33)
LS147T	59.76	55.75	4.87(0.10)
SW1222	96.70	64.625	2.71(-0.29)

Figure 4.12. Histograms of inter-vessel distance distributions in: (A) normal mucosa, (B) adenoma, (C) adenocarcinoma, (D) LS147T and (E) SW1222.

Figure 4.13. Boxplot of the branching angle distributions and ANOVA results

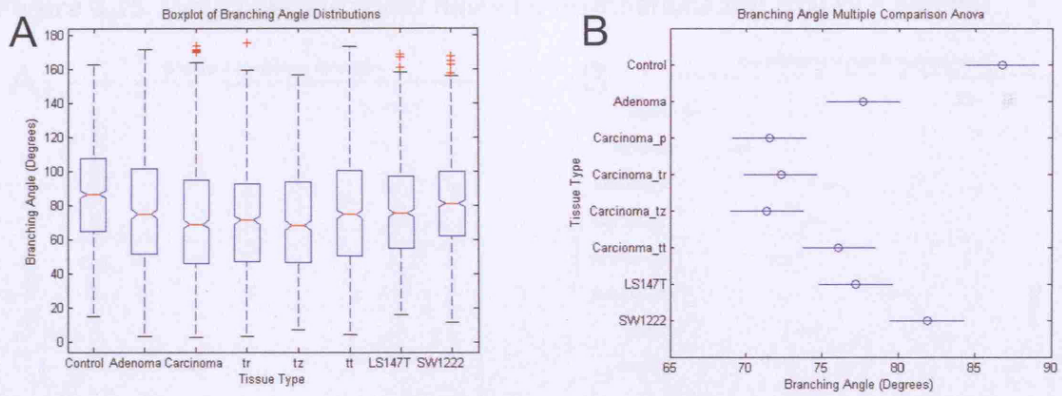

Figure 4.13. (A)Boxplot of the resampled data, (B) the result of a pairwise ANOVA. The points representing the mean values for each tissues type. Points with overlapping horizontal whiskers are not significantly different (5% significance threshold). Although the distributions of this parameter appear similar in both mean values and variation, the distribution of vessel branching angle in both adenomas and both xenografts differed significantly from the carcinoma periphery and luminal tumour surface. * *Carcinoma_p* represent pooled data from separate sub-regions *periphery (tr)*, *luminal tumour surface(tz)* and *core(tt)*.

Figure 4.14. Boxplot of the inter-branch distance distributions and ANOVA results

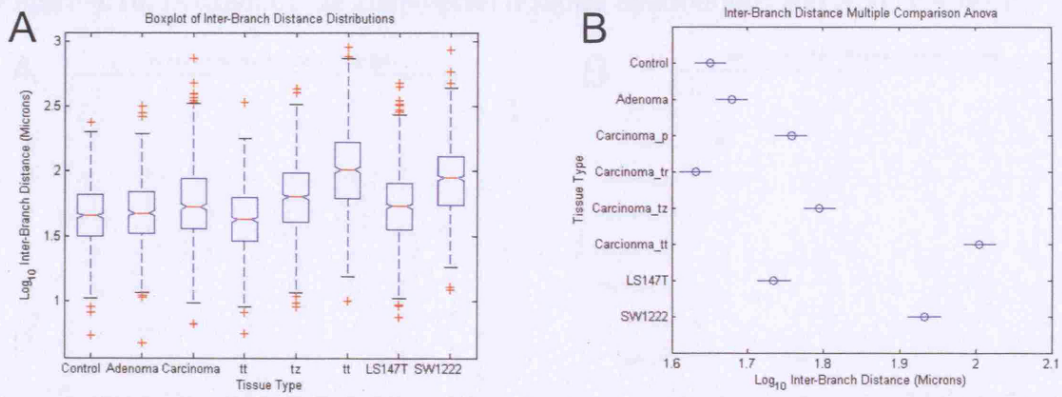

Figure 4.14. (A)Boxplot of the resampled data (log_{10} transformed), (B) the result of a pairwise ANOVA. The points representing the mean values for each tissues type. Points with overlapping horizontal whiskers are not significantly different (5% significance threshold). A general increase in the inter-branch distance from periphery to core is observed in the carcinoma tissue, a similar increase in this parameter is observed between LS147T and SW122. * *Carcinoma_p* represent pooled data from separate sub-regions *periphery (tr)*, *luminal tumour surface(tz)* and *core(tt)*.

Figure 4.15. Boxplot of the vessel diameter distributions and ANOVA results

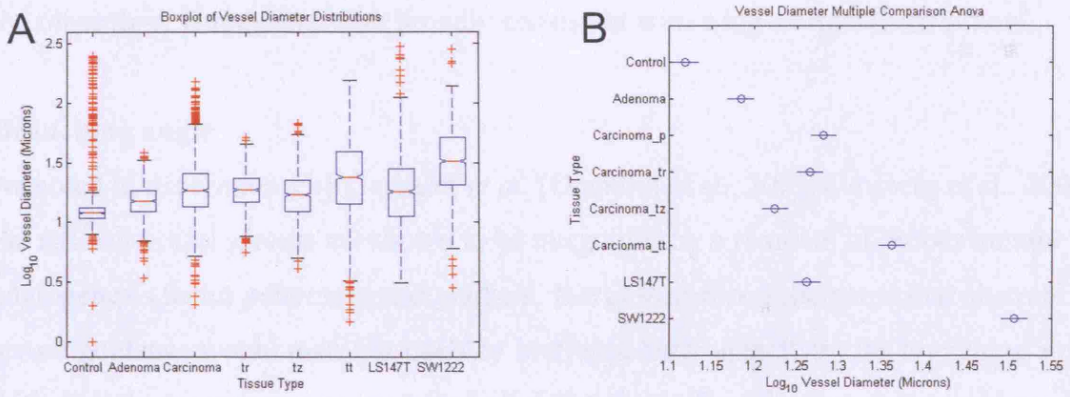

Figure 4.15. (A)Boxplot of the resampled data (log_{10} transformed), (B) the result of a pairwise ANOVA. The points representing the mean values for each tissues type. Points with overlapping horizontal whiskers are not significantly different (5% significance threshold). The variability is a clearly feature of these distributions of this parameter, compare the relatively narrow range in the control mucosa and the increasing variability progressing from carcinoma periphery to core. The variability of the two xenografts is more comparable to the variability in the carcinoma core than the adenoma. * *Carcinoma_p* represent pooled data from separate sub-regions *periphery (tr)*, *luminal tumour surface(tz)* and *core(tt)*.

Figure 4.16. Boxplot of the inter-vessel distance distributions and ANOVA results

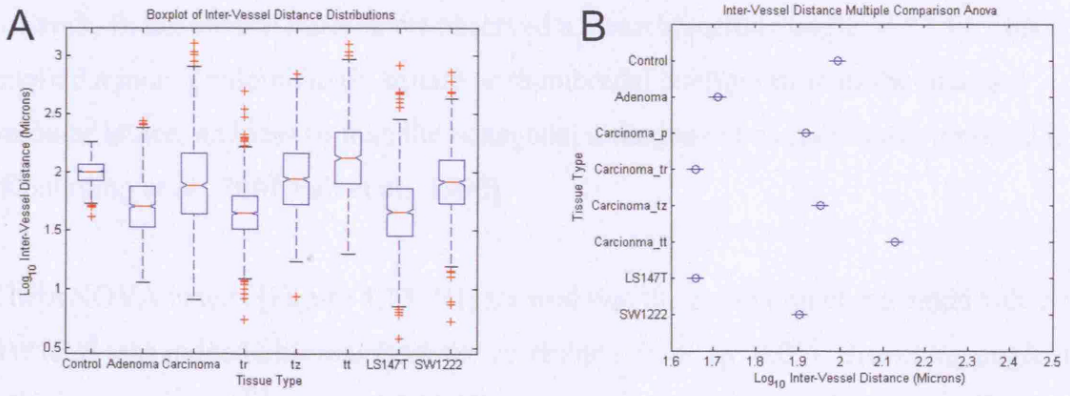

Figure 4.16. (A)Boxplot of the resampled data (log_{10} transformed), (B) the result of a pairwise ANOVA. The points representing the mean values for each tissues type. Points with overlapping horizontal whiskers are not significantly different (5% significance threshold). * *Carcinoma_p* represent pooled data from separate sub-regions *periphery (tr)*, *luminal tumour surface(tz)* and *core(tt)*.

4.4.4 Discussion: stereo-image morphometry and ANOVA results

With exception to the approximately normal distribution seen in the branching angle, the other three parameters were broadly consistent with a log-normal distribution[6].

Branching angle

As noted in experiments by Gerhardt *et al.* [Gerhardt et al., 2003;Ruhrberg et al., 2002], the nascent vessel sprouts are shown to be misguided by a removal of proper tumour angiogenesis factor patterning and gradient. It was therefore anticipated that aberrant sprout guidance would manifest itself by increased heterogeneity in the branching angle. Although the tumour tissues evaluated all differed significantly from the control mucosa in terms of their mean value, the different tumour samples and regions had similar mean branching angle and did not appear significantly different from each other. The standard deviation of all the distributions also appeared very close, even between control and the tumour types; this was surprising as it suggested that the heterogeneity in branching angles was more conserved across the different tissues [Figure 4.9].

This normal distribution shape was only observed for branching angle data. This symmetry suggests a strong developmental control may be acting to inhibit extremes of branching, which would in turn have adverse effects on flow through the vascular network. In the control mucosa we observed a mean branching angle of 87.14° this implied a more predominantly square or rhomboidal configuration of the mucosal vascular lattice, and less so than the hexagonal arrangement as previously reported in [Konerding et al., 2001;Fait et al., 1998].

The ANOVA results [Figure 4.13 (B)] showed that the mean branching angle value of SW1222 was indeed different from the carcinoma tissue ($p<0.05$). Branching angle for adenoma, carcinoma (core) and LS147T tissues are not significantly different from each other. Mean values of branching angle in both peripheral and luminal tumour surface samples of carcinoma tissue are both narrower than in the core (although narrowly outside of the significance boundary). This may be a consequence of the greater

[6] Probability Model-Based Analysis of Tumor Vasculature Data, it was argued here that the branching angle may be better represented by a beta-distribution, because the range of this distribution effectively has an upper and lower limit [Ogunnaike et al., 2005].

branching density in these regions, as indicated by the smaller inter-branch and inter-vessel distances in these regions [Figure 4.14 (B)].

In relation to which xenograft provided the best approximation of clinical carcinoma architecture, mean branching angles are: LS147T (mean 77.16°), SW1222 (mean 81.85°) and carcinoma (mean 73.31°). Despite being slightly larger in the SW1222, the ANOVA results do not show significant differences between the xenograft [Figure 4.13 (B)].

Inter-branch distance

Insight into the vessel density and branching rate in each tissue sample was provided by distributions of inter-branch distance [Figure 4.10]. In carcinoma samples, the most angiogenic regions bordered the normal and tumour tissue (i.e. the carcinoma periphery samples), the greater sprouting frequency results manifests through the reduced mean inter-branch distance measures [Figure 4.14 (A)]. Due to their relatively small size, xenografts and adenomas were not analysed by region, however a visual inspection of the casts scanning electron micrographs suggest smaller inter-branch distances are also present in the peripheral regions of both LS147T and SW1222 [Figure 4.8 (C)].

Pavlopoulos *et al.* report that "branching counts are significantly higher" in carcinoma than adenoma [Pavlopoulos et al., 1998], in their study bifurcation density was determined by the number of ramifications per 100 sections. The stereoimaging analysis here shows that this may only the case in the carcinoma periphery. This can be seen in [Figure 4.14 (B)] which clearly shows inter-branch distance in the pooled carcinoma data, carcinoma luminal tumour surface and core are all significantly higher than in the adenoma, consequently these tissues have a lower branching frequency. However as no delineation was made between the different carcinoma regions in the study by Pavlopulos *et al.* it was not possible to establish whether this conclusion is due to the regions of carcinoma tissue selected or the limitations of the two-dimensional method used to evaluate branching.

Mean inter-branch distances in clinical control, adenoma and carcinoma periphery are not significantly different from each other. Mean inter-branch distances for the carcinoma regions show a significant increase from both luminal tumour surface and

periphery to the carcinoma core. In the case of the tumour core, this region is outside the highly angiogenic edge of the tumour, and has reduced sprout formation, consequently longer regions between branches. The reason for the differences in branching distance in the luminal tumour surface and periphery were not clear as both these regions lie on the periphery of the tumour.

In relation to which xenograft provided the best approximation of clinical carcinoma architecture, mean inter-branch distances are: LS147T (mean 66.94μm), SW1222 (mean 104.75μm) and carcinoma (mean 78.49μm). ANOVA results suggested there was no significant difference between the means of the LS147T and the pooled carcinoma, which was not the case for SW1222. Therefore with respect to inter-branch distance, a better match was made by the LS147T to the carcinoma vascular architecture Figure 4.14 (B)].

Vessel diameter

One noticeable difference in the vessel diameter distributions was the range of variability in this parameter [Figure 4.11 (A)]. This can be seen to increase from the carcinoma margins (both *tr* and *tz*) through to the core where the spread of diameter was largest [Figure 4.15 (A)]. The incremental trend in increasing vessel diameter from control mucosa › adenoma › carcinoma has been correlated with tumour progression from benign to malignant states. These results concur with findings of Pavlopulos *et al.* where several vessel size-defining parameters where measured in both adenoma and adenocarcinoma tissues (from two-dimensional sections). All parameters relating to vessel calibre (perimeter, major and minor axes, and area) were found to be significantly larger in the adenocarcinoma by comparison to the benign adenomas [Pavlopoulos et al., 1998].

In relation to which xenograft provided the best approximation of clinical carcinoma architecture, the mean values of vessel diameter are: LS147T (mean 23.5μm) and SW1222 (mean 38.96μm) and carcinoma (mean 22.66μm). The ANOVA results showed that the mean vessel diameter of LS147T was not significantly different from the pooled carcinoma data and therefore provided a closer match to the carcinoma tissue than SW1222 which was significantly larger [Figure 4.15 (B)].

Inter-vessel distance

Although the inter-vessel distance does not directly contribute to the haemodynamical properties of the tumour vascular system, it is nevertheless an important attribute in determining the hypoxia in the tissue and it is also an indicator of local metabolic burden of the tumour tissue [Hlatky et al., 2002]. Increased variability in this parameter was observed in the tumour tissues relative to the normal mucosa samples which have a very narrow range for this parameter, again confirming the loss of vessel density from the peripheral regions. Increased angiogenic activity and consequently vascular density in the periphery carcinoma samples results in a transition from a wider mean inter-vessel distance in the normal mucosa to a shorter distance in the tumour periphery which increases again in the luminal tumour surface and tumour core as vascular density drops Figure 4.16 (A)].

In relation to which xenograft provided the best approximation of clinical carcinoma architecture, mean inter-vessel distances are: LS147T (mean 59.76μm), SW1222 (mean 96.7μm) and pooled-carcinoma (mean 113.52μm). ANOVA results suggested that with respect to inter-vessel distance, a better match is made in this case by the SW1222 to the carcinoma vascular architecture Figure 4.16 (B)][7].

4.5.1 Method: X-ray micro-computed tomography

Micro computed tomography or 'micro-CT' is an X-ray imaging technique similar in principle to the 'computed (aided) tomography' (CT or CAT) systems used in hospitals though as the name implies, micro-CT scanning resolution is greatly increased by several orders of magnitude. With the most recently available micro-CT machines such as the SkyScan 2011 x-ray nanotomograph, very fine scales of internal structure can be determined at resolutions of up to 150 nm^3. The scanning resolutions of these machines are more than sufficient to capture the finest microvascular vessel elements, as the scanning resolution is several orders of magnitude lower than the smallest vessels observed *in-vivo*.

[7] Some doubt is cast over the reliability of stereoimage inter-vessel distance metric and its use as an estimate of microvascular density, as the results from micro-tomography measures [Sections 4.5.2-3], which provide a more direct measure of microvascular density, showed that SW1222 have higher vessel densities than LS147T.

Micro-computed tomography works by collecting several hundred of x-ray projections (shadowgram) of a sample object from different angular views, as it rotates on a high-precision stage illuminated by a micro-focused x-ray source [Figure 4.17 (A)]. From this series of shadowgram projections (an X-ray attenuation image), a computer cluster is used to reconstruct cross-section images of the object using a modified Feldkamp cone-beam algorithm [Figure 4.17 (B)]. These reconstructed images represent the internal microstructure and density of the sample. The series of cross-sections (*z*-stack) through the sample object can be scrolled through to: inspect internal structure, select particular volumes of interest, perform 3D morphometry, and generate virtual-models of the object for visual inspection using volume or surface rendering algorithms. Three dimensional representations of the tomography z-stacks were produced by ray-tracing volume rendering using *Volsuite* [Bryan, 2005].

Micro-CT provides the advantage of visualising corrosion casts as a truly three-dimensional object. This technique enables very accurate measures of vessel density and cross-sectional area, which were previously crudely estimated by inter-vessel distance and vessel diameter in the prior stereo-imaging system. Microvascular specific vessel surface area was also measured using a count of the edge-lining voxels.

Corrosion cast samples for high resolution scans were frozen in water and cut to appropriate sizes, then thawed in a freeze-drier. This step was necessary to prevent damage to the delicate casts. Prior to scanning, whole or cropped samples of the corrosion casts were fixed to an acrylic sample podium with epoxy adhesive (Araldite, Huntsman Advanced Materials). The casts were scanned in a micro-CT scanner (Skyscan 1172, Kartuizersweg, Belgium) at voxel resolutions of between 1-3 μm^3, with an angular rotation interval of 0.25°. Scanning time was approximately 8-10 hours. Reconstruction of the scanned sample was carried out on a 3-node computer cluster (using Nrecon/NreconServer application), taking approximately 8-16 hours.

Once scanned and reconstructed the tomography data is then assembled into a RAW file; due to memory constraints this process required a reduction in resolution by 33-50% depending on the size of the initial sample and scan settings. Thresholding of the grey-scale images was performed with *ImageJ* [Rasband, 2006] to a yield a binary 8-bit

image of segmented vessel and void space. Generation of the binary image however resulted in a number of 'holes' [Figure 4.18 (A)] due to lower polymer density in the axial regions of the cast vessels (and hence a lower grey-scale value) and small localised inhomogeneities in the polymer. These holes were digitally 'filled' using an *ImageJ* hole-filling algorithm. Another technical problem identified related to a characteristic distortion around a portion of the smaller vessels in a small number of samples. The result was a 'star' shaped artefact in the reconstructed tomography image [Figure 4.18 (B)]. Possible causes include 'beam hardening' where lower energy X-rays are absorbed as the polychromatic beam passes thought the specimen. The effects of beam hardening are known to produce pronounced edges and streak artefacts, however these effects were relatively unaffected by beam hardening correction filters. This effect was always seen in the smaller vessels, particularly those with greater spatial degrees of freedom. One possibility is resonance in the sample, due to minute vibrations made by the x-ray tomography machine's ventilation fan [Myllys, 2006]; however the capture time at each angular increment is in the order of minutes and is perhaps too long to justify this as a possible cause. One further contributing factor might be the crystallisation of the MERCOX polymer. It is noted that MERCOX sets at higher density on the surface [Figure 4.18 (A)], as the smaller vessels are thinner, it is likely that their overall density is higher and might be contributing to the observed distortion.

Three-dimensional morphometry included measures for microvascular density, specific vessel surface area and vessel cross-sectional area; all measurements were carried out on the segmented 8-bit datasets. *Microvascular density* is expressed simply as a ratio of voxels determined to be inside the vessel divided by the total number of voxels in the cuboid domain. An estimation of *specific vessel surface area* was established by counting the number of voxels adjacent to void voxels, divided by the total number of voxels in the cuboid domain. It should be noted that this metric is resolution dependant and can only be used to assess the surface area of high resolution samples. Although not studied here, a less resolution dependant estimate of surface area might be performed fitting a triangular/polygonal isosurface mesh to the vascular surface using for example some variant of the marching cubes algorithm. The *mean vessel cross-sectional area (Vessel Calibre)* [Figure 4.19 (A)] was determined by initially producing a skeleton (medial axis transform) of the 3D vessel geometry and then fitting a spline to the central axis of the skeleton (skeletonisation software was provided by Tuomas Turpinen

[Hyvaluoma et al., 2007]). A surface perpendicular to each point along the spline is then calculated as delimited by the vessel/void voxel boundary.

The micro-computed tomography datasets also presented the possibility of measuring tortuosity of the tumour microvasculature in three-dimensions. Although this property of tumour vessels is frequently observed in the literature [Gerhardt et al., 2003;Konerding et al., 2001;Konerding et al., 1999;Konerding, 2006], with the exception of a study by Tozer *et al.* [Tozer et al., 2005], this aspect remains largely unquantified. The lack of tortuosity quantification in previous studies is largely due to the absence of an accurate method for determining tortuosity due to the three-dimensional nature of this parameter in the microvasculature.

Tozer *et al.* only used a single distance-metric to define tortuosity; however tortuosity is only partly defined by this metric. A more holistic approach to quantifying tortuosity was employed by Bullitt *et al.* using a semi-automated method [Bullitt et al., 2003;Bullitt et al., 2004]. Three metrics which characterise different aspects of vessel tortuosity were calculated from the segmented vascular structures: (1) *Distance Metric* (DM) – a ratio between the actual curved path of the segmented vessel and the linear distance between its endpoints, (2) *Inflection Count Metric* (ICM) – a sum of the minima of total curvature (inflection points) made by the vessel between its endpoints, and (3) *Sum Of Angles Metric* (SOAM) – the sum of total curvature between endpoints normalised by the path distance.

Bullitt *et al.* originally developed this method to study vessel tortuosity from Magnetic Resonance Angiography (MRA). This method has been adapted by simply substituting the MRA datasets with binarized micro-computed tomography datasets. Although the resolution of the data was much higher in micro-computed tomography, the principles remained the same. The process for this analysis involved two steps: (1) semi-automated segmentation of the micro-computed tomography datasets, which was carried out using *VTree3D* [Figure 4.19 (B)], and (2) the tortuosity measurements on these segmented vessels using *AnalyseVess3* [Figure 4.19 (C)].

Figure 4.17. Schematic of the X-ray micro computed tomography device

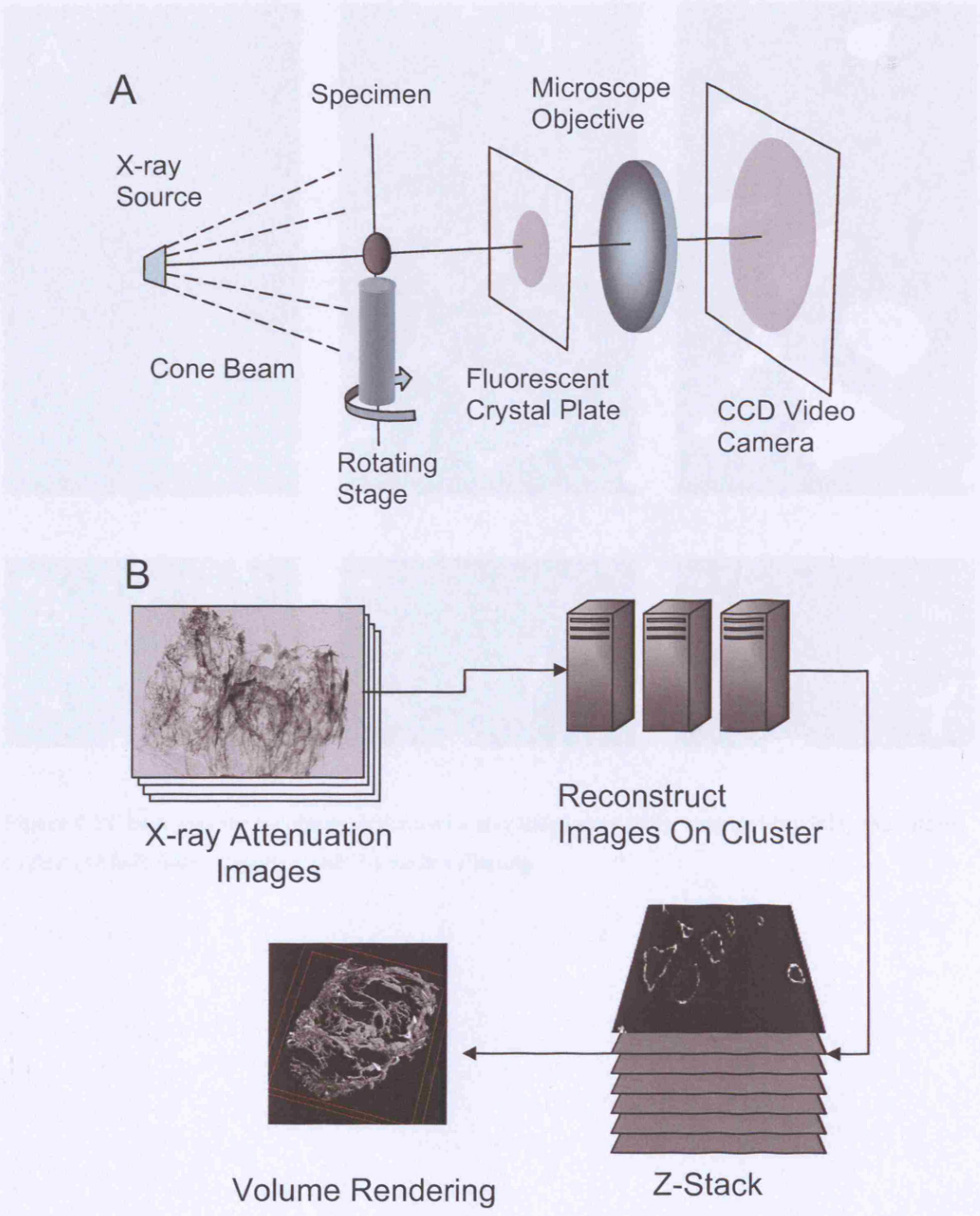

Figure 4.17. (A) Schematic of the X-ray tomography machine. Attenuation of the X-ray through a corrosion cast is used to produce a set of shadowgram images of the cast at 0.25° increments through 180°. (B) Reconstruction of the collection of x-ray attenuation images on a parallel computer yields a z-stack of images (orthogonal to the shadow-gram images). The voxel greyscale intensity is proportional to density on the reconstructed images. A ray-traced volume rendering can be used to visualise the 3D structure of the z-stack.

Figure 4.18. Pre-processing of tomography data

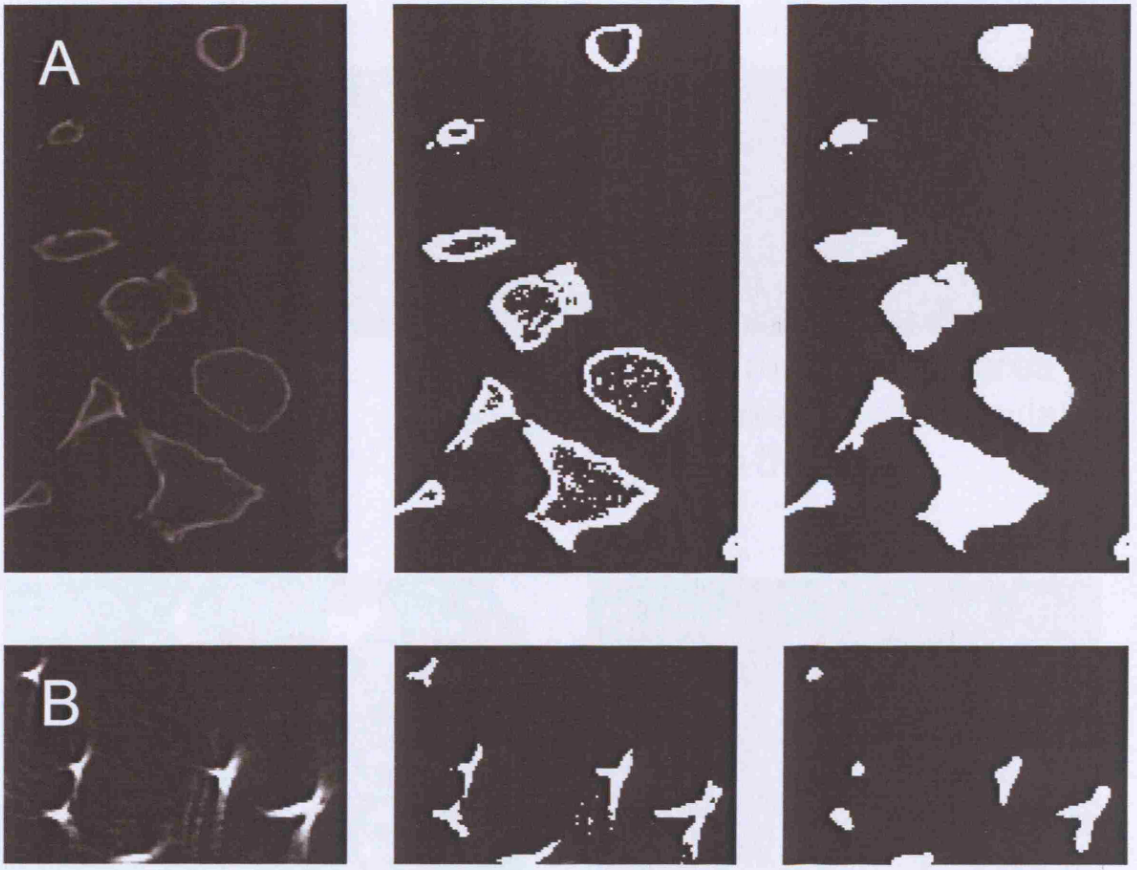

Figure 4.18. Each case the processing is done on a greyscale image (left), binarised (middle) and filtered (right): (A) hole filling algorithm and (B) median filtering

Figure 4.19. Determination of vessel cross-sectional area and vessel tortuosity

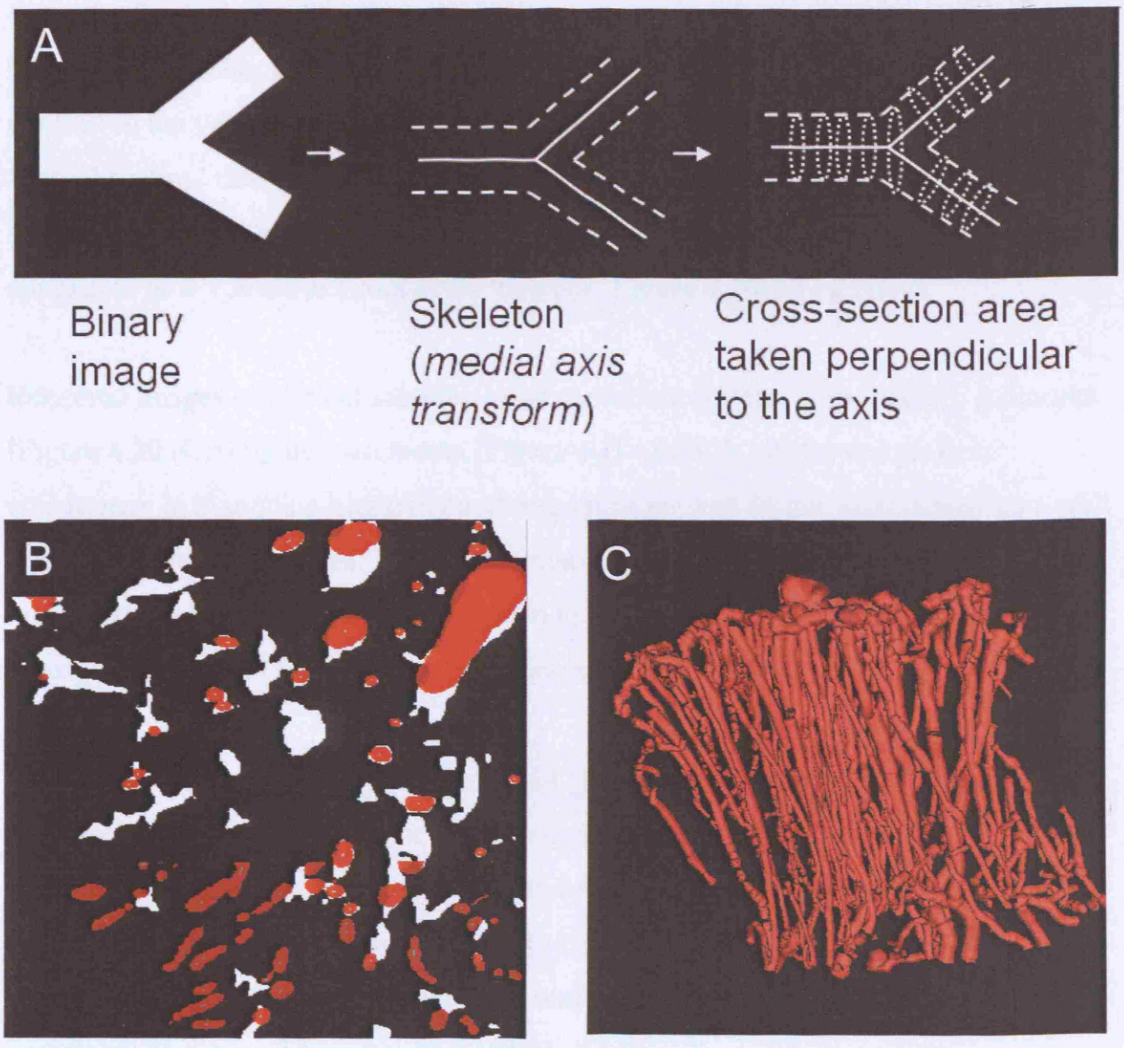

Figure 4.19. (A) The process through which the cross-sectional surface perpendicular to the vessel axis was computed. The binary image (left) is used to generate a thin skeleton (middle), which is used to fit a spline to the axis. The cross-sectional surface delimited by the vessel-void boundary is determined perpendicular to the central spline, (B) VTree3D segmentation interface; binarized tomography dataset (white), semi-automated segmented vessels (overlay in red), (C) 3D view of segmented vessels used for the tortuosity calculations (carcinoma dataset).

4.5.2 Results: 3D microvascular architecture as revealed by tomography

Both stereoimaging and tomography (3D volume reconstructions) show that the vessel hierarchy was better preserved in the control, adenoma and carcinoma vasculature in contrast to the vessels of the two xenografts [Figure 4.20 (A-L)]. The capacity to 'virtual section' the rendered structure was particularly useful for inspecting the structure beneath the immediate line of sight, using this facility it is possible to better appreciate how vessels are connected together [Figure 4.20 B,D,F,H&J].

Rendered images of clinical samples: control mucosa [Figure 4.20 (A&B)], Adenoma [Figure 4.20 (C&D)] and carcinoma [Figure 4.20 (E&F)], all showed greater consistency in branching hierarchy and organisation, with larger vessels feeding a well organised bed of capillaries. The characteristic branching patterns seen in the control mucosa stereoimaging could not be shown here as these delicate structures were damaged during cast transport between Germany and Finland.

Low resolution scans of SW1222 and LS147T reveal a substantially different vascular morphology was present in these two xenografts. Both xenografts were grown in identical conditions which suggest that the cellular environments in these two tumours are substantially different. Large vessels in LS147T can clearly be seen to be flattened in concentric layers, indicating that there was a compressive force being exerted on the vessels of the tumour [Figure 4.20 (G&H)].

A virtual section showing the core region of LS147T [Figure 4.20 (G&H)] this tumour harbours substantial avascular regions which are more abundant throughout the structure than in the SW1222 tumour [Figure 4.20 (I&J)]. One common feature of the SW1222 casts was the appearance of hyper-vascularised islands of tissue, which although observed throughout the tissue were particularly concentrated around the edges [Figure 4.20 (K&L)].

Figure 4.20. 3D renderings of micro-computed tomography data

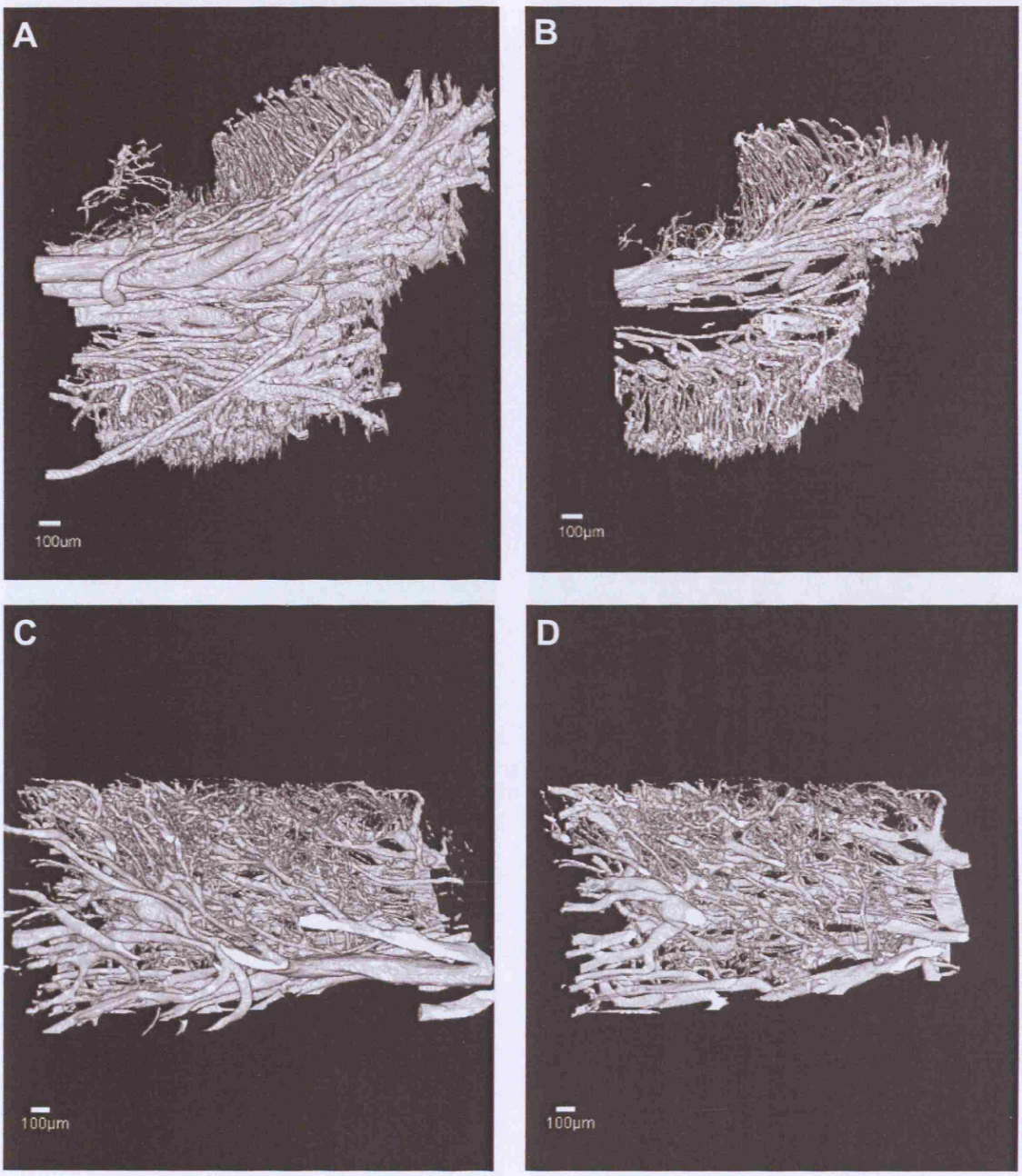

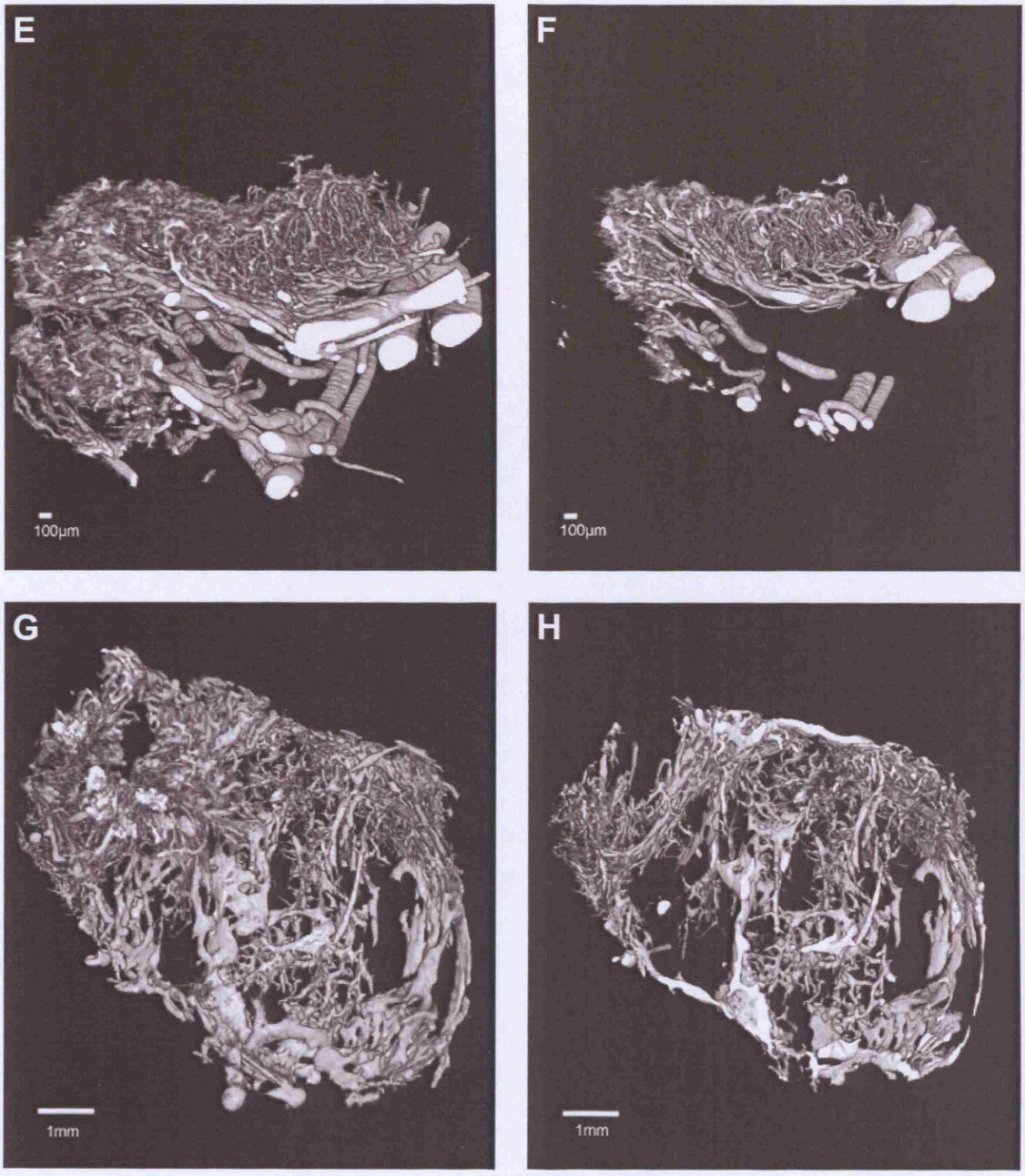
E
100µm
F
100µm
G
1mm
H
1mm

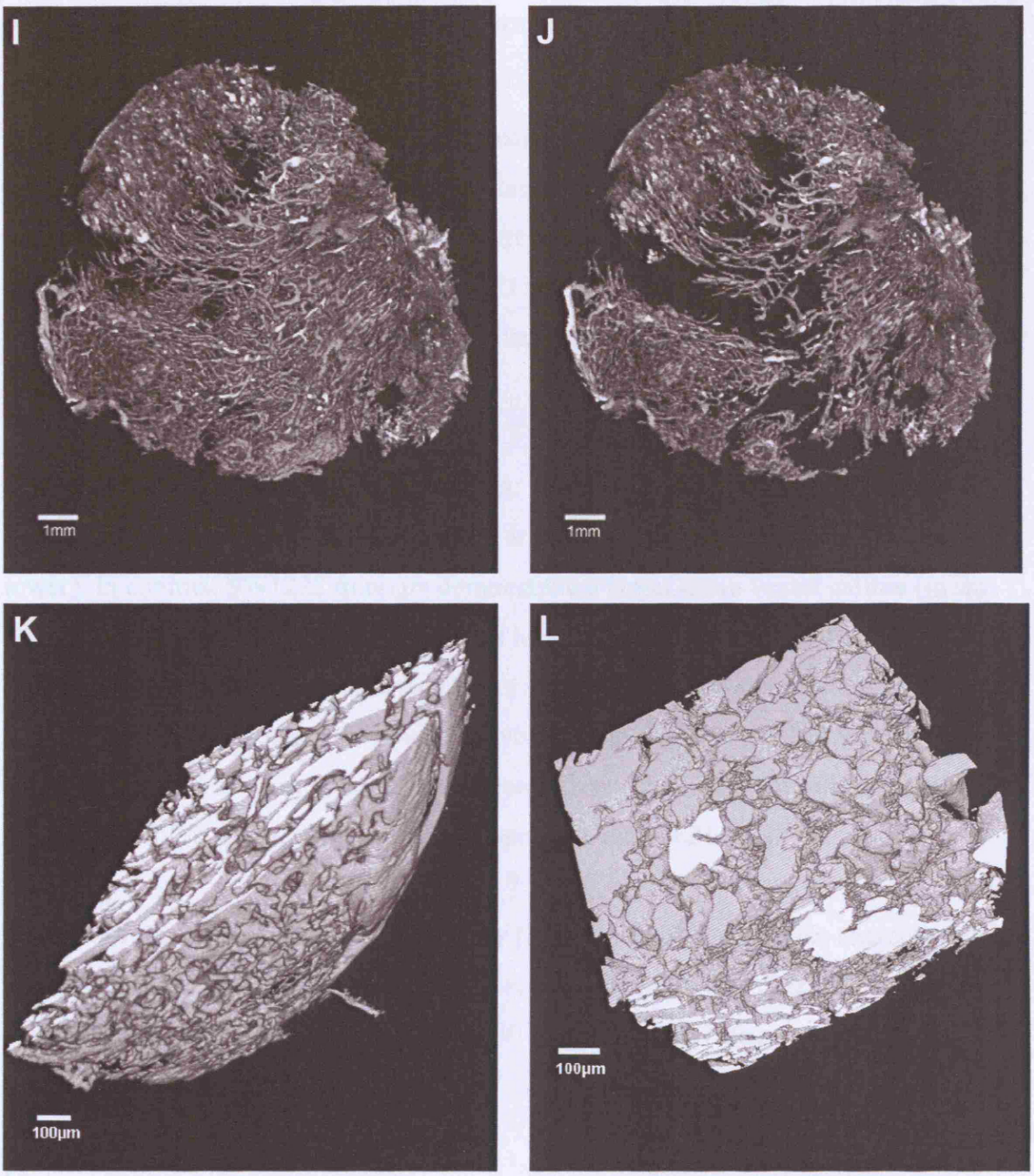

Figure 4.20. 3D rendering of corrosion cast microcomputed tomography A) normal mucosa, B) normal mucosa cut-away , C) Adenoma, D) Adenoma cut-away, E) Adenocarcinoma, F) Adenocarcinoma cut-away, G) LS147T xenograft whole digitised cast volume rendering, H) LS147T xenograft cut-away showing large avascular regions, I) SW1222 whole digitised cast volume rendering, J) SW1222 xenograft cut-away generated by virtual sectioning, (K) high resolution SW1222 and (L) a cropped volume of the high resolution SW1222 volume from the edge of the xenograft, this region is almost completely composed of vascular tissue. (G/H) and (I/J) are low resolution renderings of whole xenografts demonstrate the power of X-ray micro-computed tomography to determine vascular systems in whole tumours. These datasets however were not used in the morphometry study which was restricted to the use of high resolution scans.

4.5.3 Results: quantitative morphometry of cast micro-computed tomography

Analysis of the cast tomography data was carried out on 3-6 samples cuboid volumes of between 2-12mm^3 for each tissue type. Using the computed medial axis, several thousand cross-sectional measurements were made perpendicular to the vessel axis throughout the whole vessel network. MVD and SSA were also determined for each sample volume. The spread of measured characteristics from samples across each tissue type is shown in [Figure 4.21 (A-G)].

The vessel calibre of clinical tissue samples: control, adenoma, and LS147T are spread over a similar range and their mean values are also similar (the carcinoma values were lower). In contrast SW1222 tumours demonstrate a larger mean vessel calibre (mean ~$6x10^3$ μm^2) [Figure 4.21 (A)]. The results here parallel stereo-image measures of vessel diameter. An exact comparison is not possible since the stereo-imaging technique does not take into account the variation in vessel shape. It is also noted that the variability in vessel calibre appears consistent across the samples for all tissues except those of SW1222 where there is a greater spread [Figure 4.21 (B)].

Results for the microvascular density study [Figure 4.21 (C)] show this characteristic is elevated in SW1222 tumours (mean 0.25) by comparison to the other tissues: control mucosa (mean 0.13), adenoma (mean 0.049) and carcinoma (mean 0.051) tissue), LS147T(mean 0.08).

Measurements made on the specific vessel surface area [Figure 4.21 (D)] were similar in control mucosa, adenoma and carcinoma but were particularly variable in the LS147T and SW1222 tissues. For SW1222 the surface area is generally higher due to the combination of greater MVD and larger calibre vessels.

The three measures used to describe vessel tortuosity displayed quite different results, owing to particular aspects of each tortuosity definition. DM and SOAM in particular did not exhibit any clearly interpretable results [Figure 4.21 (E&G)]. The ICM does however consistently measure higher in SW1222 samples [Figure 4.21 (F)], which on visual inspection could be qualitatively deemed the more tortuous.

Figure 4.21. Micro-computed tomography morphometry

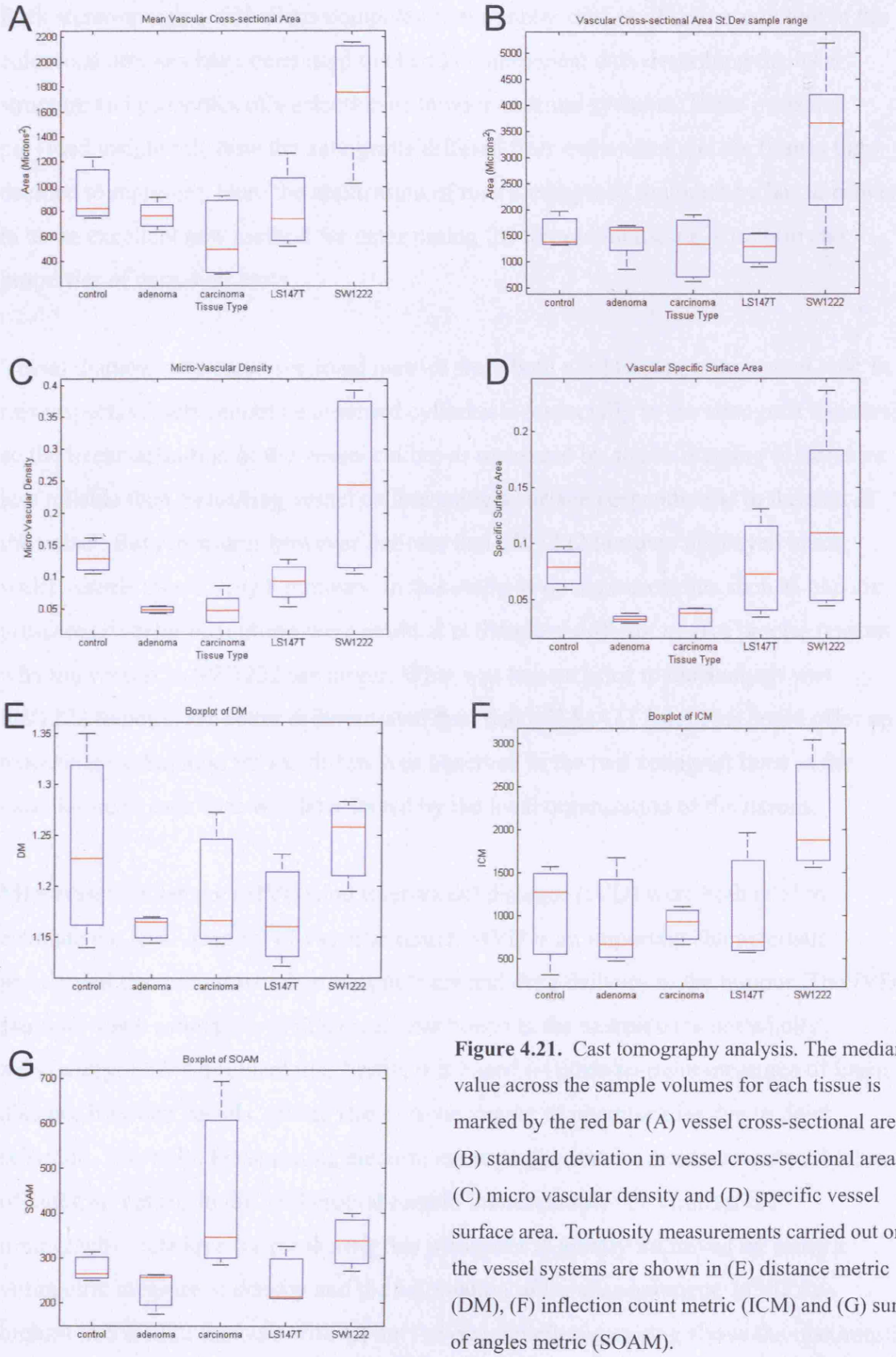

Figure 4.21. Cast tomography analysis. The median value across the sample volumes for each tissue is marked by the red bar (A) vessel cross-sectional area, (B) standard deviation in vessel cross-sectional area, (C) micro vascular density and (D) specific vessel surface area. Tortuosity measurements carried out on the vessel systems are shown in (E) distance metric (DM), (F) inflection count metric (ICM) and (G) sum of angles metric (SOAM).

4.5.4 Discussion: X-ray micro-computed tomography results

Both stereo-imaging and micro-computed tomography studies of the vasculature in the colorectal tumours have been used to elucidate numerical data describing the local structure and properties of a selection of tumour vascular systems. These measures provided insight into how the xenografts differed from each other and the tissues they deemed to represent. Here the application of micro-computed tomography has to proven to be an excellent new method for determining the three-dimensional structure and properties of corrosion casts.

Vessel diameter and cross-sectional metrics were both used to determine vessel size. In this respect, vessels cannot be assumed cylindrical (especially in the xenograft tumours) so the linear definition of the vessel calibre as measured by stereo-imaging is therefore less reliable than measuring vessel calibre using a surface perpendicular to the axis of the vessel. Both measures however indicate that SW1222 tumours displayed much wider vessels than LS147T tumours. In this study as no measurements such as oncotic pressure or vessel maturation were made, it is therefore difficult to give precise reasons why the vessels in SW1222 are larger. What was known prior to the analysis was SW1222 tumours are better differentiated than that of LS147T line. This could offer up a possible explanation for the differences observed in the two xenograft lines as the vasculature in each case will be affected by the local organisation of the tissues.

Microvascular density (MVD) and inter-vessel distance (IVD) were both used to estimate the local quantity of vascular tissue. MVD is an important characteristic property of the tumour which affects nutrient and drug delivery to the tumour. The IVD provides some estimation of this parameter however the technique is not wholly satisfactory. IVD is problematic; firstly, it is based on point-to-point measures of linear distance between vessels, giving rise to some degree of operator bias due to point selection. Secondly, the scanning electron micrographs restrict measurement to the line-of-sight, so vessels in the background remain immeasurable. By contrast the tomography technique for measuring this parameter is greatly improved by using a volumetric measure of density and the automation of the measurement. MVD was highest in SW1222 tumours with all but the one sample registering above the maximum value found for the clinical and control tissues.

The greater MVD in the SW1222 tissues could explain the improved response to therapy in this tumour line [Sharma et al., 2005], and a similar dependence of tumour growth on vessel density is shown at least phenomenologically by Alarcon *et al.* [Alarcon et al., 2004]. MVD has also been cited as a prognostic value [Janot et al., 1996]. Although MVD was found to demonstrate some difference between carcinoma and adenoma, additional study would be required to determine the value of micro-computed tomography for use as a prognostic tool. Further to this, the knowledge of avascular spaces shape, size and distribution is important to the hypoxic properties of tumours and so is of value to the fields of radiobiology, and the development of radiosensitizer and bioreductive drugs.

A further advance of micro-computed tomography is the capacity to measure new parameters relating to the vessel architecture. The specific vessel surface area (SSA) of the vasculature cannot be estimated from the stereo-image data. This provides some insight into the underlying architecture in the vascular network, as it is dictated by both the vessel shape and volume. SSA represents a better measure than MVD for defining the transport capacity of the vascular tissue as it is directly dependent of the calibre of vessel in the volume, whereas a the MVD is ambiguous in this respect. Consistent values of MVD were found in the tissues studied, and the specific vessel surface area mapped fairly closely to the MVD in most cases. The exception here was the LS147T tumours where the specific vessel surface area is relatively larger, which was due to a greater abundance of smaller vessels in some of the LS147T samples.

The possibility of analysing vessel tortuosity at the microvascular level will be of particular interest to the field of anti-angiogenesis/vascular therapy, as a number of studies such as those by Jain *et al.* show these treatments were followed by a reduction in vessel tortuosity [Jain, 2001b], this process termed 'vascular renormalisation' is evident in the use of anti-angiogenesis antibodies, such as DC101 [Tong et al., 2004]. Much of the prior works on vessel tortuosity are focused on specific tissues such as mesentery and retina which are convenient since these vessels grow as a planar two-dimensional layer. Outside this limited context, only the use of two-photon microscopy on window chambers has enabled the calculation of tortuosity metrics in three dimensions in microvascular [Tozer et al., 2005]. The use of micro-computed

tomography datasets in this study here shows that tortuosity values can be determined in three-dimensions from any tissue where a vascular cast can be generated (this is important as 2-photon microscopy is restricted to use with window chambers, where the tumours are somewhat squashed by comparison to their normal growth).

Tortuosity measures for the control and clinical tissues were generally similar in magnitude. ICM is elevated in all samples of SW1222, as shown in the cast stereo-images and volume renderings. These tumour vessels form highly dense networks with a tightly packed structure that necessitates higher frequency curves. The SOAM data was less clear to interpret than the ICM results. One carcinoma sample did show a much higher SOAM value; on inspection this sample showed the presence of a large number of coiled surface capillaries, which was interesting because the ICM is less sensitive to these types of structures – demonstrating the value of multiple tortuosity metrics.

The results of this study suggest both ICM and SOAM are better metrics for vascular tortuosity than DM. Tozer *et al.* also found that DM is an ineffective discriminator of vessel tortuosity for differentiating between the vasculature of two tumour types. The problem with DM as a measure of tortuosity is, that it is purely the ratio between effective and linear distances. It is for example, unable to differentiate between, a highly sinusoidal vessel and one with a gentler but larger curvature, where both vessels have equivalent length and displacement.

4.6 Chapter conclusions

The decision to use the corrosion casts rather than an injected radiopaque contrast agent was primarily due to the consultation with Skyscan [Corps and Folarin, 2006] which suggested greater image quality and segmentation would be achieved by scanning the naked casts. With hindsight there are some reasons why scanning the un-corroded cast may prove advantageous. Adding contrast agents such as lead, osmium or iodine to the casting polymer would enable the scanning to be done without removal of the tissue [Bentley et al., 2002], so that identifying feeding vessels from the whole tumour would be greatly facilitated. It was observed that scanning distortion [Figure 4.18 (B)] was reduced where the vasculature was densely connected, so the problem with vibration in

the smaller vessels may also be resolved as the surrounding tissue would support and restrict their movement. Implementing this system is not straightforward, as other problems may arise from using an injected contrast agent as the basis of the angiograph. These include how to scan the sample without it drying up, as scanning times can exceed 10 hours, this would necessitate housing the sample in a water tight seal to prevent drying and contraction of the tissue and subsequent distortion of the tomographic data.

The corrosion casts of the tumour vascular system provide good insight into the three dimensional structure of the vasculature. Using micro-computed tomography, the analysis of the vessel structure and architecture can be automated and provides many advantages over conventional stereo-imaging techniques. The stereo-imaging and micro-computed tomography techniques used in this chapter complement of each other. The resolution of scanning electron microscopy currently exceeds that of micro-tomography imaging systems, so it is good for studying the more qualitative aspects of the cast (particularly the surface detail). While the use of micro-computed tomography data opens up many more possibilities for quantitative morphometry of the vascular network.

The stereo-imaging and micro-computed tomography results suggest that although both xenografts studied here differ from the architecture of the clinical tumours the architecture of the LS147T tumour is a better match of the clinical carcinomas presented in the current study.

Micro-computed tomography results here demonstrate that the vascular network can be accurately resolved for a whole xenograft tumour. The technique has significant advantages over other tomographical method such as serial sectioning employed by Brey et al. [Brey et al., 2002] [Braumann et al., 2005] or the 2-photon microscope system used by Barber et al. [Barber et al., 2003b]. Further to its use as a morphological tool for studying the structure of the tumour vascular system, the tomography data is also used to define three-dimensional vascular network geometries for use in blood flow simulations in the next chapter.

CHAPTER 5: Blood flow simulation in tumour vasculature

5.1 Introduction

Modelling the behaviour of the tumour vascular system is of great therapeutic interest as it is central to the pathology of all solid tumours, determining aspects such as: hypoxia, drug/nutrient delivery, tumour growth and metastases [Chapters 1-4]. Several studies have highlighted the importance of tumour vascular architecture and structure as the primary factor of aberrant haemodynamics and transvascular flow [Jain, 1988] [Fujimori et al., 1999;Huxley and Rumbaut, 2000;Munn, 2003;Konerding, 2006].

Attempts to address flow phenomena in tumours using a range of computational models have tended to focus on network flow models, see [Chapter 3] [Baish et al., 1996;Chaplain and Anderson, 2004;Chaplain, 1995], Stephanou [Stephanou et al., 2004;Alarcon et al., 2004;Alarcon et al., 2005]. One factor common to each of these model systems is the use of a highly abstracted or simplified vascular architecture which cannot adequately describe the functional properties of the microcirculatory system. Since vascular architecture is so strongly coupled to the haemodynamic function, this lack of fidelity remains a major shortcoming in these models and greatly limits their application and validity [Pries et al., 1995b]. To address this gap, a novel computational method for modelling blood flow in a morphologically correct three-dimensional vascular system is presented here.

Through studies of corrosion cast architecture in [Chapter 4], it was shown that vessels in clinical and experimental colorectal tumours exhibit substantial differences in architecture and structure. These differences not only encompass the distinction between normal and tumours vessels, but also define characteristics associated with each tumour type. In this chapter an investigation is carried into whether the hydrodynamic contribution of different vascular morphologies can be determined through simulation. X-ray micro-computed tomography datasets of corrosion casts determined in [Chapter 4] were used to define *virtual* vascular networks for a lattice-Boltzmann fluid flow simulation.

It is acknowledged here that the fluid-model of blood referred to in this chapter is highly idealised as the single phase fluid does not take into consideration the known non-

Newtonian properties of blood[8] discussed in [Section 3.3.1]. Although a visco-elastic, multiphase colloidal model of blood is theoretically possible using the lattice Boltzmann method, these models are still in development. Additionally the use of a non-Newtonian/single-phase simplification was necessary to meet the computational demands of simulations with the available resources.

5.2 Chapter aims

Objectives for this chapter include:

I. Adapt the lattice-Boltzmann method (LBM) and appropriate flow boundary conditions to use with X-ray microcomputed tomography images of vascular corrosion casts.

II. Test the LBM model in a simple symmetric bifurcation, to determine if there is a hydrodynamic justification for the highly conserved distributions of tumour branching angles.

III. Using the LBM model, evaluate blood flow in portions of vascular networks from control and tumour datasets. Determine how characteristic changes in the network affect blood flow through the system.

IV. Demonstrate the viability of blood flow simulations using the LBM model in the vascular system of a whole xenograft tumour.

[8] The non-Newtonian properties of colloidal suspensions such as blood are active area of research in the field of lattice-Boltzmann methods. The application of more complex representations of blood is discussed in [Chapter 6] as a possible extension to this model.

5.1. Workflow schema

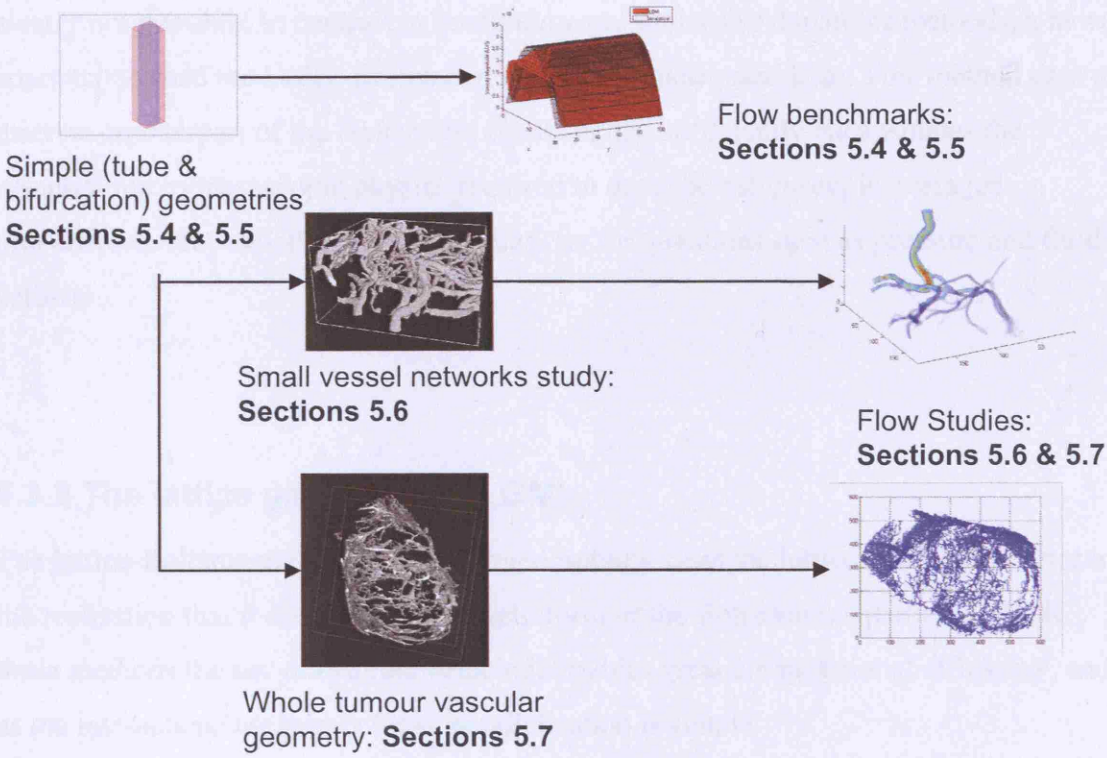

Figure 5.1 Shows the passage of work from simple tube flows where the simulations were benchmarked through progressively complex vessel geometries derived from microcomputed tomography datasets (from Chapter 4).

5.3.1 Background: mesoscopic fluid models

The balancing act between domain size, resolution and computation power bear very strongly on most non-trivial computational fluid dynamics problems. The choice of fluid model was therefore important to the problem of simulating blood flow in the complex vascular space of a tumour.

Continuum methods like the Navier-Stokes equation have significant limitations in handling geometrically complex boundaries, such as those encountered in tumour vascular systems. At the other extreme are techniques such as molecular dynamics where the time evolution of a molecular system is (usually) governed by Newtonian mechanics and for computational purposes, the analytical equations describing the

motion of individual molecules are discretised. However due to the scale of the tumour vascular system, using molecular dynamics for modelling blood flow problems is clearly not possible. In contrast to continuum and molecular dynamics methods, a newer approach termed the lattice-Boltzmann method has been used here. This method uses a discrete counterpart of the Boltzmann equation that sufficiently encapsulates the essential micro/mesoscopic physics required to describe macroscopic averaged properties so they satisfy the known equations for quantities such as pressure and fluid velocity.

5.3.2 The lattice gas method (LGM)

The lattice-Boltzmann method was derived initially from the lattice gas method prior to the realisation that it constituted a discrete form of the Boltzmann equation. In both these methods the use of discrete velocities enables great computational efficiency, and as the interactions are purely local, parallelisation is simple.

The computational limitations of molecular dynamics methods in the mid-1980s resulted in a new approach based purely on conservation laws (particle number, momentum, energy). This method, called the 'lattice gas cellular automata', considers a system of lattice bound 'fictitious particles' that represent underlying groups of smaller molecular components of the fluid [Frisch et al., 1986]. These particles, although larger than the underlying molecules in the fluid are much smaller than the smallest length scale. This is acceptable as the macroscopic attributes do not directly depend on microscopic behaviour of the fluid, as can be seen from low-Mach flow simulations in air and water at equivalent Reynolds numbers, the results remain the same despite the clear difference microscopic behaviour in a gas and fluid. Using a limited number of particles which are restricted to a small number of velocities forms the central basis for LGM. These spatial discretisations, coupled with discrete time and simple momentum conserving Boolean collision rules, allow large scale simulations to be run at comparatively low computational cost. There were however problems associated with lattice gas methods, for example equations of motion may depend on

inertial/translational frames, a contradiction of Galilean invariance[9], and there is a tendency for the results to harbour a large amount of noise, requiring substantial averaging to generate meaningful results [Succi, 2001]. These problems are addressed by the lattice-Boltzmann model.

5.3.3 The lattice-Boltzmann method (LBM)

The LBM was developed to solve the problems associated with LGMs and further develops the concept of fluid discretisation. The two most important differences in LBM lie in the treatment of the fluid particles and their collision. Firstly in LBM the individual fluid particles from the LGM are no longer the fundamental unit of the fluid discretisation. In their place floating point numbers are used to represent the *ensemble average* of the fictitious particle density and velocity distributions. So in effect, LBM represents pre-averaged version of the LGM.

The field of LBM as a fluid dynamics method is comparatively new, and has seen strong development over the last two decades. LBM is considered an alternative to other finite-element and finite difference Navier-Stokes solvers due to its relatively simple implementation, parallelisation, handling complex geometrical boundaries and multi-component flows.

The initial appeal of LBMs for use in modelling flow in tumours was their successfully application to micro-scale flow simulations in other porous media such as rock [Manwart et al., 2002] and paper [Rasi et al., 1999]. In these media, the pore length-scale are similar (~10-10^3 μm) to that of the finest vessels (capillaries) in the tumour microvasculature. Furthermore the complexity of the boundry surfaces of these porous media is similar to that of the microvasculature. As noted by Buick *et al.,* LBM fluid models could also be applied to the full range of vascular flow regimes, ranging from large-scale flows, such as those observed in the aorta, down to micro-vascular blood flow in the smaller vessel systems [Buick.J.M. et al., 2003]. The relative simplicity and

[9] Galilean invariance: a principle of relativity stating that physical laws remain constant for all initial frames.

success of LBM at treating complex boundaries was a key attribute of the method, especially in light of the tomography results in [Chapter 4].

The LBM as noted previously can actually be derived by discretising the Boltzmann equation [Chen and Doolen, 1998]. For a particle density distribution entering site r at time t denoted $f_i(r,t)$, the direction of the velocity of this particle distribution is given by c_i, i being the index of the lattice directional vectors. For a given lattice with a time step η and lattice spacing λ the particle velocities v_i are thus:

$$v_i = c_i \frac{\lambda}{\eta} \qquad [5.1]$$

The evolution of the distribution is given by a convective streaming step and the collision from the prior distribution state:

$$f_i(r + \lambda c_i, t + \eta) = f_i(r,t) + \Omega_i(r,t) \qquad [5.2] ,$$

where $\Omega_i(r,t)$ is the collision operator. The effect of the collision term produces either an increase or decrease in particles of type i. The collision operator used in this case is the Lattice-BGK (Lattice Bhatnagar-Gross-Krook) [Bhatnagar et al., 1954]. The major simplification is achieved by replacing the function associated with relaxation to equilibrium by a single relaxation time parameter ξ.

$$\Omega_i = \frac{1}{\xi}\left(f_i^{(eq)}(r,t) - f_i(r,t)\right) \qquad [5.3],$$

$$f_i(r + \lambda c_i, t + \eta) = f_i(r,t) + \frac{1}{\xi}\left(f_i^{(eq)}(r,t) - f_i(r,t)\right) \qquad [5.4]$$

where $f_i^{(eq)}$ is the local equilibrium distribution equation [5.5]. For a three dimensional 19-velocity lattice such as D3Q19, the available velocities are 0 for the rest 'particle', 6 velocities to the nearest neighbour (face-centred), and 12 velocities to the next-nearest-neighbour (edge-centred) [Figure 5.2 A]. The $f_i^{(eq)}$ for the D3Q19 model is given by:

$$f_i^{(eq)}(r,t) = \rho\omega_i\left(1+\frac{1}{c_s^2}(c_i\cdot u)+\frac{1}{2c_s^4}(c_i\cdot u)^2-\frac{1}{2c_s^2}u^2\right) \qquad [5.5]\ ,$$

where the lattice speed of sound is:

$$c_s = 1/\sqrt{3} \qquad [5.6],$$

the weight factor ω_i is *1/3* for rest particles, *1/18* for particles moving nearest-neighbours and *1/36* for particles moving to next-nearest neighbours.

Macroscopic properties of the fluid such as density ρ, velocity u and momentum tensor Π are recovered by summing suitable moments of the distribution functions:

$$\rho(r,t) = \sum_{i=1}^{I} f_i(r,t) \qquad [5.7]$$

$$\rho(r,t)u(r,t) = \sum_{i=1}^{I} v_i f_i(r,t) \qquad [5.8]$$

$$\Pi_{\alpha\beta}(r,t) = \sum_{i=1}^{I} v_{i\alpha} v_{i\beta} f_i(r,t) \qquad [5.9]$$

I is the number of lattice directions given by c_i and α and β are spatial components of the velocity vectors.

Interaction between the fluid domain and the vessel wall on the lattice are specified by the boundary conditions imposed at the solid nodes neighbouring fluid nodes [Figure 5.2 (B)].

Figure 5.2. Schematic of the lattice-Boltzmann model

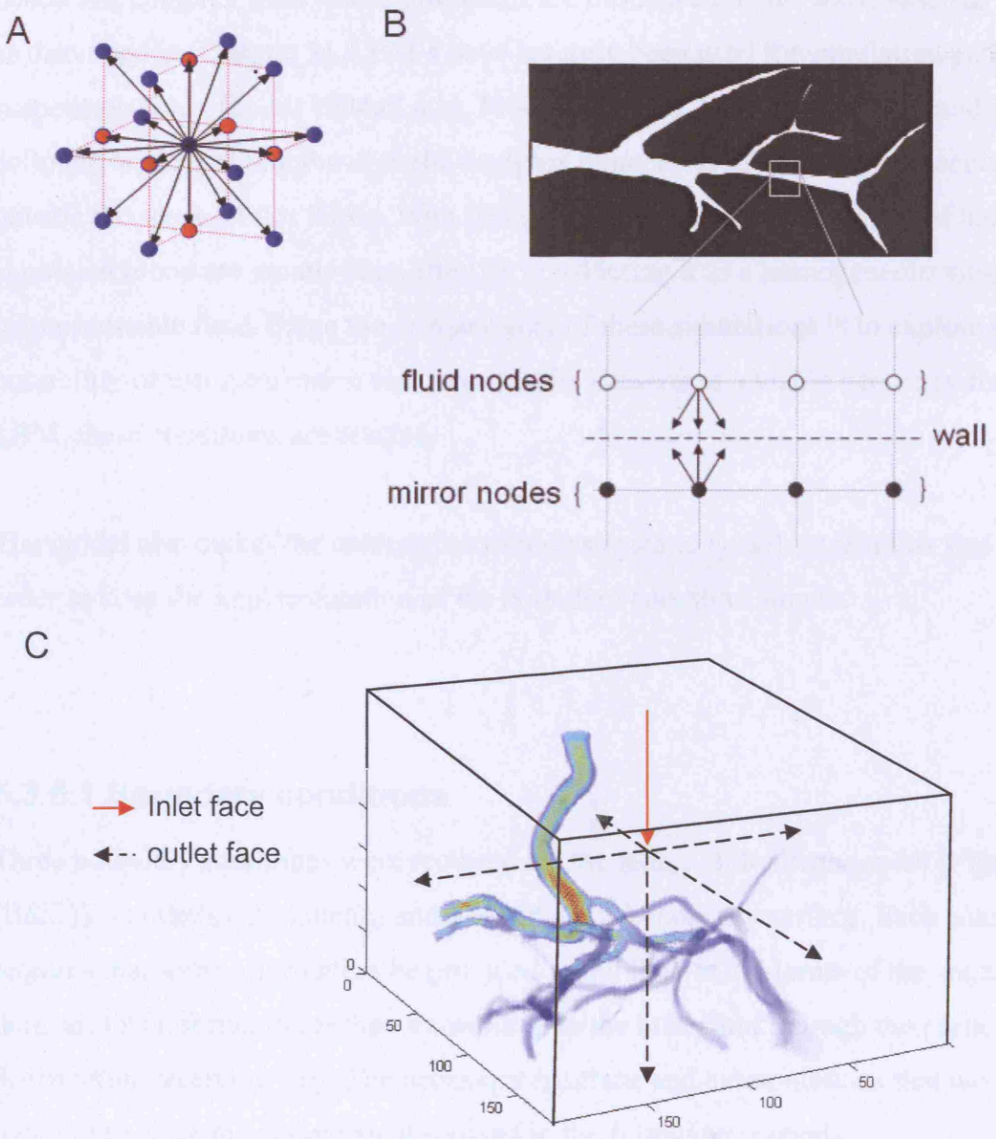

Figure 5.2. Features of the lattice-Boltzmann model boundary conditions. (A) Shows the velocities of the three-dimensional face-centred-hypercubic (D3Q19) lattice. The vertices are on the intersection of 3 orthogonal planes i.e. 6 face centred (red) and 12 edge-centred (blue) (B) a two dimensional schematic of the digitised vessel, showing the interaction of fluid nodes (white) with the digitised vessel 'wall' which lies half way between the solid/fluid nodes, the void space is shown with the (black) nodes, and the resulting velocity (black arrows) [note in 3D the number of outgoing velocities is actually 5 not 3]. (C) An example of a small vessel geometry (velocity field), showing the inlet and outlet faces of the flow simulation domain.

5.3.4 Simplifications

Blood is a complex fluid whose properties are influenced by the local vascular system as discussed in [Chapter 3]. LBM's have recently been used for simulating particle suspension flows [Ladd, 1994a;Ladd, 1994b;Ding and Aidun, 2006], but modelling the colloidal aspects of blood within the complex boundaries of the tumour vasculature are outside the scope of this thesis. With this caveat in mind, flow properties of the simulated blood are greatly simplified by considering it as a homogeneous single-phase, incompressible fluid. Since the primary goal of these simulations is to explore the possibility of using corrosion cast tomography datasets as a viable geometry for the LBM, these conditions are relaxed.

The model also makes the assumption of inelastic static vessels; again this was done in order to keep the implementation of the boundary condition simple.

5.3.5.1 Boundary conditions

Three boundary conditions were required for the lattice-Boltzmann model [Figure 5.2 (B&C)]: 1) inlet(s), 2) outlet(s) and 3) fluid-vessel boundary surface. Each condition requires that some information be provided to the fluid at the limits of the simulated domain; this information is then transmitted to the bulk fluid through the particle distribution streaming step. The necessary heuristic and extrapolations that were required to close the system are discussed in the following sections.

5.3.5.2 Fluid-vessel interface no-slip boundary condition

The vessel lumen-fluid interface was implemented using the no-slip boundary condition described by Succi [Succi, 2001]. This boundary condition was considered physically appropriate as the vessel wall glycocalyx (endothelial surface layer) strongly attenuates net fluid motion at the wall [Pries et al., 2000;Pries et al., 1997;Secomb et al., 1998]. The no-slip boundary condition makes the assumption that the fluid adjacent to the solid interface has a zero velocity relative to the vessel wall in this instance. This approach is

realised by implementing the half-way bounce-back rule where the discretised 'fluid particle' momentum is reversed half-way between the adjacent fluid and solid nodes. The half-way bounce-back scheme was also attractive for practical reasons as it is both simple and computationally efficient. The half-way bounce back boundary condition can give second-order accuracy in simple geometrical applications; however for our complex vascular system it is first-order accurate [He et al., 1997] [Chen and Doolen, 1998;Ziegler, 1993] provided minimum of ~10 of lattice nodes spanning the average vessel [Buick.J.M., 2005]. More sophisticated fluid-solid boundary conditions have been suggested and are second-order [Filippova and Hänel, 1998], but these are largely restricted to regular geometrical domains or require neighbouring nodes for interpolation where many schemes have non-trivial mass conservation problems.

5.3.5.3 Inlet(s) boundary condition

One obstacle was how to define a driving force for the flow study, as commonly used solutions such as pressure gradient and body force could not be applied to the problem. In the case of the pressure gradient boundary condition, the pressure gradient across the multiple inlets and outlets was not known *a posteriori*, whereas a bodyforce term could not be used due to the multiple directions of flow [Figure 5.2 (C)]. However the inlet velocity could be defined as estimates for arteriolar blood flow are known [Table 5.1]. The difficulty with this approach was that the vessel inlet shapes tended to be irregular, as they were determined by the cross-section of the tomography image at the inlet face. This meant defining a parabolic velocity profile [Zou and He, 1997] was not possible. Instead 'Ladd's moving wall', effectively a constant uniform velocity distribution, was implemented for the inlet(s) [Ladd, 1994b]. This inlet condition was applied to one face of the domain [Figure 5.2 (C)].

A problem encountered in the LBM simulations was the presence of oscillations in the velocity field; these were transmitted from the inlet to the rest of the fluid domain. A method for handling this problem was found by averaging the distribution functions of the incoming inlet-links. At each time-step the five inbound links (D3Q19) are calculated as defined by Ladd's velocity boundary condition. In the following time step,

an average value for each inbound link is calculated over the present and preceding time steps.

5.3.5.4 Outlet(s) boundary condition

Simple periodic boundary conditions have been used with the lattice-Boltzmann method for the study of fluid flows in complex porous materials such as rock and paper [Manwart et al., 2002]. In these materials the boundary surface is defined by the connectivity of thousands of independent pores. The 'porous' structure of microvasculature, although complex, is quite different to that of paper and rock. This means the direction of flow is strongly dependent on the sample, which is not guaranteed to be unidirectional. In the vascular geometries derived from micro-computed tomography datasets, each of the vessel geometries used evolved from inlet vessel(s) into a network that eventually exited the limits of the domain through multiple outlet faces. The remaining 5 faces where the vessels exited the simulated domain were dedicated as outlet-faces [Figure 5.2 (C)].

The outlets of the domain also required special attention. In this situation, off-lattice in-coming links from the 'open' outlets must be handled in such a way that the velocity of the bulk fluid remains unchanged or minimised. This represents a particular application of the 'missing-data' (incoming links) problem described by Chikatamarla *et al.* where a practical solution is to approximate the missing information using Grad's Distribution [Chikatamarla et al., 2006].

5.3.5.5 LBM simulator applications and input parameters

Two simulator codes developed in collaboration with Keijo Mattila (University of Jyvaskyla, Finland) were used in the following studies [Mattila and Hyvaloma, 2006]. The first was used for testing boundary conditions, benchmarking behaviour and accuracy of the fluid dynamics model in the case of simple channel flows. The second program was developed for simulating flows using micro-computed tomography datasets.

The ultimate goal was simulation of flows in whole xenograft scans, so substantial computing facilities would be required. To meet these requirements simulations were carried out on an Altix 3700 (Silicon Graphics Incorporated, Mountain View, California), with 112GB shared memory, 56 processors (Itanium2 1.3 Ghz/3 MB cache processors) and an operational speed of up to 135GFlops.

Geometry data for flow simulations in the tumour vascular networks was supplied in a binary format generated by the *Sampler* program [Mattila and Hyvaloma, 2006], whose input was a stardust file derived from an 8-bit X-ray micro-computed tomography z-stack (RAW format). Files file relating to the geometry constitution are listed in (Appendix A1.2-4). A parameters *file* (*.in) (Appendix A1.1) detailing the various simulation parameters (such as lattice decomposition and velocity) was used for configuring the simulator application. Output from the simulation takes the form of three files: *an output summary file* (*.dat), *an evolution record file* (*.evol), and a binary *velocity/density fields file* (*.fields) (formats are listed in Appendix A2.1-3).

The flow regime for the simulation is matched through the dimensionless Reynolds number determined from published values of kinematic viscosity and velocity as related through equations [5.10 and 5.11]. The velocity at the inlet tumour vessel(s) was taken to be equivalent to that of normal vessels; this was considered a reasonable estimation as noted by Jain *et al.*, where microvascular pressures in the arterial side of the tumour are nearly equal in tumour and normal vessels [Jain, 1988].

$$\mathrm{Re} = \frac{VL}{\nu} \qquad [5.10]$$

The Reynolds number [Section 3.3.2] was calculated using published values for kinematic viscosity (ν) 5.48×10^{-6} $m^2.sec^{-1}$ [Kobayashi et al., 2002] and velocity (V) 1×10^{-3} $m.sec^{-1}$ [Bloor, 1968] over a similar size range of microvascular blood vessels. The characteristic length scale L was taken as the diameter of the tumour vessels as determined in the previous chapter (7×10^{-6} m to 4×10^{-5} m). Together this situates the dimensionless Reynolds number for this flow regime between ($3.7\times10^{-3}$to 7.3×10^{-3}), which is firmly in the laminar range. In order to match this to the simulation, the lattice

kinematic viscosity, as specified by He *et al.* [He et al., 1997], is given as a function of the relaxation time ξ.

$$\nu = \frac{2\xi - 1}{6} \qquad [5.11]$$

Using a single relaxation time ($\xi = 1$) equation [5.11] gives a viscosity of 1/6. By taking a characteristic distance of 10 lattice units so suitable hydrodynamic behaviour is recovered and the above Reynolds number range, the appropriate velocity for the simulation is given by equations [5.10] as (2.2×10^{-5} to 1.2×10^{-4}) lattice units per time step.

Table 5.1. Relevant physiological parameters

Parameter	**Value**	**Reference**
Reynolds Number	0.51, 1, 2	†[Kobayashi et al., 2002]
	3×10^{-4}	* [Popel and Johnson, 2005]
	1	‡[Bloor, 1968]
Microvascular Flow Velocity	1×10^{3} μm/sec	‡[Bloor, 1968]
	2, 5, 10×10^{3} μm/sec	†[Kobayashi et al., 2002]
Kinematic Viscosity	5.48×10^{-6} m^2/sec	†[Kobayashi et al., 2002]
	1.2×10^{-6} m^2/sec (for blood plasma)	[Lee et al., 2004]
Mean Vessel Diameter range	20-40 μm	Chapter 4 [Section 4.4.3]
Minimum Vessel Diameter	7-40 μm	Chapter 4 [Section 4.4.3]

Table 5.1. Note: † parameters in [Kobayashi et al., 2002] relate to arteriolar diameter 110 μm and ‡ [Bloor, 1968] refers to a smaller representative vessel diameter of 10 μm in human. * In [Popel and Johnson, 2005] refer to cat sartorius muscle.

5.4.1.1 Method: error analysis in straight channels and tubes

The lattice-Boltzmann simulations using the boundary conditions described in [Section 5.3.5.1-5] were investigated numerically to determine the behaviour of flow at the inlet and outlet of the domain. Although these simple geometries do not imply the same behaviour in the complex system of vessels, they provide an important benchmark for the behaviour in a system with a known analytical solution.

Benchmark studies were carried to estimate the Error E_v of the lattice-Boltzmann simulation using the velocity inlet/open-flow outlet boundary conditions defined in [Section 5.3.5.1-3] within channel and tube flows.

The global error in the velocity of the z component (in this case) E_v is given by equation [5.12]. The flow is taken in the direction of the z axis.

$$E_v = \frac{\sum_{xyz}\left|u_z^s - u_z^a\right|}{\sum_{xyz}\left|u_z^a\right|} \qquad [5.12]$$

where u^a is the analytical and u^s the simulated LBM velocity in the z direction of the channel.

The analytical solution for the velocity in a channel formed between two walls separated by a distance H, where h is the distance from the centre of the channel is most conveniently expressed in terms of the maximum velocity [White, 2006a]:

$$u_z^a(h) = u_{\max}\left[1 - \left(\frac{h}{(H/2)}\right)^2\right] \qquad [5.13]$$

$$\text{where, } u_{\max} = \frac{3}{2}u_{ave}$$

Similarly the analytical solution for velocity in a tube with a radius R, where r is the distance from the centre of the tube [White, 2006b] is expressed as:

$$u_z^a(r) = u_{\max}\left[1-\left(\frac{r}{R}\right)^2\right] \qquad [5.14]$$

where, $u_{\max} = 2u_{ave}$

In both equations [5.13] and [5.14] u_{max} is the velocity at the centre of the channel and u_{ave} is the injection velocity at the inlet.

5.4.1.2 Method: flow in cylindrical tubes

The shape of the velocity profile of the inlet and outlet was studied using a cylindrical tube geometry. This shape represents the best approximation of a micro-tomography dataset vessel for analytical purposes. The analytical velocity field in these regions was compared with the solutions derived using the lattice-Boltzmann method with particular attention to the inlet and outlet boundary conditions.

Each simulation was carried out using a straight tube geometry with the dimensions: 23 by 23 by 101 lattice units. The inlet velocity was set to $+2.6\times10^{-4}$ lattice units/time-step and the simulation was run till a steady state was achieved. Inlet-link averaging over 2 time-steps was used on the incoming links at the inlet.

5.4.1.3 Method: a study of error behaviour

Two specific anomalies were observed in the velocity profile of the tube simulations, the first being a distortion at the inlet and outlet and the second a small, but definite oscillation of the velocity field through the channel. These two sources of error could pose problems for simulations in more complex geometries, so their behaviour was studied further to determine how they could either be eliminated or managed.

The inlet and outlet both distorted the velocity profile of a number of adjacent nodes extending into the tube. The distance this distortion extended into the channel was investigated further by considering the effect of inlet velocity [Figure 5.4 (A)] and

channel height [Figure 5.4 (B)] on the anomaly. The error E_v is given as a function of distance from the inlet or outlet in each case. The simulations were carried out in a channel geometry: 10x by 100y by z^* lattice units (periodic boundaries in the x-axis limits of the domain and flow in the y direction). For the 'inlet velocity' experiments: inlet velocity range was 1×10^{-2} - 1×10^{-5} lattice units/time-step and a constant channel height (z-axis=10^*). For the 'channel height' experiments: channel height z-axis range used was 5 – 90^* lattice units with a constant inlet velocity of $+2.6\times10^{-4}$ lattice units/time-step.

The transient oscillations in the velocity profile with and without inlet-link averaging [Figure 5.4 (C)] were investigated to determine how these could be removed. The simulations were carried out in a channel with the dimensions: 10 by 100 by 10 lattice units (periodic boundaries in the x-axis limits of the domain and flow along the y-axis). The inlet velocity was set to $+2.6\times10^{-4}$ lattice-units/time-step.

All simulations were run till a steady state was achieved.

5.4.2.1 Results: error analysis in straight channels and tubes

The following sections ([Sections 5.4.2.2-4]) present observations of error analysis as demonstrated in channel and tube flows.

5.4.2.2 Results: flow in cylindrical tubes

The velocity profile surface for the analytical solution equation [5.14] [Figure 5.3 (A)] shows the symmetrical velocity profile which runs along the tube. The recovered velocity profile from the lattice-Boltzmann model shows a marked distortion at the inlet and outlets [Figure 5.3 (B)]. A superimposition of the two surfaces is shown in [Figure 5.3 (C)], and shows there is very little difference between the two solutions in the central region of the tube.

The error surface plot [Figure 5.3 (D)] shows clearly where the analytical and numerically determined fields are different, giving a clear impression of the effects of the shapes of the distortions in the field at the inlet and outlet of the channel.

The shape of the inlet [Figure 5.3 (E)] and outlet [Figure 5.3 (F)] distortions, as revealed by their transverse views, are similar though not identical. This is shown more clearly by the peaks of an error surface plot [Figure 5.3 (D)], where the inlet has 4 fairly equally sized error peaks while the outlet region has 6 of differing size.

Figure 5.3. Properties of the inlet and outlet boundaries

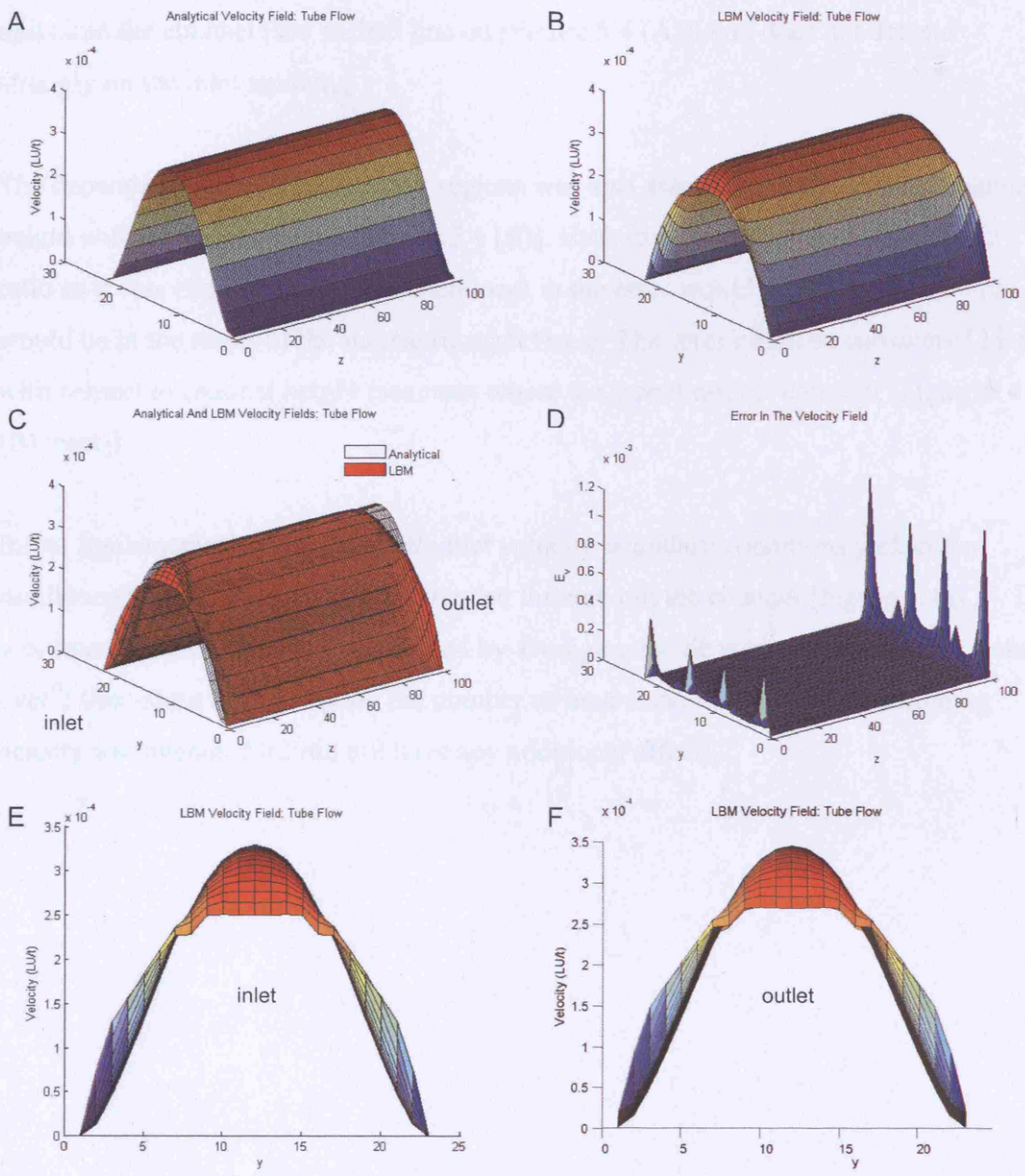

Figure 5.3. Flow behaviour at the inlet (z=0) and outlet (z=100) faces for flow in a cylindrical tube. (A) Analytical parabolic velocity surface, (B) LBM velocity surface, (C) superimposition of the velocity profile in the LBM (solid-red) and analytic solution (clear-grid) for tube flow – the analytical profile is almost completely recovered ~10 nodes, (D) mean error in the velocity field, (E) inlet velocity profile viewed along the z-axis, and (F) outlet velocity profile viewed along the z-axis. In each case flow is in the z-axis, velocity (2.6×10^{-4} LU/t).

5.4.2.3 Results: a study of error behaviour

The error contributed by the inlet and outlet regions appear to resolve after 8-10 lattice units into the channel (see dashed line on [Figure 5.4 (A)]) and does not depend strongly on the inlet velocity.

The dependence of inlet/outlet error regions was also assessed as a function of channel height with a constant length [Figure 5.4 (B)]. Each experiment increases the aspect ratio so it was expected that some increment in the error would be observed, but this would be in the range of the increased aspect ratio. The error could be considered local with respect to channel height (see inset where the aspect ratio is constant [Figure 5.4 (B) inset]).

Initial implementations of the inlet/outlet velocity boundary conditions yielded an oscillating velocity profile which extended through out the channel [Figure 5.4 (C)]. It was found that this could be minimised by averaging the density of the incoming links over 2 time-steps (incrementing the number of time-steps over which the incoming density was averaged >2 did not have any additional effect).

Figure 5.4. Inlet/outlet and artefact propagation

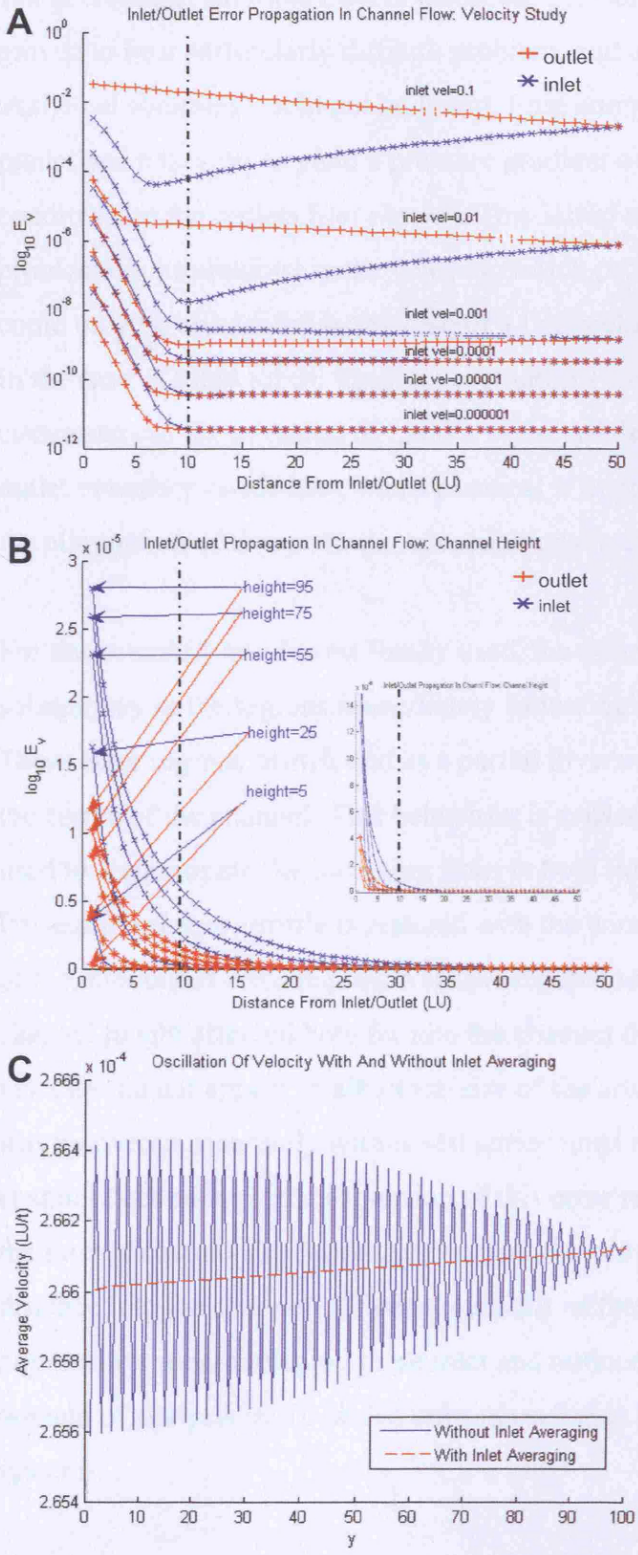

Figure 5.4. Error introduced by the boundary conditions. (A) Penetration of the inlet(blue)/outlet(red) error as a function of distance from each boundary and inlet velocity, (B) penetration of the inlet(blue)/outlet(red) error as a function of distance from each boundary and channel height (equivalent expansion at a constant channel aspect ration: inset) and (C) cumulative error perpendicular to flow shows the oscillations in the velocity profile using the inlet/outlet boundary conditions without averaging (blue), these oscillation are almost totally removed by averaging the velocity at the incoming links of the inlet (red), averaging was over 2 time steps. Flow is in the y-axis, velocity (2.6×10^{-4} LU/t).

5.4.3 Discussion

The presence of multiple outlets where the pressure gradient was unknown *a posteriori* proved to be a particularly difficult problem, and a complete agreement with the analytical solutions could not be found. First attempts at a solution employed a predefined (density) to yield a pressure gradient over the system and open boundary conditions at the outlets [*not shown*]. This initial attempt system suffered from problematic oscillations in the velocity, which propagated through the channel and could only be eliminated in the case of a linear channel perpendicular to the inlet plane. In the case of tilted tubes, transient oscillations caused large error to accrue. Under these circumstances the adoption of Ladd's velocity inlet in conjunction with multiple open outlet boundary conditions, was a practical if imperfect approach which at least allowed the elimination of these transients oscillations in all simple geometries studied.

For the boundary conditions finally used, the main deviation from the analytical solution lay in the regions immediately following the inlet and preceding the outlet. These error regions manifested as a partial inversion of the parabolic velocity profile in the centre of the channel. This behaviour is caused by the uniform and Grad distribution used to approximate the incoming links at both inlet and outlet, after 10 nodes normal Poiseuille velocity profile is restored with the correct shape and amplitude. Localisation of the inlet/outlet error regions was investigated to determine if the inlet velocity and channel height affected how far into the channel the distortion extended. The inlet velocity did not appear to affect the size of the artefact region, as normal Poiseuille flow was recovered accurately within ~10 lattice units into the channel. The height of the channel does cause some expansion of this error region (however if the aspect ratio of the tube or channel is restored, the normal flow is restored within ~10 lattice units distance into the channel). Given the results of these tests in simple geometries, a practical solution managing these inlet and outlet artefact would be to contract the domain of analysis by 10 lattice units at each side of the micro-tomography vessel systems.

The transient oscillations observed without inlet incoming link averaging, seemed to arise from the use of the velocity inlet boundary condition (Ladd's moving wall) in

conjunction with the open-outlet boundary conditions. These transients could be almost completely eliminated by including an inlet-averaging step over two time steps.

In conclusion, the boundary condition requirements for simulating flows in complex vessel systems were substantially more complicated than initially anticipated. Solutions to these problems necessitated new ideas and combinations of boundary conditions. Here significant progress was made on the problem of simulating fluid injection at an inlet in conjunction with multiple outlet regions of undefined size, direction and shape.

5.5.1 Method: simple bifurcating channels

The next series of experiments extended the simple tube and channel flow by simulating flow in more complex bifurcating tube geometries. Here the parent vessel element was used as the inlet and the termini of each daughter vessel the outlet. This geometry also allowed the multiple outlet faces of the simulation domain to be tested.

Despite the variability of other parameters such as inter-branch distance and vessel diameter, the branching angle distribution from each tumour type was remarkably consistent with respect to the tissues studied. In [Section 4.4.3] it was shown that mean branching angle of the control mucosa was 87.14°, while that of the tumour types was adenoma=77.74°, carcinoma=73.31°, LS147T=77.16° and SW1222=81.85°. Konerding *et al.* have suggested that this may "indicate a common basic architectural principle which cannot be transgressed, and which is retained across different types of normal tissues and tumours" [Konerding et al., 1999]. The simple bifurcating vessel geometry forms the fundamental repeating unit of most vascular systems and provides an opportunity to observe how flow behaviour is affected by branching angle.

Simulations were carried out on this basic symmetrical bifurcation [Figure 5.5 (A)] geometry for branching angles in the observed range of ~15-180° and rarely observed branching angles with (>180°). For each simulation a symmetrical bifurcating channel with daughter branches at a specified angle θ was used. A z-stack 8-bit image of the bifurcating vessel was constructed with the *ImageJ* application and compressed into a RAW file then subsequently converted into a geometry dataset for the simulation.

Bifurcating vessels were constructed with branching angles ranging from 30-240°, the channels were 30 lattice units high and between 80 and 140 lattice units long, and the inlet on the right was set to a velocity of 2.67×10^{-4} lattice units per time step.

An estimate of shear stress above the no slip boundary was given by evaluating the relative rate of parallel flow in the simulated velocity field, post simulation. This is given by, equation [5.15], where shear stress τ is expressed by: μ the dynamic viscosity, gradient of the u the velocity perpendicular to y.

$$\tau = \mu \frac{\partial u}{\partial y} \qquad [5.15]$$

The simple bifurcating structure was additionally used to test the boundary conditions of the outlet domain which were perpendicular to the inlet.

5.5.2 Result: simple bifurcating channels

The velocity, pressure and shear fields are shown in the panels of [Figure 5.5]. A constant channel width was used to factor out the effect of the calibre of the parent and daughter vessels so the effective channel size doubles between the parent and daughter elements. Consequently both pressure and velocity drop after the bifurcation point. The boundary conditions appear to perform well with the inlet and outlet error regions localised and normal Poiseuille flow recovered in the main channel regions.

Plotting global maximum velocity as a function of branching angle shows the velocity is fairly consistent until 120° after which it drops sharply to a low of 180° [Figure 5.6]. It is interesting to note this coincides with the bulk of bifurcation angles measured for tumours and control tissue.

Figure 5.5. Flow properties at the vessel bifurcation

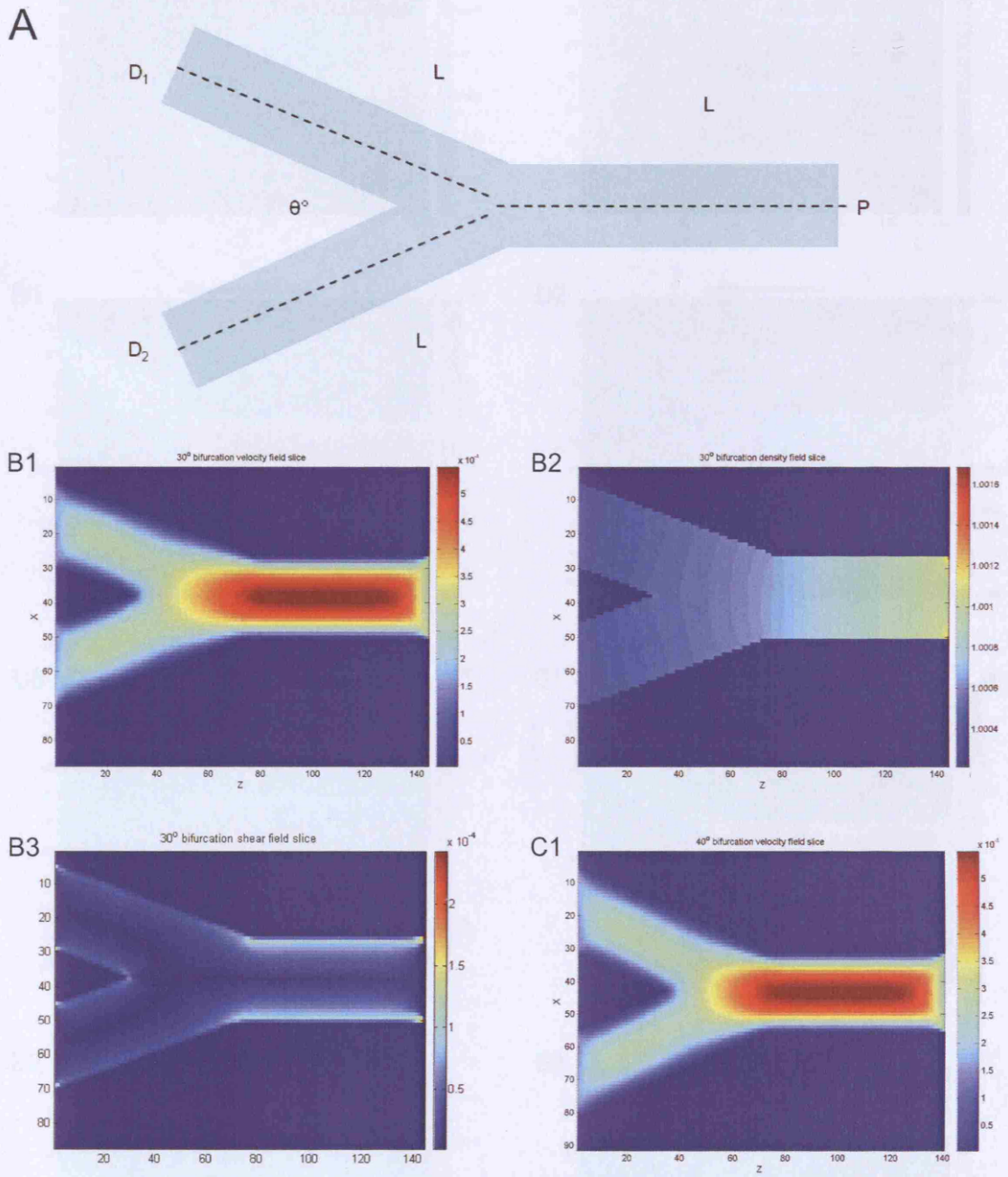

C2

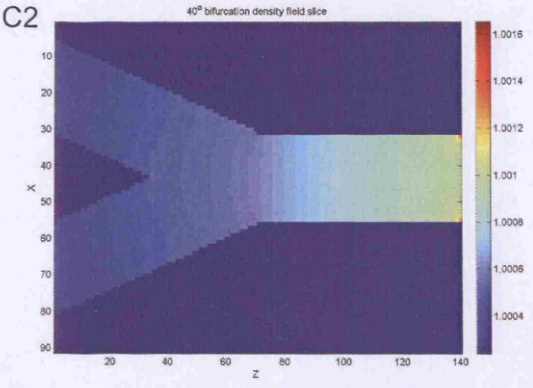

C3

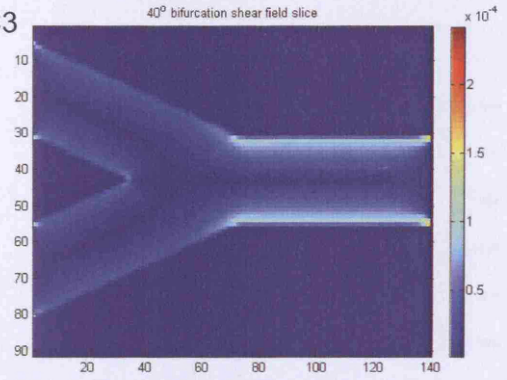

D1

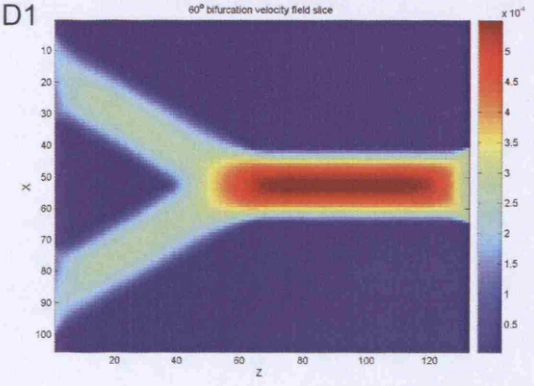

D2

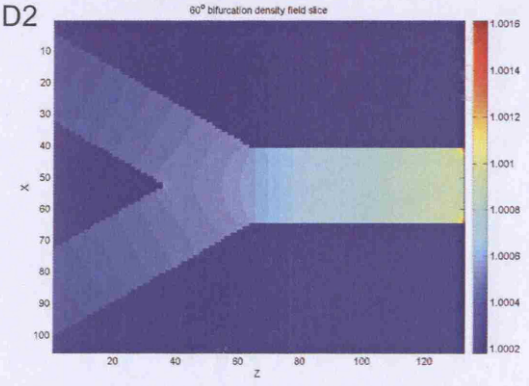

D3

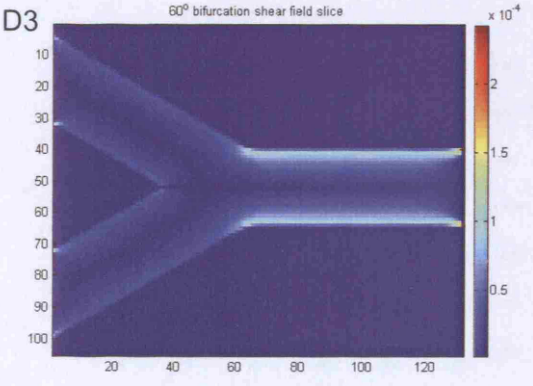

E1

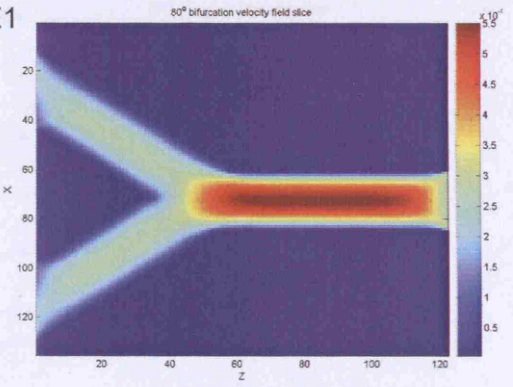

E2

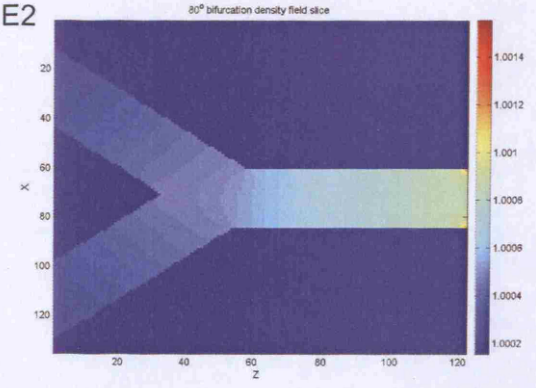

E3

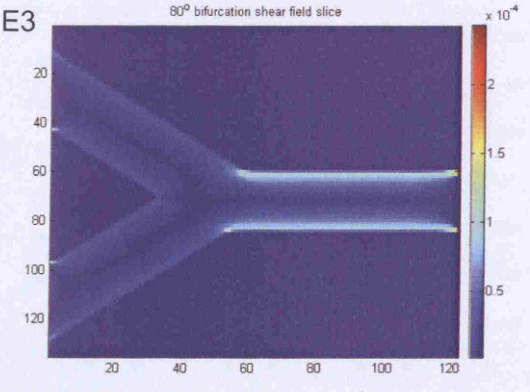

F1

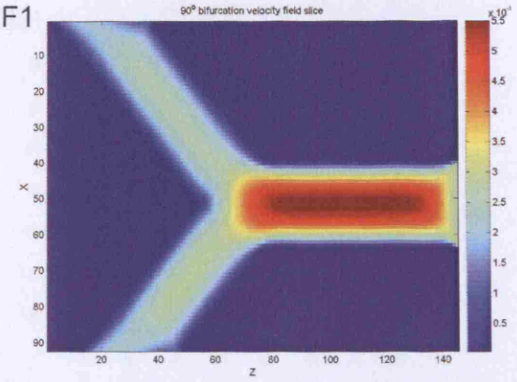

F2

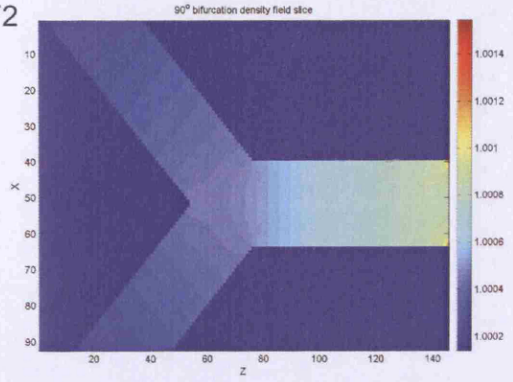

F3

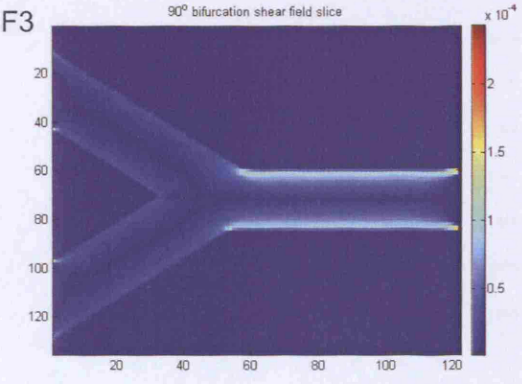

G1

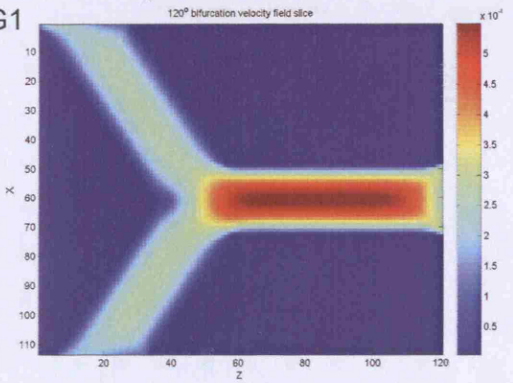

G2

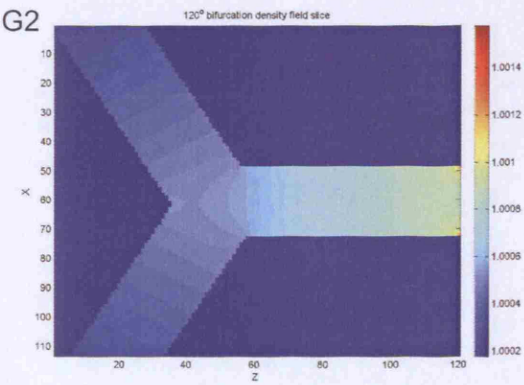

G3

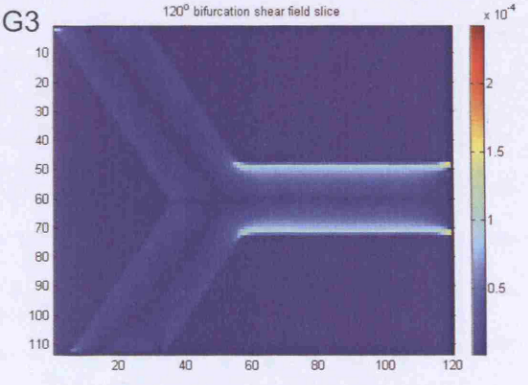

H1

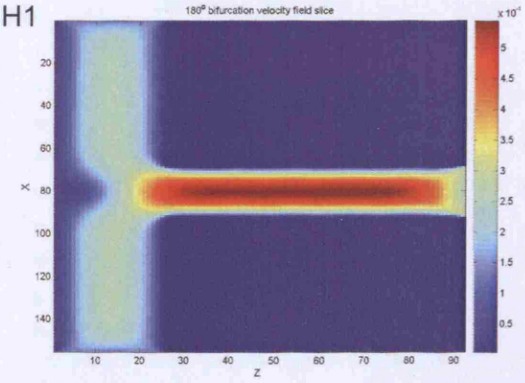

H2

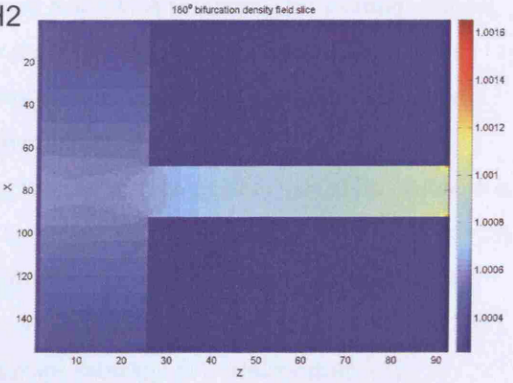

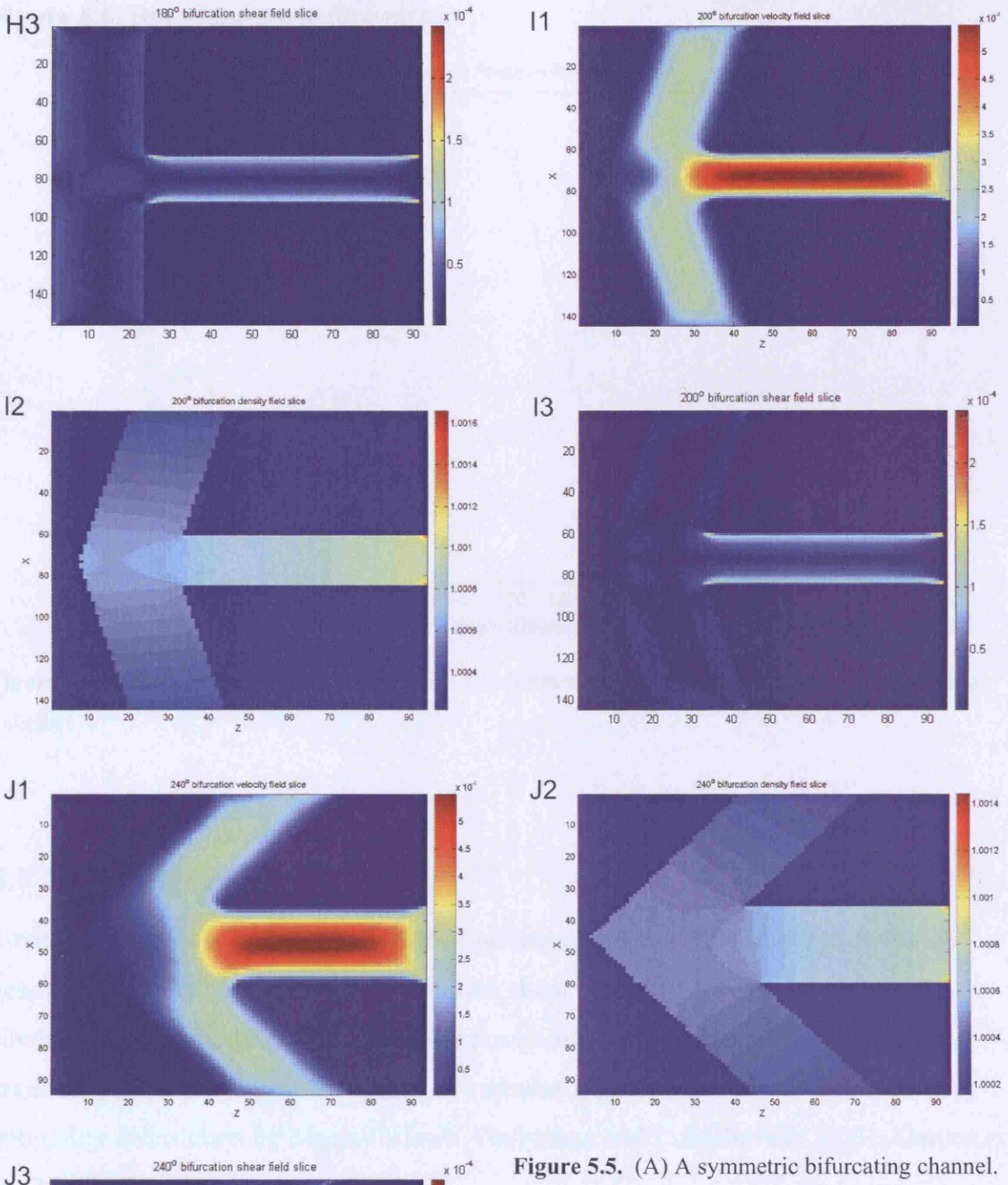

Figure 5.5. (A) A symmetric bifurcating channel. *L* is the length of each vessel elements, P is the parent element and inlet, $D_{1\&2}$ are the daughter elements and outlets. The diameter of both daughter elements is equal to that of the parent, θ is the branching angle. Element width=24, height=29, length=60 lattice units. (B-J) Bifurcating angles: 30°, 40°, 60°, 80°, 90°, 120°, 180°, 200° and 240°. Heatmaps showing: (1) velocity field, (2) 'pressure' density fields and (3) shear stress.

Figure 5.6. Branching angle flow effects

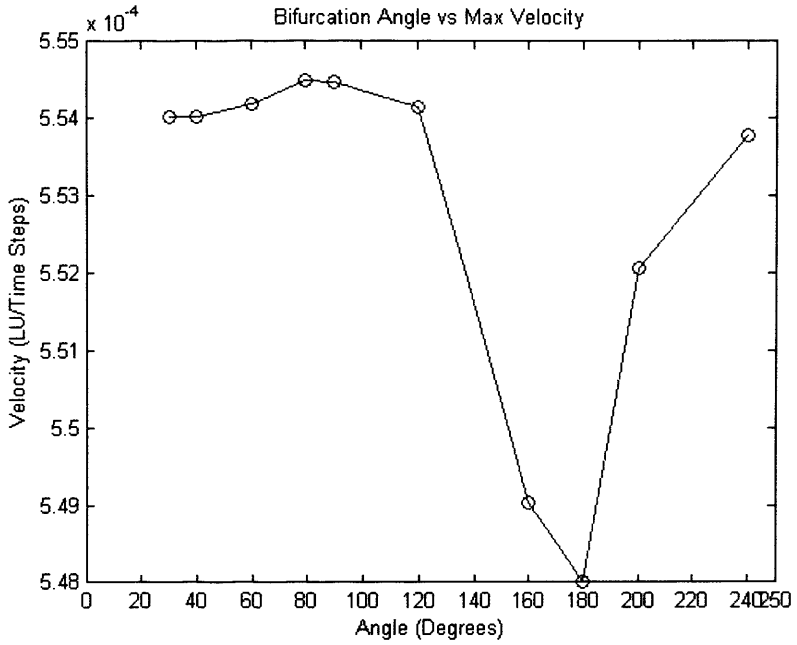

Figure 5.6. Simulation of flow a single symmetrical bifurcating channel showing the global maximum velocity.

5.5.3 Discussion

Stereoimaging measurements suggested that branching angle distributions in tumour vessels were consistent with the distribution shape observed for normal vessels. The similarity in distribution shape raised the possibility that branching outside optimal range may incur a hydrodynamic cost in a similar way to the vessel calibre branching optimality determined by Murray's laws [Gafiychuk and Lubashevsky, 2001;Alarcon et al., 2005].

The hypothesis that branching in tumour vessels is restricted to the more acute range of angles stands to reason, as beyond angles of 120° the pressure reflecting off the far wall of the daughter vessels becomes greater as the wall straightens out. This is also seen in the shear stress, with high shear values on the apex of the bifurcation. These studies, although currently quite simplified, are an example of how simulations can be applied to biological questions.

5.6.1 Method: comparison of flow simulations in small vascular networks for all 5 tissues

Building on progressively more complex geometries, the next group of experiments attempted to replicate a well defined behaviour of *in-vivo* blood flow in tumours. The behaviour in question was an observation by Leunig and Yuan *et al.*, that correlation between vessel diameter and the corresponding local velocity was high in regular networks, but low in more chaotic networks of tumour vessels [Leunig et al., 1992] [Yuan et al., 1994], (see [Chapter 2] [Figure 2.5 (A&B)]). In the study by Leunig *et al.*, measurements were made on the vessels of the LS147T tumour and compared to striated muscle vessels in mice, whereas the study by Yuan *et al.* used glioma tumour xenografts and the control was phial vessels in rat.

To assess characteristics of flow in the vasculature of 4 tumours and 1 control tissue from the tomography datasets discussed in the previous chapter, vessel networks where suitable inlets could be identified were cropped from the main volume. These sub-volumes were used to define simulation geometries for each tissue.

3 control mucosa (K1-3), 4 adenoma (A1-4), 6 carcinoma (C1-6), 3 LS147T (L1-3) and 6 SW1222 (S1-6) volumes were used for this study. The uneven numbers of datasets was the results of limited supply of scanned datasets, and some scans were not of suitable quality to use for flow simulations. Each data set had previously been processed into a binary image as detailed in the previous chapter [Section 4.5.1]. Inlet velocity was set at 2.67×10^{-4} lattice-units per time step. Simulations were run until the average momentum between time iterations changed by less than 1×10^{-3}. For convenience, velocity was maintained as lattice units per time step (LU/t), this can be converted to mm per Sec, velocity (mm/sec) = simulation velocity × [effective resolution] × 1000).

As described in [Section 4.5.1], the vessel cross-sectional area was determined perpendicular to the local axis of flow. An average velocity magnitude was determined from the equivalent cross-sectional surface in the velocity field and was used to represent the local velocity. The correlation between these two values was examined graphically as a scatter plot and numerically by a Pearson correlation coefficient.

5.6.2 Result: comparison of flow simulations in small vascular networks for all 5 tissues

An example of the velocity field from a simulation is shown in [Figure 5.7], where it is possible to see how the velocity profile changes depending on the local geometry and topology of the vasculature.

The mean and standard deviation of the velocity magnitude for each simulation are given in [Figure 5.8]. From this figure the inter-sample variation appears quite large, particularly amongst both adenoma and carcinoma. In both xenografts the velocity is substantially lower.

Flow simulations carried out on different tissues [Table 5.2] are presented in [Figures 5.9-13]. Here correlation between local flow velocity and vessel calibre was most consistently positive in control mucosa, adenoma and carcinoma (control=0.32±0.1, adenoma=0.36±0.13, carcinoma=0.36±0.33) compared to xenografts (LS147T=0.15±0.23, SW1222=0.15±0.18). The degree of correlation between vessel calibre and velocity was particularly variable in the carcinoma simulations [Figure 5.11] with C1-3 showing a high much higher positive correlation [mean 0.65±0.09] between vessel size and velocity, than C4-6 [mean 0.06±0.05].

Figure 5.7. An example of a velocity magnitude field from a LBM flow simulation in a micro-CT vessel geometry

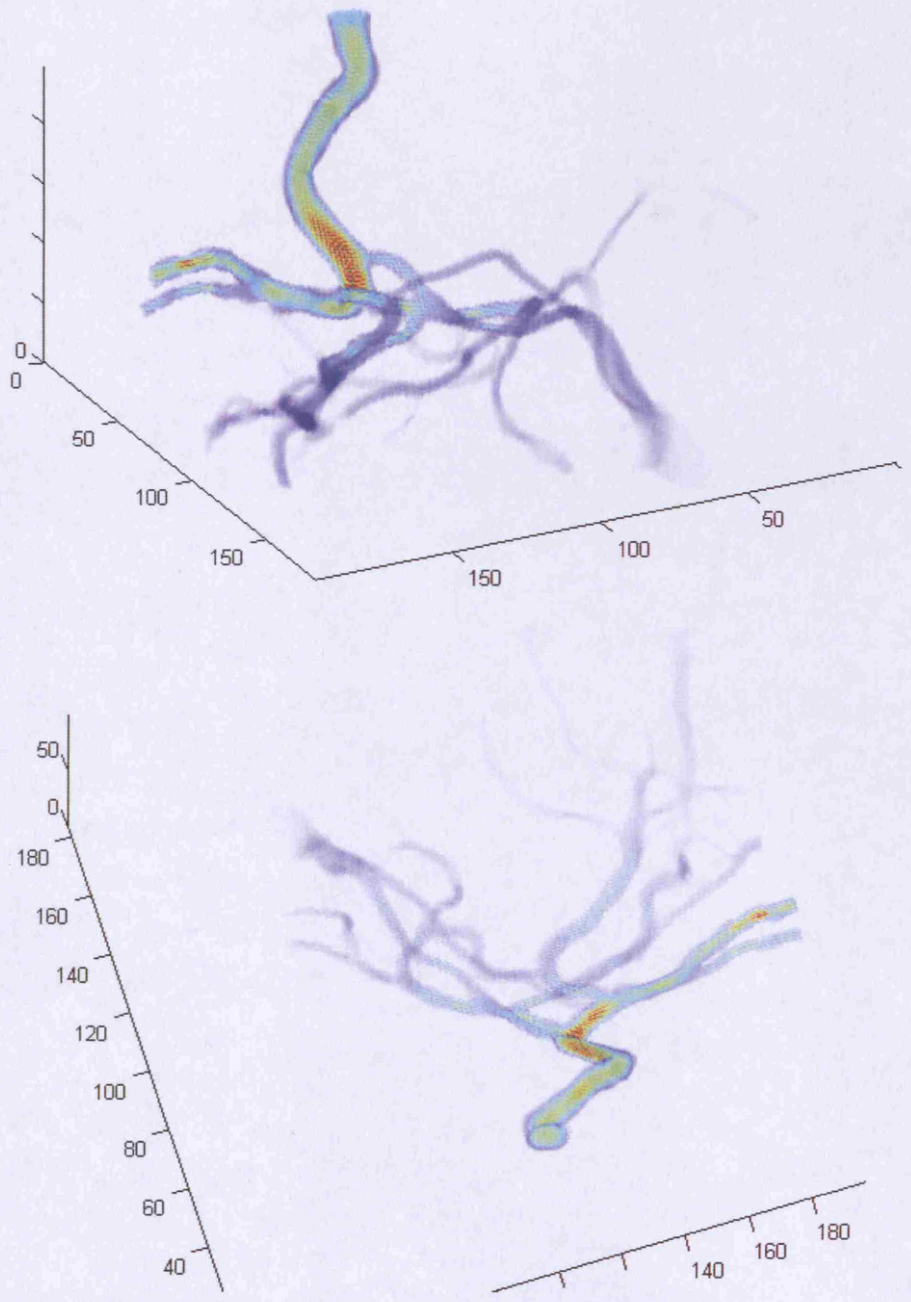

Figure 5.7. An example of a 3D velocity magnitude field (red=high, blue=low) of a small vessel network from a human carcinoma, rendered with a linear alpha map for voxel transparency in order to show internal areas of high and low velocities within the vessels. (side view, upper panel; top view, lower panel), all axes are in lattice units (here 1LU=3.3μm).

Figure 5.8. Mean and standard deviation of simulated velocity in tomography samples

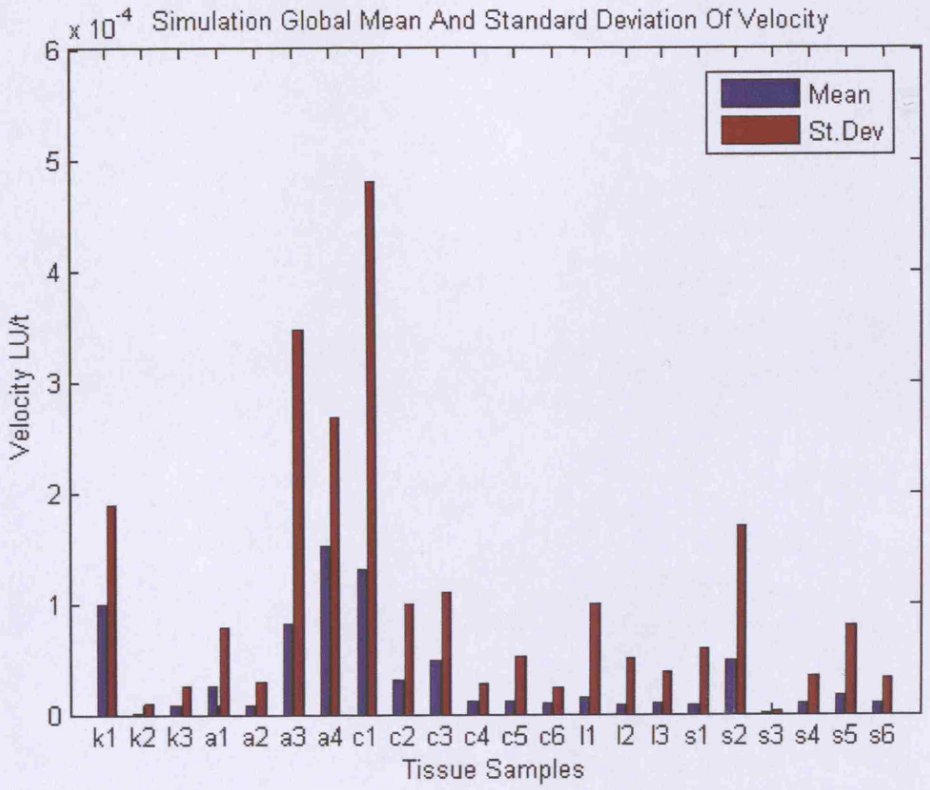

Figure 5.8. The mean and standard deviation of the fluid velocity from each of the simulations in each tissue samples. Mean velocity is given in mm per sec, as scaled according to the tissue sample scan resolution. X-axis labels relate to the relevant datasets summarised in [Table 5.2].

Table 5.2. Physical characteristics of the samples

Tissue Type	Sample	Microvascular Density (vessel fraction of total volume)	Average Cross-Sectional Area (μm^2)	Sample Resolution (μm^3)	Vessel Calibre-Velocity Pearson's Correlation Coefficient
Control	K1	0.16	1.24E+03	3.30	0.33
	K2	0.13	8.26E+02	3.30	0.22
	K3	0.11	7.46E+02	2.40	0.41
Adenoma	A1	0.05	7.99E+02	3.96	0.35
	A2	0.06	9.16E+02	3.96	0.29
	A3	0.05	7.37E+02	3.96	0.25
	A4	0.04	6.32E+02	3.96	0.54
Carcinoma	C1	0.03	2.99E+02	3.30	0.59
	C2	0.03	3.13E+02	4.29	0.61
	C3	0.03	3.83E+02	4.29	0.75
	C4	0.07	8.89E+02	3.63	0.06
	C5	0.09	9.29E+02	3.63	0.11
	C6	0.06	6.08E+02	3.63	0.02
LS147T	L1	0.08	1.27E+03	4.80	0.01
	L2	0.05	8.75E+02	4.80	0.02
	L3	0.13	5.20E+02	4.80	0.41
SW1222	S1	0.10	2.13E+03	3.96	0.07
	S2	0.11	1.55E+03	3.96	0.01
	S3	0.37	1.31E+03	3.63	0.15
	S4	0.39	1.03E+03	3.63	0.16
	S5	0.37	1.97E+03	3.63	0.02
	S6	0.12	2.16E+03	3.63	0.49

Table 5.2. Physical characteristics relating to tomography dataset of the control mucosa and 4 tumours

Figure 5.9. Scatter-plot of vessel calibre vs. simulated velocities in control mucosa

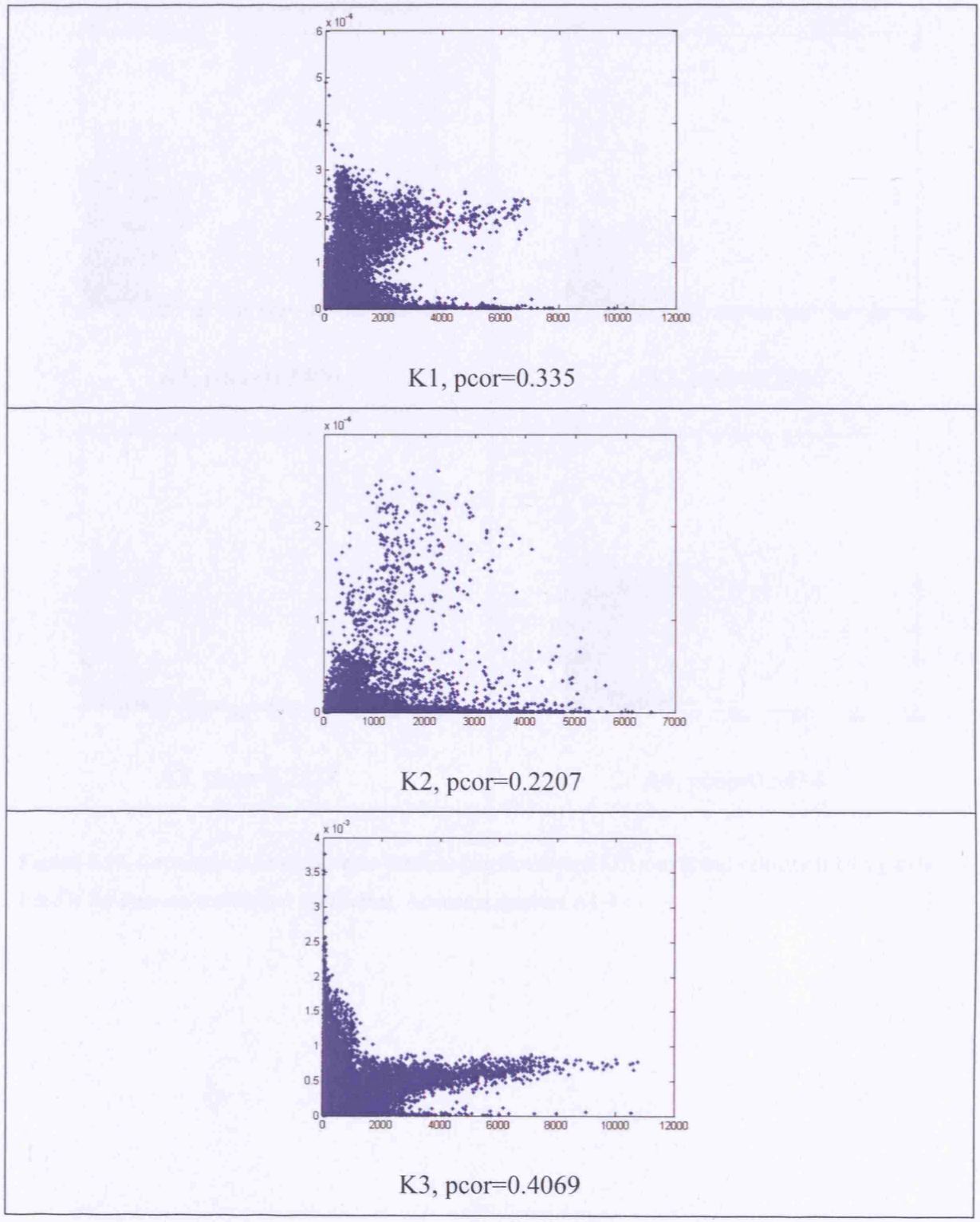

Figure 5.9. Correlations between cross-sectional surface area (LU^2) x-axis and velocity (LU/t) y-axis. *Pcor* is the Pearson correlation coefficient. Control mucosa datasets K1-3.

Figure 5.10. Scatter-plot of vessel calibre vs. simulated velocities in adenoma

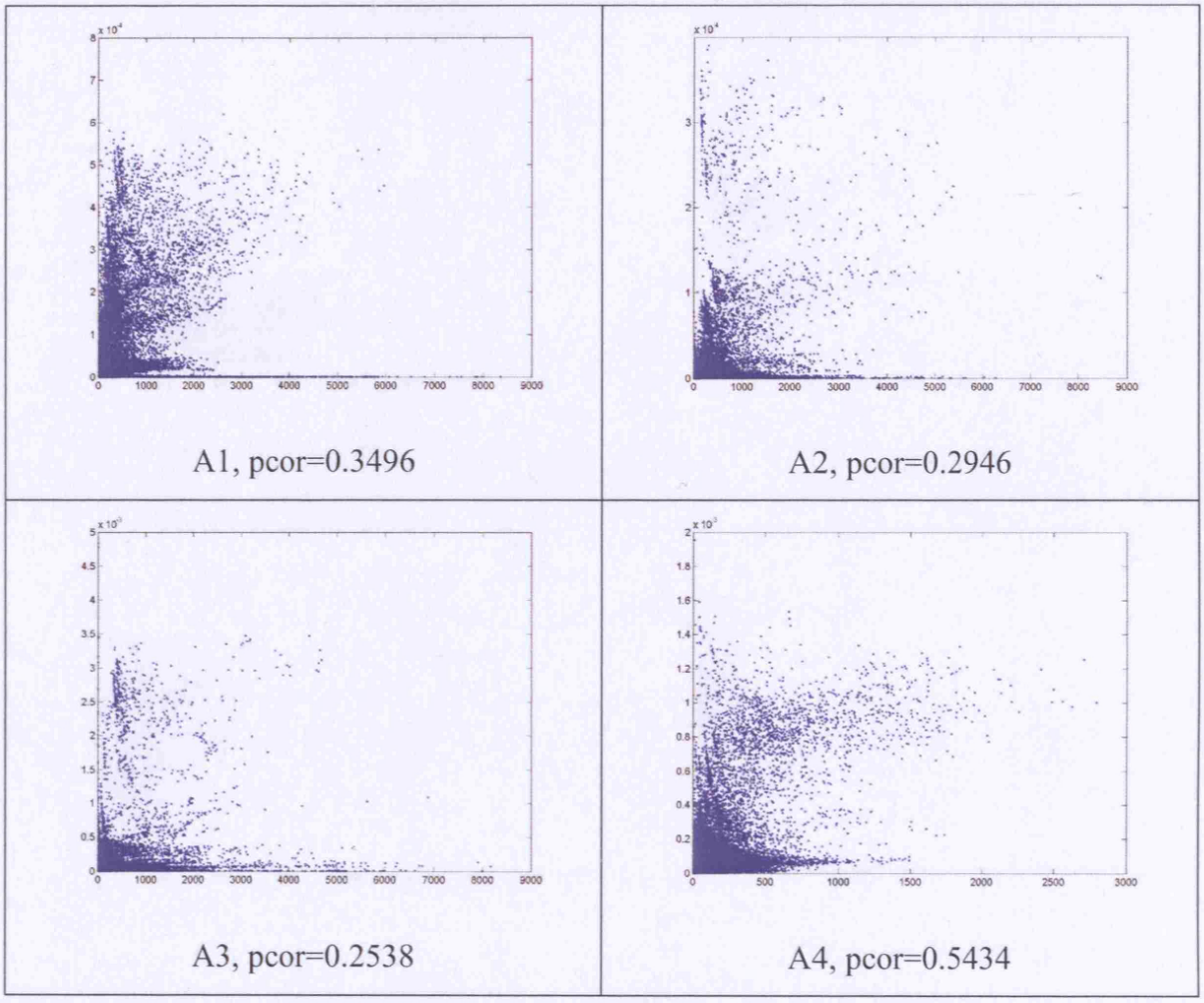

Figure 5.10. Correlations between cross-sectional surface area (LU^2) x-axis and velocity (LU/t) y-axis. *Pcor* is the Pearson correlation coefficient. Adenoma datasets A1-4.

Figure 5.11. Scatter-plot of vessel calibre vs. simulated velocities in carcinoma

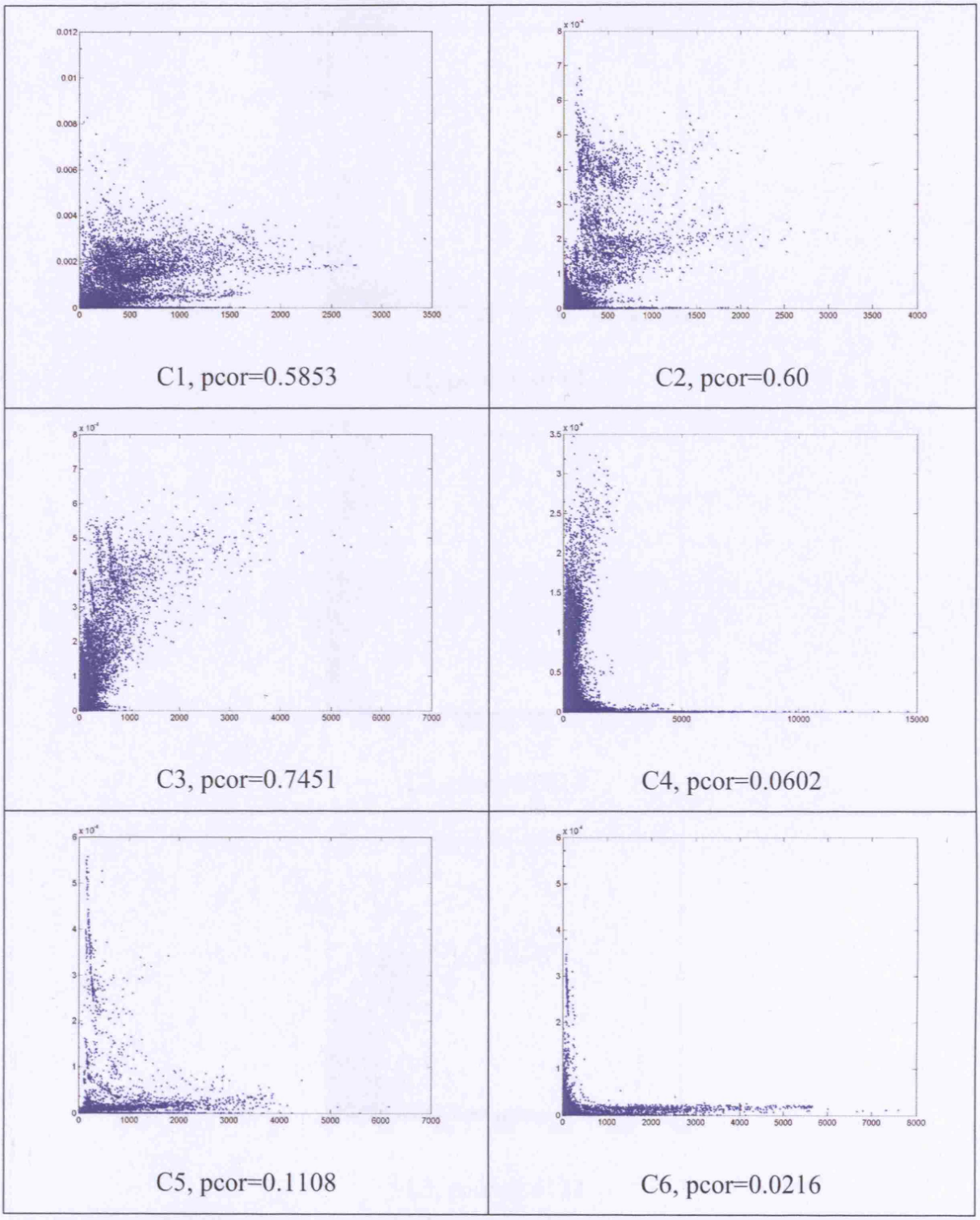

Figure 5.11. Correlations between cross-sectional surface area (LU^2) x-axis and velocity (LU/t) y-axis. *Pcor* is the Pearson correlation coefficient. Carcinoma datasets C1-6.

Figure 5.12. Scatter-plot of vessel calibre vs. simulated velocities in LS147T

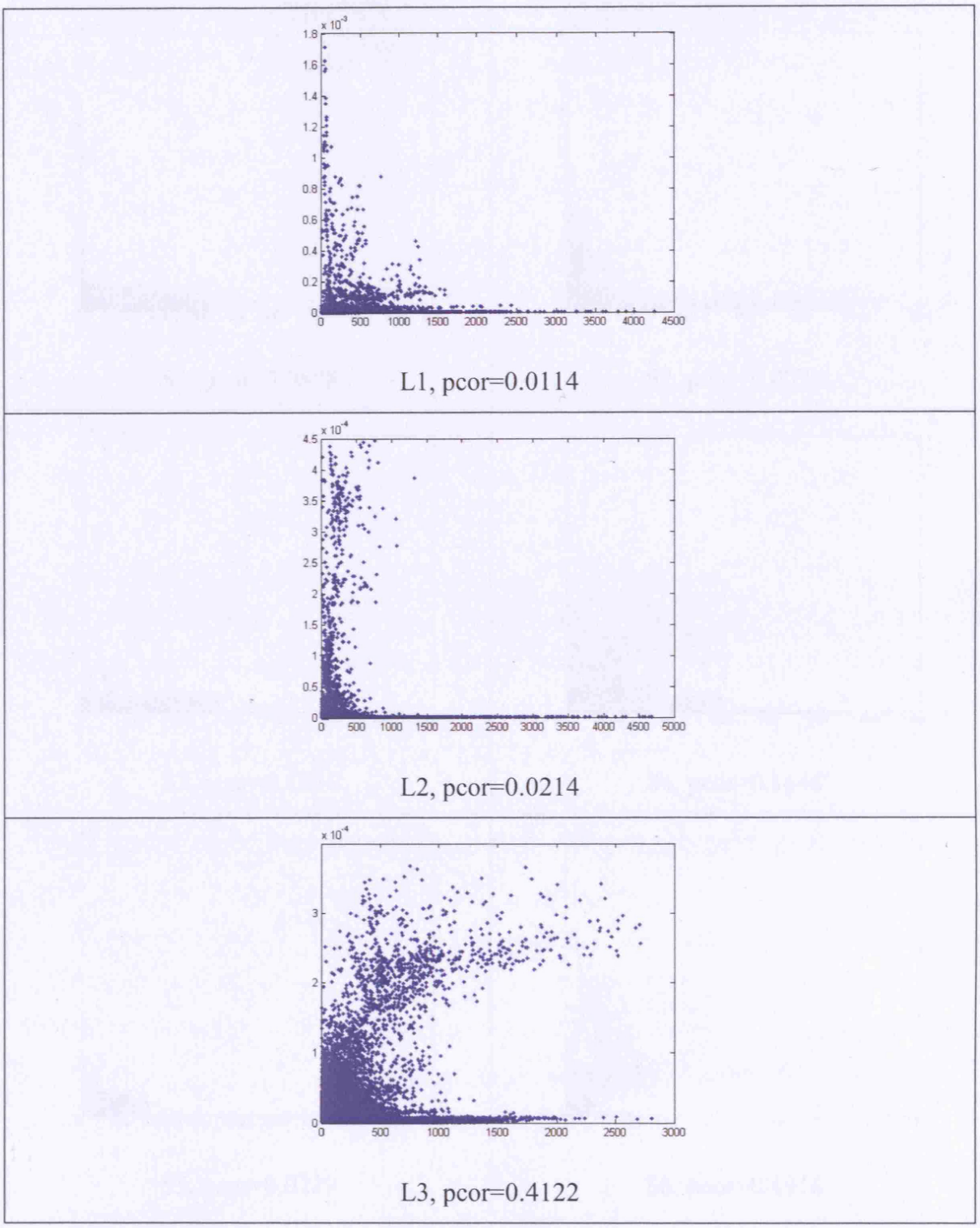

Figure 5.12. Correlations between cross-sectional surface area (LU^2) x-axis and velocity (LU/t) y-axis. *Pcor* is the Pearson correlation coefficient. LS147T datasets L1-3.

Figure 5.13. Scatter-plot of vessel calibre vs. simulated velocities in SW1222

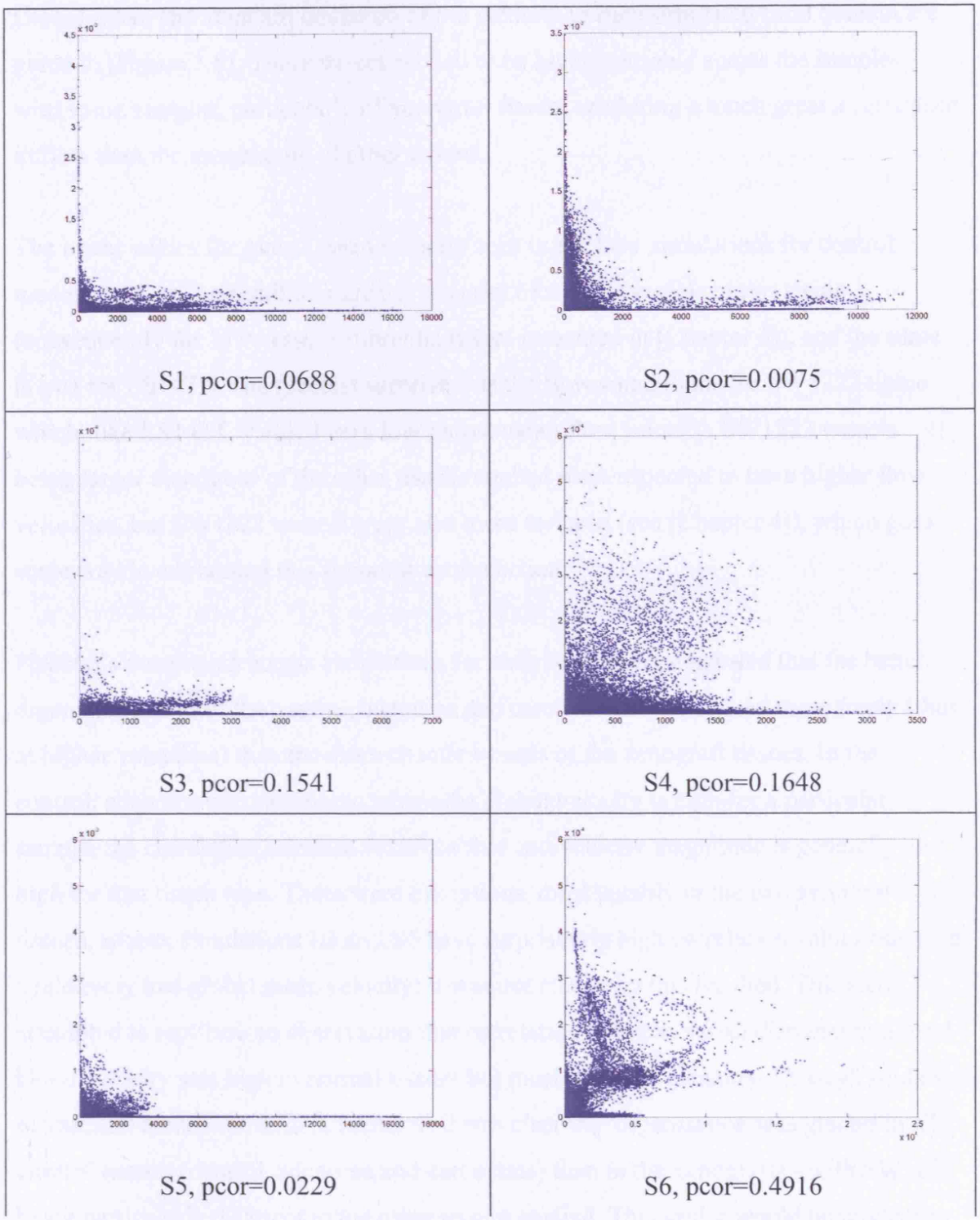

Figure 5.13. Correlations between cross-sectional surface area (LU^2) x-axis and velocity (LU/t) y-axis. *Pcor* is the Pearson correlation coefficient. SW1222 datasets S1-6.

5.6.3 Discussion

Global mean and standard deviation of the velocity in each simulated fluid domain are given in [Figure 5.8]. These values proved to be highly variable across the samples, with some samples, particularly of xenograft tissue, exhibiting a much greater resistance to flow than the vasculature of other tissues.

The lower values for global mean velocity seen in the flow simulations for control mucosa may be the result of a greater quantity of smaller vessels in this tissue (consequently the low vessel calibre/diameters measured in [Chapter 4]), and the same is true for LS147T. The greatest surprise was the flow simulations for SW1222 tissue which, like LS147T, yielded very low global mean flow velocity. SW1222 vessels being larger than those of the other tissues studied were expected to have higher flow velocities, but SW1222 vessels were also more tortuous (see [Chapter 4]), which goes some way to explaining this apparent contradiction.

Pearson's correlation across simulations for each tissue type suggested that the better organised tissues of the control, adenoma and carcinoma conduct flow more freely (thus at higher velocities) than the more chaotic vessels of the xenograft tissues. In the control, adenoma and carcinoma where the global velocity is high for a particular sample, the correlation between vessel calibre and velocity magnitude is generally also high for that tissue type. There were exceptions, most notably in the two xenograft tissues, where, simulations L3 and S6 have surprisingly high correlation values but have a relatively low global mean velocity; it was not clear why this resulted. This study attempted to replicate an observation that correlation between vessel diameter and local blood velocity was high in normal tissues but much lower in tumours. Through studies of vascular architectures in [Chapter 4] it was clear that organisation was greater in all clinical tissues (control, adenoma and carcinoma) than in the xenografts - with SW1222 being particularly different to the other tissues studied. This said it would be prudent to conduct more detailed studies using a greater number of larger samples in order to discount for the local variability in the corrosion casts.

This study represents the first attempt to simulate flows in geometrically accurate microvasculature with the view to determining how the local architecture affects the

flow behaviour. Although many aspects have been simplified for the purpose of creating a viable simulation, this method provides a genuinely new paradigm for study of microvascular flow in a biological context. Building on this, it should be possible to use this system to explore clinically important questions, such as the observation by Fujimori *et al.* ([Fujimori et al., 1999]) that blood velocity is higher in adenomas than in carcinomas – such behaviour may well be influenced by the different vascular architectures in these tumours.

5.7.1 Method: whole tumour simulations

The final study was carried out to demonstrate how corrosion cast X-ray-tomography in conjunction with an LBM model could be used to simulate flow for whole three-dimensional tumour vascular systems. This demonstration is an important stepping stone in the development of a platform for investigating drug delivery in a realistic vascular model *in-silico*. For this purpose a xenograft tumour cast (LS147T type) was scanned and processed in the same manner as detailed in [Section 4.5.1]. The use of xenograft tumour rather than clinical tumour was purely a matter of convenience as these tumours could easily be grown up to specified size for the X-ray tomography machine (which as previously indicated has certain size/resolution constraints). The roughly spheroid tumour was also delineated from the host tissue by a fibrous capsule, and the host vascular system which defined major inlet/outlets to the system could be easily identified.

The sample size largely determines the upper limit of the tomography scan resolution, and thus the computational domain of the simulation. These constraints dictated that the whole sample could not exceed ~$1 cm^3$. The scan resolution of the whole LS147T cast was made at 2.4 μm^3; due to computational requirements the simulation domain used a resolution of 15.84 μm^3, and therefore only accounted for the larger vessels in the domain. This restriction was necessary in order that the simulation of such a large volume could be achieved on the UCL Altix within the 48hr time limit (research student quota).

5.7.2 Result: whole tumour vessel simulations

The tumour vessel geometry used in the simulation is shown in [Figure 5.14 (A)]. A three-dimensional scatter-plot of the lower, inter-quartile and upper quartile ranges of velocity are shown in three separate panels [Figure 5.14 (B-D)], and demonstrate the spatial distribution of flow velocities of different magnitudes. The lower velocity regions (first quartile) [mean=0.0213 mm.sec^{-1}] are predominantly discontinuous and are distributed towards the periphery of the tumour. This was in keeping with the higher hydrostatic resistance of smaller peripheral vessels in the highly angiogenic edge of the tumour. Regions of intermediate [mean=0.4 mm.sec^{-1}] and high [mean=2.4 mm.sec^{-1}] velocity on the other hand are restricted to a smaller group of larger vessels [Figure 5.14 (D)].

Table 5.3. Mean flow velocity and vessel calibre associated with Figure 5.14

Flow velocity percentile ranges	Mean velocity	Mean vessel cross-sectional area
0-25	4.74e-6 LU/t (0.02 mm.sec^{-1})	41.47 LU^2 (656.88 mm^2)
50-75	8.95e-5 LU/t (0.4029 mm.sec^{-1})	100.60 LU^2 (1593.5 mm^2)
75-100	5.42e-4 LU/t (2.44 mm.sec^{-1})	165.85 LU^2 (2627.91 mm^2)

Table 5.3. Three flow regimes identified in the tumour simulation [Figure 5.14] which corresponds to different flow velocities and vessel sizes in the tumour.

Figure 5.14. Whole xenograft blood flow simulation

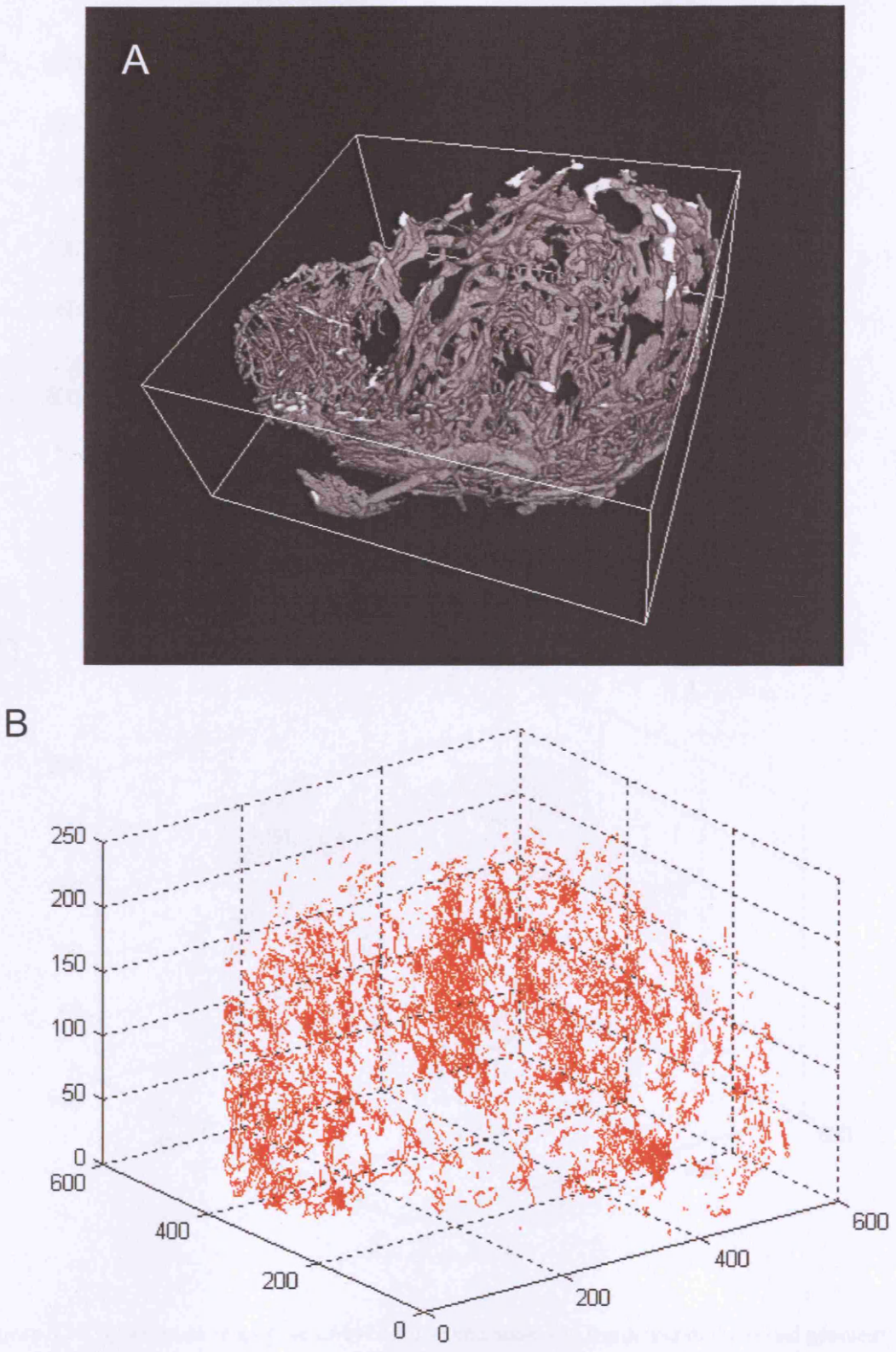

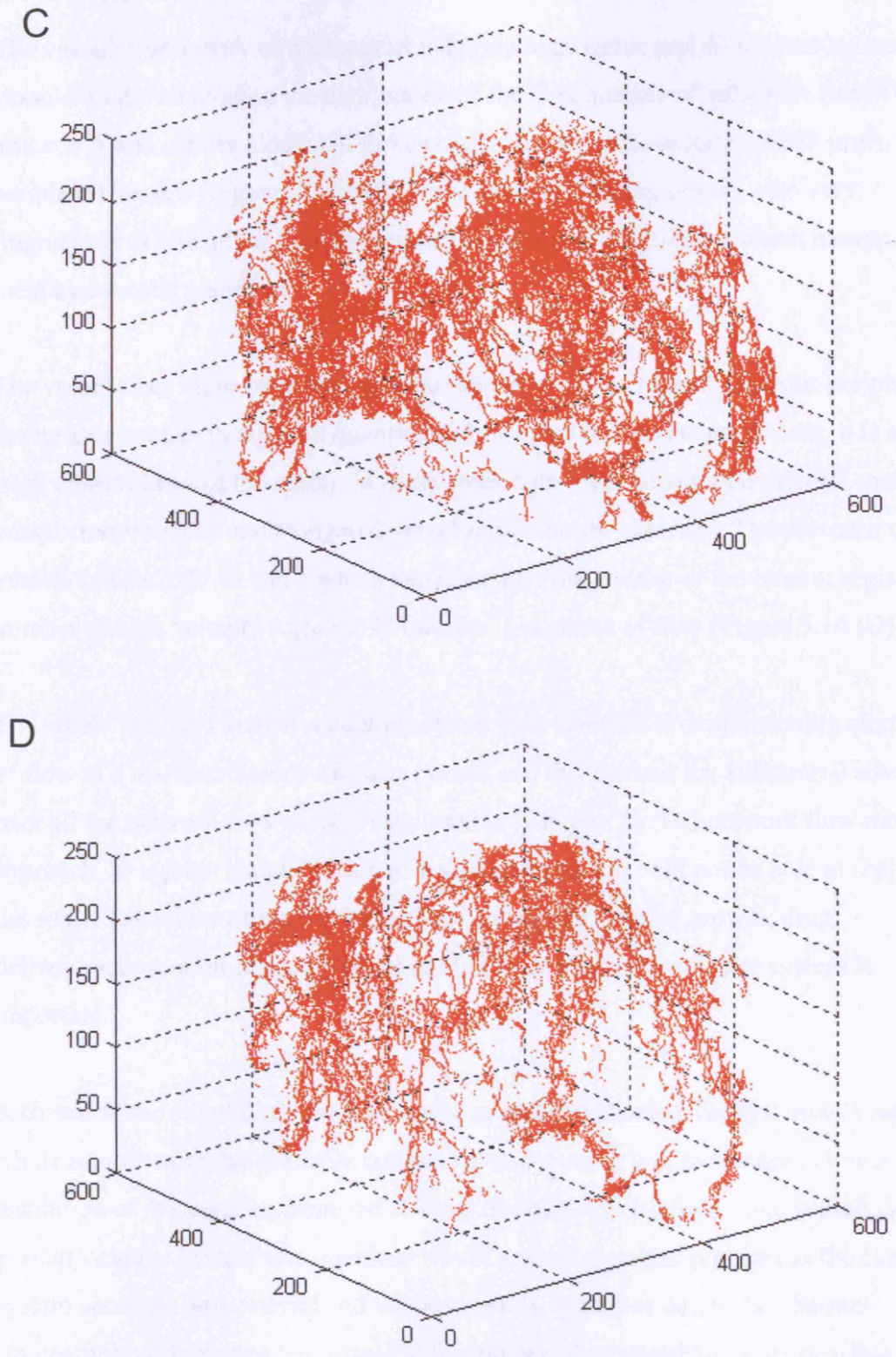

Figure 5.14. Projections of a whole LS147T flow simulation. (A) Rendering of the vessel geometry derived from the tomography dataset, (B-D) show the medial axis of the vessels with different local mean velocity: (B) 25th percentile range *mm/sec (C) 50-75percentile range (D) 75-100percentile range. (Sample Res. 15.84μm^3). Axes are the three spatial dimensions.

5.7.3 Discussion

The vascular periphery of a xenograft is highly angiogenic and dominated by small vessels. In the simulation the distribution of the first quartile of velocities (mean 0.02 $mm.sec^{-1}$) was clearly located in these smaller (mean cross-section 656.88 μm^2), peripheral vessels [Figure 5.14 (B)]. These low velocity regions are also very fragmented as a result of frequent constrictions in the vasculature, which increased the local hydrostatic resistance.

The vessel sizes increase as the vascular density declines from the tumour periphery to the tumour centre (though not quantitatively studied in the xenografts here, it is evident from observations of the casts). In these areas with reduced vascular density, numerous vessel compressions and elongated vessel segments are observed. The presence of large vessels (mean 2627.91 μm^2) which penetrate into the interior of the tumour register as a number of high velocity (mean 2.44 $mm.sec^{-1}$) conduits of flow [Figure 5.14 (D)].

The whole tumour vascular model presented here is aimed at demonstrating simulation of flow in a realistic tumour vascular system and this method has substantial advantages over all the network flow models discussed in [Chapter 3]. The network flow model approach, as a gross simplification of a vascular network, will not be able to replicate the subtle behaviour of tumour blood flow and hence, tumour growth, drug delivery/action or other such physiology function where the vascular system is important.

A caveat of the simulations used here was in order to simulate the system of vessels in a whole tumour with the available computing resources, it was necessary to lower the resolution of the vessel system and thereby discount the capillary scale vessels. In a normal vascular system this omission would present a greater problem as the capillary system connects both arterial and venous vessels. However due to the aberrant connectivity of higher order vessels in the tumour, flow simulations are possible through this network. Furthermore, there is little reason why the original data provided here should not be used for future higher resolution simulations as the micro-computed tomography data included the capillary scale elements of the xenograft.

Finally in relation to the further application of these types of models, a similar view was held by Kohandel *et al.* in their recent publication on the action of anti-angiogenic/cytotoxic drugs on tumour growth [Kohandel et al., 2007] "a better starting point might be to use high-resolution anatomic images of the vasculature derived either from non-invasive imaging or histopathologic examination of tumor specimens". With this in mind micro-CT/LBM models may provide an excellent starting point.

5.8 Chapter conclusions

In this chapter a new method for *in-silico* simulation of blood flow within a tumour microvascular system is demonstrated. The method advances previous vascular models by using a morphologically correct three-dimensional vascular architecture in conjunction with a lattice-Boltzmann fluid model, in order to compute flow in the vascular tissues in tumours and normal vessels. The use of microcomputed tomography/LBM flow to yield 3D flows in tumour vascular systems is a first, and represents a significant advancement on prior systems discussed in [Sections:3.2.1 & 3.2.2] which have typically tried to generate a highly abstracted system of vessels either from *ab-initio* angiogenesis models [Kohandel et al., 2007;Anderson and Chaplain, 1998;Chaplain and Anderson, 2004;Stephanou et al., 2004;Alarcon et al., 2004;Alarcon et al., 2005] or from simplified two-dimensional image data [Baish and Jain, 1998;Baish and Jain, 2000;Baish et al., 1996].

Development of the Lattice Boltzmann simulation

The multiple-outlet boundary problem was solved by using velocity boundary conditions at the inlet and open boundary conditions at the outlets of the vasculature near the border of the domain. To our knowledge this is the first time this has been applied. These inlet/outlet conditions used are associated with a mild distortion of the flow field around the inlet and outlet regions. However tests in channel, tube and simple bifurcation geometries suggest that the impact of this distortion was minimal and does not distort the bulk of the flow field; these regions were therefore handled post-simulation.

Flow in a symmetric bifurcation

Simulation of flow in a simple symmetric bifurcation provided a more complex geometry to test the LBM model and boundary conditions. Observation of the velocity and pressure fields suggest that the system behaves as expected.

The symmetric bifurcation also represents the fundamental unit of most vascular systems; using this we were able to show that the preferred branching angles for all tissues in the stereo-imaging study occurred over the range which is minimally resistant to flow.

Flow in small vessel networks

In order to provide an assessment of the impact of flow in each of the tumour types, a comparison of the velocity field in small sub-volumes of cast tomography derived from the 5 tissues (control, adenoma, carcinoma, LS147T and SW1222) was made. It was shown in certain cases that the vascular tissues which demonstrated better hierarchy in the organisation of the vessel elements also showed better correlation between vessel calibre (as given by the cross-sectional surface) and the mean velocity at that surface. These results suggest some parallel with *in-situ* observations by other authors. One goal of this study was to identify which xenograft type (LS147T or SW1222) better reproduced the simulated flow profiles of carcinomas. However, the observed level variability and the limited number of tomography datasets that could be acquired in the available time have hampered the conclusions in this case.

Flow in a whole tumour

The final simulation successfully demonstrated the application of the LBM model to the vascular system of a whole xenograft tumour. The objective here was to demonstrate the viability of such an approach to model flow, where the contribution of local geometry, and topology to flow was derived directly from the information in the original scanned vasculature.

The methods described for the derivation of vascular networks of whole tumours is highly effective, and the data adaptable. It is conceivable that these types of data could be used by other vascular model flow models where more complex schemes are being proposed. This could include blood-borne tracer representative of therapeutic agents,

whose transport was conducted by the lattice-Boltzmann fluid. The quantitative differences between the transport properties in normal and tumour tissues could then be assessed.

Chapter 6: Further work and development

6.1 Future work

This thesis has prompted many ideas which for reasons of limited time and resources could not be accommodated within the scope of the project. It is nevertheless fitting to discuss them briefly in this chapter.

6.2.1 Future corrosion casting and tomography work

A key outcome of the work carried out in this thesis was the generation of a detailed method for producing tomographic images from corrosion casts of tumour vessels. As demonstrated by the results obtained, the new method is very successful and to our knowledge exceeds the highest resolution rendering of tumour vascular architecture reported in the literature. This has opened up many possibilities and interesting applications. Over the course of the project, these images have generated great interest from other scientists in the field.

All the corrosion casting work was performed in Germany due to a restriction in our site-licence for carrying out this type of work. A new licence has since been secured for the Department, which will greatly facilitate future casting work and enable more robust studies to be carried out using the techniques outlined in [Chapters 4&5].

This study included two colorectal xenografts which represented either end of the pathophysiological spectrum, one being a well differentiated and one a poorly differentiated tumour. While interesting similarities and differences between these tumours and clinical samples were found, it is now important to extend this study to include an extended range of colorectal models. This will allow us to determine their wider importance as pre-clinical models, and their potential use for predicting response in clinical trials.

Clinical tumours are also of real interest as they represent the ideal basis for any vascular model. Although the X-ray micro-computed tomography machines limits the size of whole tumours that can be scanned, patients commonly have smaller polyps in

the size range of ~1cm. 3D information these smaller clinical tumours would be of great value to us and collaborators[10].

6.2.2 A 2-polymer casting strategy to differentially mark venous and arterial vessels in tumour corrosion casts

The current method employed for generating this data could be improved further for the purposes of assisting the identification of inlets and outlets of the vascular system. Clear identification of veins and arteries was more difficult for the casts as the endothelial markings were not always present on the tumour vessels. To assist this in the future, a novel method for casting the tumour vascular system with two differentiable polymers is proposed here. The system utilises two casting agents, the first is the same MERCOX polymer used previously, and the second is a mixture of MERCOX and a size-controlled microsphere suspension which can easily be identified in the tomography data. The first polymer would be perfused systemically (e.g. from aorta to right-ventricle for mouse tumours) to identify the venous vessel system. Before this is set, the second casting agent is applied to mark the arterial vessels [Figure 6.1], as the microspheres are too large to pass through the capillary system.

Size-controlled embolising agents should be formed from a suitable material that is differentially radiopaque to the MERCOX polymer, with a minimum size larger than the capillary elements (e.g >5-20microns in diameter). Readily available polystyerene based microspheres manufactured by Polysciences [Polysciences, 2007], could be used for such a purpose.

[10] Professor Moritz Konerding, Professor Elizabeth Bullitt in relation to tortuosity studies in microvascular datasets [Bullitt et al., 1999;Bullitt et al., 2003] and Dr Alfons Hoekstra, in relation to vascularised tumour simulations [Hoekstra, 2006].

Figure 6.1. A method for differentially labelled arterial and venous vascular corrosion casts

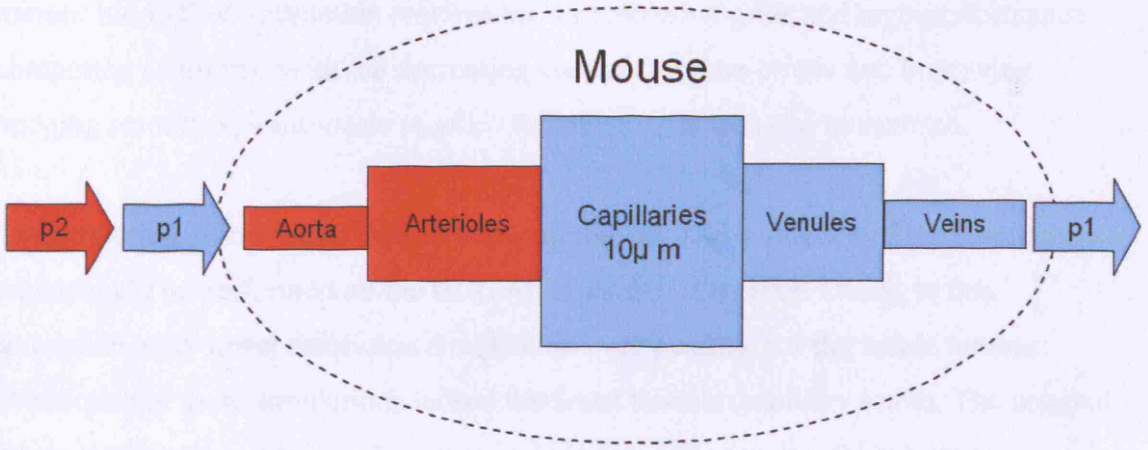

Figure 6.1. Differentially labelled artery and vein casting scheme. The primary casting polymer P1 is normal MERCOX and P2 is a secondary casting polymer containing a suspension of microspheres (15-20µm in diameter) which cannot pass through the capillaries and so P2 marks the arteries. The presence of microspheres can easily be detected in the tomography data.

6.2.3 Validation of micro-CT segmentation and flow analysis

More sophisticated benchmarks could be made between the cast vessels using stereo-imaging and micro-CT to improve confidence in the results. These could include a standard test for segmentation accuracy performed using pre-measured samples of MERCOX, under a range of imaging settings, mercox densities and sample shapes. Calibrations such as this would help further standardise of the segmentation process.

Flow analysis could be validated in conjunction with new developments in micro-MRI machines, which will allow the validation of 3D blood flow models in-situ by analysing the flow of tracer agents through the system over time.

6.3.1 Computation power

The localised interactions used in the lattice-Boltzmann method means it is readily scalable and further development of this model system for practical application of whole tumour blood flow simulation requires higher resolution grids and high-performance computing solutions. With the decreasing cost of compute-power and improving imaging resources, multi-scale *in-silico* tumour simulations can be realised.

The limitation on computer time determined the size and resolution of the simulations which could be performed on the UCL Altix parallel computer. Owing to this restriction, only lower resolution simulations were possible for the whole tumour. Consequently these simulations lacked the finest vessels (capillary scale). The original micro-tomography data does however include these finer scale capillary systems, and future plans are to use this higher resolution data for flow simulations on a larger parallel computing infrastructure, such the grid-scale simulations described by Venturoli *et al.* [Venturoli et al., 2005].

6.3.2 Extensions of the blood flow model

The main challenge facing any vertical integration project, such as modelling tumour blood flow, lies in how the different strata of the system are incorporated in the global model and what is required of the model. From an experimental perspective, measures and studies of velocity, pressure, wall shear stress, viscosity and cellular aggregation will also be of importance to the development and validation of these models. Currently much of this difficult experimental work and the infrastructure for its dissemination is underway in the Microcirculation Physiome project [Popel et al., 1999;Popel et al., 1998].

The ultimate goal of incorporating elements such as blood cells and drug molecules into the model is one example of how such systems can rapidly grow in complexity. Here again lattice-Boltzmann models are attractive. In this area authors such as Ladd [Ladd, 1994b;Ladd, 1994a] lead the way with work on lattice-Boltzmann colloidal suspensions and flows, and many groups are working on how to adapt methods to the application of cellular suspensions in blood flow. Typically, larger suspended particle are modelled off-grid. Here a particle might have a radius encompassing many grid points, and is assigned initial translational and rotational components of velocity. The boundary

conditions of the fluid are then updated at each time-step in accordance with the particle velocity, and the change in momentum of the fluid distribution functions at the particle's surface. It is abundantly clear that this is a hugely challenging problem but significant progress has being made on lattice-Boltzmann models which are inclusive of visco-elastic [Lallemand et al., 2003] and colloidal [Ding and Aidun, 2006;Chatterji and Horbach, 2005] [Cates et al., 2004;Hyvaluoma et al., 2005;Dupin et al., 2006;Dupin et al., 2007] properties.

Once a suitable method of modelling the haematocrit is established, it will be possible to develop an accurate formulation for the temporal and spatial distribution of oxygen and model its effects in the extravascular environment, particularly in relation to the metabolism of cellular components, cytotoxic drugs and radio-therapies. Preliminary work of this type was conducted on two-dimensional distributions of vessels, but many aspects of this are strongly dependent on a reliable three-dimensional model [Dasu et al., 2003;Kohandel et al., 2007]. With the availability of a detailed three-dimensional model of the vascular and avascular spaces, provided by the micro-tomography techniques developed in this thesis, progress can now be made in this area.

A further area of interest lies in the elucidation of wall shear-stress in the tumour. This has been of keen interest in regard to the action of anti-vascular drugs, where the action of shear on 'rounded up' endothelial cells may be important to the mechanism of these agents [McDougall et al., 2006]. Shear stress was not discussed in this thesis, but it can readily be determined from the velocity field data [Artoli, 2007] generated in our studies. The influence of the vascular architecture on local wall shear stress would be a very interesting extension to the current work.

These developments will provide a greater depth of understanding of microcirculation physiology in both normal and disease states such as tumours, and will assist not only with optimising the design of therapeutic agents and drug delivery vehicles, but also may also offer a way of predicting response to treatment for clinical trials.

Appendix

Appendix 1

A1.1 - Parameter input file (*.in)

```
# Input geometry (0=sample,1=surface triangles)
0
# Geometry file
channel_25x25x101_fluid_23x23x101.smp
# Resolution (x y z)
1 1 1
# Decomposition (x y z or file name)
1 1 1
# Maximum number of iterations
100000
#Relative error for convergence study
1e-4
# Flow direction (x=0,y=1,z=2) (must be z for velocity inlet)
2
# Body force # or inlet velocity
0.0002666
# Fluid layers (or clone layers in positive z face for velocity inlet)
0
# Domain bound.cond. (0=slip,1=no-slip,2=periodic,
#   3=velocity inlet and free flow outlet)
3
# Fluid-solid bound.cond. (0=SBB,1=LIBB,2=QIBB,3=MR)
0
# Momentum averaging (0=off,1=on)
0
# Relaxation mode (lin.BGK = 0, BGK = 1,
# MMM = 2, MRT = 3)
1
# Relaxation parameters (
# tau for lin.BGK and BGK;
# shear and bulk tau for MMM;
# s1,s2,s4,s9,s10,s16,we,wej, wxx,
# and mean density for MRT)
```

```
# MRT-BGK
#0.25 0.25 0.25 0.25 0.25 0.25 3.0 -5.5 -0.5 1.0
# "optimal" MRT
#1.19 1.4 1.2 0.4 1.4 1.98 0.0 -7.54 0.0 1.0
# MRT-MMM with bgk parameters
#1.0 1.0 1.0 1.0 1.0 1.0 3.0 -5.5 -0.5 1.0
#1.0 1.0
1.0
# Initial velocity (x y z)
0.0 0.0 0.0
# Initial density of the fluid
1.0
# Time interval for statistical output
100
# Time span for permeability averaging
# (or number of time steps for velocity inlet
#  averaging, 1 equals to no averaging)
2
# Time step to start IMR
100
# Time interval for IMR
50
# Time span for IMR momentum averaging
4
# Characteristic diameter of the system
20.0
# Number of velocity outputs after simulation
5
# Time interval for velocity outputs after simulation
10
# Offset for velocity output domain
0 0 0
# Domain size for velocity output
89 89 89
# base file name for output files
channel_25x25x101_fluid_23x23x101
# execution info
Simulation of fluid flow in a channel for the purpose of benchmark
studies on the Ladds velocity inlet, and Grads Open outlet boundary
conditions. This tube is a 25x25x101 lattice unit domain, with the
```

fluid domain in a square cross section 23x23x101, leaving a single node bounding wall around the fluid domain.

A1.2 - Micro-computed-tomography (*.raw)

Binary RAW file. Voxels are encoded as a sequence of:
(0=void voxel) and (255=fluid voxel)
The void voxels are analogous to the solid phase in the stardust file.

A1.3 - Stardust file (*.st)

A simple text encoding of the RAW file as a sequence of:
(1=solid node), (0=fluid node).

A1.4 - Sample file (*.smp)

```
# Dimensions of the sample (x,y,z)
25 25 101
# Order of the sample data (lead, median, rear)
# When sample data is traversed, index for the lead
# coordinate grows fastest and index for the rear
# coordinate grows slowest
0 1 2
# Number of phases or if there are only two phases,
# phase number for the first phase segment
1
regoaaf@chemd201:~/Simulator/NewSIMULATION_FILES/tube> cat
channel_25x25x101_fluid_23x23x101.smp | more
# Dimensions of the sample (x,y,z)
25 25 101
# Order of the sample data (lead, median, rear)
# When sample data is traversed, index for the lead coordinate grows
#fastest and index for the rear coordinate grows slowest
0 1 2
# Number of phases or if there are only two phases,
# phase number for the first phase segment
1
# Phase segments and if there are more than two
# phases, index of the phase for each segment
26
23
2
23 (…etc)
```

Appendix 2

A2.1 - Simulation results summary file (*.dat)

```
#Porous 3D simulation parameters
#==============================
#Input geometry format
sample
#Geometry file
channel_25x25x101_fluid_23x23x101.smp
#Resolution (x y z)
1 1 1
#Divisions (x y z)
1 1 1
#Decomposition file

#Maximum number of iterations
100000
#Relative error for convergence study
0.0001
#Flow direction
2
#Body force
0.0002666
#Fluid layer
0
#Domain boundary condition
3
#Fluid-solid boundary condition
0
#Momentum averaging
off
#Relaxation mode
1
#Relaxation parameters
1
#Kinetic viscosity
0.166667
#Initial velocities (x y z)
0 0 0
#Initial velocity file
```

```
#Initial density of the fluid
1
#Time interval for statistical output
100
#Time span for permeability averaging
2
#Time step to start IMR
100
#Time interval for IMR
50
#Time span for IMR momentum averaging
4
#Characteristic diameter of the system
20
#Base name for output files
channel_25x25x101_fluid_23x23x101
#Execution info
Simulation of fluid flow in a channel for the purpose of benchmark
studies on the Ladds velocity inlet, and Grads Open outlet boundary
conditions. This tube is a 25x25x101 lattice unit domain, with the
fluid domain in a square cross section 23x23x101, leaving a single
node bounding wall around the fluid domain.

#Porous 3D sample information
#============================
#Fluid nodes in the sample
53429
#Sample porosity
0.8464
#Specific surface area of the sample
0.1472
#Permeability
0
#Tortuosity
0
#Pressure loss coefficient k_0
0
#Total momentum (including fluid layers)(x y z)
3.91815e-12 3.17767e-12 -14.2636
#Sample momentum (x y z)
```

```
3.91815e-12 3.17767e-12 -14.2636
#Average velocity in the sample (x y z)
7.32707e-17 5.9422e-17 -0.000266642
#Total mass (including fluid layers)
53493.4
#Sample mass
53493.4

#Porous 3D simulation information
#================================
#Simulation dimensions
25 25 101
#Time iterations
2900
#Time spent in the computational kernel (s)
224.005
#Simulation date and time
Sat Sep  1 13:07:37 2007
#Number of processors involved
1

#Porous 3D workload information (process 0)
#=========================================
#Number of lattice nodes (including ghost layers)
27 27 103
#Number of fluid nodes (including ghost layers)
65391
```

A2.2 - Simulation evolution results file (*.evol)

```
# columns: 1. time step, 2. total mass, 3. total mom. x-dir, 4. total
mom. y-dir, 5. total mom. z-dir, 6. sample mass, 7. sample mom. x-dir,
8. sample mom. y-dir, 9. sample mom. z-dir
100 53443.1 -5.30874e-13 7.61596e-13 -6.07236 53443.1 -5.30874e-13
7.61596e-13 -6.07236
200 53456.6 -4.2898e-13 1.64806e-13 -10.0716 53456.6 -4.2898e-13
1.64806e-13 -10.0716
300 53465.1 -2.43076e-13 -9.77968e-14 -10.5868 53465.1 -2.43076e-13 -
9.77968e-14 -10.5868
```

400 53471.5 1.1606e-13 3.78655e-14 -11.0064 53471.5 1.1606e-13
3.78655e-14 -11.0064
500 53476.5 1.22138e-13 2.87874e-13 -11.8433 53476.5 1.22138e-13
2.87874e-13 -11.8433
600 53480.6 3.2822e-13 2.68351e-13 -12.5092 53480.6 3.2822e-13
2.68351e-13 -12.5092
700 53483.6 5.04697e-13 3.48235e-13 -12.905 53483.6 5.04697e-13
3.48235e-13 -12.905
800 53485.8 5.69884e-13 4.95198e-13 -13.2017 53485.8 5.69884e-13
4.95198e-13 -13.2017
900 53487.6 6.67504e-13 7.15341e-13 -13.4532 53487.6 6.67504e-13
7.15341e-13 -13.4532
1000 53489 9.37798e-13 8.74145e-13 -13.6482 53489 9.37798e-13
8.74145e-13 -13.6482
1100 53490 9.44352e-13 1.03466e-12 -13.7924 53490 9.44352e-13
1.03466e-12 -13.7924
1200 53490.8 1.39565e-12 1.47612e-12 -13.9023 53490.8 1.39565e-12
1.47612e-12 -13.9023
1300 53491.4 1.73028e-12 1.48846e-12 -13.9877 53491.4 1.73028e-12
1.48846e-12 -13.9877
1400 53491.9 1.80036e-12 1.54119e-12 -14.0533 53491.9 1.80036e-12
1.54119e-12 -14.0533
1500 53492.2 1.97901e-12 1.5792e-12 -14.1033 53492.2 1.97901e-12
1.5792e-12 -14.1033
1600 53492.5 2.00456e-12 1.75109e-12 -14.1416 53492.5 2.00456e-12
1.75109e-12 -14.1416
1700 53492.7 2.13539e-12 2.07515e-12 -14.171 53492.7 2.13539e-12
2.07515e-12 -14.171
1800 53492.9 2.34702e-12 1.99386e-12 -14.1936 53492.9 2.34702e-12
1.99386e-12 -14.1936
1900 53493 2.30688e-12 2.17638e-12 -14.2109 53493 2.30688e-12
2.17638e-12 -14.2109
2000 53493.1 2.4387e-12 2.16544e-12 -14.2241 53493.1 2.4387e-12
2.16544e-12 -14.2241
2100 53493.2 2.55184e-12 2.34968e-12 -14.2342 53493.2 2.55184e-12
2.34968e-12 -14.2342
2200 53493.2 2.61946e-12 2.57199e-12 -14.242 53493.2 2.61946e-12
2.57199e-12 -14.242
2300 53493.3 2.88269e-12 2.86557e-12 -14.248 53493.3 2.88269e-12
2.86557e-12 -14.248

```
2400 53493.3 3.12808e-12 2.90452e-12 -14.2526 53493.3 3.12808e-12
2.90452e-12 -14.2526
2500 53493.3 3.24749e-12 2.94072e-12 -14.2561 53493.3 3.24749e-12
2.94072e-12 -14.2561
2600 53493.3 3.43202e-12 3.05523e-12 -14.2587 53493.3 3.43202e-12
3.05523e-12 -14.2587
2700 53493.3 3.66802e-12 3.1455e-12 -14.2608 53493.3 3.66802e-12
3.1455e-12 -14.2608
2800 53493.4 3.64017e-12 3.0007e-12 -14.2624 53493.4 3.64017e-12
3.0007e-12 -14.2624
2900 53493.4 3.91815e-12 3.17767e-12 -14.2636 53493.4 3.91815e-12
3.17767e-12 -14.2636
```

A2.3 - Simulation fields file (density *r* and velocity *u*) (*.fields)

The file is layed out in this format.

positions: [x] [y] [z]) [density] (velocity components: [xv][yv][zv]

Appendix 3

List of Publications

- Three-dimensional Analysis of tumour vascular corrosion casts using Stereo-imaging and Micro-computed Tomography. AA Folarin, MA Konerding, J Timonen, B, Pedley, S Nagl. American Journal of Physiology (pending publication).
- Simulation of microvascular hydrodynamics using Lattice Boltzmann Method with X-ray micro-computed tomography of tumour vascular corrosion casts, AA Folarin, J Timonen, MA Konerding, S Nagl (pending publication).
- A boundary condition for arbitrary shaped inlets in Lattice-Boltzmann simulations. K. Mattila, J. Hyv¨aluoma, A. Folarin, T. Rossi. International Journal For Numerical Methods In Fluids (Submitted for publication 2008).
- Predicting Response to Radioimmunotherapy from the Tumor Microenvironment of Colorectal Carcinomas. R. Barbara Pedley, Ethaar El Emir, Uzma Qureshi, Jason L. J. Dearling, Geoffrey M. Boxer, Innes Clatworthy, Amos A. Folarin, Mathew P. Robson, Moritz A. Konerding, Sylvia Nagl, and Richard H. J. Begent. Accepted for publication 2007. Cancer Res. 2007 Dec 15;67(24):11896-905.
- Conference Publication
    - Probability Model-Based Analysis of Tumor Vasculature Data Babatunde A. Ogunnaike[1], Claudio A. Gelmi[1], Amos Folarin[2], Sylvia Nagl[2], and Moritz A. Konerding[3], The 2005 Annual Meeting (Cincinnati, OH) Cincinnati, OH

Appendix 4

Glossary of acronyms

A

ADEPT – Antibody Directed Enzyme Pro-drug Threrapy.
ANOVA – Analysis of Variance. A statistical test for comparing the mean values of multiple populations.

B

BC – Boundary Condition.
BSA – Bovine Serum Albumin.

C

CCD – Charged Coupled Device, the light sensitive array used various forms of digital image capture.

D

D3Q19 – A lattice of three dimensions associated with 18 velocities and 1 rest velocity. This lattice system is one of a number that satisfies the symmetry requirements of the Lattice Boltzmann Method.
DM – Distance Metric. A tortuosity metric determined by the ratio of tortuous distance to linear distance made by a path in space.
DNA – Deoxyribonucleic Acid.

E

EC – Endothelial Cell.
ECM – Extracellular Matrix, a collection of proteins and proteoglycans that occupy the space between cells.
ESL – Endothelial Surface Layer. A layer of hydrated glycoproteins that lubricate the internal surface of the blood vessel.

F

FPC – Familial Polyposis Coli, a hereditary condition associated with the formation of multiple colo-rectal polyps.
FGF-2 – Fibroblast Growth Factor 2.

H

HIF – Hypoxia Inducible Factor, the transcription factor associated with regulating gene expression at HRE sites.
HRE – Hypoxia Response Element, a promoter associated with mediating response to oxygen deprivation.

I

ICM – Inflection Count Metric. A measure of tortuosity based on the number of full inflections made by a line in space.
IFP – Interstitial Fluid Pressure.

L

LBM – Lattice Boltzmann Method.
LGM – Lattice Gas Method.
LS147T – a moderate-to-poorly differentiated xenograft tumour consisting of solid chords of cells with numerous signet ring forms, a few glandular acini and large necrotic regions.
LU – Lattice Units.

M

MERCOX, Mercox-CL2B – a epoxy resin with a low viscosity when unset, commonly used as a filling agent for casting biological specimens.
MRM – Magnetic Resonance Microscopy, a high resolution magnetic resolution imaging system.
MVD – Microvascular Density. A measure relating to the fraction of space occupied by vascular tissue in a whole tissue sample.

R

RBC – Red Blood Cell.

S

SEM – Scanning Electron Microscope.
SOAM – Sum Of Angles Metric. The integral of angles made by a tortuous path in space relative to the linear distance between start and end points.
SSA – Specific Surface Area. A measure of surface area relative to volume.
SW1222 – a well differentiated xenograft, with extensive vascularisation and noticeable structural organisation and morphology.

T

TAF – Tumour Angiogenesis Factor, a generic reference to agents involved in the vascularisation process.
TNM – tumour, node, metastasis classification system for colorectal cancers. This scheme qualifies a tumours progression depending on the extent of the presence and absence of these traits.

U

UCL – University College London.

V

VEGF – A range of diffusible cytokines associated with promoting vessel growth.
VCT – Volume Computed Tomography.

X

X-ray Micro-CT, Micro-CT, (μCT) – Micro Computed Tomography.

Reference List

1. Alarcon T, Byrne HM, Maini PK: A cellular automaton model for tumour growth in inhomogeneous environment. J Theor Biol 2003;225:257-274.

2. Alarcon T, Byrne HM, Maini PK: Towards whole-organ modelling of tumour growth. Prog Biophys Mol Biol 2004;85:451-472.

3. Alarcon T, Byrne HM, Maini PK: A design principle for vascular beds: the effects of complex blood rheology. Microvasc Res 2005;69:156-172.

4. Alexandrakis G, Brown EB, Tong RT, McKee TD, Campbell RB, Boucher Y, Jain RK: Two-photon fluorescence correlation microscopy reveals the two-phase nature of transport in tumors. Nat Med 2004;10:203-207.

5. Anderson AR, Chaplain MA: Continuous and discrete mathematical models of tumor-induced angiogenesis. Bull Math Biol 1998;60:857-899.

6. Artoli, A. M. Mesoscopic Computational Haemodynamics. 2007. University of Amsterdam.

7. Bagchi P: Mesoscale simulation of blood flow in small vessels. Biophys J 2007;92:1858-1877.

8. Baish JW, Gazit Y, Berk DA, Nozue M, Baxter LT, Jain RK: Role of tumor vascular architecture in nutrient and drug delivery: an invasion percolation-based network model. Microvasc Res 1996;51:327-346.

9. Baish JW, Jain RK: Cancer, angiogenesis and fractals. Nat Med 1998;4:984.

10. Baish JW, Jain RK: Fractals and cancer. Cancer Res 2000;60:3683-3688.

11. Baish JW, Netti PA, Jain RK: Transmural coupling of fluid flow in microcirculatory network and interstitium in tumors. Microvasc Res 1997;53:128-141.

12. Bando H, Toi M, Kitada K, Koike M: Genes commonly upregulated by hypoxia in human breast cancer cells MCF-7 and MDA-MB-231. Biomed Pharmacother 2003;57:333-340.

13. Barber, P. R., Armeer-Beg, S. M., Vojnovic, B., Hodgkiss, R. J., Tozer, G. M., Wilson, J., and Prise, V. E. 3D Imaging and Quantification of Complex Vascular Networks. 5139. 2003a. Proceedings of SPIE-OSA Biomedical Optics.

14. Barber PR, Vojnovic B, Ameer-Beg SM, Hodgkiss RJ, Tozer GM, Wilson J: Semi-automated software for the three-dimensional delineation of complex vascular networks. J Microsc 2003b;211:54-62.

15. Bassingthwaighte JB, Li Z, Qian H: Blood flows and metabolic components of the cardiome. Prog Biophys Mol Biol 1998;69:445-461.

16. Bentley MD, Ortiz MC, Ritman EL, Romero JC: The use of microcomputed tomography to study microvasculature in small rodents. Am J Physiol Regul Integr Comp Physiol 2002;282:R1267-R1279.

17. Bhatnagar PL, Gross EP, Krook M: A Model for Collision Processes in Gases. I. Small Amplitude Processes in Charged and Neutral One-Component Systems. Phys Rev 1954;94:511.

18. Bloor MI: The flow of blood in the capillaries. Phys Med Biol 1968;13:443-450.

19. Boryczko K, Dzwinel W, Yuen DA: Dynamical clustering of red blood cells in capillary vessels. J Mol Model (Online) 2003;9:16-33.

20. Boucher Y, Baxter LT, Jain RK: Interstitial pressure gradients in tissue-isolated and subcutaneous tumors: implications for therapy. Cancer Res 1990;50:4478-4484.

21. Boucher Y, Leunig M, Jain RK: Tumor angiogenesis and interstitial hypertension. Cancer Res 1996;56:4264-4266.

22. Braumann UD, Kuska JP, Einenkel J, Horn LC, Loffler M, Hockel M: Three-dimensional reconstruction and quantification of cervical carcinoma invasion fronts from histological serial sections. IEEE Trans Med Imaging 2005;24:1286-1307.

23. Brey EM, King TW, Johnston C, McIntire LV, Reece GP, Patrick CW, Jr.: A technique for quantitative three-dimensional analysis of microvascular structure. Microvasc Res 2002;63:279-294.

24. Bryan, J. Volsuite 3.3 (http://www.osc.edu/archive/VolSuite). [3.3]. 2005.

25. Buetow PC, Buck JL, Carr NJ, Pantongrag-Brown L: From the archives of the AFIP. Colorectal adenocarcinoma: radiologic-pathologic correlation. Radiographics 1995;15:127-146.

26. Buick.J.M. Minimum vessel-spanning lattice units for lattice-Boltzmann flow simulations. 13-9-2005.

27. Buick.J.M., Cosgrove JA, Tounge SJ, Mulholland AJ, Steves BA, Collins MW: The Lattice Boltzmann equation for modelling arterial flows: review and application. Biomedicine and Pharmacotherapy 2003;57:345-346.

28. Bullitt E, Ewend MG, Aylward S, Lin W, Gerig G, Joshi S, Jung I, Muller K, Smith JK: Abnormal vessel tortuosity as a marker of treatment response of malignant gliomas: preliminary report. Technol Cancer Res Treat 2004;3:577-584.

29. Bullitt E, Gerig G, Pizer SM, Lin W, Aylward SR: Measuring tortuosity of the intracerebral vasculature from MRA images. IEEE Trans Med Imaging 2003;22:1163-1171.

30. Bullitt E, Liu A, Aylward SR, Coffey C, Stone J, Mukherji SK, Muller KE, Pizer SM: Registration of 3D cerebral vessels with 2D digital angiograms: clinical evaluation. Acad Radiol 1999;6:539-546.

31. Bunde A, Havlin S: A brief introduction to fractal geometry.; Fractals in Science. 2004 pp 1-25.

32. Carmeliet P, Jain RK: Angiogenesis in cancer and other diseases. Nature 2000;407:249-257.

33. Cates ME, Stratford K, Adhikari R, Stansell P, Desplat J-C, Pagonabarraga I, Wagner AJ: Simulating Colloid Hydrodynamics with Lattice Boltzmann. J Phys : Condens Matter 2004;16:S3903-S3915.

34. Chantrain CF, Shimada H, Jodele S, Groshen S, Ye W, Shalinsky DR, Werb Z, Coussens LM, DeClerck YA: Stromal matrix metalloproteinase-9 regulates the vascular architecture in neuroblastoma by promoting pericyte recruitment. Cancer Res 2004;64:1675-1686.

35. Chaplain M, Anderson A: Mathematical modelling of tumour-induced angiogenesis: network growth and structure. Cancer Treat Res 2004;117:51-75.

36. Chaplain MA: The mathematical modelling of tumour angiogenesis and invasion. Acta Biotheor 1995;43:387-402.

37. Chatterji A, Horbach J: Combining molecular dynamics with Lattice Boltzmann: a hybrid method for the simulation of (charged) colloidal systems. J Chem Phys 2005;122:184903.

38. Chen S, Doolen GD: Lattice Boltzmann Method Fof Fluid Flows. Annual Review of Fluid Mechanics 1998;30:329-364.

39. Cheung N, Wong MP, Yuen ST, Leung SY, Chung LP: Tissue-specific expression pattern of vascular endothelial growth factor isoforms in the malignant transformation of lung and colon. Hum Pathol 1998;29:910-914.

40. Chikatamarla SS, Ansumali S, Karlin IV: Grad's approximation for missing data in lattice Boltzmann simulations. Europhysics Letters (EPL) 2006;74:215-221.

41. Corps, N. and Folarin, A. A. Skyscan Microcomputed Tomography (Technical Staff Communication). 2006.

42. Dasu A, Toma-Dasu I, Karlsson M: Theoretical simulation of tumour oxygenation and results from acute and chronic hypoxia. Phys Med Biol 2003;48:2829-2842.

43. Desjardins C, Duling BR: Heparinase treatment suggests a role for the endothelial cell glycocalyx in regulation of capillary hematocrit. Am J Physiol 1990;258:H647-H654.

44. Ding EJ, Aidun CK: Cluster size distribution and scaling for spherical particles and red blood cells in pressure-driven flows at small Reynolds number. Phys Rev Lett 2006;96:204502.

45. Dupin MM, Halliday I, Care CM: A multi-component lattice Boltzmann scheme: towards the mesoscale simulation of blood flow. Med Eng Phys 2006;28:13-18.

46. Dupin MM, Halliday I, Care CM, Alboul L, Munn LL: Modeling the flow of dense suspensions of deformable particles in three dimensions. Phys Rev E Stat Nonlin Soft Matter Phys 2007;75:066707.

47. Eisenberg B, Decosse JJ, Harford F, Michalek J: Carcinoma of the colon and rectum: the natural history reviewed in 1704 patients. Cancer 1982;49:1131-1134.

48. Erickson K, Braun RD, Yu D, Lanzen J, Wilson D, Brizel DM, Secomb TW, Biaglow JE, Dewhirst MW: Effect of longitudinal oxygen gradients on effectiveness of manipulation of tumor oxygenation. Cancer Res 2003;63:4705-4712.

49. Fait E, Malkusch W, Gnoth SH, Dimitropoulou Ch, Gaumann A, Kirkpatrick CJ, Junginger Th, Konerding M: Microvascular patterns of the human large intestine: morphometric studies of vascular parameters in corrosion casts. Scanning Microscopy 1998;12:641-651.

50. Feldkamp LA, Davis LC, Kress JW: Practical cone-beam algorithm. Journal of the Optical Society of America A: Optics, Image Science, and Vision 1984;1:612-619.

51. Filippova O, Hänel D: Boundary-Fitting and Local Grid Refinement for Lattice-BGK Models. International Journal of Modern Physics C 1998;9:1271-1279.

52. Fink C, Morgan F, Loew LM: Intracellular fluorescent probe concentrations by confocal microscopy. Biophys J 1998;75:1648-1658.

53. Folkman J, Watson K, Ingber D, Hanahan D: Induction of angiogenesis during the transition from hyperplasia to neoplasia. Nature 1989;339:58-61.

54. Frisch U, Hasslacher B, Pomeau Y: Lattice-Gas Automata for the Navier-Stokes Equation. Phys Rev Lett 1986;56:1505-1508.

55. Fujimori S, Kishida T, Yoshida Y, Kobayashi M: Superficial blood flow, blood volume, and blood velocity in colorectal tubular adenomas and adenocarcinomas. J Gastroenterol 1999;34:467-473.

56. Gafiychuk VV, Lubashevsky IA: On the principles of the vascular network branching. J Theor Biol 2001;212:1-9.

57. Gazit Y, Berk DA, Leunig M, Baxter LT, Jain RK: Scale-Invariant Behavior and Vascular Network Formation in Normal and Tumor Tissue. Phys Rev Lett 1995;75:2428.

58. Gerhardt H, Golding M, Fruttiger M, Ruhrberg C, Lundkvist A, Abramsson A, Jeltsch M, Mitchell C, Alitalo K, Shima D, Betsholtz C: VEGF guides angiogenic sprouting utilizing endothelial tip cell filopodia. J Cell Biol 2003;161:1163-1177.

59. Gerhardt H, Ruhrberg C, Abramsson A, Fujisawa H, Shima D, Betsholtz C: Neuropilin-1 is required for endothelial tip cell guidance in the developing central nervous system. Dev Dyn 2004;231:503-509.

60. Giavazzi R, Sennino B, Coltrini D, Garofalo A, Dossi R, Ronca R, Tosatti MP, Presta M: Distinct role of fibroblast growth factor-2 and vascular endothelial growth factor on tumor growth and angiogenesis. Am J Pathol 2003;162:1913-1926.

61. Gillies RJ, Raghunand N, Karczmar GS, Bhujwalla ZM: MRI of the tumor microenvironment. J Magn Reson Imaging 2002;16:430-450.

62. Glover P, Mansfield P: Limits to magnetic resonance microscopy. Rep Prog Phys 2002;**65**:1489-1511.

63. Goldbrunner RH, Bendszus M, Tonn JC: Models for angiogenesis in gliomas. Cancer Treat Res 2004;117:115-135.

64. Goldsmith HL, Cokelet GR, Gaehtgens P: Robin Fahraeus: evolution of his concepts in cardiovascular physiology. Am J Physiol 1989;257:H1005-H1015.

65. Grunstein J, Masbad JJ, Hickey R, Giordano F, Johnson RS: Isoforms of vascular endothelial growth factor act in a coordinate fashion To recruit and expand tumor vasculature. Mol Cell Biol 2000;20:7282-7291.

66. Grunstein J, Roberts WG, Mathieu-Costello O, Hanahan D, Johnson RS: Tumor-derived expression of vascular endothelial growth factor is a critical factor in tumor expansion and vascular function. Cancer Res 1999;59:1592-1598.

67. Guo L, Burke P, Lo SH, Gandour-Edwards R, Lau D: Quantitative analysis of angiogenesis using confocal laser scanning microscopy. Angiogenesis 2001;4:187-191.

68. He X, Zou QS, Luo LS, Dembo M: Analytic solutions of simple flows and analysis of nonslip boundary conditions for the lattice Boltzmann BGK model. Journal of Statistical Physics 1997;87:115-136.

69. Hlatky L, Hahnfeldt P, Folkman J: Clinical application of antiangiogenic therapy: microvessel density, what it does and doesn't tell us. J Natl Cancer Inst 2002;94:883-893.

70. Hoekstra, A. Vascularised tumour simulations. 2006.

71. Holash J, Wiegand SJ, Yancopoulos GD: New model of tumor angiogenesis: dynamic balance between vessel regression and growth mediated by angiopoietins and VEGF. Oncogene 1999;18:5356-5362.

72. Huxley VH, Rumbaut RE: The microvasculature as a dynamic regulator of volume and solute exchange. Clin Exp Pharmacol Physiol 2000;27:847-854.

73. Hyvaluoma J, Raiskinmaki P, Koponen A, Kataja M, Timonen J: Lattice-Boltzmann Simulation of Particle Suspensions in Shear Flow. Journal of Statistical Physics 2005;121:149-161.

74. Hyvaluoma J, Turpeinen T, Raiskinmaki P, Jasberg A, Koponen A, Kataja M, Timonen J, Ramaswamy S: Intrusion of nonwetting liquid in paper. Phys Rev E Stat Nonlin Soft Matter Phys 2007;75:036301.

75. Jain RK: Determinants of tumor blood flow: a review. Cancer Res 1988;48:2641-2658.

76. Jain RK: Barriers to drug delivery in solid tumors. Sci Am 1994;271:58-65.

77. Jain RK: Transport of molecules, particles, and cells in solid tumors. Annu Rev Biomed Eng 1999;1:241-263.

78. Jain RK: Delivery of molecular and cellular medicine to solid tumors. Adv Drug Deliv Rev 2001a;46:149-168.

79. Jain RK: Normalizing tumor vasculature with anti-angiogenic therapy: a new paradigm for combination therapy. Nat Med 2001b;7:987-989.

80. Janot F, Klijanienko J, Russo A, Mamet JP, de Braud F, El Naggar AK, Pignon JP, Luboinski B, Cvitkovic E: Prognostic value of clinicopathological parameters in head and neck squamous cell carcinoma: a prospective analysis. Br J Cancer 1996;73:531-538.

81. Kiessling F, Greschus S, Lichy MP, Bock M, Fink C, Vosseler S, Moll J, Mueller MM, Fusenig NE, Traupe H, Semmler W: Volumetric computed tomography (VCT): a new technology for noninvasive, high-resolution monitoring of tumor angiogenesis. Nat Med 2004;10:1133-1138.

82. Kobayashi H, Takizawa N, Negishi T, Tanishita K: Intravascular inhomogeneous oxygen distribution in microvessels: theory. Respir Physiol Neurobiol 2002;133:271-275.

83. Kohandel M, Kardar M, Milosevic M, Sivaloganathan S: Dynamics of tumor growth and combination of anti-angiogenic and cytotoxic therapies. Phys Med Biol 2007;52:3665-3677.

84. Konerding, M. A. Corrosion cast extrusion domains and blood lakes. 2005

85. Konerding MA: Tumor versus Normal Microvasculature; Encyclopedia of Microvascular Research. 2006 pp 955-959.

86. Konerding MA, Fait E, Dimitropoulou C, Malkusch W, Ferri C, Giavazzi R, Coltrini D, Presta M: Impact of fibroblast growth factor-2 on tumor microvascular architecture. A tridimensional morphometric study. Am J Pathol 1998;152:1607-1616.

87. Konerding MA, Fait E, Gaumann A: 3D microvascular architecture of pre-cancerous lesions and invasive carcinomas of the colon. Br J Cancer 2001;84:1354-1362.

88. Konerding MA, Malkusch W, Klapthor B, van Ackern C, Fait E, Hill SA, Parkins C, Chaplin DJ, Presta M, Denekamp J: Evidence for characteristic vascular patterns in solid tumours: quantitative studies using corrosion casts. Br J Cancer 1999;80:724-732.

89. Konerding MA, Miodonski AJ, Lametschwandtner A: Microvascular corrosion casting in the study of tumor vascularity: a review. Scanning Microsc 1995;9:1233-1243.

90. Kubota T: Metastatic models of human cancer xenografted in the nude mouse: the importance of orthotopic transplantation. J Cell Biochem 1994;56:4-8.

91. Ladd AJC: Numerical simulations of particulate suspensions via a discretized Boltzmann equation. Part 2. Numerical results. J Fluid Mech 1994a;271-311.

92. Ladd AJC: Numerical simulations of particulate suspensions via a discretized Boltzmann equation. Part 1. Theoretical foundation. J Fluid Mech 1994b;271-285.

93. Lallemand P, D'Humieres D, Luo LS, Rubinstein R: Theory of the lattice Boltzmann method: three-dimensional model for linear viscoelastic fluids. Phys Rev E Stat Nonlin Soft Matter Phys 2003;67:021203.

94. Leach MO: Application of magnetic resonance imaging to angiogenesis in breast cancer. Breast Cancer Res 2001;3:22-27.

95. Lee J, Pullan AJ, Smith NP: A computational model of microcirculatory network structure and transient coronary microcirculation. Conf Proc IEEE Eng Med Biol Soc 2004;5:3808-3811.

96. Leunig M, Yuan F, Menger MD, Boucher Y, Goetz AE, Messmer K, Jain RK: Angiogenesis, microvascular architecture, microhemodynamics, and interstitial fluid pressure during early growth of human adenocarcinoma LS174T in SCID mice. Cancer Res 1992;52:6553-6560.

97. Levine HA, Sleeman BD, Nilsen-Hamilton M: Mathematical modeling of the onset of capillary formation initiating angiogenesis. J Math Biol 2001;42:195-238.

98. Longo R, Sarmiento R, Fanelli M, Capaccetti B, Gattuso D, Gasparini G: Anti-angiogenic therapy: rationale, challenges and clinical studies. Angiogenesis 2002;5:237-256.

99. Maddah M, Soltanian-Zadeh H, Afzali-Kusha A, Shahrokni A, Zhang ZG: Three-dimensional analysis of complex branching vessels in confocal microscopy images. Comput Med Imaging Graph 2005;29:487-498.

100. Maehara N: Experimental microcomputed tomography study of the 3D microangioarchitecture of tumors. Eur Radiol 2003;13:1559-1565.

101. Malkusch W, Konerding MA, Klapthor B, Bruch J: A simple and accurate method for 3-D measurements in microcorrosion casts illustrated with tumour vascularization. Anal Cell Pathol 1995;9:69-81.

102. Maniotis AJ, Folberg R, Hess A, Seftor EA, Gardner LM, Pe'er J, Trent JM, Meltzer PS, Hendrix MJ: Vascular channel formation by human melanoma cells in vivo and in vitro: vasculogenic mimicry. Am J Pathol 1999;155:739-752.

103. Manwart C, Aaltosalmi U, Koponen A, Hilfer R, Timonen J: Lattice-Boltzmann and finite-difference simulations for the permeability for three-dimensional porous media. Phy Rev E 2002;66.

104. Marinakis GN, Barbenel JC, Fisher AC, Tsangaris SG: A new capillary viscometer for whole blood viscosimetry. Biorheology 1999;36:311-318.

105. Mattila, K and Hyvaloma, J. Lattice Boltzmann Simulator Code. 2006.
Department of Physics
P.O. Box 35
40014 UNIVERSITY OF JYVÄSKYLÄ
Finland, University of Jyvaskyla.

106. Maxwell RJ, Wilson J, Prise VE, Vojnovic B, Rustin GJ, Lodge MA, Tozer GM: Evaluation of the anti-vascular effects of combretastatin in rodent tumours by dynamic contrast enhanced MRI. NMR Biomed 2002;15:89-98.

107. McDonald DM, Baluk P: Significance of blood vessel leakiness in cancer. Cancer Res 2002;62:5381-5385.

108. McDonald DM, Munn L, Jain RK: Vasculogenic mimicry: how convincing, how novel, and how significant? Am J Pathol 2000;156:383-388.

109. McDougall SR, Anderson AR, Chaplain MA: Mathematical modelling of dynamic adaptive tumour-induced angiogenesis: clinical implications and therapeutic targeting strategies. J Theor Biol 2006;241:564-589.

110. McDougall SR, Anderson AR, Chaplain MA, Sherratt JA: Mathematical modelling of flow through vascular networks: implications for tumour-induced angiogenesis and chemotherapy strategies. Bull Math Biol 2002;64:673-702.

111. Minnich B, Lametschwandtner A: Lengths measurements in microvascular corrosion castings: two-dimensional versus three-dimensional morphometry. Scanning 2000;22:173-177.

112. Mollica F, Jain RK, Netti PA: A model for temporal heterogeneities of tumor blood flow. Microvasc Res 2003;65:56-60.

113. Munn LL: Aberrant vascular architecture in tumors and its importance in drug-based therapies. Drug Discov Today 2003;8:396-403.

114. Muto T, Bussey HJ, Morson BC: The evolution of cancer of the colon and rectum. Cancer 1975;36:2251-2270.

115. Myllys, M. A. Distortion in small vessel micro-computed tomography scans. 2006.

116. Netti PA, Hamberg LM, Babich JW, Kierstead D, Graham W, Hunter GJ, Wolf GL, Fischman A, Boucher Y, Jain RK: Enhancement of fluid filtration across tumor vessels: implication for delivery of macromolecules. Proc Natl Acad Sci U S A 1999;96:3137-3142.

117. Nicosia RF, Zhu WH, Fogel E, Howson KM, Aplin AC: A new ex vivo model to study venous angiogenesis and arterio-venous anastomosis formation. J Vasc Res 2005;42:111-119.

118. Nishisho I, Nakamura Y, Miyoshi Y, Miki Y, Ando H, Horii A, Koyama K, Utsunomiya J, Baba S, Hedge P: Mutations of chromosome 5q21 genes in FAP and colorectal cancer patients. Science 1991;253:665-669.

119. Office For National Statistics. Death rates from selected cancers: by sex: Social Trends 34. Office For National Statistics 2006.

120. Ogunnaike, B. A., Gelmi, C. A., Folarin, A. A, Nagl, S. B., and Konerding, M. A. Probability Model-Based Analysis of Tumor Vasculature Data. 2005. American Institute of Chemical Engineers (Annual Meeting 2005).

121. Orme ME, Chaplain MA: A mathematical model of the first steps of tumour-related angiogenesis: capillary sprout formation and secondary branching. IMA J Math Appl Med Biol 1996;13:73-98.

122. Orme ME, Chaplain MA: Two-dimensional models of tumour angiogenesis and anti-angiogenesis strategies. IMA J Math Appl Med Biol 1997;14:189-205.

123. Patientcenters. Cross-section of the colon wall. Patientcenters http://www.patientcenters.com/colon/news/crc.0101.gif. 2007.

124. Pavlopoulos PM, Konstantinidou AE, Agapitos E, Kavantzas N, Nikolopoulou P, Davaris P: A morphometric study of neovascularization in colorectal carcinoma. Cancer 1998;83:2067-2075.

125. Pedley RB, El Emir E, Flynn AA, Boxer GM, Dearling J, Raleigh JA, Hill SA, Stuart S, Motha R, Begent RH: Synergy between vascular targeting agents and antibody-directed therapy. Int J Radiat Oncol Biol Phys 2002;54:1524-1531.

126. Pedley RB, Hill SA, Boxer GM, Flynn AA, Boden R, Watson R, Dearling J, Chaplin DJ, Begent RH: Eradication of colorectal xenografts by combined radioimmunotherapy and combretastatin a-4 3-O-phosphate. Cancer Res 2001;61:4716-4722.

127. Plank MJ, Sleeman BD, Jones PF: A mathematical model of tumour angiogenesis, regulated by vascular endothelial growth factor and the angiopoietins. J Theor Biol 2004;229:435-454.

128. Polysciences. Polysciences Microspheres. 2007.

129. Popel AS, Greene AS, Ellis CG, Ley KF, Skalak TC, Tonellato PJ: The Microcirculation Physiome Project. Ann Biomed Eng 1998;26:911-913.

130. Popel AS, Johnson RS: Microcirculation and hemorheology. Annu Rev Fluid Mech 2005.

131. Popel AS, Pries AR, Slaaf DW: Microcirculation Physiome Project. J Vasc Res 1999;36:253-255.

132. Potter JD: Reconciling the epidemiology, physiology, and molecular biology of colon cancer. JAMA 1992;268:1573-1577.

133. Pries AR, Secomb TW, Gaehtgens P: Design principles of vascular beds. Circ Res 1995a;77:1017-1023.

134. Pries AR, Secomb TW, Gaehtgens P: Structure and hemodynamics of microvascular networks: heterogeneity and correlations. Am J Physiol 1995b;269:H1713-H1722.

135. Pries AR, Secomb TW, Gaehtgens P: Biophysical aspects of blood flow in the microvasculature. Cardiovasc Res 1996a;32:654-667.

136. Pries AR, Secomb TW, Gaehtgens P: Relationship between structural and hemodynamic heterogeneity in microvascular networks. Am J Physiol 1996b;270:H545-H553.

137. Pries AR, Secomb TW, Gaehtgens P: Structural adaptation and stability of microvascular networks: theory and simulations. Am J Physiol 1998;275:H349-H360.

138. Pries AR, Secomb TW, Gaehtgens P: The endothelial surface layer. Pflugers Arch 2000;440:653-666.

139. Pries AR, Secomb TW, Jacobs H, Sperandio M, Osterloh K, Gaehtgens P: Microvascular blood flow resistance: role of endothelial surface layer. Am J Physiol 1997;273:H2272-H2279.

140. Rasband, W. S. ImageJ 1.36B. 2006.
U. S. National Institutes of Health, Bethesda,
Maryland, USA.

141. Rasi M, Koponen A, Aaltosalmi U, Timonen J, Kataja M: Permeability of Paper: Experiments and Numerical Simulation. International Paper Physics Conference 1999.

142. Retsky MW, Swartzendruber DE, Bame PD, Wardwell RH: Computer model challenges breast cancer treatment strategy. Cancer Invest 1994;12:559-567.

143. Reynolds O: An experimental investigation of the circumstances which determine whether the motion of water shall be direct or sinuous, and of the law of resistance in parallel channels. Philosophical Transactions of the Royal Society 1883;174:935-982.

144. Richman PI, Bodmer WF: Control of differentiation in human colorectal carcinoma cell lines: epithelial-mesenchymal interactions. J Pathol 1988;156:197-211.

145. Rofstad EK: Orthotopic human melanoma xenograft model systems for studies of tumour angiogenesis, pathophysiology, treatment sensitivity and metastatic pattern. Br J Cancer 1994;70:804-812.

146. Rorden, C. EzAnova. 2007.

147. Ruggeri BA, Robinson C, Angeles T, Wilkinson J, Clapper ML: The chemopreventive agent oltipraz possesses potent antiangiogenic activity in vitro, ex vivo, and in vivo and inhibits tumor xenograft growth. Clin Cancer Res 2002;8:267-274.

148. Ruhrberg C, Gerhardt H, Golding M, Watson R, Ioannidou S, Fujisawa H, Betsholtz C, Shima DT: Spatially restricted patterning cues provided by heparin-binding VEGF-A control blood vessel branching morphogenesis. Genes Dev 2002;16:2684-2698.

149. Ruoslahti E: Specialization of tumour vasculature. Nat Rev Cancer 2002;2:83-90.

150. Saltzman WM: Drug Delivery: Drug Transport by Fluid Motion; in Gubbins KE (ed): Engineering Principles for Drug Therapy. Oxford University Press, 2001 pp 159-174.

151. Secomb TW, Hsu R, Pries AR: A model for red blood cell motion in glycocalyx-lined capillaries. Am J Physiol 1998;274:H1016-H1022.

152. Secomb TW, Hsu R, Pries AR: Blood flow and red blood cell deformation in nonuniform capillaries: effects of the endothelial surface layer. Microcirculation 2002;9:189-196.

153. Serini G, Ambrosi D, Giraudo E, Gamba A, Preziosi L, Bussolino F: Modeling the early stages of vascular network assembly. EMBO J 2003;22:1771-1779.

154. Sevick EM, Jain RK: Viscous resistance to blood flow in solid tumors: effect of hematocrit on intratumor blood viscosity. Cancer Res 1989;49:3513-3519.

155. Sharma SK, Pedley RB, Bhatia J, Boxer GM, El Emir E, Qureshi U, Tolner B, Lowe H, Michael NP, Minton N, Begent RH, Chester KA: Sustained tumor regression of human colorectal cancer xenografts using a multifunctional

mannosylated fusion protein in antibody-directed enzyme prodrug therapy. Clin Cancer Res 2005;11:814-825.

156. Skinner SA, Tutton PJ, O'Brien PE: Microvascular architecture of experimental colon tumors in the rat. Cancer Res 1990;50:2411-2417.

157. Smith NP, Pullan AJ, Hunter PJ: Generation of an anatomically based geometric coronary model. Ann Biomed Eng 2000;28:14-25.

158. Sobin LH, Wittekind FL: TNM Classification of Malignant Tumours. 2002.

159. Soltanian-Zadeh, H., Shahrokni, A., and Zoroofi, R. A. A voxel-coding method for quantification of vascular structure from 3D images. 4321, 263-270. 2001. Proceedings of SPIE Medical Imaging Conference (SPIE--The International Society for Optical Engineering). Medical Imaging 2001: Physiology and Function from Multidimensional Images.

160. Steinberg F, Konerding M, Donhuijsen K, Budach V, Streffer C: Investigations on the individuality of tumours from 20 xenotransplanted sarcomas on nude mice. Strahlenther Onkol 1989;165:504-505.

161. Stephanou A, Anderson A, Chaplain M: Mathematical modelling of flow in 2D and 3D vascular networks: Applications to anti-angiogenic and chemotherapeutic drug strategies. Mathematical and Computer Modelling 2005;41:1137-1156.

162. Stephanou, A., McDougall, S. R., Anderson, A. R. A., Chaplain, M. A., and Sherratt, J. A. Mathematical Modelling of Flow in 2D and 3D Vascular Networks: Applications to Anti-angiogenic and Chemotherapeutic Drug Strategies. 2004.

163. Stokes CL, Lauffenburger DA: Analysis of the roles of microvessel endothelial cell random motility and chemotaxis in angiogenesis. J Theor Biol 1991;152:377-403.

164. Succi S: The Lattice Boltzmann Equation for fluid dynamics and beyond. Oxford : Oxford University Press, c2001, 2001.

165. Sun C, Munn LL: Particulate nature of blood determines macroscopic rheology: a 2-D lattice Boltzmann analysis. Biophys J 2005;88:1635-1645.

166. Tan M, Fang HB, Tian GL, Houghton PJ: Repeated-measures models with constrained parameters for incomplete data in tumour xenograft experiments. Stat Med 2005;24:109-119.

167. Tong RT, Boucher Y, Kozin SV, Winkler F, Hicklin DJ, Jain RK: Vascular normalization by vascular endothelial growth factor receptor 2 blockade induces a pressure gradient across the vasculature and improves drug penetration in tumors. Cancer Res 2004;64:3731-3736.

168. Tozer GM, Ameer-Beg SM, Baker J, Barber PR, Hill SA, Hodgkiss RJ, Locke R, Prise VE, Wilson I, Vojnovic B: Intravital imaging of tumour vascular

networks using multi-photon fluorescence microscopy. Adv Drug Deliv Rev 2005;57:135-152.

169. Tozer GM, Prise VE, Wilson J, Cemazar M, Shan S, Dewhirst MW, Barber PR, Vojnovic B, Chaplin DJ: Mechanisms associated with tumor vascular shut-down induced by combretastatin A-4 phosphate: intravital microscopy and measurement of vascular permeability. Cancer Res 2001;61:6413-6422.

170. UCL BEACON project. UCL BEACON project. 2007.

171. Vaupel P, Kallinowski F, Okunieff P: Blood flow, oxygen and nutrient supply, and metabolic microenvironment of human tumors: a review. Cancer Res 1989;49:6449-6465.

172. Venturoli, M., Harvey, M. J., Giupponi, G., Coveney, P. V., Pinning, R. L., Porter, A. R., and Pickles, S. M. Robust Grid-based environment for large scale lattice-Boltzmann simulations. UK e-Science All Hands Meeting 2005 . 2005.

173. Vink H, Duling BR: Capillary endothelial surface layer selectively reduces plasma solute distribution volume. Am J Physiol Heart Circ Physiol 2000;278:H285-H289.

174. White FM: Differential Relations for a Fluid Particle; Fluid Mechanics. McGraw-Hill Science Engineering, 2006a pp 258-261.

175. White FM: Viscous Flow in Ducts; Fluid Mechanics. McGraw-Hill Science Engineering, 2006b pp 338-342.

176. Wilkinson D, Willemsen FJ: Invasion percolation: a new form of percolarion theory. J Phys A:Math Gen 1983;16:3365-3376.

177. Woo MM, Salamanca CM, Minor A, Auersperg N: An improved assay to quantitate the invasiveness of cells in modified Boyden chambers. In Vitro Cell Dev Biol Anim 2007;43:7-9.

178. Yamagishi S, Imaizumi T: Pericyte biology and diseases. Int J Tissue React 2005;27:125-135.

179. Yao X, Hu JF, Daniels M, Yien H, Lu H, Sharan H, Zhou X, Zeng Z, Li T, Yang Y, Hoffman AR: A novel orthotopic tumor model to study growth factors and oncogenes in hepatocarcinogenesis. Clin Cancer Res 2003;9:2719-2726.

180. Yu JL, Rak JW, Klement G, Kerbel RS: Vascular endothelial growth factor isoform expression as a determinant of blood vessel patterning in human melanoma xenografts. Cancer Res 2002;62:1838-1846.

181. Yuan F, Dellian M, Fukumura D, Leunig M, Berk DA, Torchilin VP, Jain RK: Vascular permeability in a human tumor xenograft: molecular size dependence and cutoff size. Cancer Res 1995;55:3752-3756.

182. Yuan F, Salehi HA, Boucher Y, Vasthare US, Tuma RF, Jain RK: Vascular permeability and microcirculation of gliomas and mammary carcinomas transplanted in rat and mouse cranial windows. Cancer Res 1994;54:4564-4568.

183. Ziegler DP: Boundary conditions for lattice Boltzmann simulations. Journal of Statistical Physics 1993;71:1171-1177.

184. Zipfel WR, Williams RM, Webb WW: Nonlinear magic: multiphoton microscopy in the biosciences. Nat Biotechnol 2003;21:1369-1377.

185. Zou Q, He X: On pressure and velocity boundary conditions for the lattice Boltzmann BGK model. Physics of Fluids 1997;9:1591-1598.